

BWR Anticipated Transients Without Scram in the MELLLA+ Expanded Operating Domain

Part 1:
Model Development and Events
Leading to Instability

AVAILABILITY OF REFERENCE MATERIALS IN NRC PUBLICATIONS

NRC Reference Material

As of November 1999, you may electronically access NUREG-series publications and other NRC records at NRC's Library at www.nrc.gov/reading-rm.html. Publicly released records include, to name a few, NUREG-series publications; *Federal Register* notices; applicant, licensee, and vendor documents and correspondence; NRC correspondence and internal memoranda; bulletins and information notices; inspection and investigative reports; licensee event reports; and Commission papers and their attachments.

NRC publications in the NUREG series, NRC regulations, and Title 10, "Energy," in the *Code of Federal Regulations* may also be purchased from one of these two sources.

1. The Superintendent of Documents

U.S. Government Publishing Office
Mail Stop IDCC
Washington, DC 20402-0001
Internet: bookstore.gpo.gov
Telephone: (202) 512-1800
Fax: (202) 512-2104

2. The National Technical Information Service

5301 Shawnee Rd., Alexandria, VA 22312-0002
www.ntis.gov
1-800-553-6847 or, locally, (703) 605-6000

A single copy of each NRC draft report for comment is available free, to the extent of supply, upon written request as follows:

Address: **U.S. Nuclear Regulatory Commission**
Office of Administration
Publications Branch
Washington, DC 20555-0001
E-mail: distribution.resource@nrc.gov
Facsimile: (301) 415-2289

Some publications in the NUREG series that are posted at NRC's Web site address www.nrc.gov/reading-rm/doc-collections/nuregs are updated periodically and may differ from the last printed version. Although references to material found on a Web site bear the date the material was accessed, the material available on the date cited may subsequently be removed from the site.

Non-NRC Reference Material

Documents available from public and special technical libraries include all open literature items, such as books, journal articles, transactions, *Federal Register* notices, Federal and State legislation, and congressional reports. Such documents as theses, dissertations, foreign reports and translations, and non-NRC conference proceedings may be purchased from their sponsoring organization.

Copies of industry codes and standards used in a substantive manner in the NRC regulatory process are maintained at—

The NRC Technical Library

Two White Flint North
11545 Rockville Pike
Rockville, MD 20852-2738

These standards are available in the library for reference use by the public. Codes and standards are usually copyrighted and may be purchased from the originating organization or, if they are American National Standards, from—

American National Standards Institute

11 West 42nd Street
New York, NY 10036-8002
www.ansi.org
(212) 642-4900

Legally binding regulatory requirements are stated only in laws; NRC regulations; licenses, including technical specifications; or orders, not in NUREG-series publications. The views expressed in contractor-prepared publications in this series are not necessarily those of the NRC.

The NUREG series comprises (1) technical and administrative reports and books prepared by the staff (NUREG-XXXX) or agency contractors (NUREG/CR-XXXX), (2) proceedings of conferences (NUREG/CP-XXXX), (3) reports resulting from international agreements (NUREG/IA-XXXX), (4) brochures (NUREG/BR-XXXX), and (5) compilations of legal decisions and orders of the Commission and Atomic and Safety Licensing Boards and of Directors' decisions under Section 2.206 of NRC's regulations (NUREG-0750).

DISCLAIMER: This report was prepared as an account of work sponsored by an agency of the U.S. Government. Neither the U.S. Government nor any agency thereof, nor any employee, makes any warranty, expressed or implied, or assumes any legal liability or responsibility for any third party's use, or the results of such use, of any information, apparatus, product, or process disclosed in this publication, or represents that its use by such third party would not infringe privately owned rights.

BWR Anticipated Transients Without Scram in the MELLLA+ Expanded Operating Domain

Part 1: Model Development and Events Leading to Instability

Manuscript Completed: April 2014
Date Published: June 2015

Prepared by:
Lap-Yan Cheng, Joo Seok Baek, Arantxa Cuadra, Arnold Aronson,
David Diamond, and Peter Yarsky*

Nuclear Science and Technology Department
Brookhaven National Laboratory

*U.S. Nuclear Regulatory Commission

Tarek Zaki, NRC Project Manager

NRC Job Codes V6150 and F6018

Office of Nuclear Regulatory Research

ABSTRACT

We developed models of a BWR/5 boiling water reactor for use with TRACE/PARCS and thereafter to analyze anticipated transients without scram (ATWS). We established the models for three different times during a fuel cycle, and included therein all systems needed for events initiated by turbine trip or the closure of a main steamline isolation valve. They include the standby liquid-control system, recirculation pumps, feedwater and water level control, reactor core isolation cooling system, safety and relief valves, suppression-pool cooling, and other systems. The modeling in the core that we undertook is detailed relative to state-of-the-art models, with four different fuel-rod types included in each fuel assembly, and 382 channels to represent all assemblies, taking into account half-core symmetry. The models we developed can be used for multiple ATWS applications, and for many transients with the reactor trip operational.

The models were applied to ATWS events initiated by a turbine trip while operating in the expanded operating domain "MELLLA+." Sensitivity calculations were undertaken at the beginning-of-cycle to determine the effect of bypass fraction (10%, 25%, 50%, and 100%) and also at peak-hot-excess-reactivity to determine the effect of including a spectral-history correction on the void density. A calculation at end-of-full-power-life allowed us to compare three different times in the fuel cycle.

The regulatory purpose of the current work is to demonstrate the use of TRACE/PARCS in evaluating the potential consequences of ATWS events in BWRs operating under MELLLA+ conditions. Our study offers insights into the reactor's behavior during these events, and in particular the impact of assumed operator actions on the observed oscillatory behavior caused by the reactor's instability and on the eventual shutdown of the reactor. In addition, our study examined the ability of the TRACE/PARCS code system to calculate the complex phenomena during these events. We also gained insights into effective modeling of those phenomena. Hence, this study may be used as a basis for developing rigorous modeling guidance for similar application.

TABLE OF CONTENTS

ABSTRACT.....	iii
TABLE OF CONTENTS.....	v
LIST OF FIGURES.....	ix
LIST OF TABLES.....	xiii
ACKNOWLEDGMENTS.....	xv
ACRONYMS.....	xvii
1 INTRODUCTION.....	1-1
1.1 Background.....	1-1
1.2 Objectives.....	1-4
1.3 Organization of Report.....	1-5
2 METHODOLOGY.....	2-1
2.1 The TRACE/PARCS Coupled Codes.....	2-1
2.1.1 TRACE Overview.....	2-1
2.1.2 PARCS Overview.....	2-2
2.2 TRACE BWR/5 Model.....	2-3
2.2.1 System Model.....	2-3
2.2.2 Global Modifications.....	2-6
2.2.3 ATWS-Specific Enhancements.....	2-6
2.2.4 MATLAB Script.....	2-7
2.2.5 Turbine Bypass Valve.....	2-7
2.2.6 SRV/ADS.....	2-8
2.2.7 Feedwater and Reactor Water Level Control.....	2-8
2.2.8 Reactor Core Isolation Cooling System.....	2-9
2.2.9 Standby Liquid Control System.....	2-9
2.2.10 Lower Plenum Flow Valve.....	2-9
2.2.11 Suppression Pool Cooling.....	2-10
2.3 Core Input Model for PARCS.....	2-10
2.3.1 Introduction.....	2-10
2.3.2 Reactor and Fuel Bundle Properties.....	2-10
2.3.3 Core Geometry and Control Rod Banks.....	2-11
2.3.4 Cross Sections and Other Bundle Parameters.....	2-12
2.3.5 TRACE/PARCS Mapping.....	2-14
2.4 Code Execution Methodology.....	2-18
2.4.1 Preparation of the Base TRACE Model.....	2-18
2.4.2 Steady-State Initialization.....	2-18
2.4.3 Execution Procedure.....	2-19
2.4.4 Steady-State Convergence Check.....	2-20
2.4.5 TRACE Transient Input Deck.....	2-21
2.4.6 Outputs.....	2-22
3 STEADY-STATE RESULTS.....	3-1
3.1 ATWS-I 382-Channel BOC Model.....	3-1
3.1.1 Initial and Boundary Conditions.....	3-1
3.1.2 Radial Power Distribution.....	3-2
3.1.3 Axial Power Distribution.....	3-3
3.1.4 First Harmonic.....	3-3
3.2 ATWS-I 382-Channel PHE Model.....	3-5
3.2.1 Initial and Boundary Conditions.....	3-5
3.2.2 Radial Power Distribution.....	3-6
3.2.3 Axial Power Distribution.....	3-6

3.2.4	First Harmonic	3-8
3.2.5	Effect of Spectrally Corrected Void History	3-8
3.3	ATWS-I 382-Channel EOFPL Model	3-11
3.3.1	Initial and Boundary Conditions	3-11
3.3.2	Radial Power Distribution	3-12
3.3.3	Axial Power Distribution	3-12
3.3.4	First Harmonic	3-14
4	TURBINE TRIP EVENTS WITH REPRESENTATIVE BYPASS	4-1
4.1	Introduction	4-1
4.2	Limiting Case: PHE with 100% Bypass Capacity (Case 2)	4-2
4.2.1	Initial and Boundary Conditions	4-2
4.2.2	Sequence of Events	4-2
4.2.3	Steamline Flow	4-3
4.2.4	Core Power	4-4
4.2.5	Fuel Bundle Power and Flow	4-11
4.2.6	RPV Steam Dome Pressure	4-13
4.2.7	Core Flow	4-13
4.2.8	Core Inlet Subcooling	4-14
4.2.9	Feedwater Flow and RPV Water Level	4-15
4.2.10	Boron Inventory in Core	4-18
4.2.11	Fuel Cladding Temperature	4-18
4.3	Effect of Bypass Fraction	4-23
4.3.1	Bypass Fractions	4-23
4.3.2	Initial Conditions	4-24
4.3.3	Sequence of Events	4-24
4.3.4	Steamline Flow	4-25
4.3.5	Core Power	4-27
4.3.6	Core Flow	4-31
4.3.7	Feedwater Flow and RPV Water Level	4-32
4.3.8	Boron Inventory in Core	4-33
4.3.9	Core Inlet Subcooling	4-34
4.3.10	Fuel Cladding Temperature	4-35
4.3.11	Summary	4-36
4.4	Effect of Time in Cycle	4-36
4.4.1	Time in Fuel Cycle	4-36
4.4.2	Initial Conditions	4-37
4.4.3	Sequence of Events	4-37
4.4.4	Steamline Flow	4-38
4.4.5	Core Power	4-39
4.4.6	Core Flow	4-45
4.4.7	Boron Inventory in Core	4-48
4.4.8	Core Inlet Subcooling	4-48
4.4.9	Fuel Cladding Temperature	4-49
4.4.10	Summary	4-50
4.5	Effect of Void History Modeling	4-51
4.5.1	Void History Modeling	4-51
4.5.2	Initial Conditions	4-51
4.5.3	Sequence of Events	4-51
4.5.4	Steamline Flow	4-52
4.5.5	Core Power	4-53
4.5.6	Core Flow	4-56
4.5.7	Boron Inventory in Core	4-59

4.5.8	Core Inlet Subcooling.....	4-59
4.5.9	Fuel Cladding Temperature	4-60
4.5.10	Summary	4-62
4.6	Stability Figures-of-Merit	4-62
4.6.1	Initial Stage	4-64
4.6.2	Natural Circulation Stage	4-65
4.6.3	Stage of Onset through Normal Growth	4-66
4.6.4	Stage of Large Amplitude Limit Cycle Oscillations	4-71
4.6.5	Stage of Bimodal Power Oscillations	4-72
4.6.6	Stage of Non-Linear Bi-Modal Power Oscillations	4-73
4.6.7	Decay Stage	4-74
4.6.8	Long-Term Stage.....	4-80
4.6.9	Summary	4-81
4.7	Summary and Conclusions	4-81
5	CONCLUSIONS AND RECOMMENDATIONS.....	5-1
5.1	TRACE/PARCS Application to ATWS Events	5-1
5.2	ATWS Events Initiated by Turbine Trip	5-1
5.3	Modeling in TRACE/PARCS	5-3
5.3.1	TRACE	5-3
5.3.2	PARCS	5-6
5.3.3	Use of Analysis Results	5-8
6	REFERENCES	6-1
	APPENDIX A - TRACE Calculation Notebook.....	A-1
	APPENDIX B - PARCS Calculation Notebook.....	B-1
	APPENDIX C - MATLAB Script for Generating TRACE CHAN Input.....	C-1

LIST OF FIGURES

Figure 1.1	Illustration of a Flow Control Window [1].....	1-2
Figure 1.2	Boundaries of the MELLLA+ Operating Domain [1].....	1-3
Figure 1.3	Natural Circulation Conditions Following Dual Recirculation Pump Trip [1]	1-4
Figure 2.1	Component View of the BWR/5 Plant.....	2-4
Figure 2.2	GE14 Rod Layout.....	2-5
Figure 2.3	Axial Layout of a Generic GE14 Fuel Bundle	2-11
Figure 2.4	Control Rod Bank Positions in the Core	2-12
Figure 2.5	Mapping for ATWS-I – 382 Channels	2-16
Figure 2.6	Mapping for ATWS-ED – 27 Channels	2-17
Figure 2.7	Preparation of the TRACE Stand-Alone Steady-State model	2-18
Figure 2.8	TRACE/PARCS Code Execution Procedure	2-20
Figure 2.9	Null Transient Results at PHE, 382-Channel Model	2-21
Figure 3.1	Axially Averaged Radial Power Distribution at BOC	3-3
Figure 3.2	Radially Averaged Axial Power Distribution at BOC	3-4
Figure 3.3	Radially Averaged Axial Moderator Density at BOC	3-4
Figure 3.4	First Harmonic Shape at BOC	3-5
Figure 3.5	Axially Averaged Radial Power Distribution at PHE.....	3-7
Figure 3.6	Radially Averaged Axial Power Distribution at PHE.....	3-7
Figure 3.7	Radially Averaged Axial Moderator Density at PHE	3-8
Figure 3.8	First Harmonic Shape at PHE	3-9
Figure 3.9	Axially Averaged Radial Power Distribution at PHE, UH versus UHSPH.....	3-10
Figure 3.10	Radially Averaged Axial Power Distribution at PHE, UH versus UHSPH.....	3-11
Figure 3.11	Axially Averaged Radial Power Distribution at EOFPL	3-13
Figure 3.12	Radially Averaged Axial Power Distribution at EOFPL	3-13
Figure 3.13	Radially Averaged Axial Moderator Density at EOFPL	3-14
Figure 3.14	Harmonic Shape at EOFPL.....	3-15
Figure 4.1	Steam Mass Flow Rate in Steamline in Case 2	4-5
Figure 4.2	Core Power in Case 2	4-5
Figure 4.3	Reactor Pressure Vessel Dome Pressure in Case 2	4-6
Figure 4.4	Normalized Core Total Mass Flow Rate in Case 2	4-6
Figure 4.5	Core Inlet Subcooling in Case 2	4-7
Figure 4.6	First Indication of Bi-Modal Oscillation of Power at 143.9 s in Case 2	4-8
Figure 4.7	Recognizable Bi-Modal Oscillation of Power at 152.2 s in Case 2.....	4-9
Figure 4.8	Downcomer Water Level in Case 2	4-10
Figure 4.9	Boron Inventory in Reactor Core in Case 2	4-10
Figure 4.10	Power in Bundle with Maximum Steady-State Power in Case 2	4-11
Figure 4.11	Power in Bundle with Maximum First Harmonic Power in Case 2.....	4-12
Figure 4.12	Mass Flow in Bundle with Maximum Steady-State Power in Case 2	4-12
Figure 4.13	Mass Flow in Bundle with Maximum First Harmonic Power in Case 2.....	4-13
Figure 4.14	Feedwater Temperature in Case 2.....	4-14
Figure 4.15	Feedwater Flow Rate in Case 2	4-16
Figure 4.16	Mass in Ring-1 Separator in Case 2.....	4-17
Figure 4.17	Void Fraction in Upper RPV Region in Case 2	4-17
Figure 4.18	Peak Cladding Temperature in Bundles with Maximum Steady-State Power in Case 2.....	4-19
Figure 4.19	Peak Cladding Temperature in Bundles with Maximum First Harmonic Power in Case 2.....	4-19
Figure 4.20	Axial Cladding Temperatures in Bundle 544 in Case 2.....	4-21
Figure 4.21	Axial Cladding Temperatures in Bundle 243 in Case 2.....	4-21
Figure 4.22	Axial Cladding Temperatures in Bundle 403 in Case 2.....	4-22

Figure 4.23	Axial Cladding Temperatures in Bundle 388 in Case 2.....	4-22
Figure 4.24	Maximum Cladding Temperature in Core in Case 2.....	4-23
Figure 4.25	Steam Mass Flow Rate in Steamline in BOC Cases.....	4-26
Figure 4.26	RPV Pressure in BOC Cases.....	4-27
Figure 4.27	Reactor Core Power in BOC Cases.....	4-28
Figure 4.28	Reactor Core Power at BOC with 10% Bypass Fraction (Case 1A).....	4-29
Figure 4.29	Reactor Core Power at BOC with 25% Bypass Fraction (Case 1B).....	4-29
Figure 4.30	Reactor Core Power at BOC with 50% Bypass Fraction (Case 1F).....	4-30
Figure 4.31	Reactor Core Power at BOC with 100% Bypass Fraction (Case 1).....	4-30
Figure 4.32	Example of Non-Linear Oscillation Contour for BOC Cases.....	4-31
Figure 4.33	Reactor Core Flow Rate in BOC Cases.....	4-31
Figure 4.34	Feedwater Flow Rate in BOC Cases.....	4-32
Figure 4.35	Downcomer Water Level in BOC Cases.....	4-33
Figure 4.36	Boron Inventory in Core in BOC Cases.....	4-34
Figure 4.37	Core Inlet Subcooling in BOC Cases.....	4-35
Figure 4.38	Maximum Cladding Temperature in Core in BOC Cases.....	4-36
Figure 4.39	Steam Mass Flow Rate in Steamline - Effect of Time in Cycle.....	4-39
Figure 4.40	Reactor Core Power - Effect of Time in Cycle.....	4-40
Figure 4.41	Reactor Core Power at PHE (Case 2).....	4-40
Figure 4.42	Reactor Core Power at BOC (Case 1).....	4-41
Figure 4.43	Reactor Core Power at EOFPL (Case 3).....	4-41
Figure 4.44	Comparison of Void Reactivity - Effect of Time in Cycle.....	4-42
Figure 4.45	Relative Power at Steady-State - Effect of Time in Cycle.....	4-43
Figure 4.46	Oscillation Contour Showing First Harmonic Excitation for PHE.....	4-43
Figure 4.47	Oscillation Contour Showing the Fundamental Mode (Top) and Higher Harmonic Excitation (Bottom) for BOC.....	4-44
Figure 4.48	RPV Pressure - Effect of Time in Cycle.....	4-45
Figure 4.49	Reactor Core Flow Rate - Effect of Time in Cycle.....	4-46
Figure 4.50	Feedwater Flow Rate - Effect of Time in Cycle.....	4-47
Figure 4.51	Downcomer Water Level - Effect of Time in Cycle.....	4-47
Figure 4.52	Boron Inventory in Reactor Core - Effect of Time in Cycle.....	4-48
Figure 4.53	Core Inlet Subcooling - Effect of Time in Cycle.....	4-49
Figure 4.54	Maximum Cladding Temperature in Core - Effect of Time in Cycle.....	4-50
Figure 4.55	Steam Mass Flow Rates in Steamline - Effect of Void History.....	4-53
Figure 4.56	Reactor Core Power - Effect of Void History.....	4-54
Figure 4.57	Core Power in a Narrow Range - Effect of Void History.....	4-54
Figure 4.58	Example of Non-Linear Oscillation Contour Showing Higher Harmonic Mode - PHE, UHSPH Void History.....	4-55
Figure 4.59	Example of Non-Linear Oscillation Contour Showing First Harmonic Mode - PHE, UHSPH Void History.....	4-55
Figure 4.60	RPV Pressure - Effect of Void History.....	4-56
Figure 4.61	Reactor Core Flow Rate - Effect of Void History.....	4-57
Figure 4.62	Feedwater Flow Rate - Effect of Void History.....	4-58
Figure 4.63	Downcomer Water Level - Effect of Void History.....	4-58
Figure 4.64	Boron Inventory in Core - Effect of Void History.....	4-59
Figure 4.65	Core Inlet Subcooling - Effect of Void History.....	4-60
Figure 4.66	Maximum Cladding Temperature in Core - Effect of Void History.....	4-61
Figure 4.67	Local Peak Power for PHE Cases - Effect of Void History.....	4-61
Figure 4.68	Comparison of System Pressures.....	4-64
Figure 4.69	Power Ratio FOMs in Limiting Bundles.....	4-66
Figure 4.70	Core Power - BOC, 10% Bypass (Case 1A).....	4-68
Figure 4.71	Core Power - BOC, 25% Bypass (Case 1B).....	4-68

Figure 4.72	Core Power - BOC, 50% Bypass (Case 1F)	4-69
Figure 4.73	Core Power - BOC, 100% Bypass (Case 1)	4-69
Figure 4.74	Core Power - PHE, UH Void History (Case 2)	4-70
Figure 4.75	Core Power - PHE, UHSPH Void History (Case 2G)	4-70
Figure 4.76	Comparison of Downcomer Water Level	4-72
Figure 4.77	Amplitude of Fast Fourier Transform of Power for PHE–UH Case	4-74
Figure 4.78	Total vs Local Power at BOC, 100% Bypass	4-75
Figure 4.79	Limiting Channel Inlet Mass Flow Rate at BOC, 10% Bypass	4-77
Figure 4.80	Limiting Channel Inlet Mass Flow Rate at BOC, 25% Bypass	4-77
Figure 4.81	Highest Local Power Peaking Factor - BOC, 50% Bypass (Case 1F)	4-78
Figure 4.82	Highest Local Power Peaking Factor - BOC, 100% Bypass (Case 1)	4-78
Figure 4.83	Highest Local Power Peaking Factor - PHE, UH Void History (Case 2)	4-79
Figure 4.84	Highest Local Power Peaking Factor - PHE, UHSPH Void History (Case 2G)	4-79
Figure 4.85	Pressure Drop Ratios in Limiting Bundles	4-81

LIST OF TABLES

Table 2.1	Characteristics of Rod Groups in Bundles	2-5
Table 2.2	ADS/SRV Valve Opening	2-8
Table 2.3	Branch Calculation States for 0% Void History Tree	2-13
Table 2.4	Signal Variables Re-Defined in a Transient Input Deck	2-22
Table 2.5	TRACE Outputs.....	2-22
Table 2.6	PARCS Outputs	2-23
Table 3.1	Comparison of Steady-State Thermal-Hydraulic Parameters at BOC	3-2
Table 3.2	Comparison of Steady-State Thermal-Hydraulic Parameters at PHE	3-6
Table 3.3	Comparison of Steady-State Thermal-Hydraulic Parameters at EOFPL	3-12
Table 4.1	Simulation Conditions of ATWS-I Cases	4-1
Table 4.2	Comparison of Steady-State Thermal-Hydraulic Parameters in Case 2.....	4-2
Table 4.3	Sequence of Events for Case 2 at PHE with UH Void History.....	4-3
Table 4.4	Turbine Bypass Fractions and Simulation Conditions	4-23
Table 4.5	Comparison of Steady-State Parameters in BOC Cases	4-24
Table 4.6	Sequence of Events at BOC with Four Turbine Bypass Capacities.....	4-25
Table 4.7	Simulation Conditions - Effect of Time in Cycle.....	4-37
Table 4.8	Comparison of Steady-State Thermal-Hydraulic Parameters - Effect of Time in Cycle	4-37
Table 4.9	Sequence of Events - Effect of Time in Cycle	4-38
Table 4.10	Simulation Conditions - Effect of Void History.....	4-51
Table 4.11	Comparison of Steady-State Thermal-Hydraulic Parameters - Effect of Void History	4-51
Table 4.12	Sequence of Events - Effect of Void History	4-52
Table 4.13	Characterization of ATWS-I Phases and Figures-of-Merit [15].....	4-63
Table 4.14	Times of Reactor Instability Onset and Growth Ratios.....	4-67
Table 4.15	Times of Onset of Bi-Modal Power Oscillation	4-73
Table 4.16	Times of Frequency Change and Frequencies	4-74
Table 4.17	Time of Onset of Decay of Power Oscillation and Decay Ratio.....	4-76

ACKNOWLEDGMENTS

This project was a joint effort of Brookhaven National Laboratory (BNL) and U.S. Nuclear Regulatory Commission staff. The authors wish to thank Istvan Frankl for his support and technical feedback as the original Project Manager, and, similarly, Tarek Zaki for his support as the final Project Manager. We greatly appreciated the efforts of the staff in the Office of Nuclear Regulatory Research, Reactor Systems Code Development Branch, to quickly assess and implement improvements, as they were identified, in the computer codes used in the project. The authors would like to thank Thomas Downar and Yunlin Xu at the University of Michigan for their technical advice about the PARCS code, and Kenneth Jones at Applied Programming Technology, Inc., for his support on the application of SNAP. We also appreciate the work done by Lynda Fitz in finalizing this document and providing administrative support.

ACRONYMS

3D	Three Dimensional
ADF	Assembly Discontinuity Factor
ADS	Automatic Depressurization System
ANM	Analytical Nodal Method
ARO	All Rods Out
ATWS	Anticipated Transient Without SCRAM
ATWS-ED	Anticipated Transient Without SCRAM with Emergency Depressurization
ATWS-I	Anticipated Transient Without SCRAM with Instability
BNL	Brookhaven National Laboratory
BOC	Beginning-of-Cycle
BWR	Boiling Water Reactor
CB	Control Block in TRACE Input
CMFD	Coarse-Mesh Finite-Difference
CONTAN	Containment Component in TRACE Input
CSS	Constrained Steady-State
CST	Condensate Storage Tank
CW	Core-Wide
DC	Downcomer
DW	Drywell
DWO	Density-Wave Oscillation
ED	Emergency Depressurization
EOFPL	End-of-Full-Power-Life
EPU	Extended Power Uprate
FCT	Fuel Centerline Temperature
FCW	Flow Control Window
FOM	Figure-of-Merit
FW	Feedwater
FWH	Feedwater Heater
GE	General Electric
GEH	GE Hitachi
HCTL	Heat Capacity Temperature Limit
ICF	Increased Core Flow
ISL	Information Systems Laboratories
LOCA	Loss-of-Coolant Accident
LP	Lower Plenum
LPV	Lower Plenum Valve
MELLLA+	Maximum Extended Load Line Limit Analysis Plus
MSIV	Main Steam Isolation Valve
NEM	Nodal Expansion Method
NMP2	Nine Mile Point Unit 2
NRC	U.S. Nuclear Regulatory Commission
OLTP	Original Licensed Thermal Power
OOP	Out of Phase
OOS	Out of Service
PARCS	Purdue Advanced Reactor Core Simulator
PCT	Peak Clad Temperature
PHE	Peak-Hot-Excess-Reactivity
PWR	Pressurized Water Reactor
RCF	Rated Core Flow

RCIC	Reactor Core Isolation Cooling
RHR	Residual Heat Removal
RPS	Reactor Protection System
RPT	Recirculation Pump Trip
RPV	Reactor Pressure Vessel
RWL	Reactor Water Level
SBLOCA	Small Break Loss-of-Coolant Accident
SETS	Stability Enhancing Two-Step method
S-I	Semi-Implicit Numerics
SLCS	Standby Liquid Control System
SP	Suppression Pool
SRV	Safety Relief Valve
TAF	Top-of-Active Fuel
TBV	Turbine Bypass Valve
TRACE	TRAC-RELAP Advanced Computational Engine
TRACG	Transient Reactor Analysis Code, GE Version
TSV	Turbine Stop Valve
TT	Turbine Trip
UH	Void History
UHSPH	Void History Spectrally Corrected
WLR	Water Level Reduction
WR	Water Rod

1 INTRODUCTION

In recent years, the operating power of boiling water reactors (BWRs) has been increased, sometimes to 120% of their original licensed thermal power (OLTP). This places them in an expanded operating domain and changes the manner in which they maneuver in the power-flow operating map. One option being pursued, namely maximum extended load line limit analysis plus (MELLLA+) operation, raises questions about how the plant will respond to anticipated transients without scram (ATWS). This report describes how we simulated these events with state-of-the-art codes, and the results of that analysis.

1.1 Background

The MELLLA+ operating domain utilizes a flow control window (FCW) at high reactor power. It is very similar to the MELLLA concept, except, this FCW is utilized at extended power uprate (EPU) levels of 120% of the OLTP. Figure 1.1 illustrates the FCW concept. At rated thermal power, the reactor may be maneuvered along the FCW to compensate for changes in reactivity through cycle depletion. The FCW offers licensees two notable advantages. First, it affords flexibility in controlling reactivity by providing an alternative to control blade pattern swaps. Second, the FCW supports operation at high power-to-flow ratio. At the high point of this ratio, the high void fraction in the upper portion of the core promotes the production of plutonium. Such enhanced plutonium conversion, due to the harder spectral conditions, confers some economic benefits on the fuel cycle.

Figure 1.2 shows a typical power/flow operating map depicting the MELLLA+ upper boundary. The MELLLA+ domain expands allowable operation at EPU power levels down to low core flow rates (i.e., 80% of rated core flow). The operation at the low-flow point along the MELLLA+ upper boundary at EPU power levels (Point D in Figure 1.2) introduces new safety questions relative to normal EPU operation (between Points A and B in this Figure). In particular, these questions are associated with the consequences of postulated ATWS events initiated at Point D.

Figure 1.3 illustrates a typical forced recirculation trajectory in a BWR plant following a postulated ATWS event [1]. From Point D, the reactor power decreases in response to a dual recirculation pump trip (2RPT), an automated plant response intended to reduce the reactor's gross thermal power. As is evident in the figure, the power is reduced; however, it begins to climb again as the flow rate approaches the natural circulation line. This increase in the reactor's power is the response to a loss of extraction steam to the feedwater heater (FWH) cascade. For example, if the postulated initiating event is a turbine trip, the closure of the turbine stop valve (TSV) causes a loss of extraction steam to the FWH cascade. In response, the FW temperature starts to decrease. The reactor's core responds to the reactivity insertion associated with the elevated subcooling of the core inlet and power increases.

If unmitigated, the plant will evolve to a state point wherein the reactor achieves a critical void fraction similar to that of the normal operating condition at relatively high power and natural circulation flow. Figure 1.3 shows the power-to-flow ratio following the 2RPT for a hypothetical MELLLA+ plant and for a plant operating at normal EPU conditions. As can be seen, the reactor power under natural circulation conditions is much higher for a plant operating at the MELLLA+ low flow/high power point in the domain.

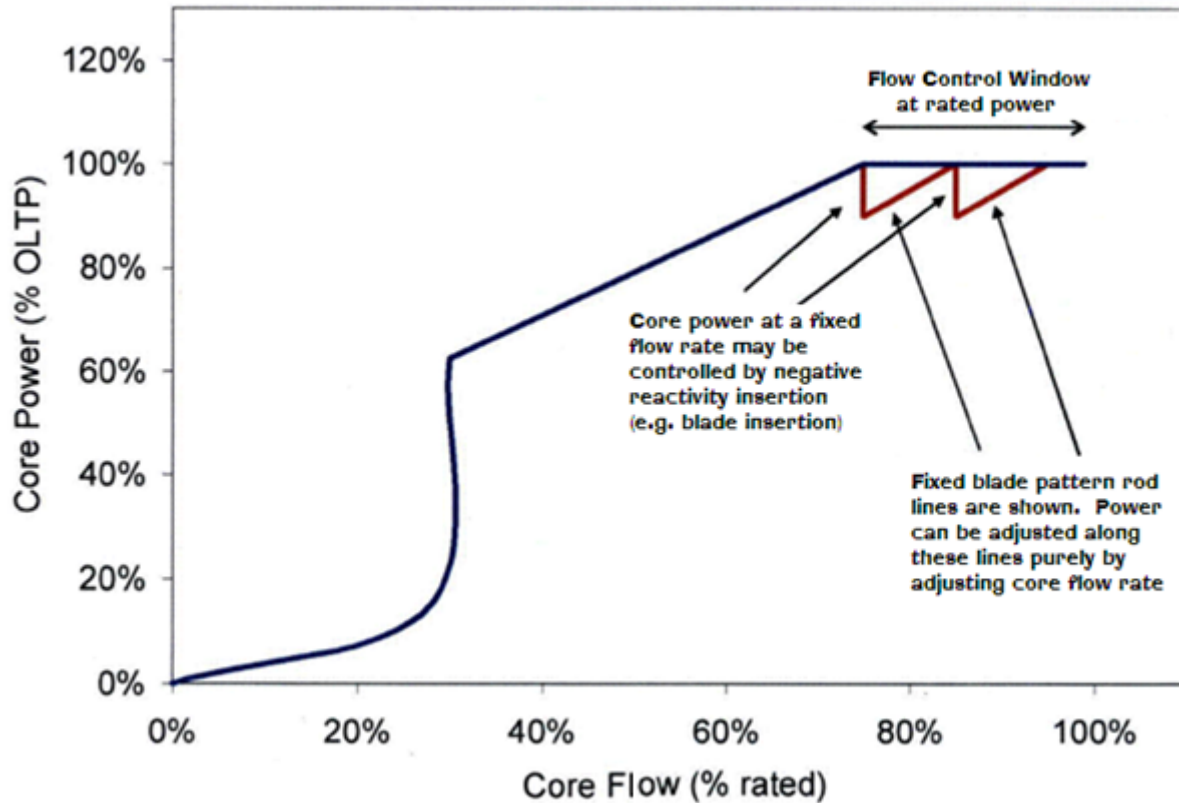


Figure 1.1 Illustration of a Flow Control Window [1]

The higher thermal load present following 2RPT for postulated ATWS events engenders two questions of safety. First, the reactor evolves to a very high power-to-flow condition, and specifically, to a region of the power/flow map where unstable power oscillations are likely to occur. If such power oscillations are left unmitigated, the fuel may be damaged [1]. Additionally, the amplitude of the power oscillations may hamper the effectiveness of mitigation strategies. For example, ATWS events typically are mitigated by injecting a dissolved neutron absorber through the standby liquid control system (SLCS); the oscillation-induced core inlet flow reversal may lower the rate at which this soluble absorber is delivered to the active region of the reactor core.

Second, since the 2RPT at MELLLA+ is less effective in reducing the reactor core power, the containment must absorb additional energy during the mitigation period. This additional thermal load may exhaust the available capacity for pressure suppression capacity of the containment wetwell, which would prompt an emergency depressurization according to standard emergency operating procedures. The manual initiation of the emergency depressurization implies that (1) the reactor has undergone a beyond-design-basis event, and fuel damage may have occurred, (2) the pressure suppression capacity of the containment has been exhausted, and, (3) the reactor coolant pressure boundary has been bypassed by manually opening the valves of the automatic depressurization system (ADS). Under these conditions, two of the three primary fission product barriers may be compromised.

MELLLA+ Domain

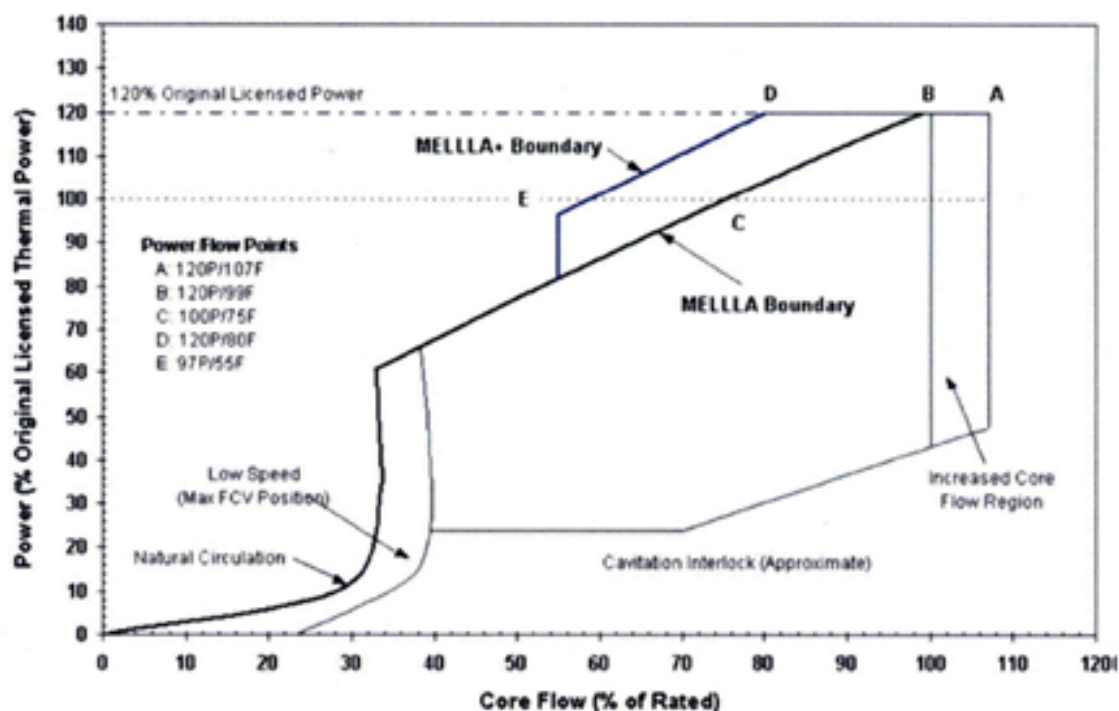


Figure 1.2 Boundaries of the MELLLA+ Operating Domain [1]

Based on these safety considerations unique to MELLLA+ operation, the primary scenarios of interest for evaluation are ATWS events with either (1) core instability (i.e., growing power oscillations), or, (2) emergency depressurization for events wherein the RPV becomes isolated.

To study these scenarios, we must have a simulation tool that models all of the significant physical phenomena. The U.S. Nuclear Regulatory Commission (NRC) is developing the TRACE/PARCS code to support analyses of large and small break loss-of-coolant accidents (LOCAs) and non-LOCA analyses (e.g., system transients and ATWS) for a wide range of nuclear plants. This code is used as an audit tool for analyses submitted by NRC licensees. Plant safety analyses in support of licensing require the analysis of a broad range of accident and transient scenarios to help understand the limiting conditions for safely operating the plant.

The NRC put considerable effort into assessing the applicability of TRACE/PARCS to analyze ATWS events, such as those of interest to this study [2]. The process involves understanding the phenomena that are important to model in the event, and then looking at the assessment of the codes for those phenomena. The conclusion of the NRC staff has been that TRACE/PARCS is applicable [1]. Hence, we adopted this package for the analysis in this study.

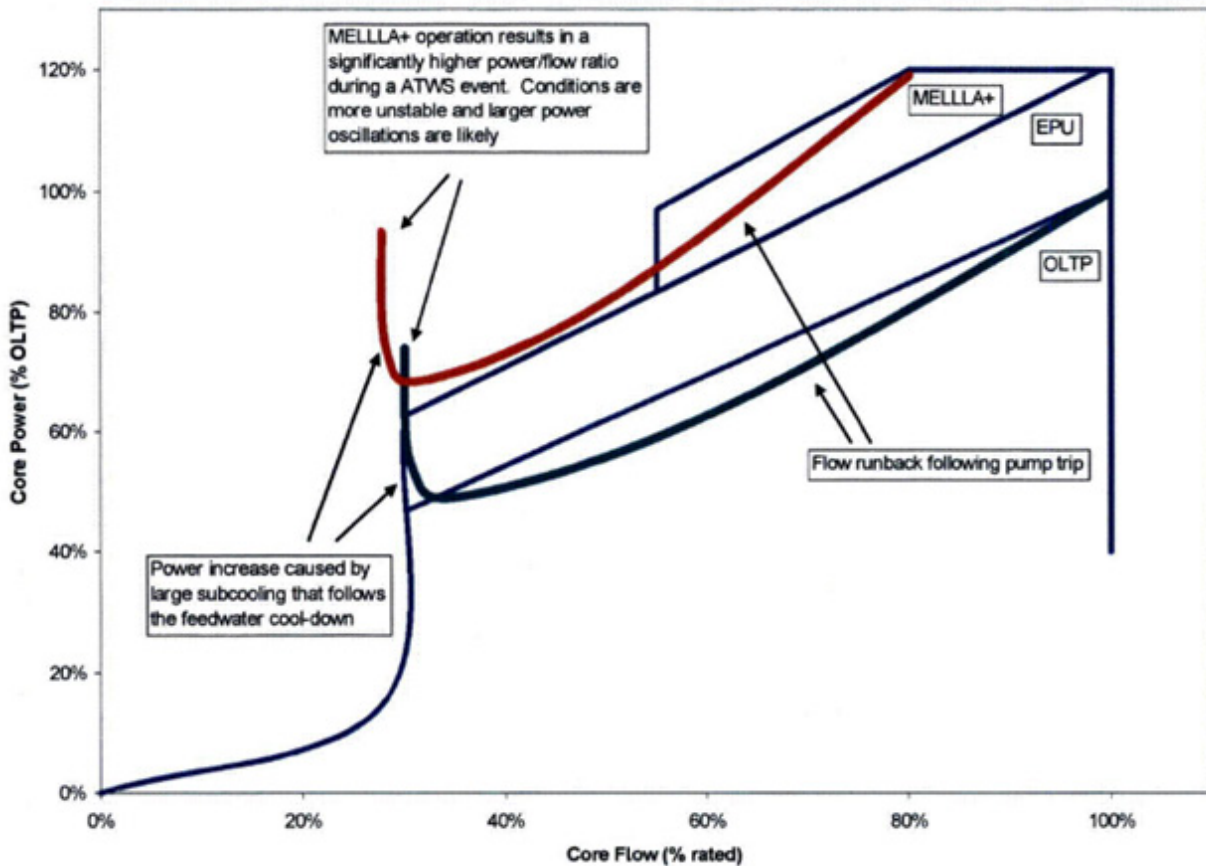


Figure 1.3 Natural Circulation Conditions Following Dual Recirculation Pump Trip [1]

1.2 Objectives

This document is a partial report of work the objective of which is to develop TRACE/PARCS models supporting ATWS confirmatory analyses at MELLLA+ operating conditions for two specific scenarios: The ATWS initiated by a turbine trip that leads to large-amplitude core instability; and, the ATWS initiated by closure of main steam isolation valves (MSIVs) that leads to emergency depressurization once the heat capacity temperature limit (HCTL) of the suppression pool is exceeded.

We follow our development of the models by the analyses of ATWS events with different assumptions about plant conditions and/or modeling. The events that are documented in this report are those initiated by a turbine trip that leads to instability. A typical BWR/5 plant was selected as the reference plant since this was the type analyzed in [1]. Our analysis of events that lead to emergency depressurization will be documented in a separate document.

In addition, the work discussed in this report further assesses the capabilities of the TRACE/PARCS code to calculate the thermal-hydraulic and neutronic phenomena associated with BWR ATWS and reactor stability events. Hence, this work: details improvements that were made to the code during the study, captures our user experiences, and documents our modeling practices.

1.3 Organization of Report

Chapter 2 discusses the methodology used in the ATWS analysis. The modeling that exists in the TRACE/PARCS codes is summarized and followed by summaries of the input models used with the codes. More details about the input models are found in the TRACE and PARCS Calculation Notebooks (Appendices A and B, respectively) and in Appendix C, which explains a MATLAB script for generating some of the TRACE input. Lastly in Chapter 2, we explain code execution, and the sequencing of calculations needed to analyze a particular event.

Chapter 3 discusses the steady-state results with figures showing the axially averaged radial power distribution and the radially averaged axial power distribution. The results of the calculations are for each of three different points in the fuel cycle.

Chapter 4 details the results for those events initiated by turbine trip (ATWS instability or ATWS-I events). We analyzed seven cases, each with different assumptions on modeling or plant condition.

Chapter 5 offers our conclusions and recommendations related to the applicability of TRACE/PARCS for this analysis and to the plant response to these events. References are supplied in Chapter 6.

2 METHODOLOGY

2.1 The TRACE/PARCS Coupled Codes

The TRACE/PARCS computational package is designed to be applicable to analyzing operational transients and accidents in light-water reactors where the coupling between the neutron kinetics (PARCS) and the thermal-hydraulics (TRACE) is important. One class of accident where the coupling is strong and over a relatively long period of time is that of anticipated transients without scram (ATWS) in boiling water reactors (BWRs). During these events, the thermal-hydraulic conditions within the core (e.g., fuel temperature and void fraction) continuously change as a result of the changes taking place in the plant (e.g., a pump trip). To understand the core conditions, it is necessary to model a large portion of the nuclear steam supply system. With given core conditions, the coupling to the neutron kinetics can be done using the fact that neutron cross sections are a function of the thermal-hydraulic variables (and the presence of soluble boron after its injection into the vessel during an ATWS).

The codes have been under development for many years and have had many successful applications. Hence, there is considerable documentation available; for the theory behind the codes, [3, 4], for code assessment of TRACE [5], for specific code assessment applicable to BWR transients, [6, 7, 8] and for the applicability of the codes to the ATWS analysis in this report [2]. The general theory behind the codes is summarized below using the overviews in [3, 4]. However, some of the important modeling applicable to this work also is explained in the discussion of the input models in Sections 2.2 and 2.3.

2.1.1 TRACE Overview

TRACE was designed to perform best-estimate analyses of loss-of-coolant accidents (LOCAs), operational transients, and other accident scenarios in pressurized water reactors (PWRs) and BWRs. It also can model phenomena occurring in experimental facilities designed to simulate transients in reactor systems. Models implemented in TRACE include multidimensional two-phase flow, non-equilibrium thermo-dynamics, generalized heat transfer, reflood, level tracking, and reactor kinetics. Automatic steady-state and dump/restart capabilities also are provided.

The partial differential equations that describe two-phase flow and heat transfer are solved using finite-volume numerical methods. The heat transfer equations are evaluated using a semi-implicit time-differencing technique. TRACE contains the option to select one of two related numerical methods for solution of the fluid dynamics equations in the spatial one-dimensional (1D), and three-dimensional (3D) components. The default Stability Enhancing Two-Step (SETS) method has the advantage of avoiding Courant stability limits on time-step size, but the disadvantage of relatively high numerical diffusion. A name list input option permits the selection of a semi-implicit method that can have substantially less numerical diffusion but has time-step sizes restricted to a material Courant limit. This should be the method of choice for BWR stability analysis, and is the one employed in the current work.

TRACE takes a component-based approach to modeling a reactor system. Each physical piece of equipment in a flow loop can be represented as some type of component, and each component can be further nodalized into some number of physical volumes (also called cells) over which the fluid, conduction, and kinetics equations are averaged. The number of reactor components in the problem and the manner in which they are coupled is arbitrary. There is no built-in limit for the number of components or volumes that can be modeled; the size of a problem theoretically is only limited by the available computer memory. Reactor hydraulic components in TRACE include PIPES, PLENUMs, PRIZERs (pressurizers), CHANs (BWR fuel

channels), PUMPs, JETPs (jet pumps), SEPDs (separators), TEEs, TURBs (turbines), HEATRs (feedwater heaters), CONTANs (containment), VALVEs, and VESSELs (with associated internals). There are available HTSTR (heat structure) and REPEAT-HTSTR components modeling fuel elements or heated walls in the reactor system to compute two-dimensional conduction and surface-convection heat-transfer in Cartesian or cylindrical geometries. POWER components are available as a means for delivering energy to the fluid via the HTSTR or hydraulic component walls. PARCS can provide three-dimensional power distributions if coupled to TRACE. FLPOWER (fluid power) components can deliver energy directly to the fluid (such as might happen in waste-transmutation facilities). RADENC (radiation enclosures) components may be used to simulate radiation heat transfer between multiple arbitrary surfaces. FILL and BREAK components are used to apply the desired coolant flow and pressure boundary conditions, respectively, in the reactor system to perform steady-state and transient calculations. EXTERIOR components are available to facilitate the development of input models designed to exploit TRACE's parallel execution features.

The code's computer execution time is highly problem-dependent and is a function of the total number of mesh cells, the maximum allowable time-step size, and the rate of change of the neutronic and thermal-hydraulic phenomena being evaluated. The stability-enhancing two-step (SETS) numeric in hydraulic components allows the material Courant limit to be exceeded, so that very large time steps can be used in steady-state and slow transients. This, in turn, can significantly speed up simulations (by one or two orders-of-magnitude) of slow developing accidents and operational transients.

2.1.2 PARCS Overview

PARCS is designed to solve the time-dependent neutron diffusion equation so as to calculate steady-state operating conditions and transient core behavior after various initiating events. The thermal-hydraulic and soluble boron conditions in the core come from TRACE when the coupled package is used. For each fuel assembly represented in the PARCS model, TRACE provides, as a function of axial mesh interval, fuel temperature, moderator density, and soluble boron concentration, the independent variables needed for the cross section representation.

The solution of the time-dependent neutron diffusion equation along with the delayed neutron precursor equations is obtained by first discretizing the balance equations in time and in space. For the temporal discretization, the theta method with exponential transformation is employed in PARCS, along with a second-order analytic precursor integration technique. The temporal discretization scheme allows sufficiently large time-step sizes even in severe transients involving super-prompt-critical reactivity insertion.

For spatial discretization, the efficient nonlinear nodal method is employed wherein the coarse mesh finite difference (CMFD) problems and the local two-node problems are repetitively solved during the nonlinear iteration. It is well-documented that the nonlinear nodal methods are more efficient than the conventional response-matrix formulation because of lower memory requirements and the efficient linear system solvers available for the CMFD problems. It is particularly advantageous in the transient calculation because the two-node calculation need not be performed at every time step, leading to a very efficient calculation of the transient. The temporal and spatial differencing of the spatial kinetics equation engenders a fixed-source type of problem at every time step. The solution of a transient fixed-source problem consists of the simultaneous solutions of the CMFD and two-node problems. The former involves a linear system with a block penta-diagonal matrix in three-dimensional problems. In PARCS, its solution is obtained using a Krylov subspace method because it is more efficient and robust

than the classical iterative methods, and also because it is easier to achieve a coarse-grain parallelism.

The two-node problems are solved to correct for the discretization error in the nodal interface current resulting from the finite difference approximation in a coarse mesh structure. They are solved using any one of a number of so-called advanced nodal diffusion methods. In PARCS, the nodal expansion method (NEM) and the analytic nodal method (ANM) can both be used to obtain the two-node solution. Because the NEM offers a more robust and faster solution than ANM, it was preferred in many other reactor physics codes, even though for some applications it can be less accurate. ANM is used as the primary nodal solver in PARCS because of the improvements which were used to produce a robust solution, regardless of the nodal condition. Such robustness was attained by providing a hybrid ANM/NEM scheme in which “near critical” two-node problems are solved with the NEM, while the ANM is used in the rest of the two-node problems.

The code contains models to handle special situations. Several are important for our analysis here. For example, a control rod cusping correction method was implemented to minimize the error when control rods are partially inserted into a coarse computational node. The cusping correction is performed by solving a three-node problem for the intranodal flux, using the fine-mesh finite difference method. The code can calculate harmonic modes. There are special models for assessing the fission products xenon and samarium and their inclusion in the cross section dependencies. Lastly, the code also evaluates decay heat.

All the computational methods introduced above are integrated into PARCS in a modular form. These computational modules must be properly coordinated to perform any given task. Since the global performance of the code largely depends on the coordination scheme as well as on the individual methods themselves, efforts were made to formulate an efficient coordination scheme for each type of task.

2.2 TRACE BWR/5 Model

The information for the TRACE BWR/5 model is from the following 1) a small break loss-of-coolant accident (SBLOCA) model [9] developed for the NRC by Information Systems Laboratories (ISL), herein referred to as the base reference model; 2) supplemental information derived from TRACG input decks and the results of the TRACG analyses from GEH [10]; and data from miscellaneous other sources at BNL and NRC. In developing the TRACE BWR/5 model for the ATWS analysis, two types of changes were made to the base reference model, viz., global modifications, and ATWS-specific enhancements. The NRC staff provided several guidance documents during our development of the TRACE model [11-16]. Appendix A gives details of the non-proprietary portions of the model; the following subsections summarize it, namely, the general layout of the BWR/5 model is first described, then the changes to the base reference model are described, and highlights of new model features implemented for the ATWS analysis.

2.2.1 System Model

The TRACE model of the BWR/5 plant consists of several hydraulic components and heat structures. There is also a POWER component (to define 100% power for the TRACE stand-alone steady-state initialization), signal variables, control blocks and trips. Additional plant configurations are included to allow the model to simulate BWR/4-like conditions (e.g., the location of the standby liquid control system (SLCS) injection into the vessel). Figure 2.1 is a node diagram giving the component view of the complete model. The model consists of a BWR

vessel (with internals consisting of one jet pump, a lower plenum flow control valve, two control rod guide tubes, fuel assembly CHANs, and two steam separators), one recirculation loop with recirculation pump and flow control valve, a feedwater line, a reactor core isolation cooling system (RCIC) line with the option to draw from the condensate storage tank (CST) or the suppression pool, two SLCS lines (for lower plenum and upper plenum injection), a main steamline with in-board and out-board main steam isolation valves (MSIVs), and a branch to safety/relief/automatic depression system valves (SRVs and ADS), turbine control valve (TCV), and a primary containment (drywell and wetwell) with suppression pool cooler.

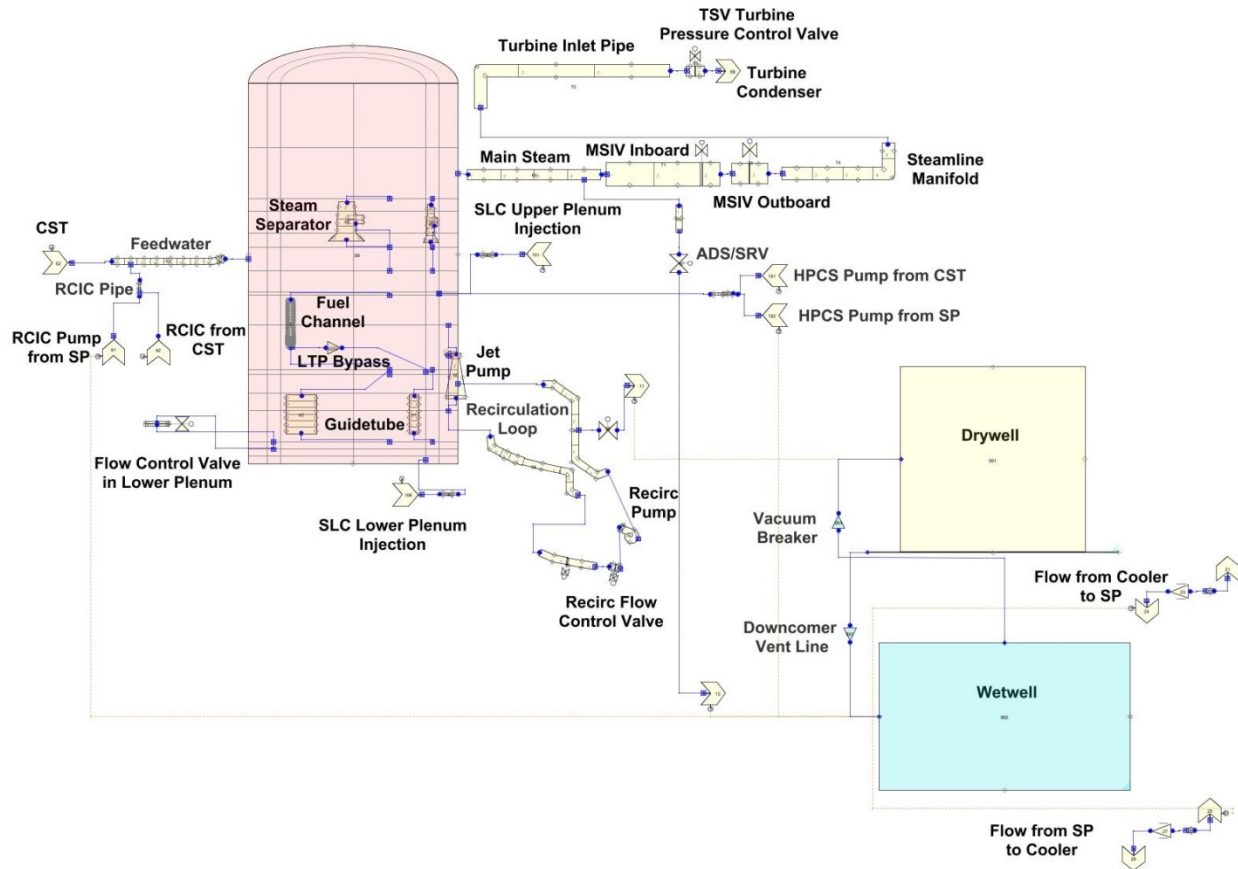


Figure 2.1 Component View of the BWR/5 Plant

The model also has a BREAK junction in the recirculation line and a high pressure core spray (HPCS) system; they are for future applications. The core is modeled by either 27 or 382 CHAN components, each representing two or more GE14 fuel assemblies. A MATLAB script [17] was used in preparing the inputs for the CHAN components as summarized in Section 2.2.4 and detailed in Appendix C.

The current TRACE model retains the ring structure of the VESSEL component from the SBLOCA deck [9]; thus, the core remains as 764 fuel assemblies with 616 assemblies in ring 1 and 148 assemblies in ring 2. Ninety-two of the fuel assemblies in ring 2 are identified as peripheral assemblies because they are located on the outer edge of the core next to the core shroud. The fuel assembly is modeled after a GE14 fuel bundle [10, 18]. Each GE14 fuel assembly has 92 fuel rods and two water rods arranged in a 10x10 array with each water rod occupying four grid positions. There are three types of fuel rods; full length, partial length, and gad rod (full length rods with integral gadolinia as burnable poison) and they are grouped together as separate rod groups in the CHAN component. Figure 2.2 displays the arrangement

of rod types in an assembly (Appendix A). A fourth and fifth rod group respectively represent the hot rod in an assembly and the water rods. Table 2.1 summarizes the characteristics of each rod group. The relative rod power values used are based on guidance from the NRC staff [11, 15].

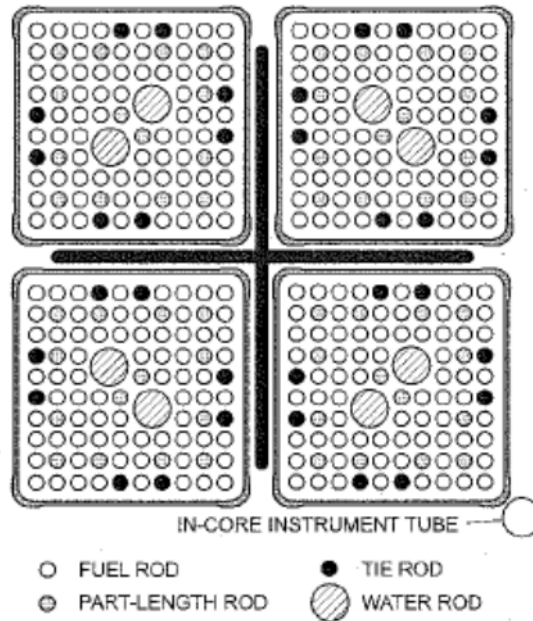


Figure 2.2 GE14 Rod Layout

Table 2.1 Characteristics of Rod Groups in Bundles

Rod Group	Rod Type	Number of Rods
1	Regular full-length fuel rod	77
3	Full-length rod with gad	
2	Partial-length fuel rod	14
4	Hot rod	1
5	Water rod (WR)	2 modeled as 1 WR

The channel component is modeled with refined axial nodalization towards the bottom of the fuel assembly to better characterize the transient motion of the boiling boundary during oscillations. The bottom 24 active nodes of the fuel are 3.81 cm high with the balance being 15.24 cm high. During the transient, cladding dryout and rewet are controlled by the critical heat flux predictions made using the Biasi correlation and minimum stable film boiling predicted using the correlation of Groeneveld and Stewart.

2.2.2 Global Modifications

The bases for the global modifications are the following:

- simplification of the base model
- correction of minor errors in the SBLOCA model
- implementation of GE14 geometry
- implementation of models to emulate features in TRACG that are not in TRACE

The following summarizes global modifications to the ISL SBLOCA model [9] (i.e., the base reference model).

1. merged two recirculation loops into one
2. combined two main steam lines into one
3. eliminated the emergency core-cooling system (ECCS) PIPES and FILLS – low pressure core spray (LPCS) and low pressure coolant injection (LPCI)
4. simplified the SRV discharge line by modeling the SRV as a single junction valve discharging to a BREAK volume connected to the wetwell
5. modified free volumes in rings 2 and 3 of the VESSEL at axial levels 11 and 12, so making the free volume fractions close to unity; also, making minor axial height adjustments in axial levels 8, 9, and 10
6. adjusted the jet-pump inlet flow area to reduce steady-state core flow from 119% to 100%
7. altered the steamline pressure loss coefficient to reduce vessel dome pressure to the rated value
8. implemented the CHAN geometry from the TRACG model
9. incorporated relative assembly power and core-averaged relative axial power in the CHAN components using data from the GEH analyses
10. included the dynamic gap model in the four rod groups (for the fuel) in each CHAN
11. enabled the use of the modified NFI correlation for fuel thermal conductivity
12. modified the inputs for guide tubes, CHAN, and VESSEL to model the core bypass flow
13. modified the inlet loss coefficients for the peripheral fuel assemblies
14. updated the model for the channel leakage flow through the lower tie plate
15. created the model for suppression pool cooler that emulates the suppression pool cooling mode of the residual heat-removal system
16. implemented 3D level tracking for the VESSEL
17. implemented steady-state controllers to initialize recirculation flow and turbine inlet pressure

2.2.3 ATWS-Specific Enhancements

The following is a summary of ATWS-specific modifications to the base reference model.

1. increased the number of CHANs from three in the base reference model to 27 and 382, respectively, for the ATWS-ED and the ATWS-I cases
2. implemented SRV and ADS control logic, assuming two SRVs out of service
3. included turbine control valve logic to emulate the bypass system with different turbine bypass capacity as a fraction of nuclear boiler rating (hereafter bypass fraction)
4. established SLCS with two injection paths – upper plenum (for ATWS-I), and lower plenum (for ATWS-ED)
5. segmented the bottom volume of the VESSEL into three axial volumes to more realistically simulate boron transport in the lower plenum

6. emplaced a flow valve in the lower plenum to simulate boron remixing.
7. established a new feedwater (FW) control logic to enable level regulation in a transient, and the termination of FW flow when the CST is depleted
8. implemented FW temperature controller to represent a lowering in FW temperature associated with a loss of extraction steam after a MSIV/turbine trip
9. established injection points and control logic for the RCIC, switching suction from the CST to the suppression pool when the CST reserve for the RCIC becomes depleted
10. ensured coupling between the TRACE stand-alone models and the PARCS module

2.2.4 MATLAB Script

A MATLAB based script was created to use the input of a single CHAN to generate the required input for a multi-channel TRACE model [17]. In addition, the MATLAB script automated the preparation of the following parameters in the CHAN component input:

1. junction connections
2. number of fuel assemblies represented by the CHAN component
3. inlet orifice loss coefficient
4. the VESSEL ring where the CHAN is located, and thus, the interface for the canister wall's heat structure
5. core-wide radial CHAN-to-CHAN power peaking factor
6. gap-gas composition for each fuel rod (group)
7. average burnup in each axial node of a fuel rod (group)
8. reference gap-gas temperature for each fuel rod (group)
9. corresponding leakage junction in the lower tie plate

Parameters (6) and (8) are part of the additional inputs required for activating the dynamic gap model in TRACE. The MATLAB script evaluates these parameters from the results of FRAPCON calculations. The fuel-clad interaction option selected for the current model is a dynamic gas-gap model with elastic cladding deformation and the clad rupture model off (NFCI=2). This option was selected because it is the simplest dynamic gap model in TRACE that approximates the phenomena modeled in TRACG. The burnup information together with the gadolinia content in a fuel rod is used in evaluating the fuel's thermal conductivity according to the modified NFI correlation (namelist option USE_MODNFI_K = .TRUE.). The gad rods are assumed to have a uniform gadolinia content of 7 wt% (GADC = 0.07). Appendix C provides more details of the MATLAB script.

2.2.5 Turbine Bypass Valve

In the event of a turbine trip with bypass, the turbine bypass valve will open to relieve the RPV pressure by dumping steam to the condenser. Simply reopening the turbine control valve after closure will not accurately represent the bypass function because it is assumed that the turbine bypass system would strive to maintain reactor pressure at a fixed setpoint to prevent inventory loss, full reactor trip, and the actuation of the emergency core cooling system (ECCS), in the configuration of a real plant. To simplify the simulation of the turbine bypass system controller, the model applies a back-pressure boundary condition to the BREAK downstream of the turbine control valve, which will mimic a pressure controller. The break pressure is set to be equivalent to the long-term RPV pressure response predicted by a reference TRACG calculation for an ATWS initiated by turbine trip with bypass [1]. This back pressure also serves to initialize the steady-state conditions for a transient with turbine bypass actuation. An auxiliary calculation was performed to determine the appropriate areas of the turbine's control valve to represent 10%, 25% and 50% bypass scenarios. We also note that the current TRACE model simplifies

the main steam system by merging into one all steam lines, i.e., four in a typical BWR/5. This simplification is consistent with the single azimuthal cell assumption applied to the VESSEL component. It also avoids having to duplicate the main steam components, such as SRVs, MSIVs, and turbine stop/bypass valves, for each main steam line.

2.2.6 SRV/ADS

The model BWR/5 plant has 18 safety-relief valves (SRVs) arrayed in five banks (Table 2.2). The lowest pressure SRV bank includes two valves. However, they are assumed out of service (OOS) [11, 13]. In the current TRACE model the SRVs are represented by a single lumped valve whose partial opening simulates the opening of separate SRV banks. This lumped valve represents all available SRVs. An approach for controlling the open fraction of the lumped SRV/ADS incorporates a control system that features five trips. The first four trips are intended to capture the lift and reset of each bank of SRVs. The pressure in the steamline then is used to determine if any of these individual trips are actuated. The trips then are summed, each with a value of unity, and these values are then fed into a table that relates the sum block value to the number of open SRVs.

Table 2.2 ADS/SRV Valve Opening

# of SRV Valves	# of ADS Valves ¹	Opening Pressure ²		Closing Pressure		Remark
		psig	MPa(a)	psig	MPa(a)	
2	0	1103	7.707	1048	7.327	SRV Bank 1: Assumed OOS
4	0	1113	7.775	1048	7.396	SRV Bank 2
4	0	1123	7.844	1058	7.465	SRV Bank 3
4	3 ¹	1133	7.913	1068	7.534	SRV Bank 4
4	4 ¹	1143	7.982	1078	7.603	SRV Bank 5

¹ This is the number of SRVs in a particular bank that also serves the ADS function.

² The opening and closing pressures are based on values from the Nine Mile Point 2 EPU model analyses. They correspond to the "Relief Mode" nominal trip setpoints. We note that the opening pressures are identical with the SRV parameters shown in the Nine Mile Point Unit 2 USAR (Table 6A.3-1, USAR Revision 14, February 2001).

2.2.7 Feedwater and Reactor Water Level Control

In the current model the TRACE built-in level controller is replaced with a three-element FW controller that is known to work from previous applications [19, 20]. The FW flow controller maintains the reactor water level (RWL) at the desired level setpoint, based on the following controller inputs: FW flow, steam flow, and RWL. The setpoints specified are the nominal FW flow and the desired RWL. The output of the controller is the FW demand that sends a signal to the FILL component simulating the FW system. The FW controller gets a single water-level demand value as an input, and this value is static and cannot be changed during the transient. To control water level to a different desired setpoint, a strategy was implemented whereby the signal variable that reads the instantaneous water level is adjusted. This adjustment (delta) is applied to the instantaneous water-level upstream of the RWL signal provided to the FW

controller. The delta then can be adjusted while calculating the transient. The controller input becomes the sum of the RWL and the delta, and this is the pseudo or virtual level. Depending on the magnitude of the delta, the FW controller will control the RWL to an offset level from its nominal setpoint. Appendix A, the TRACE calculation notebook, contains details of the control logic.

2.2.8 Reactor Core Isolation Cooling System

The RCIC is modeled in TRACE using two FILL components that represent the condensate storage tank (CST) and the suppression pool (SP). The RCIC with its steam-driven pump takes suction from either the CST or the SP and injects through a side pipe connection to the FW line. The RCIC is included in the current TRACE model to provide coolant when the reactor is isolated, in particular after MSIV closure. The system is to supply coolant to maintain the level of reactor water between L3 and L8 (water-level setpoints that are different from the axial levels in the VESSEL component). The rated flow of RCIC is 39.414 kg/s [9]. The RCIC will take suction first from the CST until the reserve is depleted and then from the SP. The control logic for the RCIC accounts for net positive suction head, low-pressure operation, and the capacity of the condensate storage tank [13].

2.2.9 Standby Liquid Control System

The standby liquid control system (SLCS) ultimately is responsible for terminating the ATWS event and bringing the reactor to a stable shutdown condition. In the case of ATWS-I, the SLCS injection point is into the upper plenum inside the shroud. The modeling of SLCS is done using a FILL component that injects a borated solution into the appropriate node within the VESSEL component in TRACE.

2.2.10 Lower Plenum Flow Valve

NRC staff provided technical direction on modeling boron mixing in the reactor vessel when the SLCS injection is to the vessel's lower plenum [12, 14, 16]. Boron transport for lower plenum injection configurations is modeled using a valve (Valve 34) inside the vessel's lower plenum that opens and closes to simulate the effect of boron stratification and remixing. Below the stratification core's flow-rate setpoint, the lower plenum valve (LPV) closes to isolate the lower regions of the lower plenum, and prevent effective entrainment of borated water into the active core region. When the core flow rate increases above the remixing threshold, the LPV opens with a flow-gradient-based area curve to simulate the increased effectiveness of remixing. For the ATWS-I cases, the flow valve is modeled with two cells and is located in ring 2 between the top of axial level 3 and the top of axial level 2. We note that for the BWR/5, the SLCS injects into the upper plenum and the modeling of the lower plenum valve is less important for those ATWS-I cases than for cases involving lower plenum SLCS injection, i.e., the ATWS-ED cases that are based on a BWR/4 plant configuration. Details of the LPV model are in Appendix A, the TRACE calculation notebook.

2.2.11 Suppression Pool Cooling

The suppression-pool cooler is modeled to emulate the cooling mode of the residual heat removal system (RHR). The built-in cooler of the CONTAN component can only be on or off; it is impossible to activate/deactivate the containment wetwell cooler with a control system. To enable the activation of suppression pool cooling by control logic, we developed a scheme to remove energy from the suppression pool water by feed-and-bleed (remove warm pool water and replenish with cold water). The scheme has two parts; a source to supply the feed, and a sink to receive the bleed. Two BREAK components serve as connections to the wetwell. The required mass flow to remove a certain amount of energy from the suppression pool is calculated by noting the RHR heat exchanger's capacity for removing heat. In modeling the SP cooler, the mass flow is provided by a single junction valve. The derivation of the model is described in Appendix A, the TRACE calculation notebook.

2.3 Core Input Model for PARCS

2.3.1 Introduction

The core models developed for use with PARCS were for a BWR/5 at three different points in the fuel cycle: beginning-of-cycle (BOC), peak-hot-excess-reactivity (PHE), and end-of-full-power-life (EOFPL). They were intended to be used in coupled TRACE/PARCS steady-state calculations, PARCS stand-alone steady-state calculations, and transient TRACE/PARCS calculations. The PARCS models were developed for evaluating two types of anticipated transients without scram (ATWS): 1) ATWS initiated by a turbine trip that undergoes a period of instability causing power oscillations (designated ATWS-I); and, 2) ATWS initiated by the closure of main steam isolation valves that depressurizes the reactor when the temperature limit for heat capacity of the suppression pool is reached (designated ATWS-ED). Although designed for these events, the core models have broader applicability and can be used for a variety of transients/accidents. Non-proprietary details of the PARCS model are found in Appendix B. The following summarizes the models.

2.3.2 Reactor and Fuel Bundle Properties

Nine Mile Point is a two-unit nuclear power plant designed by General Electric (now GE Hitachi, GEH). Unit 2 (NMP2) is a BWR/5 and, although not licensed to operate in this expanded operating domain, is the basis for the TRACE/PARCS ATWS model at MELLLA+ operating conditions developed in the present study.

Under hypothetical MELLLA+ conditions, NMP2 could be assumed to operate at 120% of its original licensed power, at less than the rated flow for most of the cycle (which is a key feature of the MELLLA+ domain). At the end of the cycle, the flow is increased to maintain the power level. In the BWR/5 PARCS model, the total thermal power is 3988 MWt, or 5.22 MWt per fuel assembly on average. The flow is imposed by TRACE, and is not specified in the PARCS model.

The model assumes an equilibrium core of 764 GE14 assemblies. Each assembly [10] is a 10x10 fuel bundle consisting of the following:

- 63 full-length fuel rods without gadolinia (with natural uranium top and bottom blankets)
- 15 full-length fuel rods with gadolinia (with natural uranium bottom blankets only)
- 14 partial-length fuel rods without gadolinia (with natural uranium bottom blankets only)
- two water rods (2x2 pitch each; hence, eight rod positions)

Fuel enrichment varies from rod to rod, and gadolinia concentration changes for different types of rod and axial levels. Figure 2.3 shows a generic GE14 fuel assembly with rod-by-rod enrichment and gadolinia concentration for distinct axial segments (Appendix B). The layout within the fuel bundle is shown in Figure 2.2.

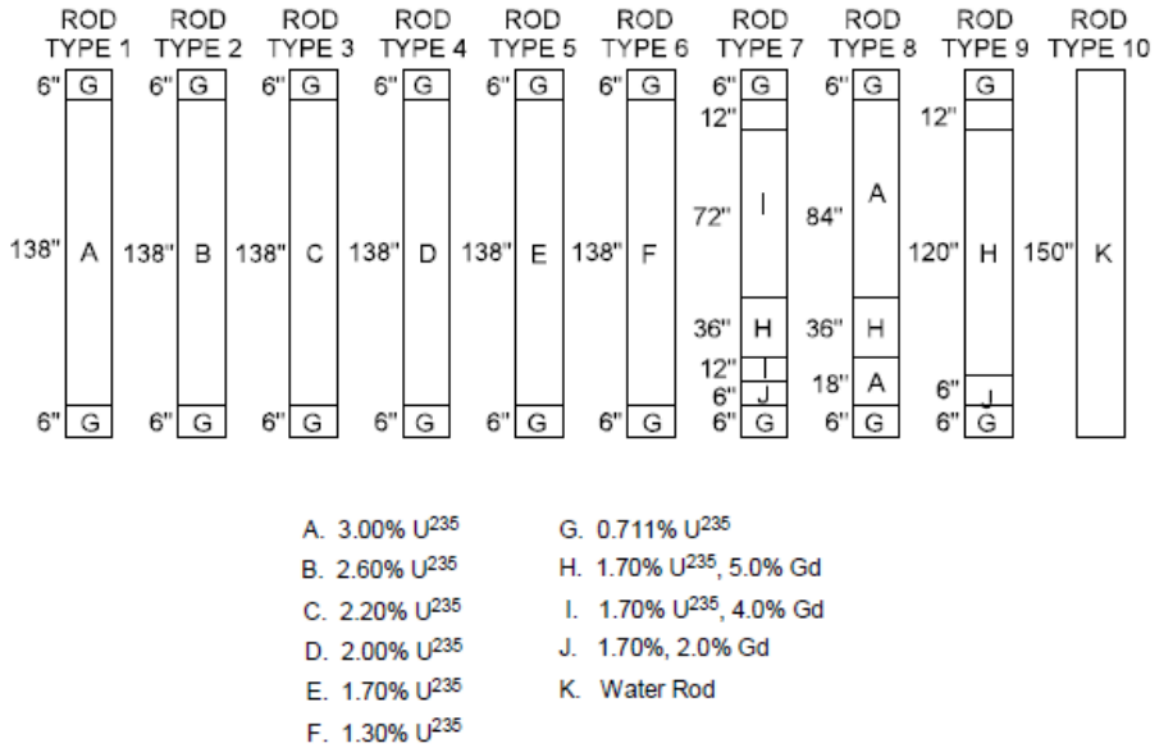


Figure 2.3 Axial Layout of a Generic GE14 Fuel Bundle

2.3.3 Core Geometry and Control Rod Banks

The core model contains 32x32 radial (x-y) meshpoints, and 27 axial planes. Radially, a meshpoint represents one of the 764 fuel bundles, or a radial reflector. The meshpoint interval in the radial plane is 15.24 cm (6"), i.e., the pitch of the fuel bundles in the reactor core. The axial core layout contains 25 layers of fuel, including the top and bottom natural uranium blankets, and one mesh for a reflector at both top and bottom. The axial meshpoint interval is 15.24 cm (6") matching the overall active fuel length of GE14 bundles. Zero flux boundary conditions are used at the outside of the reflectors.

The core model includes eight planar regions with unique materials, representing two reflectors (top and bottom), and the six distinct fuel compositions.

The control rods were modeled taking into account the quarter-core symmetry of the core. Figure 2.4 shows the location of each of the 54 control rod banks in the core taking into account symmetry across the y-axis and with the positions denoted "0" representing reflector cells. The control rods can move 48 steps axially, with each step 7.62 cm [21]. In its fully inserted position, the position of the top of a control rod is 52.857 cm below the top of the core (or 15.24 cm below the top of active fuel). The positions of the control rods vary throughout the cycle, and are given by [10], as follows:

- for BOC: banks 10, 21, 23 are 10 steps inserted; banks 19, 33, 35, 34 steps inserted; and all other banks fully withdrawn
- for PHE: banks 34, 43 are 10 steps inserted; banks 36, 45, 40 steps inserted; bank 41, 38 steps inserted; bank 20, fully inserted; and all other banks fully withdrawn
- for EOFPL: all banks are fully withdrawn

The solution for the two-group fluxes in each of the nodes in the core was obtained differently for the two ATWS events of interest. The nodal kernel most commonly used in PARCS is a hybrid between the analytic nodal method (ANM) and the nodal expansion method (NEM). This HYBRID kernel was chosen for our steady-state and the ATWS-I calculations.

									0	0	0	0	0	0	0	0	0	0				
								0	0	3	3	2	2	1	1	1	1	47				
							0	0	0	0	3	3	2	2	1	1	1	47				
							0	0	7	7	6	6	5	5	4	4	4	46				
							0	0	0	7	7	6	6	5	5	4	4	46				
							0	0	0	12	12	11	11	10	10	9	9	8	8	45		
							0	0	0	12	12	11	11	10	10	9	9	8	8	45		
							0	0	18	18	17	17	16	16	15	15	14	14	13	13	44	
							0	0	0	18	18	17	17	16	16	15	15	14	14	13	13	44
							0	25	25	24	24	23	23	22	22	21	21	20	20	19	19	43
							0	25	25	24	24	23	23	22	22	21	21	20	20	19	19	43
							0	32	32	31	31	30	30	29	29	28	28	27	27	26	26	42
							0	32	32	31	31	30	30	29	29	28	28	27	27	26	26	42
							0	39	39	38	38	37	37	36	36	35	35	34	34	33	33	41
							0	39	39	38	38	37	37	36	36	35	35	34	34	33	33	41
							0	54	54	53	53	52	52	51	51	50	50	49	49	48	48	40

Figure 2.4 Control Rod Bank Positions in the Core

2.3.4 Cross Sections and Other Bundle Parameters

The NRC provided the cross sections used by PARCS. They were generated with SCALE/TRITON and converted into the PMAXS format for use by PARCS at Oak Ridge National Laboratory [22]. The cross section files for fuel assemblies include four void histories, multiple burn-up steps (up to a maximum exposure of 60 GWd/MTU), and 39 branches selected by combining five moderator densities, three fuel temperatures, four boron concentrations, and two control states (controlled/uncontrolled). Table 2.3 shows the branch structure for 0% void history.

Cross sections are provided for the top, bottom, and two radial reflectors. One radial reflector represented a node adjacent to a single fuel bundle, and the second reflector’s composition represented a corner position next to two bundles. The radial reflectors were modeled with constant properties.

In PARCS, an effective model for coolant density was implemented [23] to account for the impact of multiple fluid region water densities in the new BWR fuel designs. The effective coolant density (ρ_{eff}) is defined as follows:

$$\rho_{\text{eff}} = \rho_{\text{cool}} + \frac{A_{\text{wr}}}{A_{\text{cool}}} (\rho_{\text{wr}} - \rho_{\text{sat}}) + \frac{A_{\text{byp}}}{A_{\text{cool}}} (\rho_{\text{byp}} - \rho_{\text{sat}})$$

where ρ_{cool} is the density of the coolant in the active heated channel, ρ_{sat} is the saturated moderator liquid density, ρ_{wr} , the moderator density in the water rod, ρ_{byp} , the moderator density in the bypass, and $A_{\text{wr}}/A_{\text{cool}}$ and $A_{\text{byp}}/A_{\text{cool}}$ respectively are the area ratio of water rods to coolant and bypass to coolant.

Not all fission energy is deposited in the fuel pellet. The direct energy deposition to the coolant was 1%, to the bypass 0.9%, and to the water rods 0.2% [24].

PARCS requires node-by-node burn-up information to use the cross sections that are functions of exposure and spectral history. The latter can be void or moderator density history, and control-rod history. For the present study, we obtained information on the exposure (MWd/kg) and moderator density history (kg/m^3) from data received from GEH [10] for the three points of the cycle under consideration (BOC, PHE, and EOFPL). Although there was no control rod history information available, GEH provided “spectrally corrected” void histories for BOC, PHE, and EOFPL. The effect of the latter was used in a sensitivity case.

Table 2.3 Branch Calculation States for 0% Void History Tree

Branch no.	Control rod state (0=out, 1=in)	Moderator Density (g/cm^3)	Soluble Boron (ppm)	Fuel Temperature (K)
0	0	0.45843	0	863.15
1	1	0.45843	0	863.15
2	0	0.03653	0	863.15
3	0	0.17716	0	863.15
4	0	0.73970	0	863.15
5	0	1.00000	0	863.15
6	1	0.03653	0	863.15
7	1	0.17716	0	863.15
8	1	0.73970	0	863.15
9	1	1.00000	0	863.15
10	0	0.03653	600	863.15
11	0	0.03653	1400	863.15
12	0	0.03653	2200	863.15
13	0	0.17716	600	863.15
14	0	0.17716	1400	863.15
15	0	0.17716	2200	863.15
16	0	0.45843	600	863.15
17	0	0.45843	1400	863.15
18	0	0.45843	2200	863.15
19	0	0.73970	600	863.15
20	0	0.73970	1400	863.15
21	0	0.73970	2200	863.15
22	0	1.00000	2200	863.15

Branch no.	Control rod state (0=out, 1=in)	Moderator Density (g/cm ³)	Soluble Boron (ppm)	Fuel Temperature (K)
23	1	0.03653	2200	863.15
24	1	0.17716	2200	863.15
25	1	0.45843	2200	863.15
26	1	0.73970	2200	863.15
27	1	1.00000	2200	863.15
28	0	0.03653	0	293.15
29	0	0.03653	0	2073.15
30	0	0.17716	0	293.15
31	0	0.17716	0	2073.15
32	0	0.45843	0	293.15
33	0	0.45843	0	2073.15
34	0	0.73970	0	293.15
35	0	0.73970	0	2073.15
36	0	1.00000	0	293.15
37	0	1.00000	2200	293.15
38	1	1.00000	0	293.15
39	1	1.00000	2200	293.15

2.3.5 TRACE/PARCS Mapping

The mapping defines the correspondence between neutronic nodes and hydraulic volumes / heat structures. The “auto-mapping” feature of TRACE/PARCS was used, whereby the mapping file was reduced to a radial map specifying the CHAN(s) to be coupled to each neutronic node. In the TRACE model, the CHAN components themselves are distributed amongst the first two rings of the VESSEL component. With “automap” the nodes in the reflector are not mapped into any thermal-hydraulic volume, but instead, have fixed properties defined in the same mapping file.

While a TRACE/PARCS model can be built with one-to-one correspondence between neutronic and thermal-hydraulic nodes, it is usually not practical because of the long run times. In general, a compromise between accuracy and run times is reached, based on the expected behavior of the transient to be analyzed.

For ATWS-I, the starting point was a TRACE model with 764 channels and one-to-one correspondence between neutronic and thermal-hydraulic nodes. However, this model was onerous to run, so we decided to take into account a fundamental symmetry in the problem; i.e., the half-core symmetry along the y-axis. Not also taking into account the quadrant symmetry of the core allows more modes of oscillation. The resulting 382-channel model proved successful for all points in the cycle and for steady-state conditions it was shown that the first harmonic only had an axis of symmetry along the y-axis (Chapter 3). Since the core is quadrant symmetric, the 2-to-1 channel grouping does not impact the steady-state calculations. A different prediction of the first harmonic symmetry axis (i.e., not along the y-axis) would require our adjusting the channel grouping to align the symmetry axes before calculating the transient. The mapping is shown in Figure 2.5 and is referred to as the 382-channel model.

For ATWS-ED, the core response is expected to be fairly uniform, allowing a coarser TRACE representation. The grouping was based on geometrical and fuel cycle considerations. The

logic also took into account the relative flatness of the power in the core's "interior" region. This negates, to some extent, considering the usual means of grouping bundles according to similar power level.

The "interior" region of the core, mapped into ring 1 of the VESSEL, was divided in five annular regions with approximately the same number of assemblies in them. In each annular region, fresh and burned assemblies were separated and assigned to two different channels (251/252 for annular region 1, 351/352 for annular region 2, 451/452 for annular region 3, 551/552 for annular region 4 and 651/652 for annular region 5). Further detail was introduced around the control rods that are "significantly" inserted (more than 10 steps inserted) either for BOC or PHE; for assemblies next to each of the seven control rods in a quadrant, we added two new channels (for fresh and burned bundles).

Next, the fuel assemblies mapped into ring 2 of the vessel component were selected and defined as a peripheral region. The outermost assemblies therein (with different effective loss coefficients for the lumped leakage flow path), were lumped together into channel 752, while the remaining assemblies were assigned to channels 751 (fresh assemblies), and 753 (burned assemblies).

The result was a TRACE model with 27 channels for the ATWS-ED analysis, with mapping (Figure 2.6). The resulting PARCS model is referred to as the 27-channel model.

2.4 Code Execution Methodology

The multi-step approach to achieve steady-state convergence of the BWR/5 model for subsequent transient is based on experience at NRC [25]. The mechanics of creating a TRACE input model is described in Section 2.4.1. The three-step process of approaching steady-state convergence is outlined in Section 2.4.2, and the execution procedure of the TRACE/PARCS inputs is summarized in Section 2.4.3. Section 2.4.4 describes a procedure to verify the convergence of a TRACE/PARCS coupled steady-state calculation and the creation of the harmonic data for use by the PARCS noise model. Section 2.4.5 summarizes the output files from executing the TRACE/PARCS code system. We note that all ATWS-I cases were analyzed using the semi-implicit method to reduce numerical diffusion in the solution of the TRACE model equations.

2.4.1 Preparation of the Base TRACE Model

The TRACE model exists as a SNAP 'med' file and its corresponding ASCII input deck. The SNAP 'med' model is a useful tool for developing a model and checking basic errors. It also affords a graphical visualization of the model when appropriate templates are used. The ASCII input deck is preferred for its ease of use when running calculations, in particular those in batch mode. It also is more practical for developing models in instances where many (nearly) identical components must be inserted in the model, as is the case for the multi-channel ATWS models. Figure 2.7 shows how the ATWS models were prepared, taking advantage of the capabilities of SNAP and incorporating (pasting) therein multiple components (channels, pipes) replicated from a template and customized by a MATLAB script.

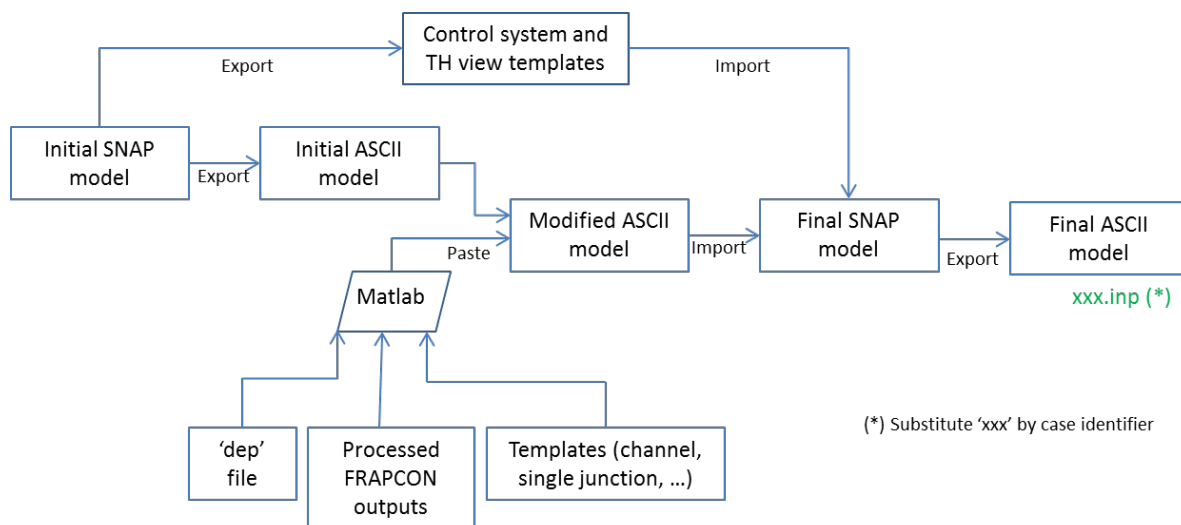


Figure 2.7 Preparation of the TRACE Stand-Alone Steady-State model

2.4.2 Steady-State Initialization

The initial steady-state for a transient calculation is determined by a sequence of calculations. Since the transient will be analyzed using the TRACE/PARCS coupled code system, the same code system is used to determine the initial steady-state. However, a TRACE stand-alone steady-state calculation first is completed to initialize the BWR/5 model. A null transient is used as the last step to initialize, in a three-step process, the BWR/5 model for transient calculations, as described below.

1. TRACE Stand-Alone

A constrained steady-state (CSS) calculation is performed with TRACE stand-alone. The two type-2 CSS controllers adjusted the flow area of two valves to achieve the following:

- Desired pressure upstream of the turbine stop-valve – this establishes the pressure boundary condition at the end of the main steamline, and, therefore, for the reactor vessel component.
- Desired recirculation flow rate – this establishes the desired core flow rate in the reactor. Since the controller is on the recirculation flow, several runs are needed to determine the recirculation flow rate that will result in the desired core flow.

2. Coupled Steady-State

A TRACE/PARCS coupled steady-state calculation is performed, restarting from the stand-alone calculation and using the same CSS controllers as in that run. The calculation may need repeating a few times as the recirculation flow rate from the stand-alone run may not result in the same core flow in the coupled run.

3. Null Transient

The initial conditions for a transient run are established by running a ten-second null transient before the initiating event in a transient calculation. This is accomplished by conducting a coupled transient calculation without the CSS controllers and restarting from the coupled steady-state. The controllers for the turbine control valve and the recirculation flow control valve are modified in the transient input deck. A narrow control range (minimum and maximum setpoints) inferred from the coupled steady-state run is specified for these two valves. The objective is to minimize perturbation to the system when changing from a calculation in the CSS mode to a calculation in null transient. After ten seconds of problem time, the initiating event is simulated, thus ending the null transient period of the transient calculation.

2.4.3 Execution Procedure

The simulation with TRACE/PARCS of an ATWS event requires three successive steps (Figure 2.8). In the steps below, substitute 'xxx' for the appropriate case identifier (e.g., 'boc382chan-atws12'):

- Undertake a TRACE stand-alone calculation for flow initialization (invoking no PARCS calculations). A restart file ('xxx.tpr') is generated at the end of this calculation.
- Using this restart file (renamed 'xxx-rc.rst'), run the coupled steady-state calculation, by setting the itdmr flag to 1 in the TRACE input deck ('xxx-rc.inp'), and having the PARCS input deck ('xxx-rc.parc_inp') in the same directory. Restart files are generated for both PARCS ('xxx-rc_parc_rst' and 'xxx-rc.dep') and TRACE ('xxx-rc.tpr'). The degree of convergence of the coupled steady-state can be checked by performing an additional PARCS stand-alone calculation, as described in Section 2.4.4.
- Using the above restart files ('xxx-rc_parc_rst' and 'xxx-rc.tpr' renamed to 'xxx-tr.rst'), run the coupled transient calculation. The itdmr flag in the TRACE input deck ('xxx-tr.inp') is 1, and the PARCS input deck ('xxx-tr.parc_inp') is in the same directory. Also, the harmonic file generated from a PARCS stand-alone steady-state run (Section 2.4.4) is placed in the same directory as the PARCS input file for use as an input by the PARCS white-noise model. Section 2.4.5 describes some of the outputs generated.

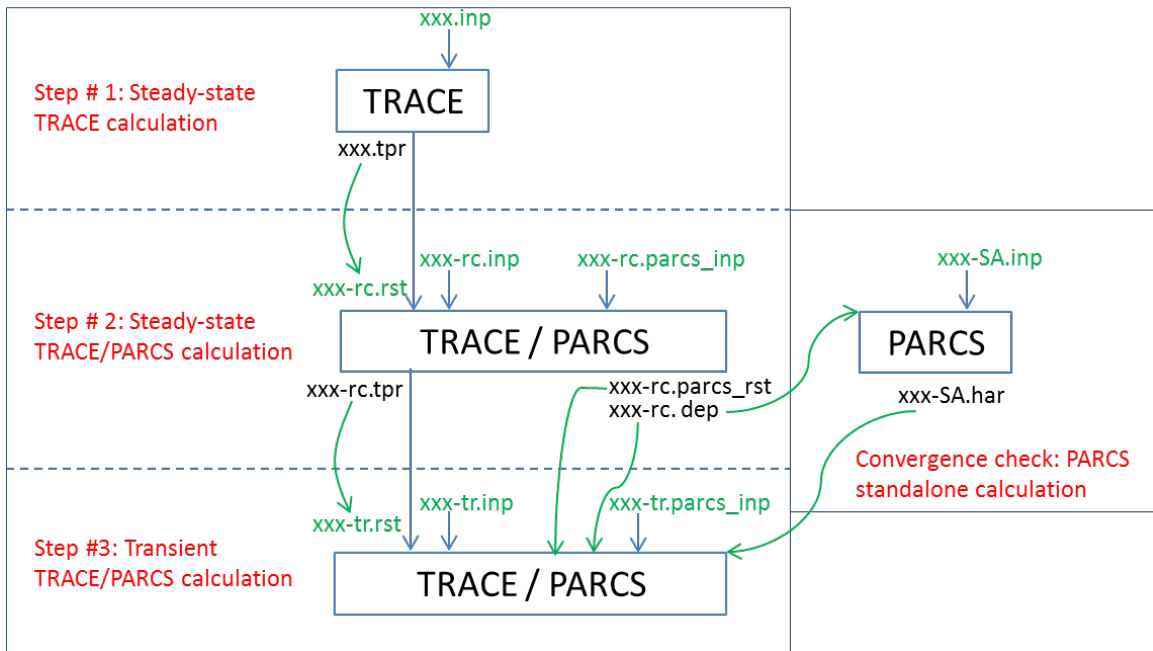


Figure 2.8 TRACE/PARCS Code Execution Procedure

2.4.4 Steady-State Convergence Check

To assure proper convergence of the coupled steady-state calculation, a PARCS stand-alone steady-state calculation is performed using the thermal-hydraulic information obtained during the coupled TRACE/PARCS steady-state calculation. The file 'xxx-rc.dep', written at the end of the coupled steady-state (Figure 2.8), is read by PARCS at the beginning of the stand-alone calculation; the first harmonic is evaluated during this calculation. The harmonic data written to a file 'xxx-SA.har' is used by PARCS in a coupled transient calculation that activates the white noise model in PARCS. The eigenvalues obtained during the coupled steady-state and the stand-alone steady-state are compared to assess the degree of convergence.

A secondary convergence check was performed by running a ten-second null transient at the beginning of each transient. Figure 2.9 shows the reactor power, dome pressure, total core mass flow rate, and downcomer level during the null transient at PHE. The power clearly is constant (3988 MW) before noise is introduced at five seconds, and oscillates around the same value (3988 MW) afterwards. The variation in power with applied noise is $\pm 0.3\%$. The figures demonstrate good convergence of the steady-state solution: The dome pressure, total core mass flow, and downcomer level are constant before five seconds, and show minimal impact from introducing noise after five seconds.

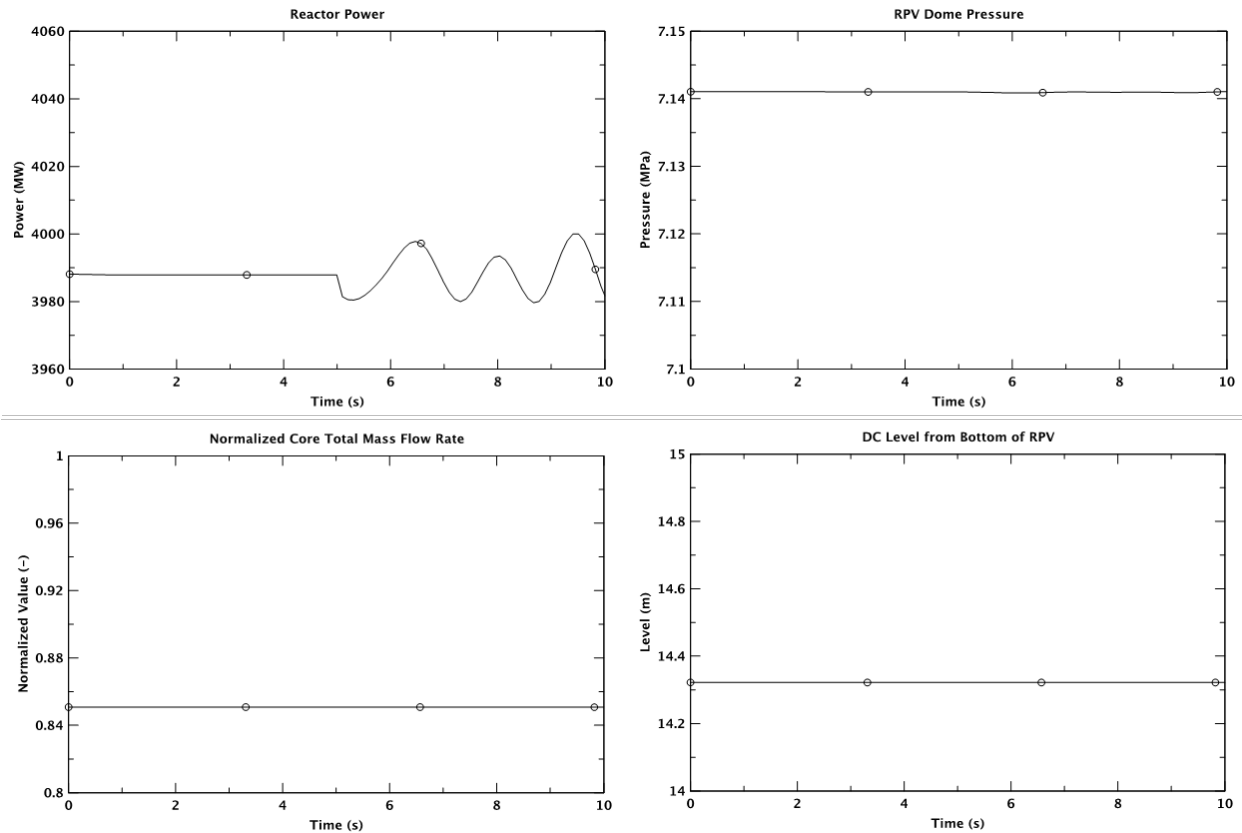


Figure 2.9 Null Transient Results at PHE, 382-Channel Model

2.4.5 TRACE Transient Input Deck

The transient input decks for all ATWS-I cases are assembled as restart cases (restarting from the corresponding coupled steady-state runs). In all ATWS-I transient cases the turbine trip is initiated at 10 s. The first 10 s of the calculation is run as a null transient; the purpose is to transition the mode of the calculation from a constrained steady-state (CSS) to a general transient.

In order to preserve a smooth switch over from CSS controllers to regular controllers the inputs for two control blocks (CB) are re-defined in the transient decks. They are CB-5 for the recirculation flow control valve and CB-61 for the turbine pressure control valve. A narrow control range (minimum and maximum open fractions) is specified for the two valves, essentially keeping the valve open areas unchanged from the coupled steady-state runs during the null transient. The desired flow (for CB-5) and the desired pressure (for CB-61) are based on the coupled steady-state results.

Two additional control blocks are re-defined in the transient restart input deck. The closure of the turbine stop/control valve and the opening of the turbine bypass valve are simulated by a table that specifies the turbine stop/control valve open area as a function of time. This set of valve operation input is defined in CB-1512. The valve flow area for 100% steam flow is obtained from the coupled steady-state and this value is used in both CB-1512 and CB-1513 which defines the operating range of the turbine stop/control valve from zero to 100% steam flow.

Each ATWS-I transient input deck defines two pairs of CHANs for additional output. Each pair consists of two channels in core positions symmetrical about the first harmonic plane. One pair represents the maximum power fuel assembly and the other pair represents the fuel assembly with the maximum first harmonic power. The CHANs to be monitored are identified from the PARCS stand-alone calculations. Since the radial power distribution in the core is different for each cycle time, the signal variables defined to provide the additional TRACE output for the ATWS-I cases need to be re-defined in the transient input deck to associate the signal variables with the appropriate CHANs. The signal variables and the corresponding CHANs that are re-defined are identified in Table 2.4.

Table 2.4 Signal Variables Re-Defined in a Transient Input Deck

Signal Variables	Maximum Power CHANs		
	BOC	PHE	EOFPL
210 – 213, 218, 220, 222, 251	269	388	271
214 – 217, 219, 221, 223, 252	520	403	522
Signal Variables	Maximum First Harmonic Power CHANS		
	BOC	PHE	EOFPL
230 – 233, 238, 240, 242, 253	245	243	233
234 – 237, 239, 241, 243, 254	546	544	555

2.4.6 Outputs

The execution of TRACE/PARCS generates a myriad of output files, some of which were not used in the analysis. Tables 2-4 and 2-5 show the TRACE and PARCS output files that were used in the analysis.

Table 2.5 TRACE Outputs

Output File	Description
xxx-tr.xtv ¹	TRACE graphics file (binary), which AptPlot can visualize (with or without AVScript)
xxx-tr.out	ASCII file containing “snapshots” of the calculation variables at specific times during the calculation.
xxx-tr.tpr	Restart file, may be used to initialize all or part of the system model for subsequent restart calculations from its data-dump edit time.

¹ The xtv file is usually further processed, or ‘demultiplexed’ into a dmx file to speed up plotting.

Table 2.6 PARCS Outputs

Output File	Description
xxx-tr.parc_out	Primary PARCS output file (ASCII). This file can be processed with MATLAB to generate a movie of transient power behavior.
xxx-tr.parc_sum	Summary file (ascii). It is used to obtain time dependent core-averaged parameters (e.g. core average moderator density) not included in the output file.
xxx-tr.parc_rho	Ascii file listing the reactivity and its components (Doppler, boron,...).
xxx-tr.parc_rst	Restart file, may be used for subsequent restart calculations from its data dump edit time.

3 STEADY-STATE RESULTS

This section summarizes the results of the coupled TRACE/PARCS steady-state calculations and provides comparisons with nodal power information received from GEH [10]. Additional GEH data, such as node-by-node burnup information or moderator density history information, were used in the coupled model. Sections 2.2 and 2.3 describe the basic inputs used in the coupled model, while Appendices A and B discuss in detail the inputs and their sources. TRACE Version 5.450-fix-7M was used. The results are summarized in Sections 3.1, 3.2, and 3.3 for the three different times during the fuel cycle that are being considered, namely, beginning-of-cycle (BOC), peak-hot-excess-reactivity (PHE), and end-of-full-power-life (EOFPL). Axially and radially averaged power distributions are found in these sections.

The steady-state calculations were carried out in two steps, as described in Section 2.4.2. The convergence of the coupled steady-state solution was verified by using the thermal-hydraulic information written at the end of the coupled steady-state calculation in a PARCS stand-alone calculation. The first harmonic shape, the basis for the channel grouping, was also obtained during this stand-alone calculation. The convergence of the coupled steady-state solution was further confirmed by running a null transient for ten seconds.

3.1 ATWS-I 382-Channel BOC Model

At beginning of cycle approximately half of the fuel bundles are fresh and half are once-burned, with exceptions in the periphery of the core where some fuel bundles are twice-burned. The power shape is bottom-peaked, and control rods are partially inserted to shape the power and control the excess reactivity.

The eigenvalue for the coupled steady-state calculation is 1.01542, consistent with the eigenvalue obtained during the stand-alone calculation with fixed thermal-hydraulics (1.01529), indicating that the solution is properly converged.

3.1.1 Initial and Boundary Conditions

Table 3-1 shows the comparison of the initial values of reactor power and some key thermal-hydraulic parameters, which are the results of the TRACE/PARCS null transient calculation for ten seconds, to the reference values based on the "Safety Analysis Report for Nine Mile Point Nuclear Station Unit 2 Constant Pressure Power Uprate" [26]. As shown in the table, calculated steady-state values are in good agreement with the reference values.

Table 3.1 Comparison of Steady-State Thermal-Hydraulic Parameters at BOC

Parameter	Units	TRACE/PARCS Value	Reference Value [26]	Diff. (%)
Core Power	MWt	3,988	3,988	0.0
Steam Dome Pressure	kPa	7,143	7,136	0.1
Main Steamline Flow	kg/s	2,222	2,222	0.0
Total Core Flow	kg/s	11,610	11,620	-0.08
Feedwater Flow	kg/s	2,220	2,222	-0.09
Feedwater Temperature	K	500.1	500.1	0.0
Downcomer Level	m	14.32	14.46	-0.97
Core Inlet Temperature	K	549.8	not available	-

3.1.2 Radial Power Distribution

Under hypothetical MELLLA+ conditions, the reactor operates at a power higher than the original design, the result of an Extended Power Uprate (EPU). The EPU core has a relatively flat radial power shape in the interior, which is apparent in the axially averaged radial normalized power calculated by PARCS shown in each box for a quarter-core in Figure 3.1. The flattening of the radial power distribution is typical of an EPU core, since this allows operation at a higher core power density without increased peak bundle power [1]. The shaded boxes in the figure correspond to partially (control) rodded locations. The darker shade is for control rods that are inserted more than 70%, and the lighter shade corresponds to rods inserted less than 25%. The effect of the control rods that are significantly inserted is to decrease the power in those locations.

The peak relative bundle power is 1.26, and occurs in a location corresponding to Channel 269 (outlined in bold in Figure 3.1). This channel, as well as Channel 520 (symmetric across the first harmonic plane), is monitored throughout the transient.

The root mean square (RMS) of the difference in relative bundle power between PARCS and GEH is 0.02 for the whole core. In order to quantify “how good” is the agreement between PARCS and GEH it is necessary to know the uncertainty in the corresponding methods used to generate each result. GEH methods for MELLLA+ were evaluated by the NRC staff [27]. For high power to flow ratios, the GEH uncertainty in radial power shape is based on using data collected during local power range monitor (LPRM) instrument calibration using the traveling incore probe (TIP) system. The corresponding number for TRACE/PARCS has not been derived although similar codes (PARCS/PATHS, [28]) have been shown to have an uncertainty of approximately 8%. The calculated RMS is comparable to the uncertainty of the two methods. Thus the PARCS and GEH results can be said to be in reasonable agreement.

									0.36	0.40	0.43	0.52	0.48	0.56	0.57
							0.43	0.64	0.72	0.75	0.81	0.82	0.86	0.84	
				0.34	0.50	0.68	0.80	0.87	0.92	0.98	1.03	1.03	1.01		
				0.46	0.71	0.83	0.93	0.99	1.07	1.09	1.14	1.16	1.15		
				0.50	0.77	0.87	0.97	1.03	1.08	1.17	1.20	1.22	1.23	1.20	
			0.34	0.46	0.77	0.92	1.01	1.06	1.11	1.16	1.23	1.24	1.26	1.25	1.26
			0.50	0.71	0.87	1.01	1.11	1.17	1.21	1.24	1.24	1.26	1.24	1.26	1.24
		0.43	0.68	0.83	0.97	1.06	1.17	1.22	1.25	1.24	1.26	1.22	1.21	1.18	1.21
0.36	0.64	0.80	0.93	1.03	1.11	1.21	1.25	1.20	1.22	1.22	1.20	0.97	0.95	1.14	
0.40	0.72	0.87	0.99	1.08	1.16	1.24	1.24	1.22	1.20	1.23	1.17	0.95	0.94	1.13	
0.43	0.75	0.92	1.07	1.17	1.23	1.24	1.26	1.22	1.23	1.21	1.19	1.13	1.12	1.12	
0.52	0.81	0.98	1.09	1.20	1.24	1.26	1.22	1.20	1.17	1.19	1.19	1.12	1.10	1.12	
0.48	0.82	1.03	1.14	1.22	1.26	1.24	1.21	0.97	0.95	1.13	1.12	0.93	0.91	1.08	
0.56	0.86	1.03	1.16	1.23	1.25	1.26	1.18	0.95	0.94	1.12	1.10	0.91	0.92	1.08	
0.57	0.84	1.01	1.15	1.20	1.26	1.24	1.21	1.14	1.13	1.12	1.12	1.08	1.08	1.10	

Figure 3.1 Axially Averaged Radial Power Distribution at BOC

3.1.3 Axial Power Distribution

The normalized, radially averaged axial power calculated by PARCS is shown in Figure 3.2. As expected, the power is bottom-peaked, consistent with the axial void distribution, or the corresponding moderator density shown in Figure 3.3. The axial power shape is also influenced by the fuel bundle design, as evidenced in the successive changes of slope of the axial power observed between 206 cm and 236 cm. The discontinuity observed at 267 cm is explained by the fact that twelve control rods in the core are inserted to 259 cm. Based on work done by GEH [27] the uncertainty in the axial power shape can be calculated. As with the radial shape, there have been no data comparisons done to assess the expected uncertainty in TRACE/PARCS. However, results for similar codes [28] give an expected uncertainty of 4%. A comparison of the axial power shape calculated by PARCS and GEH [1] shows that the RMS of the difference is 0.1 for all axial nodes, which is comparable to the uncertainty of the two methods. Thus the results can be said to be in reasonable agreement.

3.1.4 First Harmonic

A PARCS stand-alone calculation was performed to obtain the first harmonic shape at steady-state conditions. The thermal-hydraulic (boundary) conditions were fixed as they were read from an output file generated during the coupled steady-state calculation. Figure 3.4 shows the first harmonic (axially averaged) shape throughout the core in relative units. The (x,y) plane is labeled according to fuel assembly and the center of the core is between coordinate 15 and 16 on each axis.

The harmonic plane is parallel to the x-axis (the x-z plane, z being the orthogonal axis to x and y), and there is an axis of symmetry along the y-axis (90°). This is not unexpected as the 382-channel model makes use of the natural core symmetry about the y-axis. The core actually exhibits quarter-core symmetry and although there are only 382 channels in the TRACE model, the PARCS calculation is done for 764 separate assemblies. GEH reported an axis of symmetry [29] that is different from PARCS. It is difficult to compare the results obtained by PARCS with those predicted by GEH, because it is possible that the eigenvalue separation between the first and successive harmonics is very small.

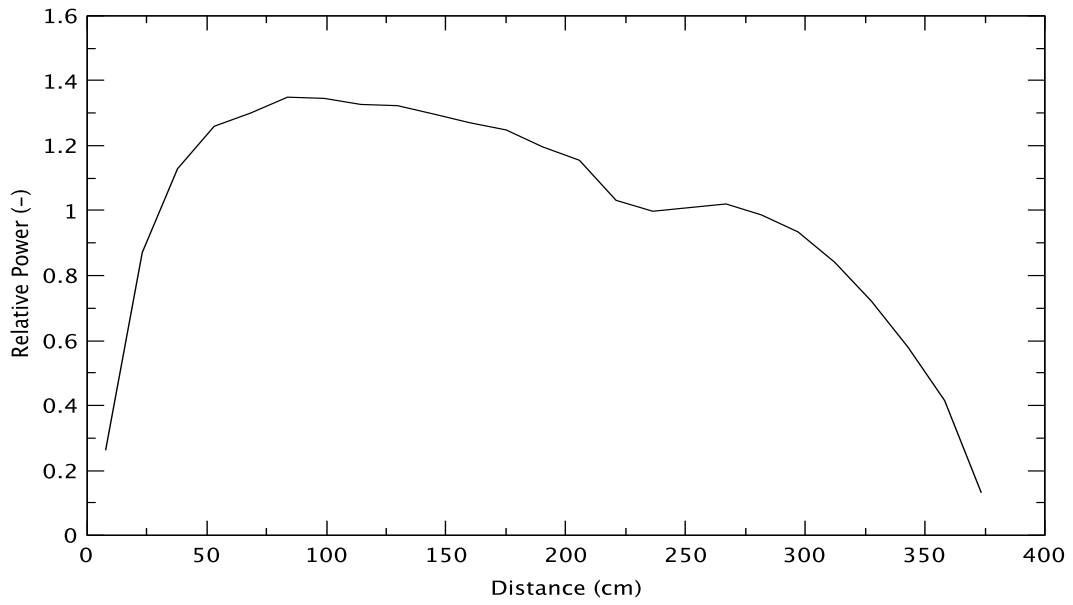


Figure 3.2 Radially Averaged Axial Power Distribution at BOC

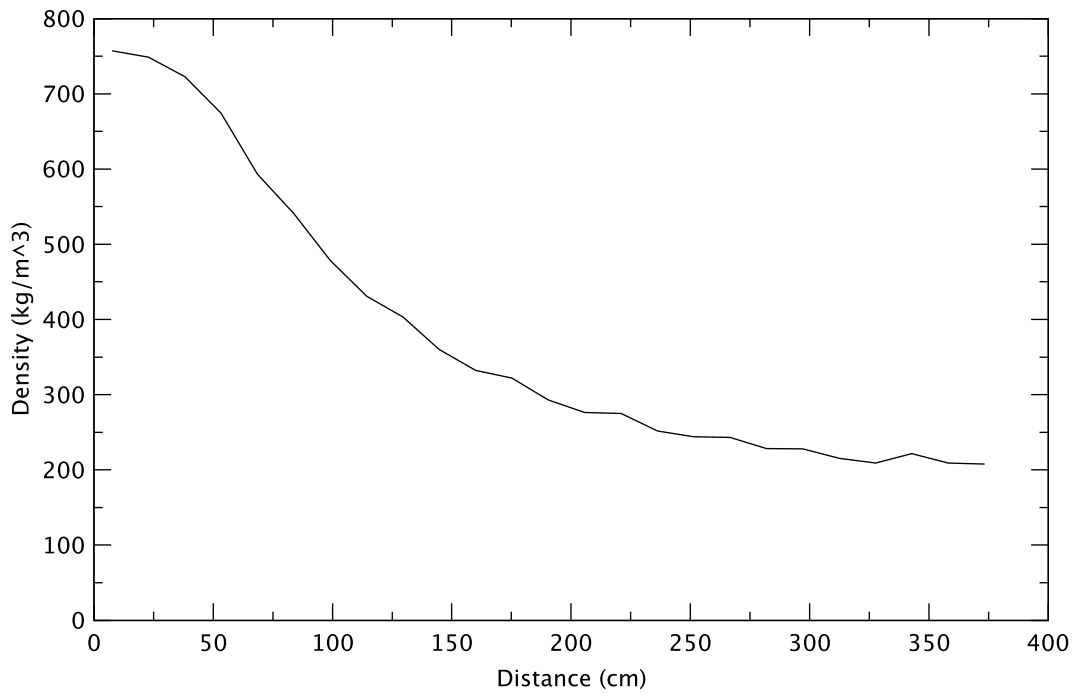


Figure 3.3 Radially Averaged Axial Moderator Density at BOC

The channels that have maximum (absolute) value of the first harmonic are Channels 245 (outlined in red in Figure 3.1) and 546 (across the first harmonic plane), and they are chosen to be followed throughout the transient together with the channels with highest power.

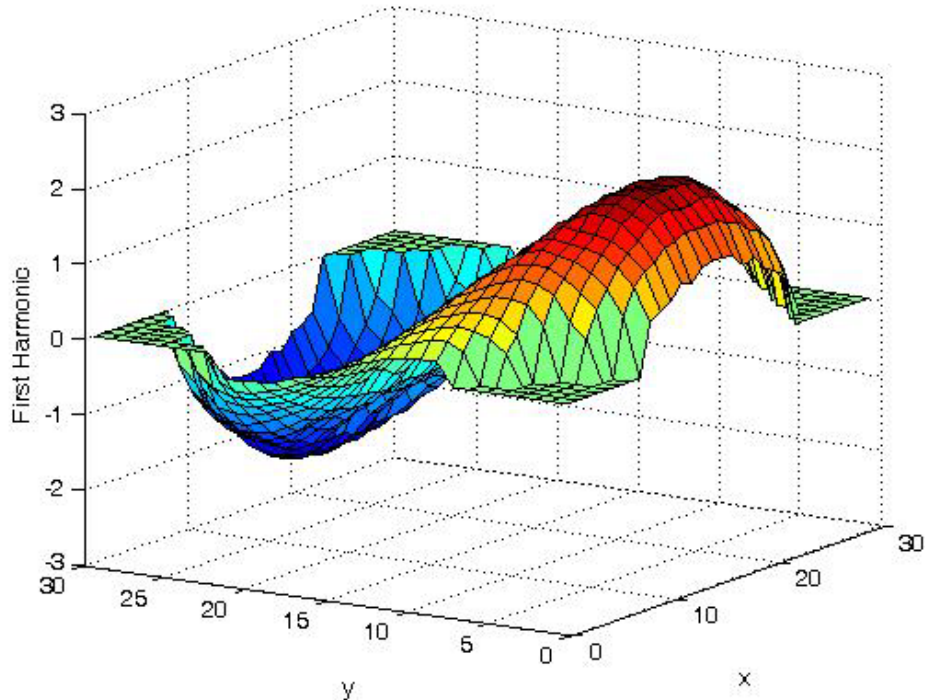


Figure 3.4 First Harmonic Shape at BOC

3.2 ATWS-I 382-Channel PHE Model

PHE corresponds to the point in the cycle with peak excess reactivity. It occurs after the gadolinia in the fuel has been depleted, close to the middle of the cycle. The power is still bottom-peaked, and control rods are partially or fully inserted to counter the excess reactivity.

The eigenvalue difference between the coupled steady-state calculation and the stand-alone calculation with fixed thermal-hydraulics is less than 1 pcm, demonstrating that the solution is properly converged. The eigenvalue is 1.00794.

3.2.1 Initial and Boundary Conditions

Table 3-2 compares to the reference values the initial values of reactor power and some key thermal-hydraulic parameters, which are the result of the TRACE/PARCS PHE coupled null-transient calculation for ten seconds. As shown in the table, calculated steady-state values agree well with the reference ones.

Table 3.2 Comparison of Steady-State Thermal-Hydraulic Parameters at PHE

Parameter	Units	TRACE/PARCS Value	Reference Value [26]	Diff. (%)
Core Power	MWt	3,988	3,988	0.0
Steam Dome Pressure	kPa	7,141	7,136	0.07
Main Steamline Flow	kg/s	2,218	2,222	-0.18
Total Core Flow	kg/s	11,630	11,620	0.09
Feedwater Flow	kg/s	2,218	2,222	-0.18
Feedwater Temperature	K	500.1	500.1	0.0
Downcomer Level	M	14.32	14.46	-0.97
Core Inlet Temperature	K	549.8	not available	-

3.2.2 Radial Power Distribution

Figure 3.5 shows the normalized, axially averaged radial power distribution for PHE, as calculated by PARCS. In the central part of the core, there is an apparent checkerboard pattern, with alternating ‘high’- (around 1.3) and ‘low’- (around 1.1) powered assemblies, except for the locations where the control rods are inserted. The “low”-powered assemblies are ones that previously burned for a full cycle, while the “high”-powered assemblies were fresh at the beginning of the cycle, and have had their gadolinia depleted. The core is still EPU, and overall, the shape of the radial power is relatively flat except at the periphery. The shaded boxes correspond to fully or partially rodded locations. The darker shade is for control rods that are inserted more than 70%, and the lighter shade corresponds to rods inserted less than 25%. The control rods that are deeply inserted function to significantly decrease the power. The peak relative power of a bundle is 1.37, and occurs in a location corresponding to Channel 388 (outlined in bold in Figure 3.5). This channel is monitored throughout the transient, as is the symmetric Channel 403. The RMS of the difference in relative bundle power between PARCS and GEH is 0.02 for the whole core, which is a reasonable agreement.

3.2.3 Axial Power Distribution

The normalized, radially averaged axial power calculated by PARCS is shown in Figure 3.6. The power is bottom-peaked, more so than for BOC because the gadolinia that initially decreased the power has been depleted. The axial-power shape is consistent with the profile of axial moderator density (Figure 3.7). The effect of the fuel bundle design also is evident, as seen in the successive changes of slope of the axial power between 206 cm and 236 cm. The RMS of the power difference between PARCS and GEH for all axial nodes is 0.08, indicating reasonable agreement.

										0.36	0.40	0.42	0.48	0.44	0.49	0.49					
									0.44	0.67	0.75	0.82	0.78	0.82	0.76	0.80					
							0.35	0.52	0.70	0.91	0.99	1.02	1.04	0.93	1.00	0.85					
							0.48	0.81	0.97	1.07	0.98	1.16	1.00	1.14	0.98	1.04					
							0.49	0.78	0.99	1.11	1.06	1.23	1.09	1.24	1.06	1.14	0.76				
							0.35	0.48	0.78	0.91	1.12	1.03	1.26	1.12	1.29	1.10	1.25	1.03	0.90		
							0.52	0.81	0.99	1.13	1.06	1.27	1.13	1.30	1.10	1.28	1.09	1.23	1.04		
							0.44	0.71	0.97	1.11	1.04	1.28	1.14	1.31	1.09	1.23	1.05	1.25	1.10	1.26	
							0.36	0.67	0.92	1.07	1.06	1.27	1.14	1.33	1.11	1.24	0.78	0.90	1.05	1.28	1.08
							0.40	0.75	0.99	0.98	1.24	1.13	1.33	1.13	1.31	1.06	0.91	0.79	1.24	1.11	1.27
							0.43	0.83	1.03	1.17	1.09	1.29	1.12	1.31	1.11	1.28	1.07	1.25	1.10	1.32	1.12
							0.49	0.80	1.05	1.01	1.24	1.08	1.24	1.07	1.28	1.12	1.31	1.19	1.33	1.12	1.28
							0.45	0.84	0.96	1.17	1.07	1.20	0.83	0.96	1.08	1.31	1.11	1.31	1.14	1.28	0.88
							0.51	0.79	1.05	1.03	1.21	1.03	0.93	0.83	1.24	1.13	1.31	1.12	1.34	1.10	1.00
							0.51	0.84	0.91	1.15	1.04	1.19	1.02	1.19	1.09	1.33	1.16	1.37	1.15	1.28	1.07

Figure 3.5 Axially Averaged Radial Power Distribution at PHE

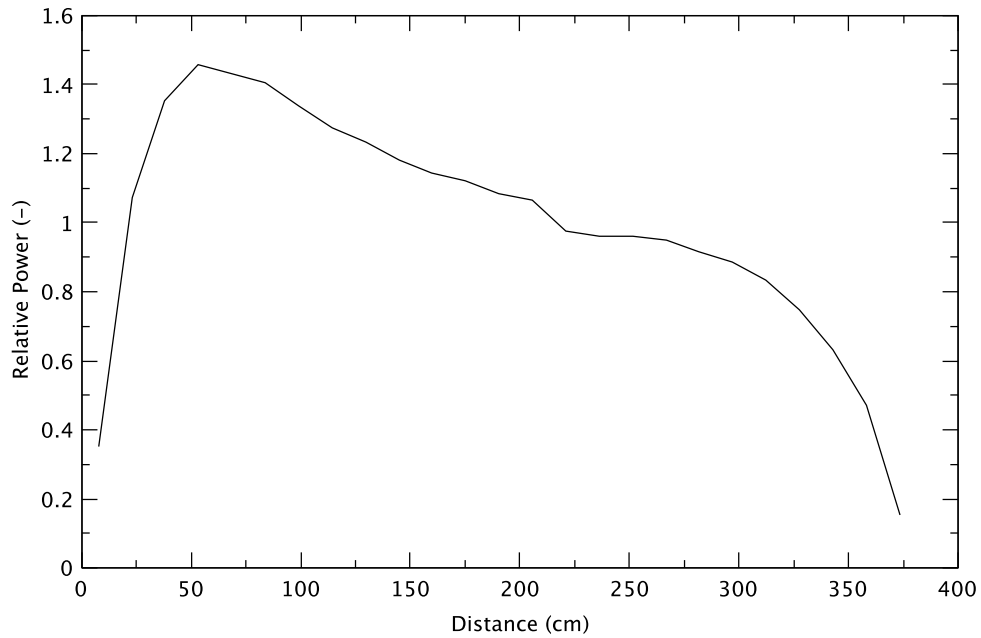


Figure 3.6 Radially Averaged Axial Power Distribution at PHE

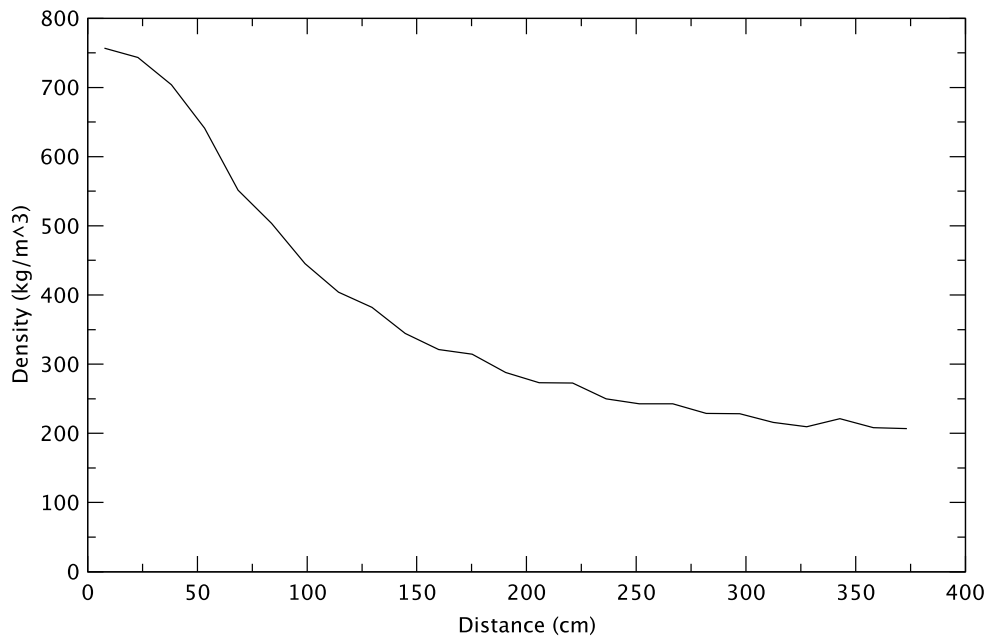


Figure 3.7 Radially Averaged Axial Moderator Density at PHE

3.2.4 First Harmonic

A PARCS stand-alone calculation was performed to obtain the first harmonic shape for steady-state conditions. The thermal-hydraulic (boundary) conditions were fixed, as they were read from an output file generated during the coupled steady-state calculation. Figure 3.8 shows the harmonic shape, exhibiting a first harmonic plane parallel to the x-axis and an axis of symmetry along the y-axis (90°). This is consistent with the BOC results, and allows our maintaining the same TRACE/PARCS mapping, described in Section 2.3. The channels 243 (outlined in red in Figure 3.5) and 544 have maximum (absolute) value of the first harmonic and they are followed throughout the transient, together with the channel with highest power. GEH reported an axis of symmetry [29] that differs from PARCS.

3.2.5 Effect of Spectrally Corrected Void History

The cross sections used by PARCS depend on the instantaneous variables moderator density, fuel temperature and boron concentration. They also depend on exposure to take into account the burnup, and one or more other “history” parameters to help correct for the effect of energy spectrum during burnup. The history parameter used to generate the cross sections for PARCS is the moderator density history (equivalent to void history, UH). However, another parameter that might be used is the history of the control rod position.

GEH has an approach whereby they take into account the control rod history by changing the void history to provide the same effect. Hence, to test the effect of this additional history, the UH distribution used with the cross section set in PARCS was replaced with a “void history spectrally corrected” (UHSPH) distribution from GEH.

Figures 3.9 and 3.10 compare the radial and axial power, respectively, for the PARCS calculations using the UH moderator-density history and the UHSPH one. They are virtually identical. This is consistent with the results obtained for transients with the two different history distributions that also are almost identical (discussed in Section 4.5).

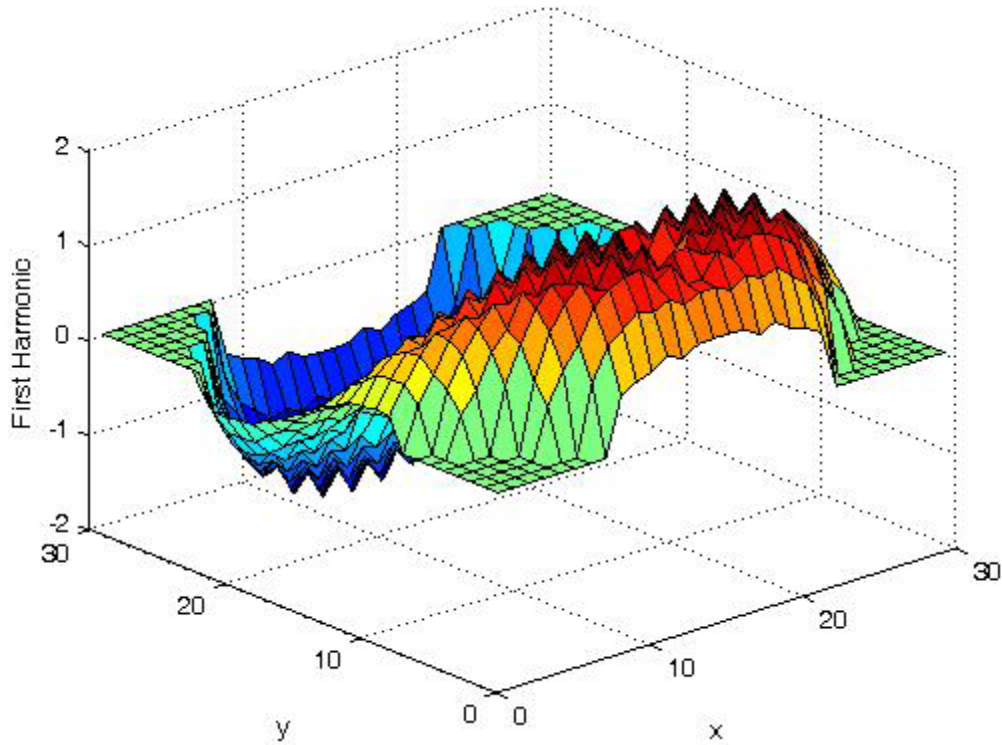


Figure 3.8 First Harmonic Shape at PHE

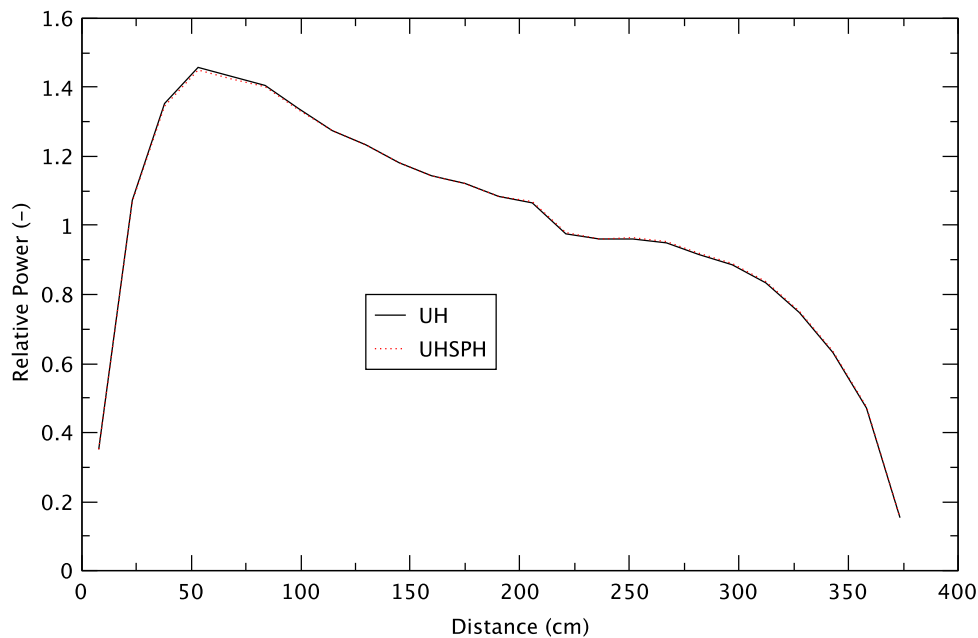


Figure 3.10 Radially Averaged Axial Power Distribution at PHE, UH versus UHSPH

3.3 ATWS-I 382-Channel EOFPL Model

EOFPL represents an end-of-full-power-life condition near the end of the reactor cycle. It is the last exposure point where the power is maintained at 120% of its original value. This condition is characterized by a top-peaked axial power shape, all control rods out (ARO) configuration, and increased core flow rate (ICF) to 105% rated.

The eigenvalue for the coupled steady-state calculation is 1.00632, fully consistent with the eigenvalue obtained during the stand-alone calculation with fixed thermal-hydraulics, indicating that the solution is converged properly.

3.3.1 Initial and Boundary Conditions

Table 3-3 compares the initial values of reactor power and some key thermal-hydraulic parameters, which are the results of the TRACE/PARCS coupled null-transient calculation for ten seconds, to reference values. As the table shows, calculated steady-state values agree well with the reference ones.

Table 3.3 Comparison of Steady-State Thermal-Hydraulic Parameters at EOFPL

Parameter	Units	TRACE/PARCS Value	Reference Value [26]	Diff. (%)
Core Power	MWt	3,988	3,988	0.0
Steam Dome Pressure	kPa	7,141	7,136	0.07
Main Steamline Flow	kg/s	2,218	2,222	-0.18
Total Core Flow	kg/s	14,330	14,350	-0.14
Feedwater Flow	kg/s	2,218	2,222	-0.18
Feedwater Temperature	K	500.1	500.1	0.0
Downcomer Level	m	14.32	14.46	-0.97
Core Inlet Temperature	K	551.9	not available	-

3.3.2 Radial Power Distribution

Figure 3.11 shows the normalized, axially averaged radial power distribution calculated by PARCS for EOFPL. As in the PHE case, in the central part of the core, a checkerboard pattern, with alternating “high” (around 1.2) and “low” (around 1.0) powered assemblies, can be distinguished. Overall, the radial power shape is flat, characteristic of an EPU core. The peak relative bundle power is 1.26, found in Channel 271 (outlined in bold in Figure 3.11). This channel, and the symmetric Channel 522, are monitored throughout the transient. The agreement between the results of PARCS and GEH [10] is reasonable, the RMS of the difference being 0.02 for the whole core.

3.3.3 Axial Power Distribution

The normalized, radially averaged axial power calculated by PARCS is shown in Figure 3.12. As expected, the power is top-peaked; the fuel in the bottom of the core has been depleted more than that in the top. The moderator density (Figure 3.13) is slightly higher at the outlet than for BOC or PHE, because the core flow has been increased from 85% to 105% so to maintain the power level. The axial power has an unexplained shoulder at around 40 cm. The axial power shape also shows a depression at around 220 cm, which reflects the fuel’s geometry. Comparing the PARCS and GEH [1] results indicates reasonable agreement, given the relatively high uncertainties associated with predicting axial power shape. The RMS of the difference for all axial nodes is 0.08.

									0.37	0.42	0.44	0.50	0.45	0.50	0.51
							0.45	0.69	0.78	0.91	0.81	0.91	0.79	0.90	
				0.36	0.54	0.73	1.01	1.08	1.11	1.11	1.11	0.94	1.09	0.89	
				0.48	0.90	1.06	1.14	0.96	1.20	0.98	1.19	1.01	1.18		
			0.48	0.78	1.06	1.16	1.03	1.22	1.04	1.23	1.04	1.23	1.01		
		0.36	0.48	0.78	0.90	1.14	0.98	1.22	1.04	1.24	1.04	1.25	1.04	1.25	
		0.54	0.90	1.06	1.14	1.00	1.22	1.04	1.24	1.04	1.26	1.03	1.26	1.03	
	0.45	0.73	1.06	1.16	0.98	1.22	1.03	1.23	1.02	1.25	1.03	1.26	1.04	1.26	
0.37	0.69	1.01	1.14	1.03	1.22	1.04	1.23	1.01	1.24	1.02	1.25	1.02	1.24	1.01	
0.41	0.78	1.08	0.96	1.22	1.04	1.24	1.02	1.24	1.01	1.25	1.01	1.24	1.00	1.22	
0.44	0.91	1.11	1.20	1.04	1.24	1.04	1.25	1.02	1.24	1.02	1.24	1.00	1.22	0.99	
0.49	0.81	1.11	0.98	1.23	1.03	1.26	1.02	1.25	1.01	1.24	1.05	1.22	0.99	1.21	
0.44	0.90	0.94	1.19	1.04	1.24	1.03	1.26	1.01	1.23	1.00	1.22	0.99	1.21	0.98	
0.50	0.79	1.09	1.00	1.22	1.04	1.26	1.03	1.24	1.00	1.21	0.99	1.21	0.99	1.20	
0.51	0.90	0.88	1.17	1.00	1.25	1.03	1.25	1.01	1.22	0.99	1.21	0.98	1.20	0.98	

Figure 3.11 Axially Averaged Radial Power Distribution at EOFPL

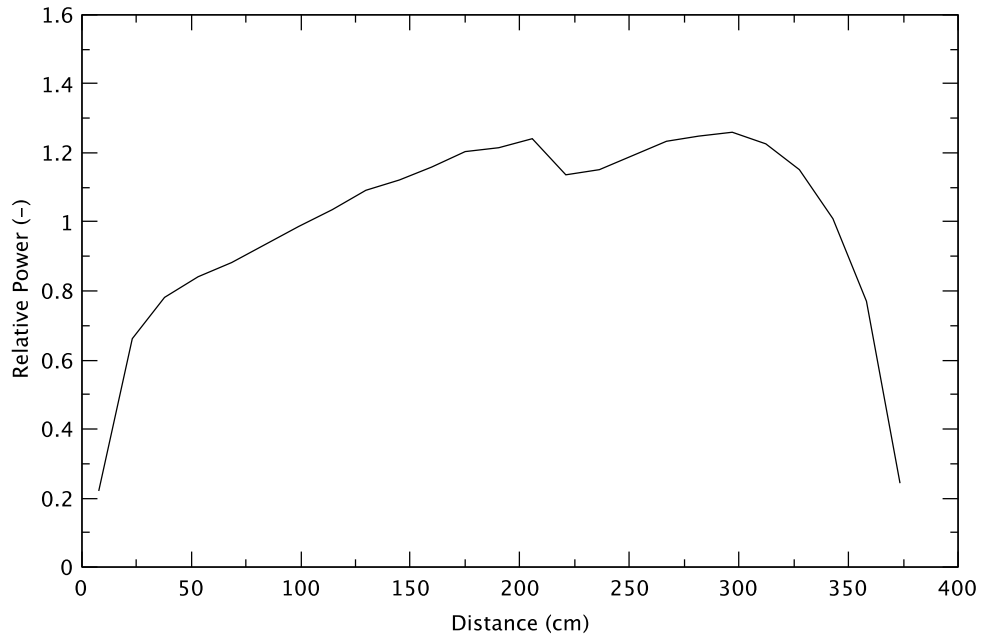


Figure 3.12 Radially Averaged Axial Power Distribution at EOFPL

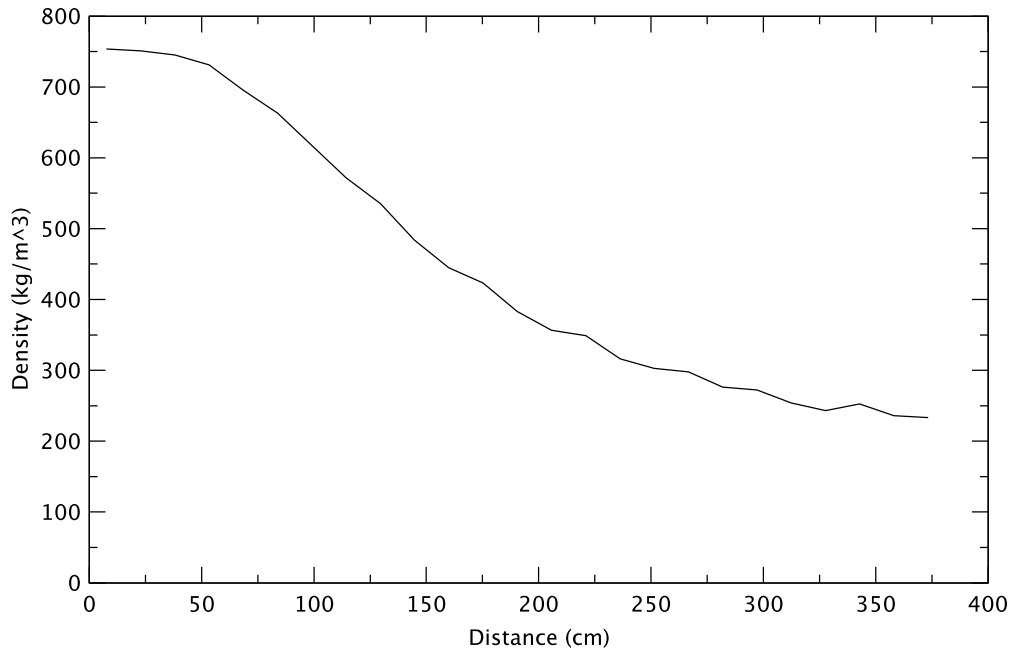


Figure 3.13 Radially Averaged Axial Moderator Density at EOFPL

3.3.4 First Harmonic

Figure 3.14 shows the harmonic shape for EOFPL conditions. The first harmonic plane is parallel to the x-axis, and the axis of symmetry is parallel to the y axis (90°), consistent with the mapping described in Section 2.3. The channels that have maximum (absolute value) of the first harmonic are Channels 233 (outlined in red in Figure 3.11) and 555, and they are followed throughout the transient together with the channels with highest power. GEH reported an axis of symmetry [29] that is different from PARCS.

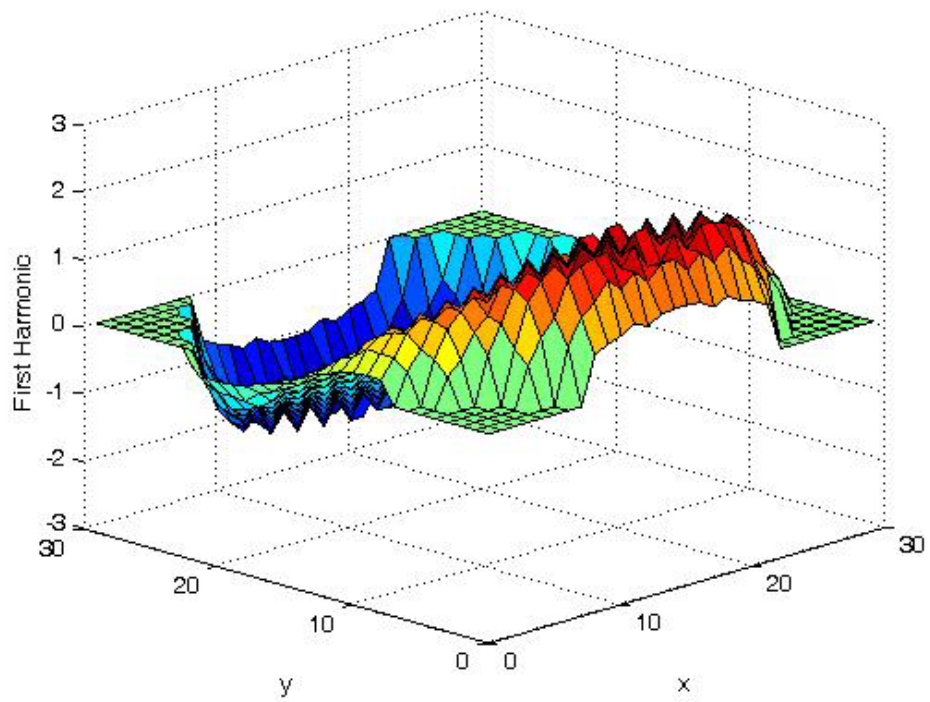


Figure 3.14 Harmonic Shape at EOFPL

4 TURBINE TRIP EVENTS WITH REPRESENTATIVE BYPASS

4.1 Introduction

The ATWS with instability event (ATWS-I) of interest is initiated by a turbine trip with turbine bypass available. Seven cases were analyzed; Table 4.1 presents the simulation conditions.

Table 4.1 Simulation Conditions of ATWS-I Cases

Case ID	Exposure ¹	Power % ²	Flow Rate % ³	Bypass Capacity, % ⁴	Spectral History ⁵
1	BOC	100	85	100	UH
1A	BOC	100	85	10	UH
1B	BOC	100	85	25	UH
1F	BOC	100	85	50	UH
2	PHE	100	85	100	UH
2G	PHE	100	85	100	UHSPH
3	EOFPL	100	105	100	UH

¹ BOC, PHE, and EOFPL represent beginning-of-cycle, peak-hot-excess-reactivity, and end-of-full-power-life, respectively.

² Power of 100% is 3,988 MWt.

³ Core flow rate of 100% is 13,670.8 kg/s.

⁴ Bypass capacity is percentage of normal steam flow to the turbine.

⁵ UH and UHSPH mean void history and spectrally corrected void history, respectively, as discussed in Section 3.2.5.

For all cases, a null transient is run for 10 s to confirm that an adequate steady-state condition has been established. The turbine trip is initiated by closing the turbine stop valve (TSV) in 0.1 s at 10 s into the simulation time. The TSV opens in 1.0 s to simulate the bypass paths with the flow area shown in the fifth column of Table 4.1. The valve timing figures are typical for a BWR [26]. The trip of the dual recirculation pumps (2RPT) is initiated at 10 s on the turbine-trip signal as specified by the so-called end-of-cycle recirculation pump trip (EOC-RPT) system. Reactor trip is assumed to fail. The 2RPT initiates the coast down of the recirculation pumps and the core flow shifts to natural circulation inside the reactor pressure vessel (RPV). Core flow rates become particularly low as downcomer water level is reduced by the assumed operator action. Isolation of the turbine steadily decreases the temperature of the feedwater (FW) because the extraction steam feed to the feedwater heater (FWH) cascade has been stopped. The reactor power remains relatively high at the reduced flow rate, putting it into a region of instability on the power-flow operating map. Power oscillations are likely to occur under these conditions, especially once core inlet subcooling rises in response to lower FW temperature.

The event scenario includes two operator actions per the emergency procedure guidelines: 1) Water level reduction (WLR) to the top-of-active-fuel (TAF); and, 2) boron injection [1]. WLR is initiated at 120 s (110 s after the turbine trip) by lowering the setpoint of the normal water level control system linearly to TAF over 180 s. Boron injection is initiated at 130 s, and then linearly ramped to full flow at 190 s (180 s after the turbine trip). The standby liquid control system (SLCS) is simulated using a FILL component (FILL-191), and boron is injected into the upper plenum. We simulated these manual operator actions to gauge their effectiveness in suppressing power oscillations and reducing power.

The simulation of the event is carried out for 400 s to include power oscillations and oscillation suppression in the first 300 s of simulation time, and the increasing stability margin over the next 100 s.

In Section 4.2, we examine in detail the most limiting case in terms of clad temperature and power oscillations to understand the phenomena that are driving the ATWS scenario, and the modeling assumptions that might be affecting the results. Sections 4.3, 4.4, and 4.5 discuss sensitivity studies. They show, respectively, the effect of bypass fraction, time in cycle, and void history modeling. Section 4.6 focuses on the oscillatory behavior in these cases by looking at figures-of-merit that commonly are used to characterize stability. Lastly, Section 4.7 summarizes our conclusions from the analysis of the seven ATWS-I cases.

4.2 Limiting Case: PHE with 100% Bypass Capacity (Case 2)

The case at PHE with 100% bypass capacity shows the most severe oscillatory behavior among the seven cases listed in Table 4.1 . PHE represents the peak-hot-excess-reactivity condition and it is characterized by a bottom peaked axial power shape with some control banks partially or fully inserted to counter the excess reactivity. A bypass capacity of 100% is simulated for the turbine bypass valve (TBV) for consistency with [1].

4.2.1 Initial and Boundary Conditions

Table 4.2 compares the initial values of some key thermal-hydraulic parameters from the TRACE/PARCS coupled null-transient calculation for 10 s to the reference values. As shown therein, the calculated values of steady-state agree well with the reference ones.

4.2.2 Sequence of Events

A turbine trip results in closure of the TSV, but the expected reactor trip is assumed to fail. The turbine trip signal also initiates a trip of the recirculation pumps. Turbine bypass is simulated by reopening the TSV to its initial 100% flow area. The trip of the dual recirculation pump ramps down the forced recirculation flow as the pumps coast down, and a natural circulation flow develops in the vessel. Isolating the turbine causes a steady decrease in FW temperature because the extraction steam feed to the FWH cascade has been stopped.

Table 4.2 Comparison of Steady-State Thermal-Hydraulic Parameters in Case 2

Parameter	Units	TRACE Value	Reference Value [26]	Diff. (%)
Core Power	MWt	3,988	3,988	0.0
Steam Dome Pressure	kPa	7,141	7,136	0.07
Main Steamline Flow	kg/s	2,218	2,222	-0.17
Total Core Flow	kg/s	11,631	11,620	0.09
Feedwater Flow	kg/s	2,218	2,222	-0.17
Feedwater Temperature	K	500.1	500.1	0.0
Downcomer Level	m	14.32	14.46	-0.96

Under natural circulation, with increased subcooling of the core inlet from decreased FW temperature, the core becomes unstable and power oscillations are likely to occur. Manual

operator actions such as reducing reactor water level and injecting boron were simulated to gauge their effectiveness in suppressing power oscillations and reducing power.

Table 4.3 shows the time sequence for this event and there are detailed discussions about the system's behavior in the following sections. The safety relief valves (SRVs) do not open in this event.

4.2.3 Steamline Flow

The general behavior of the steamline flow is similar to the total core power behavior. Figure 4.1 shows the steamline flow rate upstream of the in-board main steam isolation valve. As expected, the steam flow becomes zero (even negative) as the TSV closes at 10 s, and then increases suddenly up to about 2,800 kg/s at around 11.4 s as the turbine bypass valve (TBV), simulated by the TSV, opens. This very high steam flow rate is due to increased RPV pressure and the accompanying rise in core power. As steam mass is discharged from the RPV, the system pressure begins decreasing and the steam flow rate is reduced. The steam flow then declines rapidly due to the fast drop of the pressure and the reduction in reactor power (and steam production) in response to the 2RPT and pressure drop. It becomes almost constant from around 55-162 s. Even though reactor power is slightly increasing until around 110 s, the steam production rate remains relatively constant as the higher reactor power is essentially offsetting increased core coolant inlet subcooling following the lowering of the feedwater temperature. The steam flow starts decreasing again steadily and relatively slowly from 162 s, consistent with start of the decline in core power.

Table 4.3 Sequence of Events for Case 2 at PHE with UH Void History

Time (s)	Event
0.0	<ul style="list-style-type: none"> Null transient simulation starts.
10.0	<ul style="list-style-type: none"> Null transient simulation ends. Turbine trip is initiated by closing the TSV. Recirculation pumps are tripped on the turbine trip. Feedwater temperature starts decreasing.
10.1	<ul style="list-style-type: none"> TSV closes completely and starts opening again to simulate 100% turbine bypass.
11.1	<ul style="list-style-type: none"> TSV (bypass) completes opening.
~11.4	<ul style="list-style-type: none"> Steam flow starts decreasing.
~12.3	<ul style="list-style-type: none"> Feedwater flow starts decreasing.
~95	<ul style="list-style-type: none"> Power oscillation above noise level is apparent (instability onset).
120	<ul style="list-style-type: none"> Water level reduction (WLR) is initiated by reducing the normal water level control system setpoint linearly to TAF over 180 s.
130	<ul style="list-style-type: none"> Boron injection is initiated and linearly ramped to full flow at 190 s.
~144	<ul style="list-style-type: none"> Bi-modal oscillation of the core power is initiated.
~160	<ul style="list-style-type: none"> Boron starts accumulating in the core.
~163	<ul style="list-style-type: none"> Downcomer water level begins decreasing. Peak cladding temperature of ~1690 K occurs.
~240	<ul style="list-style-type: none"> Power oscillation ends.
400	<ul style="list-style-type: none"> Simulation ends.

4.2.4 Core Power

Figure 4.2 shows the reactor core power. Power increases suddenly when the TSV closes at 10 s. This is caused by the sudden rise of the system pressure (Figure 4.3) that engenders collapsing voids (increasing moderator density) and positive reactivity feedback.

As power increases, the fuel temperature also rises, and the Doppler effect adds negative reactivity. After some delay, the clad heat flux also increases and the formation of additional voids adds to the negative reactivity feedback. These two feedback mechanisms limit the power increase.

Upon opening of the turbine bypass valve, the system pressure starts to fall suddenly and considerably (Figure 4.3). This drop, together with the significant reduction in core flow due to the 2RPT (Figure 4.4) results in voiding in the RPV. The reactor power peaks in response to increasing negative reactivity from Doppler and void feedback (mostly due to the sudden decline in the system pressure), decreases very quickly, and then settles to a level consistent with natural circulation flow. The reactor then enters into a period of slow power increase (from approximately 30 s to 95 s), in response to an increase in the core inlet subcooling (see Section 0).

Oscillatory behavior of reactor power is observed from around 95 s through 240 s (Figure 4.2). A combination of effects dictates the reactor's instability. As the turbine trip occurs, subcooling of the inlet increases because of reduction of the feedwater temperature following the isolation of the steam supply to the feedwater heater cascade. In response, the reactor power increases and shifts towards the bottom of the core. The natural circulation condition, combined with a highly bottom-peaked power shape and increased total reactor power, engender instability.

Figure 4.4 shows the normalized core inlet total mass flow rate (see Section 4.2.7), represented by the total flow at the discharge of the jet pump; natural circulation flow is observed from around 50 s. Figure 4.5 depicts the liquid subcooling (see Section 0) at the inlet of the reactor core, and shows that it becomes more than 32.4 K from around 95-240 s. It is approximately 12.5 K during normal operating conditions. Large subcooling of the core inlet flow increases the reactor power, and shifts it toward the bottom of the reactor core.

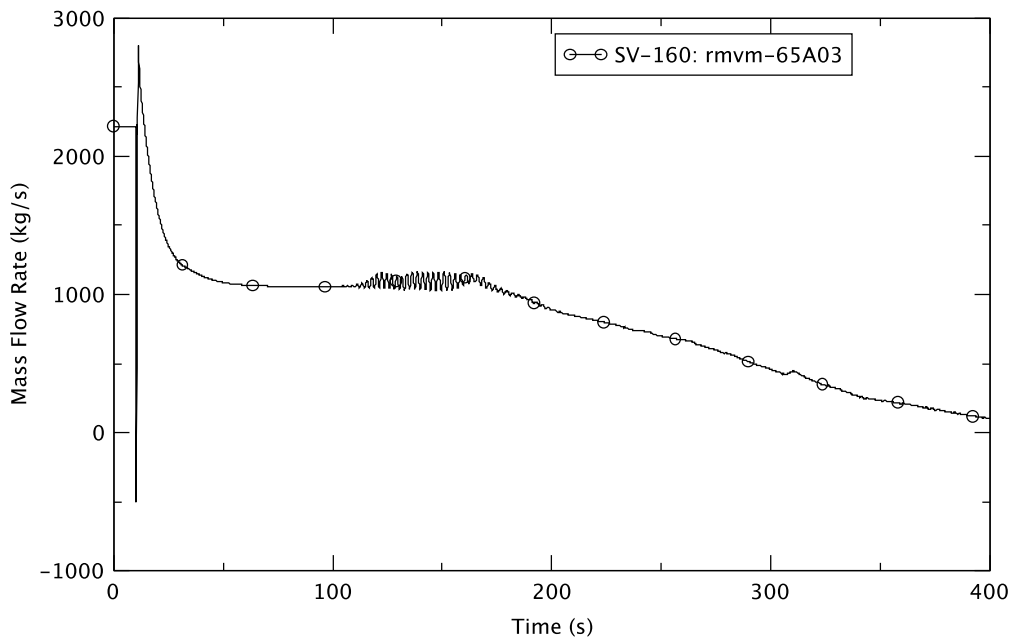


Figure 4.1 Steam Mass Flow Rate in Steamline in Case 2

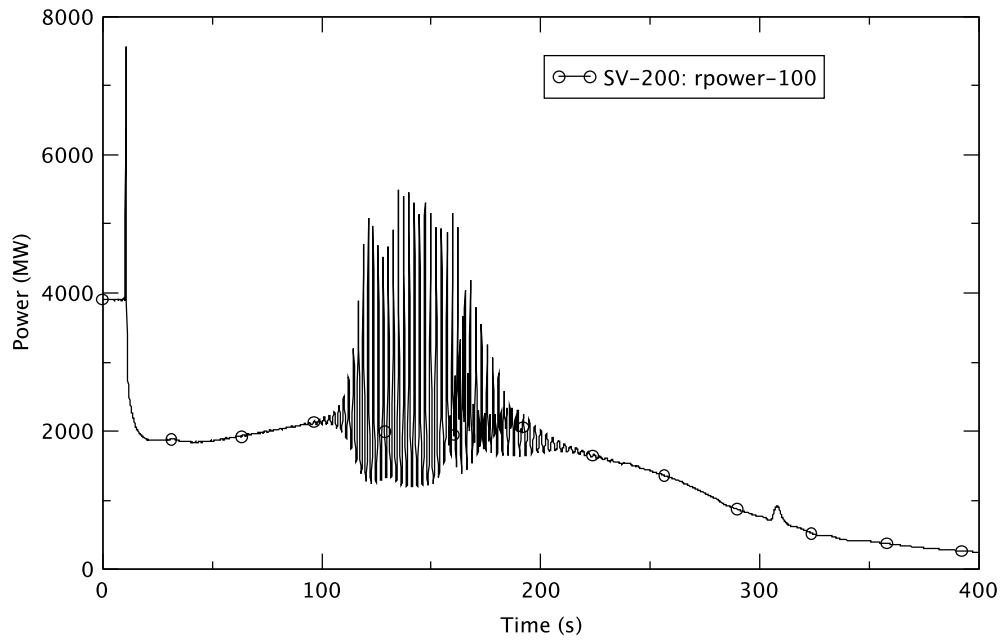


Figure 4.2 Core Power in Case 2

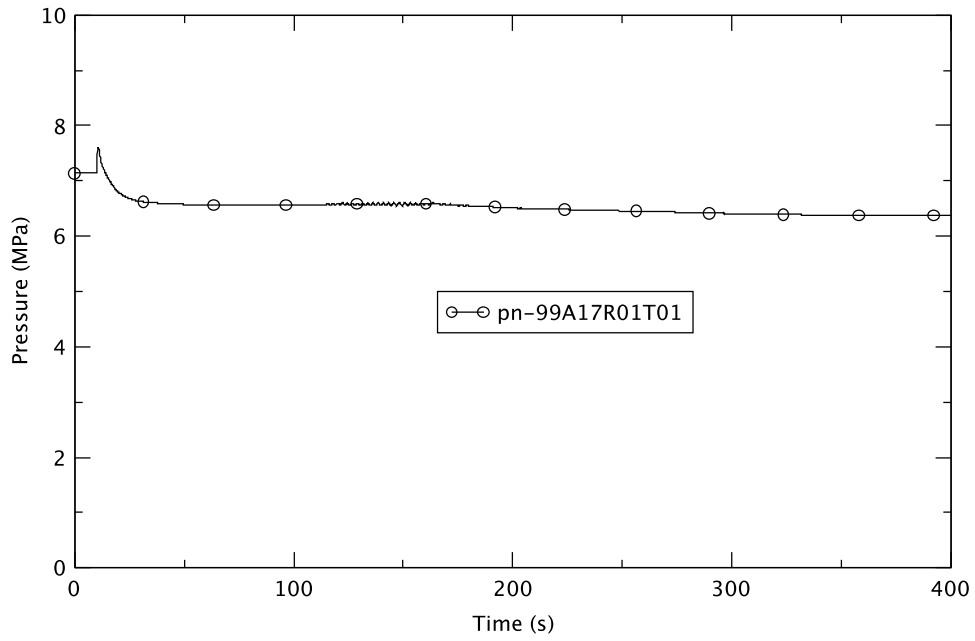


Figure 4.3 Reactor Pressure Vessel Dome Pressure in Case 2

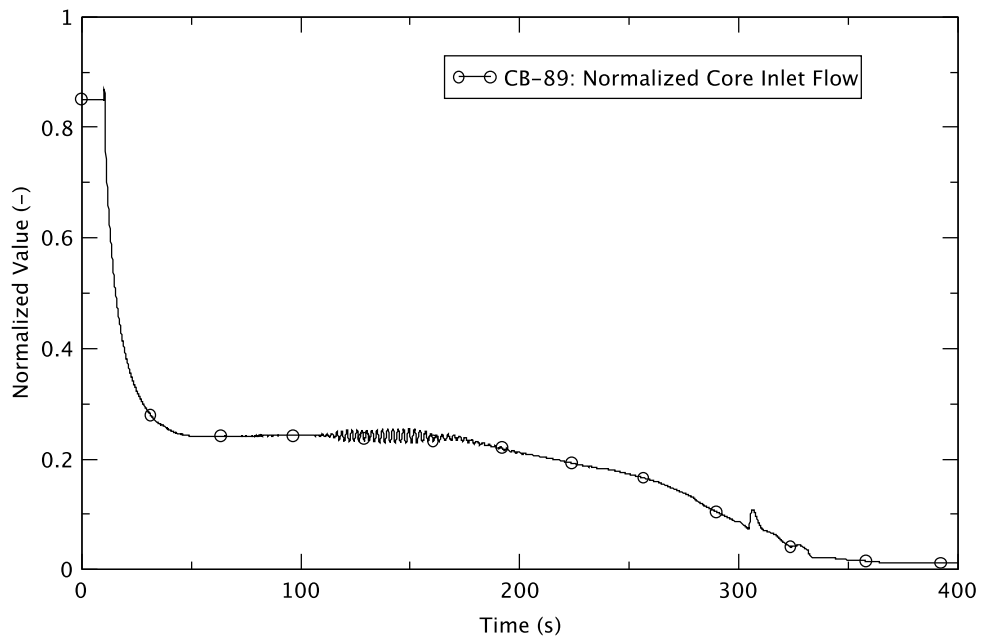


Figure 4.4 Normalized Core Total Mass Flow Rate in Case 2

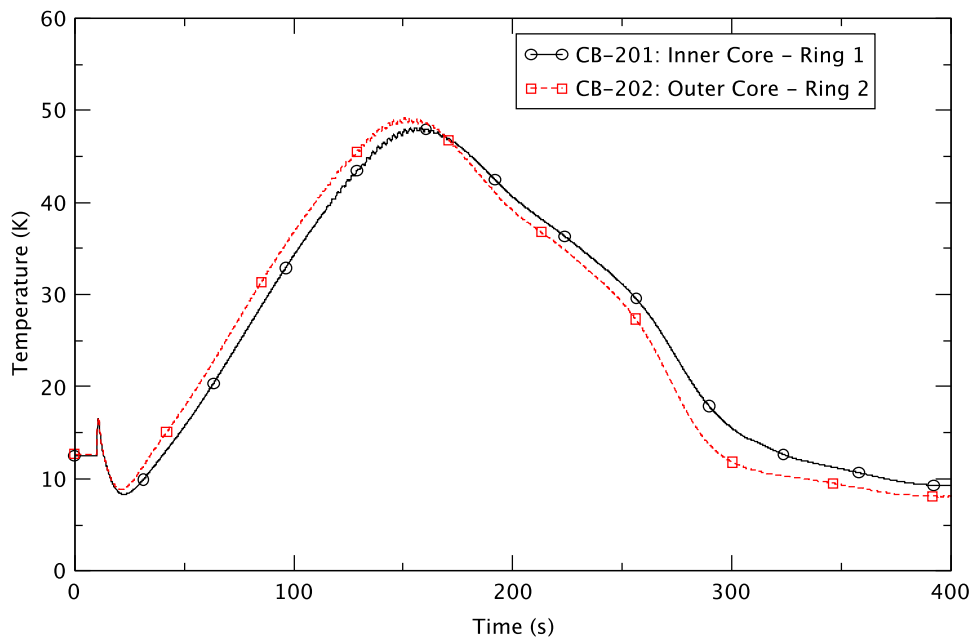


Figure 4.5 Core Inlet Subcooling in Case 2

The high power (Figure 4.2) and core flow in natural circulation with increasing inlet subcooling (Figure 4.4 and Figure 4.5) cause oscillations in reactor power from around 95-240 s seen in Figure 4.2. The reactor power is continuously perturbed by applying artificial white noise in the PARCS calculation (this perturbation approximates the noise during normal operation). The purpose of the perturbation [30] is to ensure that an unstable condition will exhibit excitation in the analysis. The input parameters to activate the noise model in PARCS are discussed in Appendix B.

The amplitude of the power oscillation continues to grow until around 120 s when the oscillation reaches a limit cycle. The peak power between subsequent pulses varies, indicating that the power oscillation has likely bifurcated. The amplitude of the oscillation remains near this limit cycle value until around 160 s and then declines quickly, the reason for which is discussed below.

Around 144 seconds the power oscillation evolves into a bi-modal mode with both a core wide and regional component. As shown in Figure 4.2 and discussed in Section 4.2.5, the contour of the oscillation begins to develop a regional (or out-of-phase) component. The evolution of a coupled bi-modal oscillation contour indicates non-linear harmonic coupling. The non-linearity also is evident in the accompanying frequency doubling. Figure 4.6 and Figure 4.7, respectively, show the power contours, axially averaged bundle powers, at 143.9 s when bi-modal oscillation is first detected, and at 152.2 s when it becomes recognizable and clear. The blue and dark red, respectively, indicate low and high power.

We note that in the TRACE/PARCS calculation, the core is represented by 764 fuel assemblies in the PARCS neutronics model, while a half-core symmetry is assumed for the TRACE hydraulic model (382 channels). As shown, the bi-modal oscillation starts from around 144 s; initially, and its magnitude is very small, but with time it becomes larger and is recognizable in

the total power at around 152 s. The bi-modal power fluctuation appears to oscillate about the harmonic plane that is perpendicular to the plane of symmetry, which is along the y direction at $x=0$ in Figure 4.6 and Figure 4.7 (east-west symmetry). The 2-to-1 mapping between neutronic nodes (fuel assemblies) and thermal-hydraulic channels is a limitation of the coupled model that can impact the contour of the oscillations. Higher harmonic modes are degenerate insofar as equivalent, symmetric harmonic shapes exist for the higher order modes. This degeneracy allows certain degrees of freedom if higher order harmonic modes are excited in the overall oscillation contour. The 2-to-1 channel mapping does not support calculations to resolve the degenerate symmetric harmonic shapes, which would potentially allow the rotation of the oscillation contour azimuthally around the core. However, imposing a half-core symmetry likely is conservative, at least as far as the hot spot is concerned, in the sense that for a “real” core response (without the half-core symmetry restriction) the rotation of the contour will relocate the spot with the peak local oscillation magnitude; this would not be the case with the imposition of the half core symmetry assumption. The fuel assembly subject to the highest local power oscillation magnitude will have some time to recover (or cool down) from the power pulses if the model allows the higher harmonic modes to rotate around the core.

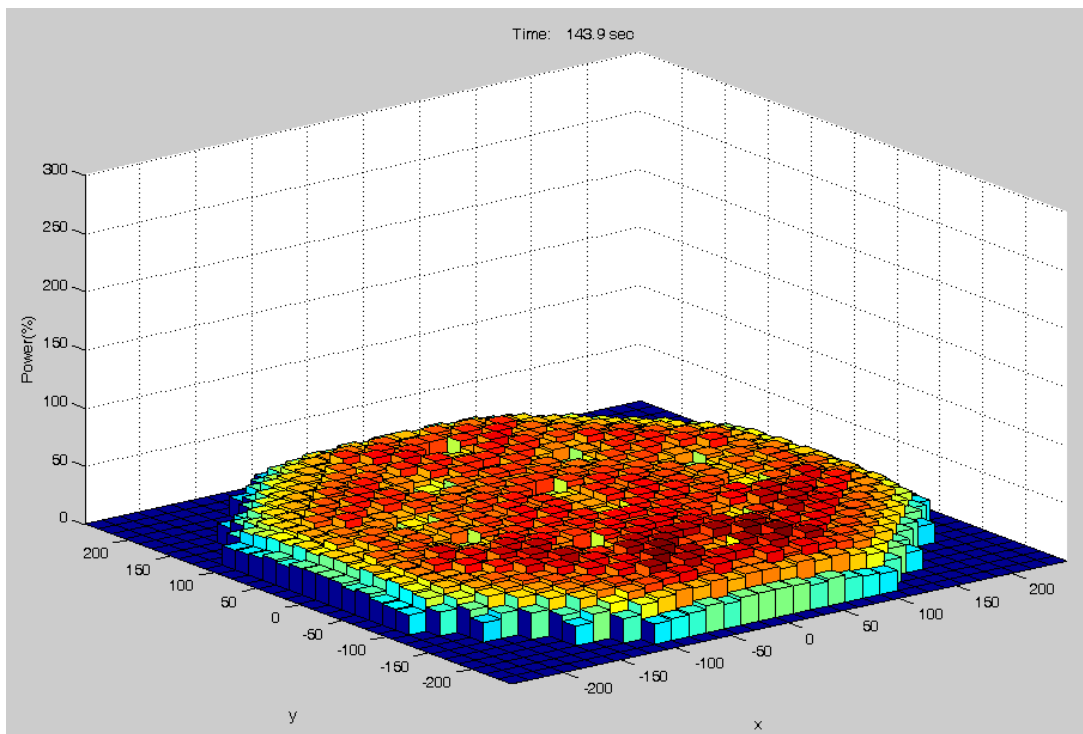


Figure 4.6 First Indication of Bi-Modal Oscillation of Power at 143.9 s in Case 2

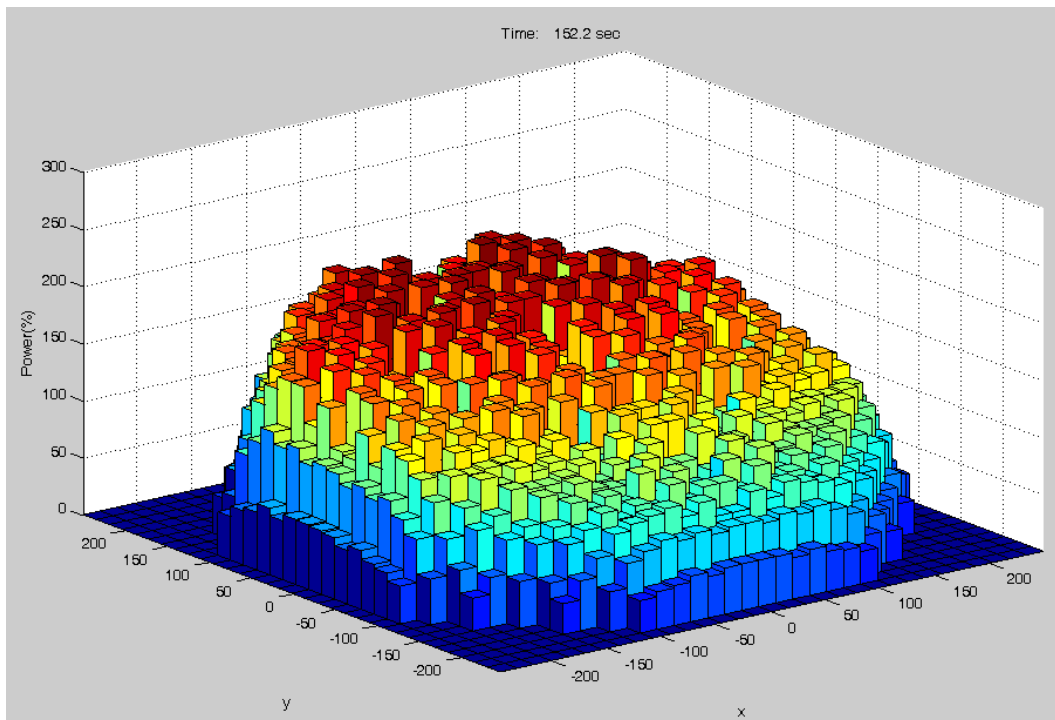


Figure 4.7 Recognizable Bi-Modal Oscillation of Power at 152.2 s in Case 2

As discussed, the amplitude of the power decreases substantially from about 160 s. However, the response of the reactor power suggests that there is a time delay before the effects of the operator's actions become evident. Core inlet flow begins to decrease from around 172 s (Figure 4.4) due to the drop in downcomer (DC) water level after reducing the setpoint of the normal water level control system at 120 s (Figure 4.8). The dynamic response of the downcomer water level is discussed in more detail in Section 4.2.9 in relation to the control of feedwater and the hydraulic responses in the RPV. Boron starts flowing to the high pressure core spray (HPCS) sparger from the SLCS at 130 s. Figure 4.9 shows the boron inventory in the reactor core starting to increase around 160 s (30 s after its injection). It is unclear whether the operator's actions are the immediate cause of the initial reduction of the amplitude of power oscillations (Figure 4.2) or are related to the evolution of power oscillations from one mode to another. A more thorough investigation is needed to clarify the reason for the onset of the decay of the total power oscillations.

After the amplitude of the power oscillation starts decreasing from 160s, its magnitude generally continues falling (especially from around 168 s) and there are no oscillations above the level of the noise after about 240 s when the combined effect of level reduction and boron injection appears to be very effective (Figure 4.2).

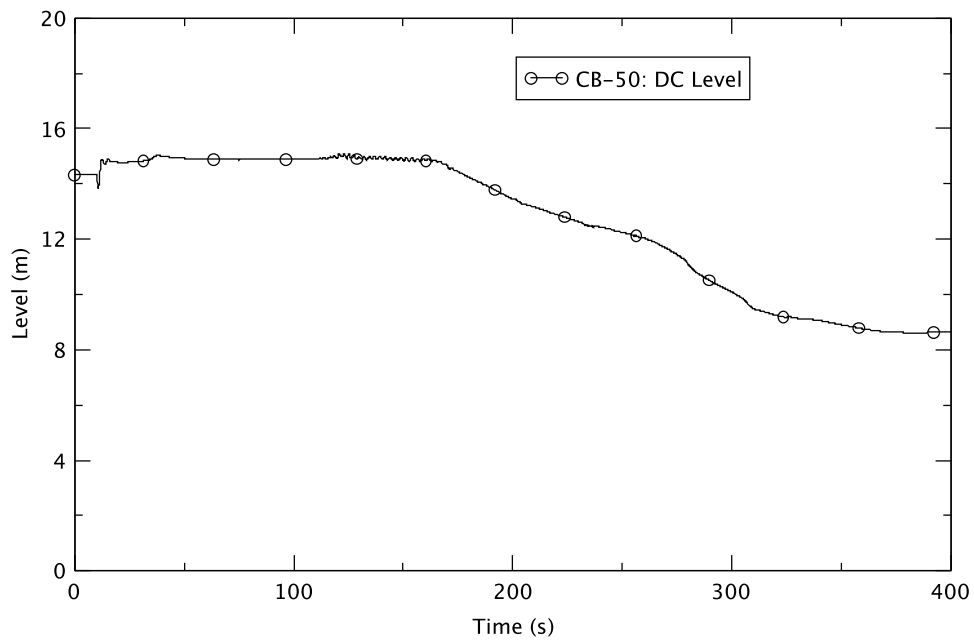


Figure 4.8 Downcomer Water Level in Case 2

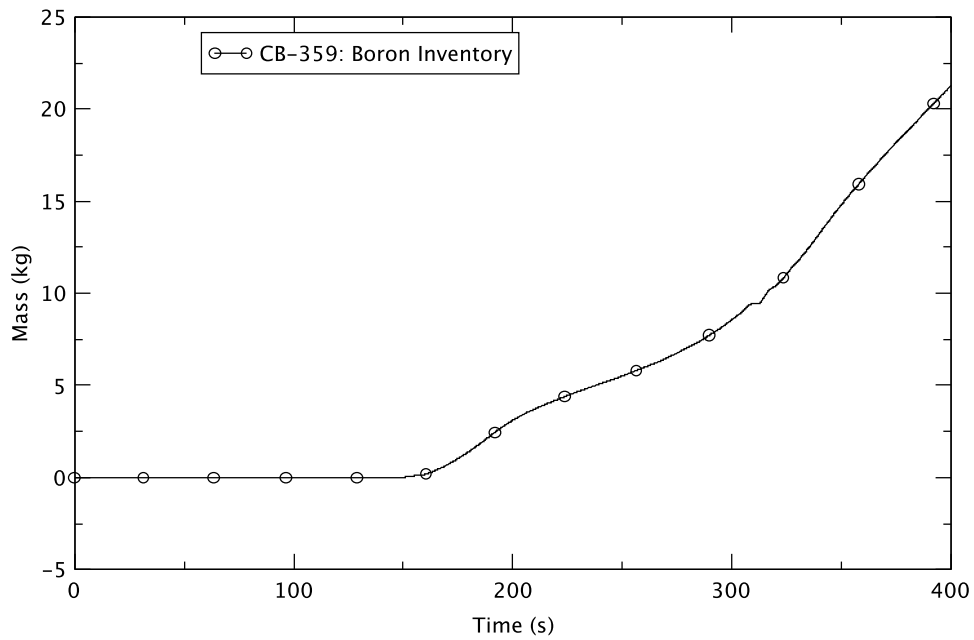


Figure 4.9 Boron Inventory in Reactor Core in Case 2

4.2.5 Fuel Bundle Power and Flow

Figure 4.10 and Figure 4.11, respectively, show fuel bundle power for two core channels, viz, the channel with the highest steady-state power and that with the highest first harmonic power (due to the assumed half-core symmetry, the channel power is the sum from two fuel bundles in symmetric core locations). As depicted in these figures, the general behavior is similar to that of the total power (Figure 4.2). Figure 4.12 and Figure 4.13 clearly reveal that these power instabilities are strongly linked with oscillatory behavior of the mass flow rates into the limiting channels. The power change produces different amounts of vapor in the channel, and this results in repeated increase and decrease of flow restriction, mostly depending upon the two-phase frictional pressure drop. Major flow reversals are observed for the limiting bundles; this seemingly contributes to the predictions of earlier and higher peak cladding temperature, as discussed in Section 4.2.11. We illustrate in Figure 4.12 and Figure 4.13 that the bundles' mass flow rate in the NE quadrant is actually the sum of two bundles, one in the NE quadrant and the other in the NW one. The same assumption applies to the power and flow for the bundle in the SE quadrant. The bundles in the NE and SE quadrants are symmetric about the harmonic plane. Closer examination reveals that the power/flow oscillations in these two corresponding channels are at times out-of-phase, indicative of regional mode oscillation.

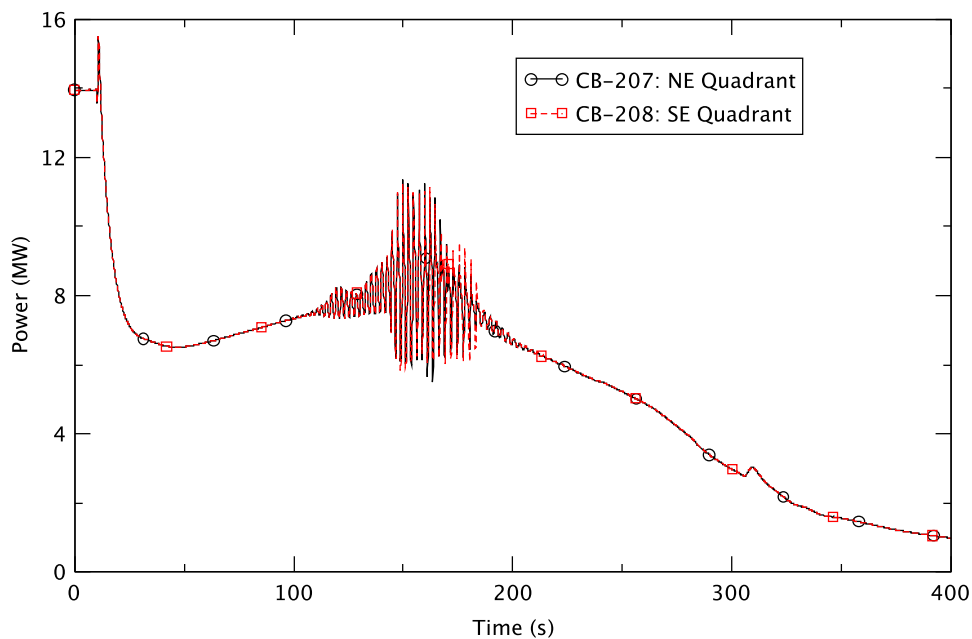


Figure 4.10 Power in Bundle with Maximum Steady-State Power in Case 2

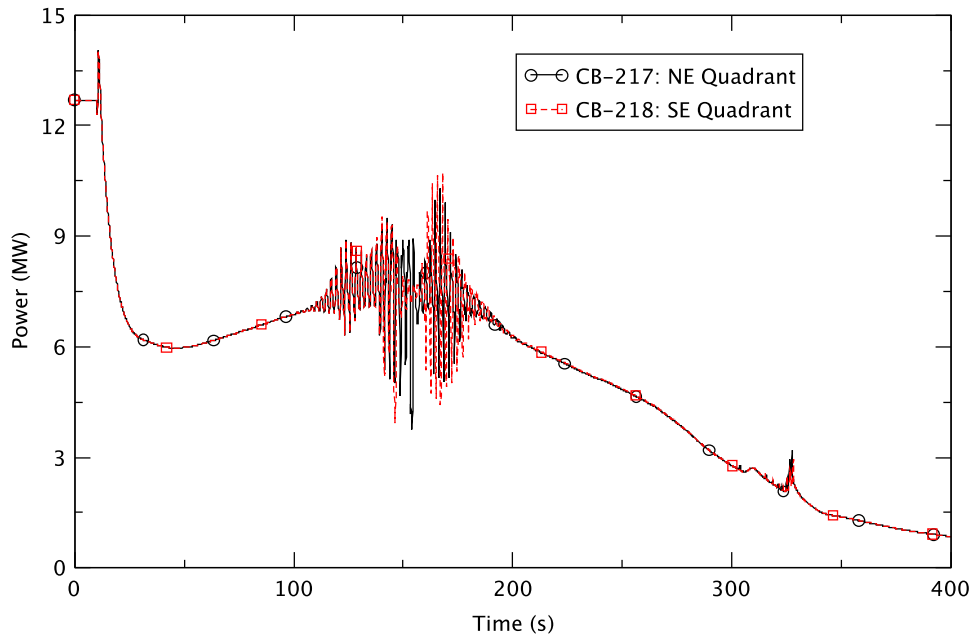


Figure 4.11 Power in Bundle with Maximum First Harmonic Power in Case 2

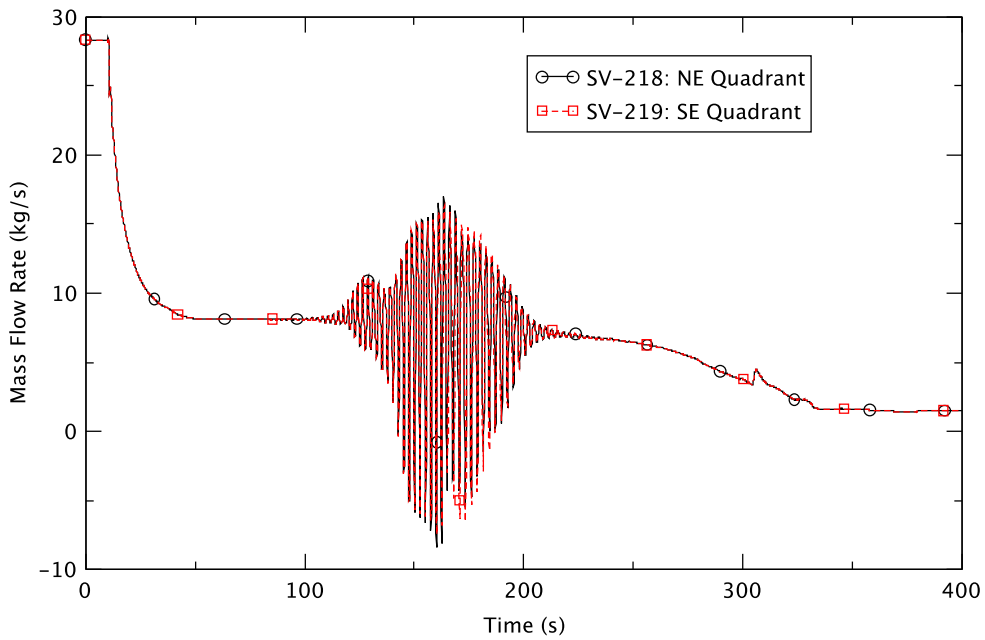


Figure 4.12 Mass Flow in Bundle with Maximum Steady-State Power in Case 2

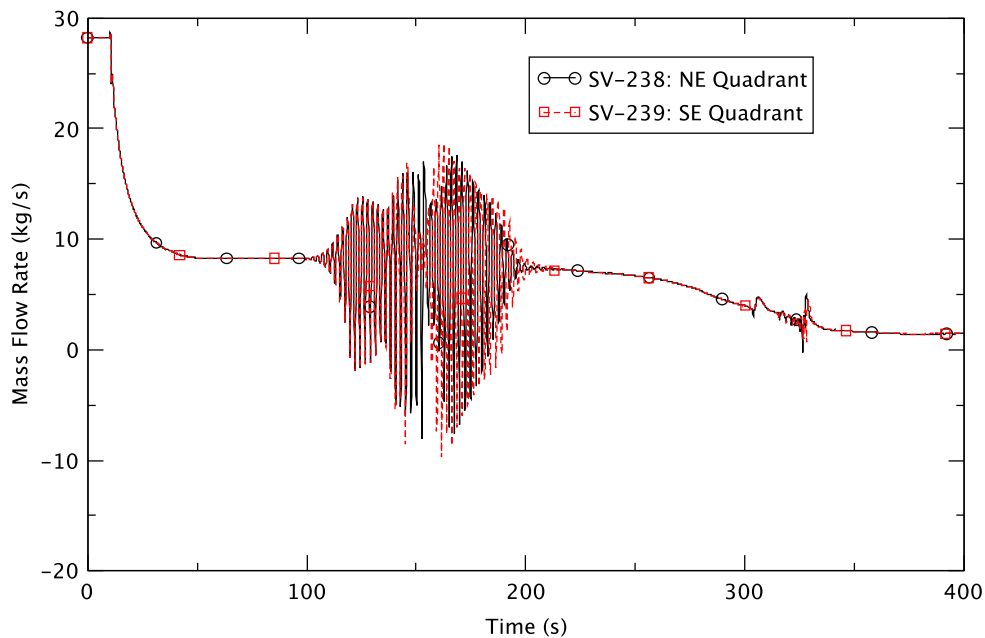


Figure 4.13 Mass Flow in Bundle with Maximum First Harmonic Power in Case 2

4.2.6 RPV Steam Dome Pressure

Figure 4.3 plots the response of the dome pressure response with time. The pressure spike at 10 s corresponds to the closure and re-opening of the turbine stop valve. For the rest of the transient, the dome pressure basically approaches the back pressure assumed as a boundary condition for the turbine bypass line.

4.2.7 Core Flow

Figure 4.4 shows the normalized core inlet total mass flow rate, represented by the total flow at the jet pump discharge. As is evident, the initial core flow rate is at 85% of the rated flow, and drops to about 25% at around 50 s. This decrease mostly is due to the trip of the dual recirculation pump at 10 s; natural circulation flow is observed from around 50 s. The flow at the core inlet is almost constant until approximately 172 s, and thereafter begins to decrease (Figure 4.4) due to the drop in the downcomer (DC) water level occasioned by lowering the setpoint of the normal water level control system at 120 s (Figure 4.8)

As Figure 4.4 shows, there is an unexpected small increase of the core flow at around 305 s, resulting in a small bump in reactor power (Figure 4.2). This flow/power anomaly seems to be associated with TRACE's prediction of the behavior of the downcomer water level. TRACE results suggest that this sudden increase in core flow occurs when the downcomer water level reaches the top face of the downcomer node that sits directly above the top (inlet) of the jet pump. Apart from this anomaly, the core flow is consistent with the expected behavior for a core in natural circulation. However, since the anomaly occurs late in the transient, it does not affect the conclusions of this study

4.2.8 Core Inlet Subcooling

Figure 4.5 shows the liquid subcooling at the inlet of the reactor core. It starts increasing at around 23 s, and from around 95 s to 240 s it rises to become larger than 32.4 K, while it is about 12.5 K during normal operating conditions. This large subcooling mostly reflects the decrease of the feedwater temperature starting at 10 s (Figure 4.14) that, in turn, is due to simulating the isolation of the steam supply to the feedwater heater cascade. Large subcooling of core inlet flow increases the reactor power and shifts it toward the bottom of the reactor core.

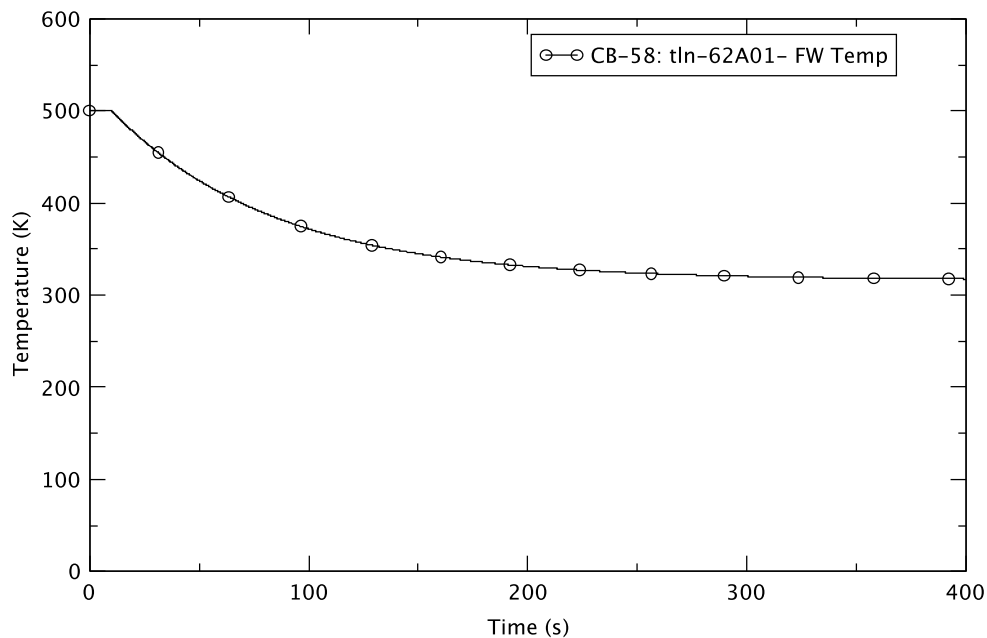


Figure 4.14 Feedwater Temperature in Case 2

Subcooling of the core inlet flow will be managed by lowering the water level in the reactor. Injecting the feedwater into the steam atmosphere above the water level results in the condensation of the steam and raises the liquid's temperature. However, Figure 4.8 shows that the DC water level falls below the FW sparger elevation (11.92 m in the simulation) from around 264 s at which time the subcooling already is small (Figure 4.5) and the FW flow is zero; the only mass flow into the vessel is from the reactor core's isolation cooling system (RCIC) taking water from the condensate storage tank. (FW flow rate is detailed in Section 4.2.9.) Therefore, the impact of condensation heat transfer on the subcooling of the core inlet flow is almost negligible in this case.

The largest subcooling of core inlet flow occurs at around 151 s and thereafter it begins declining before FW is injected into the steam atmosphere. This occurs for two reasons. First, the rate of FW flow is reduced via operator action starting at 120 s to drop the DC water level to TAF; this engenders an increase of the average liquid temperature in the mixing node of the DC. The second reason is high temperature liquid that starts being released from the separators from around 120 s. A detailed discussion of the separator behavior is presented in Section 4.2.9. As hot liquid flows from the separators to the downcomer and is mixed with cold water, the average liquid temperature increases in the downcomer and so reduces the

subcooling of the core inlet flow after the time it takes for the liquid with increased temperature to reach the core inlet. In this case, the impact of the release of hot water from the separator and reduction of FW flow on the subcooling of the core inlet flow is evident around 30 s later.

It was observed that the rate of decrease of the liquid subcooling becomes greater at around 260 s. This behavior seems to be related to the TRACE prediction of the DC water level. As it drops below the top elevation of a DC node where the feedwater spargers are located, the TRACE prediction of heat transfer between saturated gas and subcooled liquid changes. This means that the liquid temperature starts oscillating when the void fraction becomes larger than 0.003 at around 231.4 s in that node, and thereafter increases steadily after a sudden, large rise at around 236.7 s. The effect of the latter is evident in the liquid subcooling at around 260 s.

Therefore, the primary benefit of the operator's manual action to reduce RWL is the reduction in core inlet subcooling, resulting from the reduction of FW injection, rather than the mixing of FW in the DC steam atmosphere once the RWL has fallen below the location of the sparger.

4.2.9 Feedwater Flow and RPV Water Level

Figure 4.15 shows the behavior of feedwater flow rate. It decreases suddenly around 10 s as the steam flow slows because of rapid closure of the turbine stop-valve (Figure 4.1). It then rises once more as the steam starts flowing again through the turbine bypass valve (TBV), which is simulated by opening the TSVs to provide the turbine bypass paths shown in the fifth column of Table 4.1. From around 12.5 s to 43 s, the rate of feedwater flow drops rapidly, as expected, when the steamline flow declines (Figure 4.1). It continues to decrease relatively slowly until around 123 s when the rate of decrease increases after the operator's action to reduce water level to the top of active fuel (TAF) at 120 s. The rate drops to zero from around 260 s to 366 s and then starts flowing again as the mismatch between steam flow and feedwater flow diminishes. A mass flow rate of about 40 kg/s from around 260 s to 366 s typifies the mass flow of the RCIC from the CST. The RCIC flow actually starts around 216.6 s as the DC level drops below level 3 (12.9794 m from the bottom of the RPV).

The desired DC level is programmed into the FW controller to decrease linearly to the TAF in 180 s after the operator action at 120 s. However, as Figure 4.8 shows, the DC level starts dropping around 163 s. This 43 s delay in reducing the DC level results in a higher level than desired, and it tends to cause the FW control system to provide less FW flow to compensate for the difference in level. This behavior explains why the FW stops at around 260 s. Even after it falls beneath the elevation of the TAF (9.435 m from the bottom of the RPV) at around 312 s, the DC level continues decreasing until around 366 s when the FW starts again, and then rises to the elevation of the TAF (Figure 4.8). We note that we can simulate the FW control system by using a proportional integral (PI) controller. The delay in restarting FW flow to recover the level is due to the control logic requiring the proportional gain (representing the differential between the desired water level and the current level) to overcome the integral gain (representing the past history of the level differential).

Figure 4.8 illustrates the DC water level. As the pressure in the reactor rapidly rises after the closure of the turbine stop valve at 10 s (Figure 4.3), some portion of the vapor in the RPV collapses, entailing a sudden increase of core inlet flow (Figure 4.4). Then, as depicted in Figure 4.8, the DC water level drops suddenly at 10 s in response to this increase of core inlet flow (the phenomenon of "shrink"). Thereafter, the level rises as the feedwater flow rate increases again and remains slightly higher than its initial level until around 163 s, mostly due to rate of feedwater flow rate exceeding that of steam flow until around 130 s, at which time the

vapor volume has swelled inside the core as the system pressure falls below its initial value (Figure 4.3).

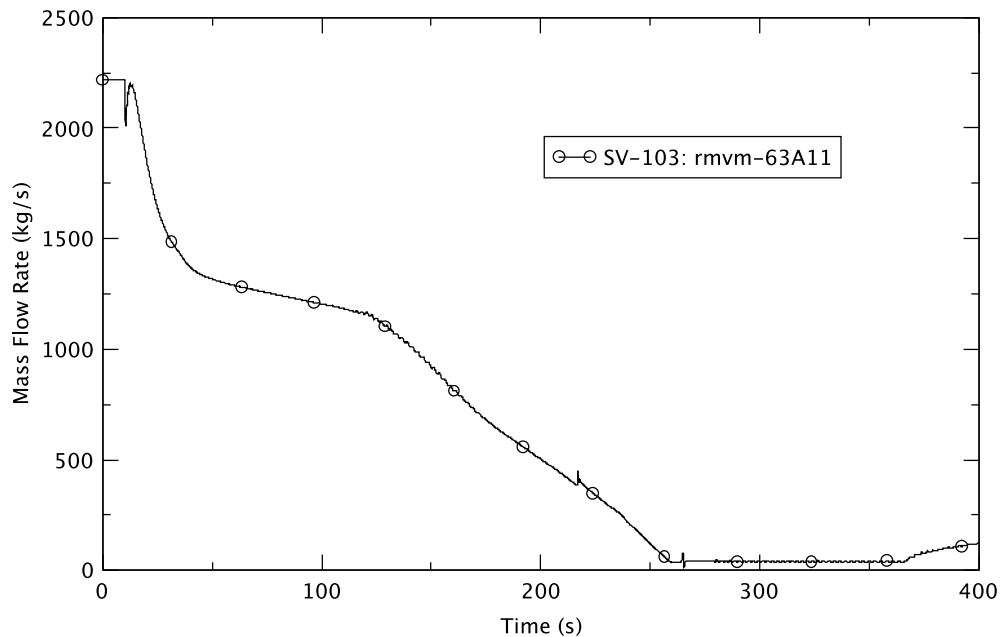


Figure 4.15 Feedwater Flow Rate in Case 2

We simulated the operator action to reduce water level to TAF starting at 120 s; Figure 4.8 reveals that its effect is not apparent until around 163 s. Investigation of the separator behavior reveals that fluid mass is accumulated from around 37 s to 122 s, and then starts being released to the RPV until around 170 s. Figure 4.16 depicts the predicted mass inside the separator located in ring-1. This mass release (integrated mass of around 5,165 kg from 122 s to 170 s) compensates for the loss in mass (integrated mass of around 7,023 kg from 122 s to 170 s) caused by the difference between the steam and FW flows and keeps the DC level at almost the same elevation from 122 s to 163 s. As the rate of mass release from the separator diminishes, the DC level begins declining from around 163 s and continues to do so until the end of the simulation.

We also can infer the downcomer water level from the axial void distribution in the vessel. Figure 4.17 shows the predicted void fractions in axial nodes 14 and 15 in ring 1 and ring 2 of the vessel. In the legend, “A” and “R” respectively represent the axial and radial nodes, and the numbers following them represent the node numbers. As shown in the figure, TRACE predicts a void fraction of almost zero in the 14th axial node, while it is almost 1.0 in the 15th axial node from around 33 s to 164 s in ring 1. The separator outlet (its top) is located at the top elevation of the 15th axial node. Very similar behavior occurs in ring 2. TRACE predicts the water level to be the same as the top elevation of the 14th axial node from around the time the separators start accumulating water in them up to the time the DC level starts declining (Figure 4.8). An ATWS-I sensitivity study [31], specifying a fixed carryover and carryunder for the separator, improves the prediction of the dynamic response of the vessel’s level ; for example, the initial reduction in water level reduction caused by the operator action occurs earlier for the sensitivity case than for the nominal case. This suggests further study of the modeling of water level tracking and

separator dynamics is warranted. The conclusions of the ATWS-I sensitivity study [31] suggest that the results of the calculations and the conclusions are not affected appreciably.

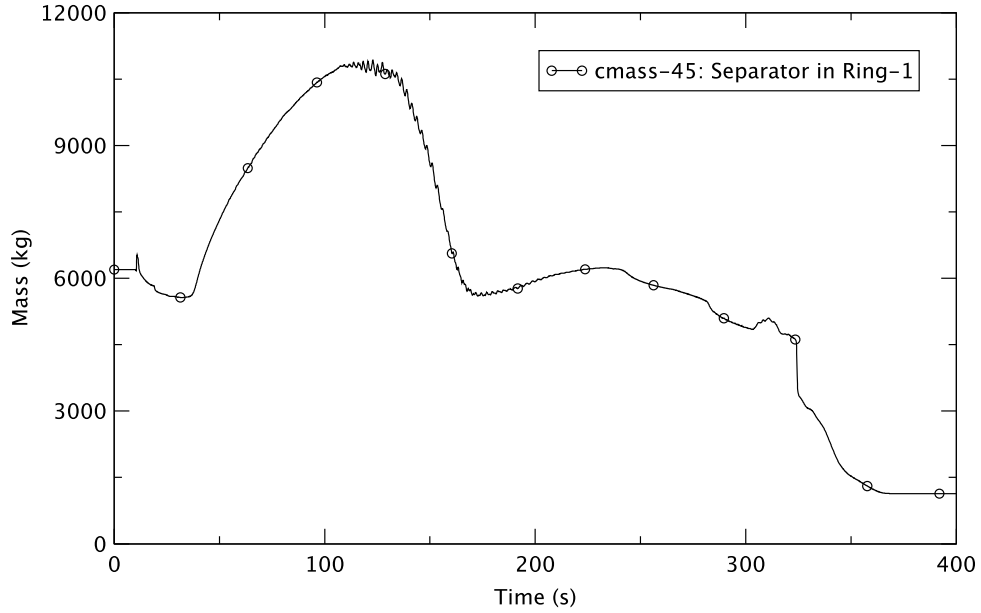


Figure 4.16 Mass in Ring-1 Separator in Case 2

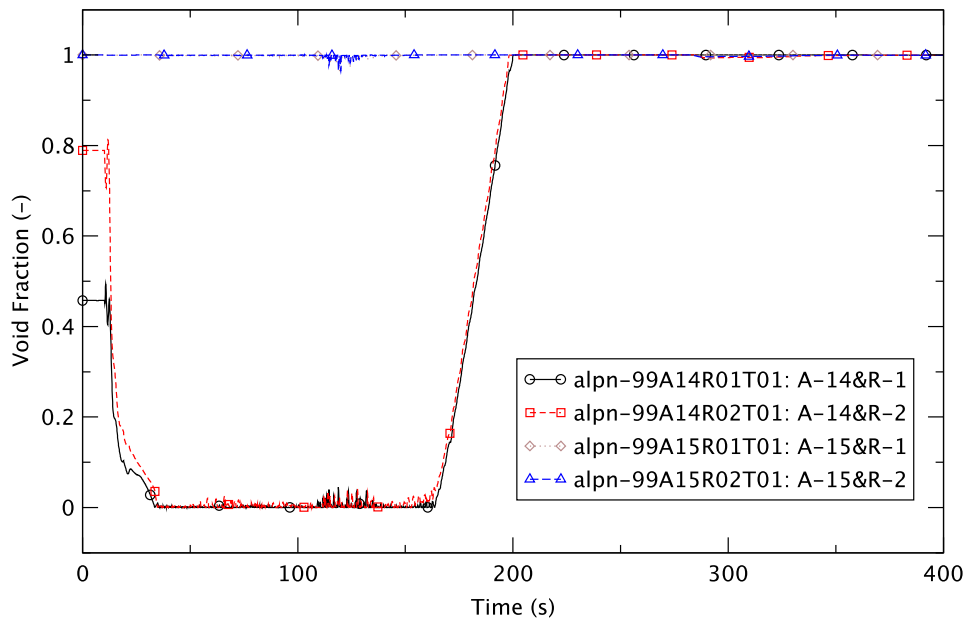


Figure 4.17 Void Fraction in Upper RPV Region in Case 2

4.2.10 Boron Inventory in Core

Figure 4.9 shows boron inventory in the core. While boron is injected into the vessel at 130 s, it does not immediately reach the core. The SLCS injection into the HPCS sparger (when the reactor power is relatively high) ensures that the borated solution is mixed in the turbulent two-phase flow above the core. The boron then is entrained in the flow leaving the upper plenum through the separators. The entrained boron then passes down the downcomer and into the core from below. The roughly 30 seconds delay in the accumulation of boron corresponds to the transit time from the upper plenum to the core's inlet.

4.2.11 Fuel Cladding Temperature

The core power oscillations can affect the temperature of the fuel cladding due to the change of the power and the efficiency of heat transfer from the fuel to coolant because of the continuous change of the void fraction in the core. Figure 4.18 and Figure 4.19 show the cladding temperatures in the bundles with the highest power at steady-state, and from the first harmonic. The CHAN component numbers of 388, 403, 243, and 544 in the legend represent, respectively, the limiting bundles in the NE quadrant with maximum power, the SE quadrant with maximum power, the NE quadrant with the first harmonic calculation, and the SE quadrant with the first harmonic calculation. The last digits of 3 and 6 of the CHAN number represent the average and the hot rods, respectively.

The peak cladding temperature of 1,631 K occurs at about 169 s in the hot rod, according to the first harmonic calculation, located in the SE quadrant; it is higher than the cladding temperature limit of 1,478 K (2,200°F) [32]. For these hot rods, we assumed in the simulation a power peaking factor of 1.2. As shown in Figure 4.18 and Figure 4.19, the cladding temperatures of average rods (power peaking factor of 1.0) behave differently from the hot rods and do not greatly increase. The highest cladding temperature of the average rods is 1,444 K, viz, lower than the limit of cladding temperature.

Figure 4.18 and Figure 4.19 show the cladding temperatures increase suddenly at around 141 s in the hot rods. This sudden rise is predicted when the heat flux (and the corresponding heat transfer coefficient) from the fuel to the coolant decreases suddenly and significantly as the void fraction becomes much larger than 0.9. Then, the heat flux increases slowly in general until around 167 s, even though the void fraction oscillates and the clad exhibits a slight fall in the rate of temperature increase (Figure 4.19). This same figure also reveals that as average core power declines from around 167 s (Figure 4.2), the cladding temperatures also drop continuously until around 328 s in the SE quadrant, and 336 s in the NE quadrant. At instances when the rewet temperature seems to be predicted, the cladding temperatures drop suddenly, becoming slightly higher than the liquid temperature, and remaining at the lower temperature for the remainder of the simulation.

It seems like there is a “lock” in predicting heat transfer after a certain criterion is met because TRACE still predicts small heat flux and a continuing rise in cladding temperature even though the coolant void fraction is almost zero. Seemingly, once the cladding temperature, as predicted by TRACE, has exceeded the minimum stable film-boiling temperature (T_{min}), the heat transfer regime becomes “locked” into a film-boiling regime. Thereafter, TRACE will not predict the rewetting of the cladding surface until its temperature is reduced below a rewet temperature, regardless of the void fraction.

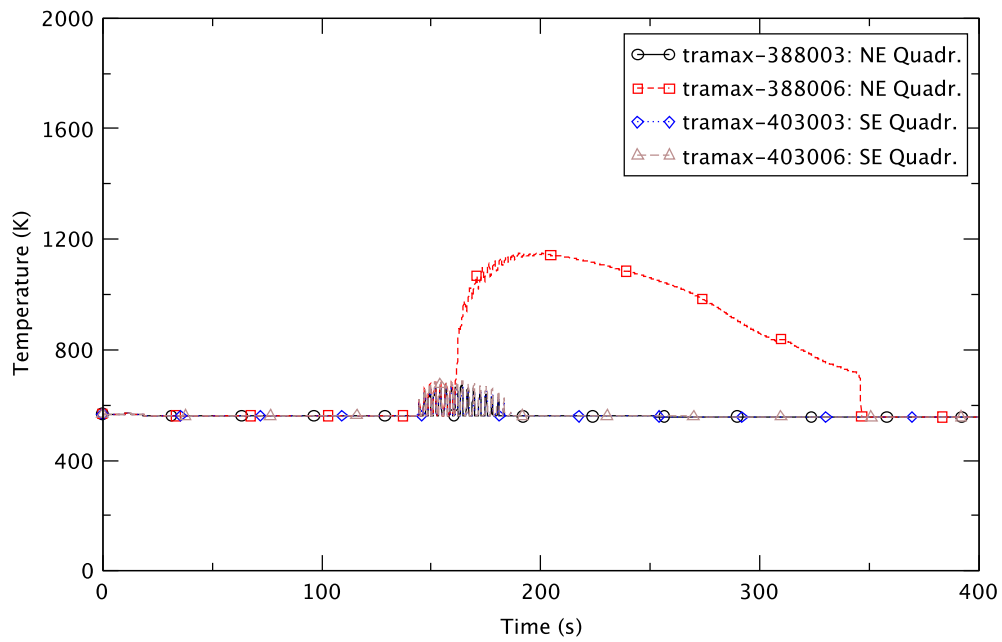


Figure 4.18 Peak Cladding Temperature in Bundles with Maximum Steady-State Power in Case 2

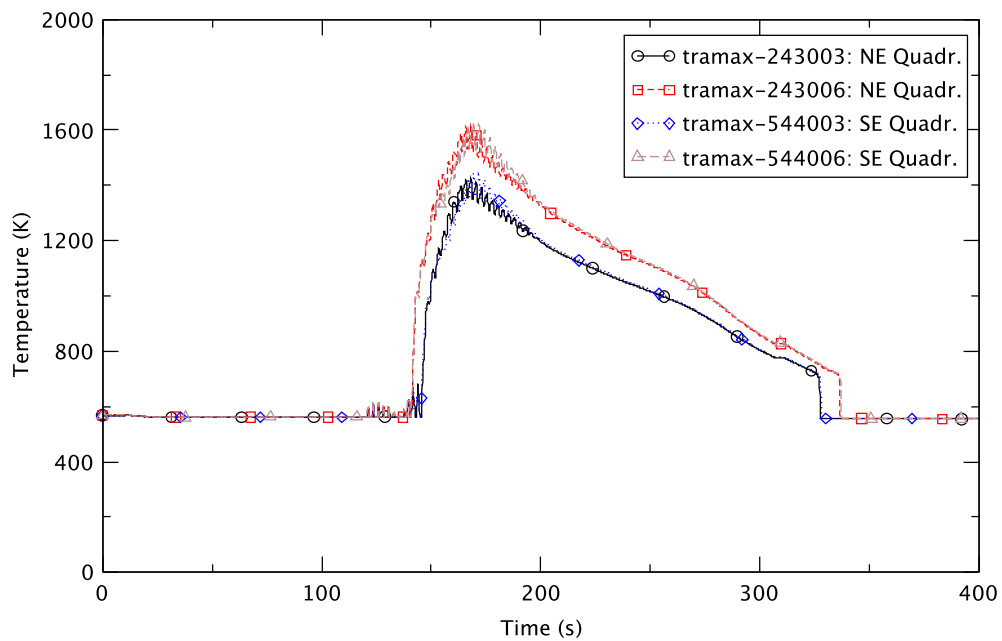


Figure 4.19 Peak Cladding Temperature in Bundles with Maximum First Harmonic Power in Case 2

Some inconsistency in the prediction of clad temperature by TRACE also was observed. For very similar coolant thermal-hydraulic conditions, TRACE predicts different trends for the clad temperature; oscillatory without increase in some nodes and a continuous increase in others.

Figure 4.20 shows the behavior of the cladding temperature along the length of the hot rods from the first harmonic calculation in the SE quadrant at 50 s, 100 s, 200 s, and 300 s. The cladding temperature remains relatively constant at 50 s and 100 s along the bundle's length before the power oscillatory behavior starts. It becomes very high during the period when the power is oscillating at 200 s, especially in the lower section of the bundle (around 0.6 m elevation), and is lower at 300 s when the power oscillation stops. The occurrence of the highest rod temperature at an elevation of around 0.6 m is because the core power has a bottom-skewed shape at 200 s. Figure 4.21 illustrates very similar behavior of the cladding temperatures in the NE quadrant in the bundles with the highest first-harmonic power. We note that in Figure 4.20 and Figure 4.21 the peak cladding temperature along the length of the bundle corresponds to the value at 200 s in the corresponding bundles in Figure 4.19.

There is no noticeable change of the hot rod's cladding temperature in the bundle with the maximum steady-state power in the SE quadrant (Figure 4.22). For the corresponding hot rod in the NE quadrant, Figure 4.23 shows that there are marked rises in cladding temperature just below the mid-core section at 200 s and 300 s, with another prominent rise at a higher section of the bundle (around 2.2 m) in the bundle with the highest steady-state power in the NE quadrant. This strange temperature behavior seems to be associated with the deficiency in predicting heat flux (or heat transfer coefficient) discussed above. The first rise of the cladding temperature in Figure 4.23 is observed in node 20 through node 23 of the heat structure, while the other rise occurred in node 27. These increases in cladding temperature reflect the fact that TRACE predicts a sudden decline in heat fluxes at around 160 s, and the heat fluxes increase slowly in general until about 180 s. In node 24 through node 26, however, TRACE predicts oscillatory heat transfer with high amplitudes from around 148 s to 178 s; this seems to cause the temperature of the cladding to not increase much since heat transfer still is efficient. A more detailed examination of these heat transfer predictions by TRACE would be informative. However, the basic phenomena predicted (dryout and failure to rewet) lead to excessive cladding temperatures, regardless of these finer points, and the current analysis consistently indicates a high PCT.

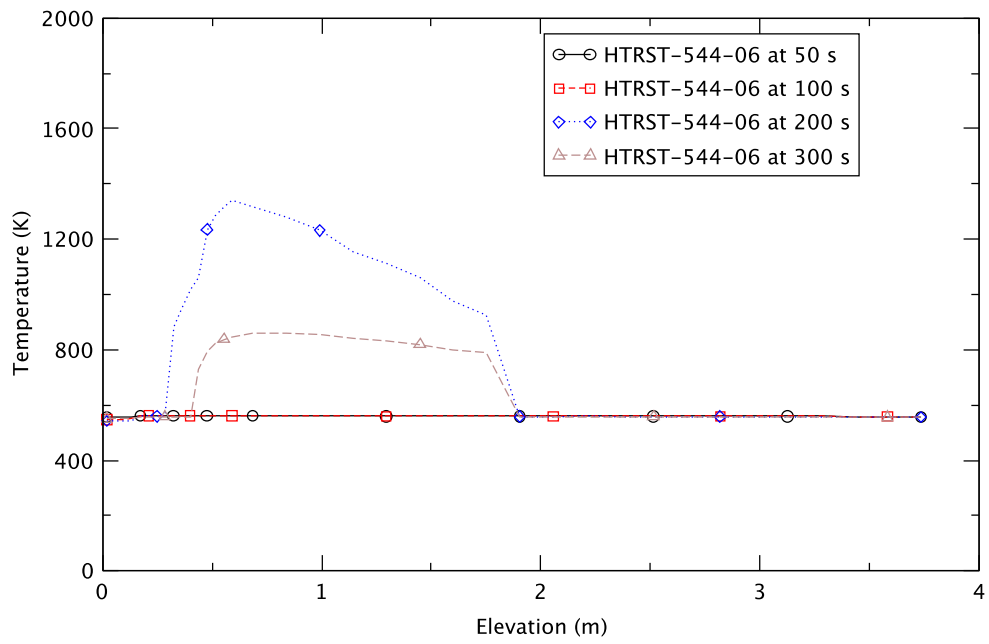


Figure 4.20 Axial Cladding Temperatures in Bundle 544 in Case 2

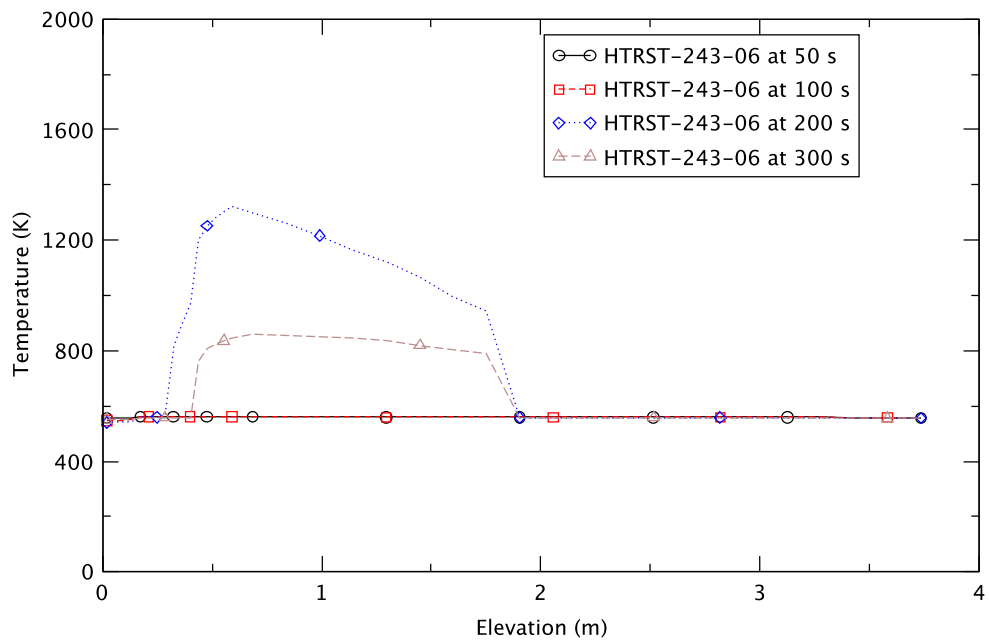


Figure 4.21 Axial Cladding Temperatures in Bundle 243 in Case 2

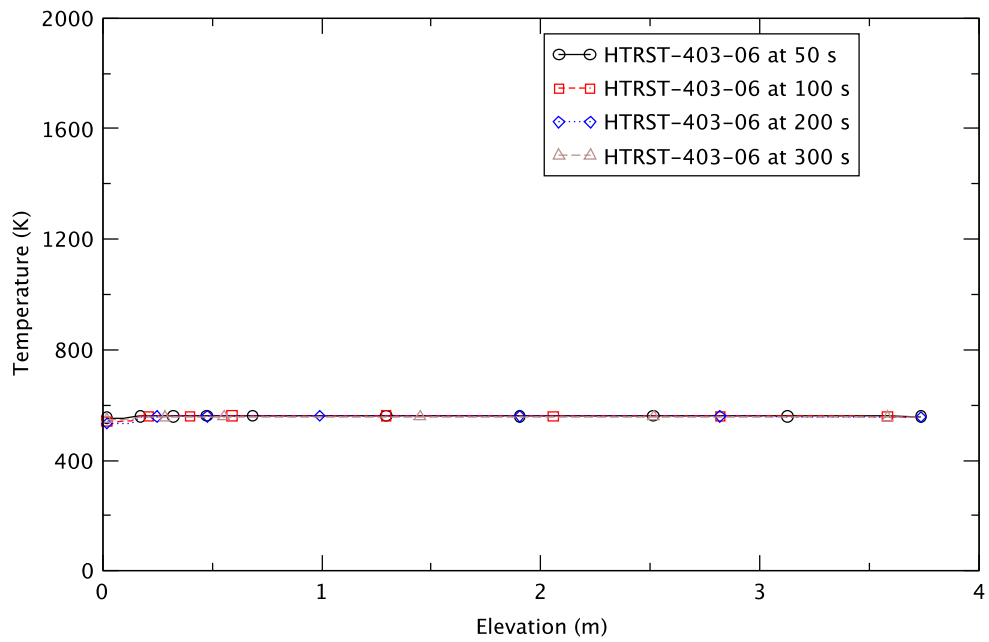


Figure 4.22 Axial Cladding Temperatures in Bundle 403 in Case 2

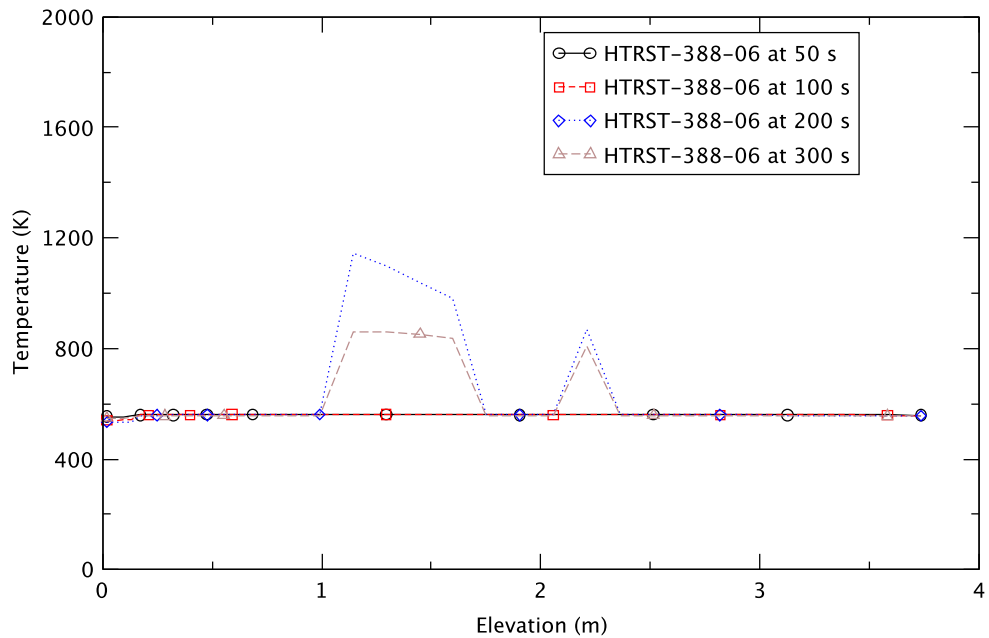


Figure 4.23 Axial Cladding Temperatures in Bundle 388 in Case 2

Figure 4.24 shows the maximum cladding temperature in all fuel in the core. Thus, the temperature shown in Figure 4.24 is the highest of the cladding for any fuel rod group in any

bundle in the core. It is expected that the location of the hottest spot will vary in the core during a transient reflecting the dynamics of the oscillation contour. Therefore, the highest value of the maximum cladding temperature differs from that shown in Figure 4.19 and is 1,691 K, occurring at around 163 s. This fact denotes that the bundle with the most severe *local* thermal-hydraulic conditions (in terms of maximum cladding temperature) occurs in other than the limiting bundles in terms of peak *total* bundle power from the steady-state calculation.

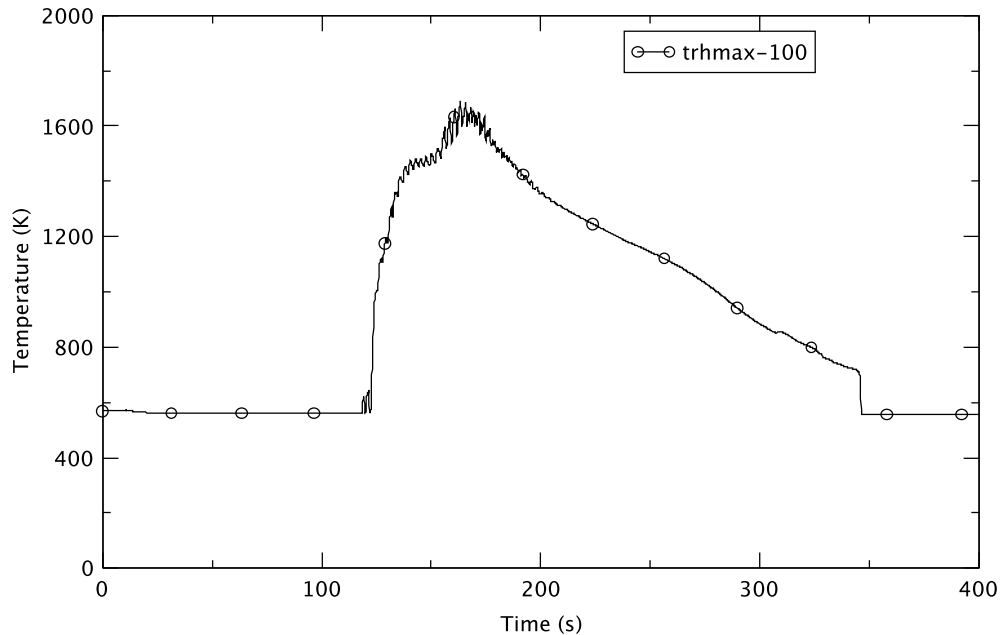


Figure 4.24 Maximum Cladding Temperature in Core in Case 2

4.3 Effect of Bypass Fraction

4.3.1 Bypass Fractions

Four bypass fractions at BOC are considered: 10% (Case 1A), 25% (Case 1B), 50% (Case 1F), and 100% (Case 1). The TSV is closed in 0.1 s on a turbine trip at 10 s of the simulation time, and opens in 1.0 s to simulate the bypass paths with the flow fractions shown in Table 4.4.

Table 4.4 Turbine Bypass Fractions and Simulation Conditions

Case ID	Exposure	Power, %	Core Flow Rate, %	Bypass Capacity, % ¹	Spectral History
1	BOC	100	85	100	UH
1A	BOC	100	85	10	UH
1B	BOC	100	85	25	UH
1F	BOC	100	85	50	UH

¹ Bypass capacity is percentage of normal steam flow to the turbine.

4.3.2 Initial Conditions

The difference between predicted initial values of key thermal-hydraulic parameters from the null transient calculation for 10 s and reference values are shown in Table 4.5. Calculated steady-state values agree well with the reference ones. Some of the differences are due to the initial core power being disturbed by random noise in the moderator density imposed in the PARCS calculation at five seconds into the null transient.

Table 4.5 Comparison of Steady-State Parameters in BOC Cases

Parameter	10% Bypass		25% Bypass		50% Bypass		100% Bypass	
	Diff.	Diff. (%)	Diff.	Diff. (%)	Diff.	Diff. (%)	Diff.	Diff. (%)
Core Power (MWt)	0	0.0	0	0.0	0	0.0	0	0.0
Steam Dome Pressure (kPa)	5	0.07	5	0.07	5	0.07	7	0.1
Main Steamline Flow (kg/s)	-4	-0.2	-4	-0.2	-4	-0.2	0	0.0
Total Core Flow (kg/s)	-4	-0.03	-4	-0.03	-4	-0.03	-6	-0.05
Feedwater Flow (kg/s)	-4	-0.2	-4	-0.2	-4	-0.2	2	-0.09
Feedwater Temperature (K)	0	0.00	0	0.00	0	0.00	0	0.00
Downcomer Level (m)	-0.1	-1	-0.1	-1	-0.1	-1	-0.1	-1

4.3.3 Sequence of Events

The sequences of the events for the cases with different bypass fractions are generally similar to that of the limiting case (Case 2) discussed in Section 4.2. Table 4.6 shows the sequence for the events; detailed discussions about the system's behavior are presented in the following sections. We note in the table where the sequence differs for different bypass fractions.

Table 4.6 Sequence of Events at BOC with Four Turbine Bypass Capacities

Time (s)	Event
0.0	<ul style="list-style-type: none"> Null transient simulation starts.
10.0	<ul style="list-style-type: none"> Null transient simulation ends. Turbine trip is initiated by closing the TSV. Recirculation pumps are tripped on the turbine trip. Feedwater temperature starts decreasing.
10.1	<ul style="list-style-type: none"> TSV closes completely and starts opening again to simulate turbine bypass flow.
11.1	<ul style="list-style-type: none"> TSV (bypass) completes opening and its open area provides the predetermined steam flow fraction shown in Table 4.4.
~11.4	<ul style="list-style-type: none"> Steam flow starts decreasing in Cases 1 and 1B. ~ 12.1 s in Case 1F. ~ 12.2 s in Case 1A.
~13.0	<ul style="list-style-type: none"> Feedwater flow starts decreasing in Case 1. ~ 14.3 s in the other cases.
~75	<ul style="list-style-type: none"> Power oscillation above noise level apparent (instability onset) in Case 1A. ~ 95 s in the other cases.
120	<ul style="list-style-type: none"> Water level reduction is initiated and the normal water level control system setpoint is reduced linearly to TAF over 180 s.
130	<ul style="list-style-type: none"> Boron injection is initiated and linearly ramped to full flow at 190 s.
~132	<ul style="list-style-type: none"> Noticeable bi-modal oscillation of the core power is initiated in Case 1A. ~ 141 s in Cases 1B and 1F. ~ 143 s in Case 1.
~138	<ul style="list-style-type: none"> Downcomer water level begins decreasing in Case 1A. ~ 139 s in Case 1B. ~ 155 s in Case 1F. ~ 158 s in Case 1.
~160	<ul style="list-style-type: none"> Boron starts accumulating in the core.
~168	<ul style="list-style-type: none"> Peak cladding temperature of ~1,491 K occurs in Case 1B. ~ 1,489 K at 150 s in Case 1A. ~ 1,418 K at 169 s in Case 1F. ~ 1,373 K at 181 s in Case 1.
~220	<ul style="list-style-type: none"> Power oscillation ends in Case 1A. ~ 240 s in Case 1B. ~ 245 s in Cases 1 and 1F.
400	<ul style="list-style-type: none"> Simulation ends.

4.3.4 Steamline Flow

Figure 4.25 compares the steamline flow rates for the four cases. Their general behavior is similar to each other and also similar to the limiting case (Case 2). However, closer examination reveals that the average steam flow is slightly larger, but not significantly so, from around 23 s to 195 s when the bypass fraction is smaller. This is caused by higher average core power with smaller turbine bypass fraction that results in more steam generation in the core. The power behavior is discussed in the next section.

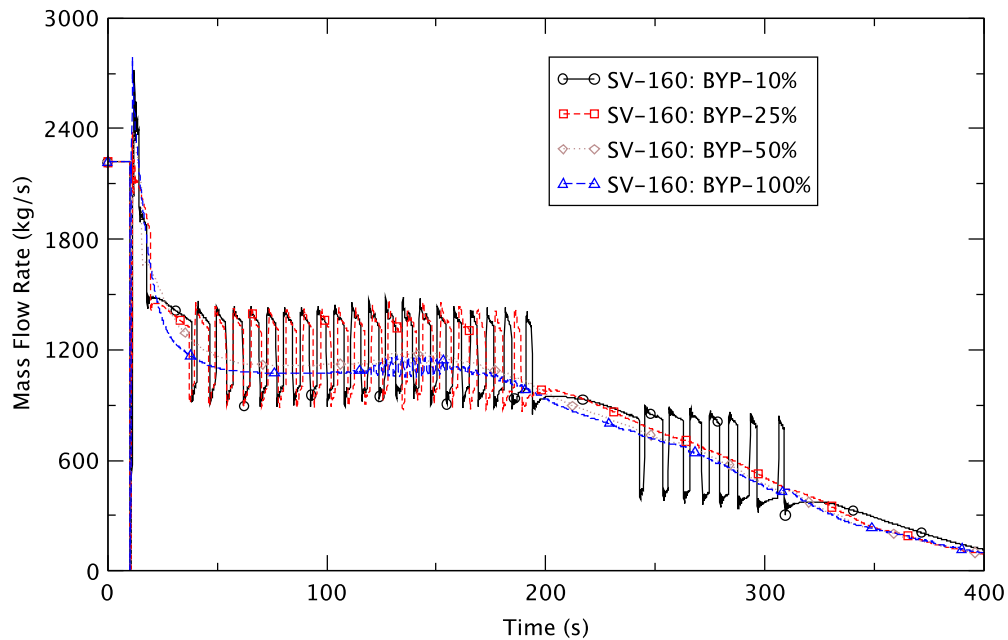


Figure 4.25 Steam Mass Flow Rate in Steamline in BOC Cases

As Figure 4.25 shows, the steam flow oscillates when the turbine bypass fraction is 10% and 25% while no oscillatory behavior is predicted with bypass fractions of 50% and 100%. This is due to the fact that when a small bypass fraction is simulated, the amount of steam generated in the core is larger than that being discharged from the RPV through the turbine bypass valve (TBV), so that the RPV pressure increases, and the safety relief valves (SRVs) are open when the pressure reaches the opening setpoint. As the SRVs provide large enough flow area for releasing the excess steam from the RPV, the RPV pressure decreases, and the SRVs are closed as the pressure falls below the closing setpoint. This behavior is repeated until the core power is small enough not to generate the excess steam to raise the system's pressure.

When the bypass fractions are large enough (50% and 100%) for steam produced in the core to be released from the RPV, the system pressure becomes almost constant from approximately 50 s to 160 s before declining as the core power begins dropping (it is clearly seen with 50% bypass fraction). Figure 4.26 compares system pressures. As expected, TRACE predicts an oscillatory behavior of system pressure with 10% and 25% bypass, while none is predicted with 50% and 100%. The figure shows that the system pressure varies inversely with the turbine-bypass fraction. The pressure is almost the same for 10% and 25% from around 50 s to 200 s because it is maintained by the SRVs. Further, as Figure 4.26 reveals, system pressure reaches an asymptotic value faster when the bypass fraction is larger.

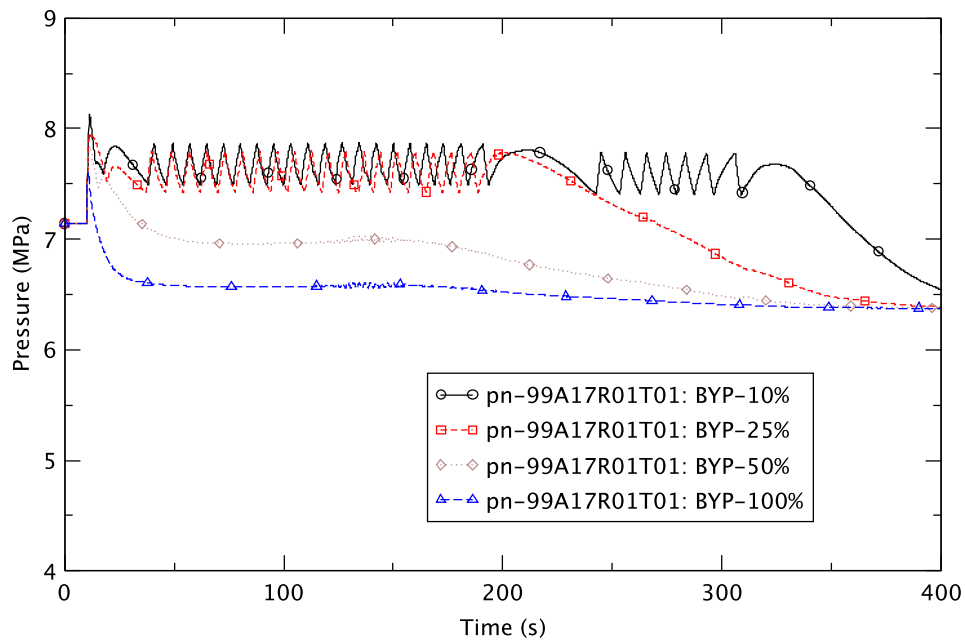


Figure 4.26 RPV Pressure in BOC Cases

4.3.5 Core Power

Figure 4.27 shows the reactor core power predicted by TRACE/PARCS. The general behavior is similar to that of the limiting case (Case 2) but the amplitudes of the power oscillation are lower in the BOC cases. Furthermore, the average power is higher as the bypass fraction becomes smaller, due to the system pressure behavior (Figure 4.26). Thus, the system's pressure is lower with larger bypass fraction resulting in larger negative reactivity feedback and lower average core power. The reactor power response to the 2RPT is similar for all cases, a decrease in power to about 50% of the initial level. This early drop in reactor power is the reason for not actuating the SRVs for the cases with turbine-bypass fractions of 50% and 100%.

As Figure 4.27 shows, power oscillation starts earlier with small bypass fractions (10% and 25%) than with larger ones (50% and 100%). These early power oscillations from around 40 s to 75 s or 95 s do not indicate reactor instability but are caused by moderator changes in density due to the oscillatory behavior of the system pressure caused by SRV cycling (Figure 4.26).

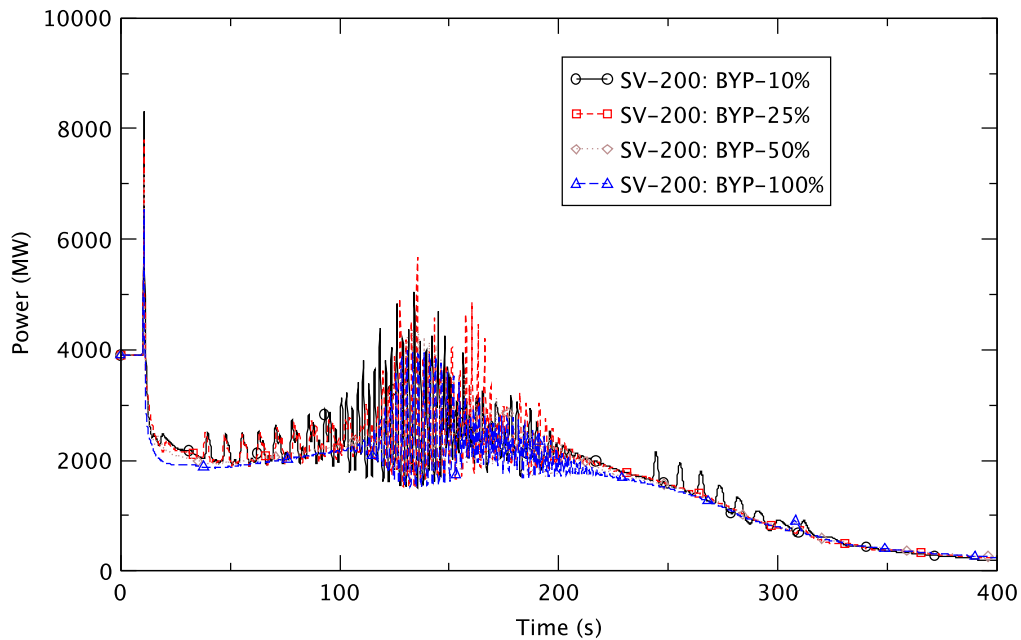


Figure 4.27 Reactor Core Power in BOC Cases

Reactor power is shown in Figure 4.28 through Figure 4.31 for 10%, 25%, 50% and 100% bypass fraction, respectively. As depicted in Figure 4.27 through Figure 4.31, the maximum amplitude of the power oscillation is higher with smaller bypass fractions but the oscillations are also more irregular due to the perturbation caused by the opening and closing of the SRVs. This implies that the reactor becomes more unstable as the system pressure becomes higher with smaller turbine bypass fractions. The cause of the higher amplitude of power oscillation at a higher pressure reflects the corresponding increase in core inlet subcooling with system pressure (Section 4.3.9 discusses the core inlet subcooling effect).

Reactor instability starts from approximately 75 s with 10% and 95 s with 25%, 50%, and 100% bypass fractions. The power oscillations initially are core-wide for all BOC cases, then at around 132 s to 143 s, depending on the case, they evolve into a bimodal form with both a core wide and regional component. The evolution of a coupled bi-modal oscillation contour indicates non-linear harmonic coupling. The non-linearity also is evident in the accompanying frequency doubling. The contour of the oscillation in the non-linear phase indicates that higher harmonic modes have been excited (see Figure 4.32), rather than the first harmonic. This observation suggests that it may be desirable to model the core with more detailed mapping between the neutronic and the thermal-hydraulic channels (i.e., 764 CHAN components to represent each fuel bundle individually).

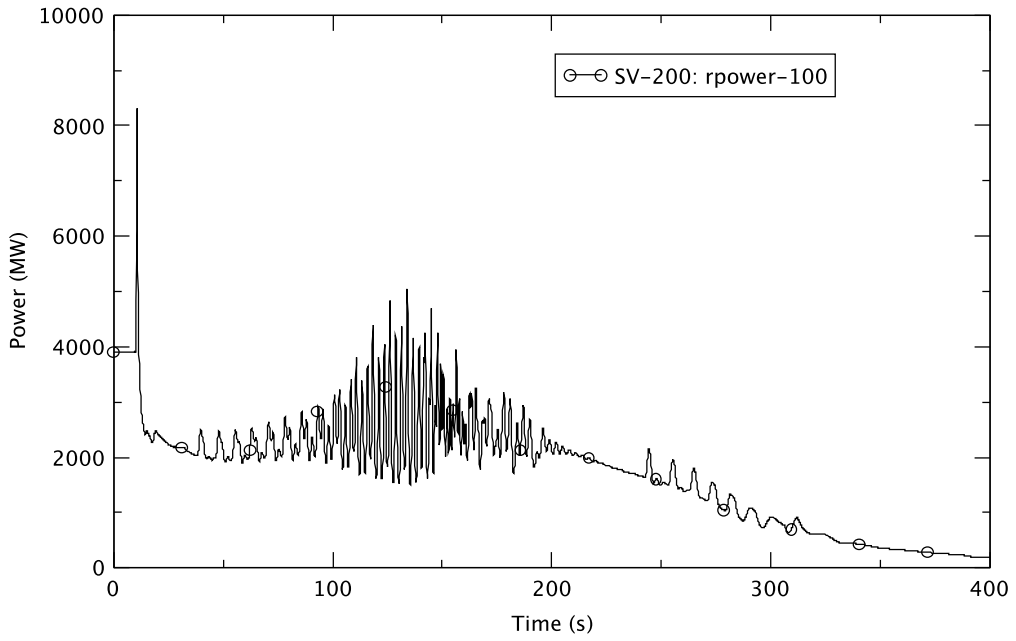


Figure 4.28 Reactor Core Power at BOC with 10% Bypass Fraction (Case 1A)

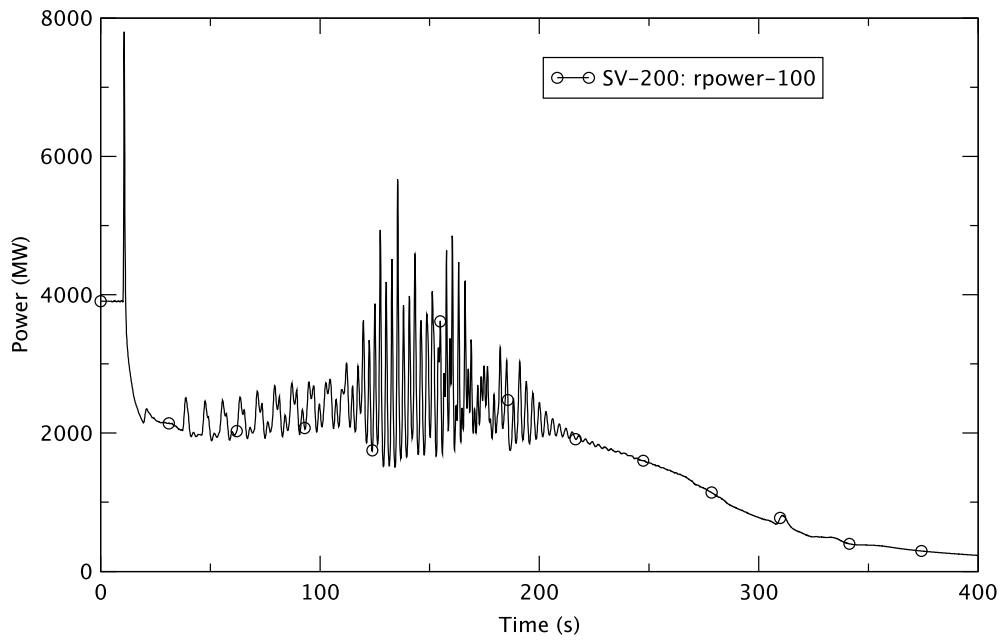


Figure 4.29 Reactor Core Power at BOC with 25% Bypass Fraction (Case 1B)

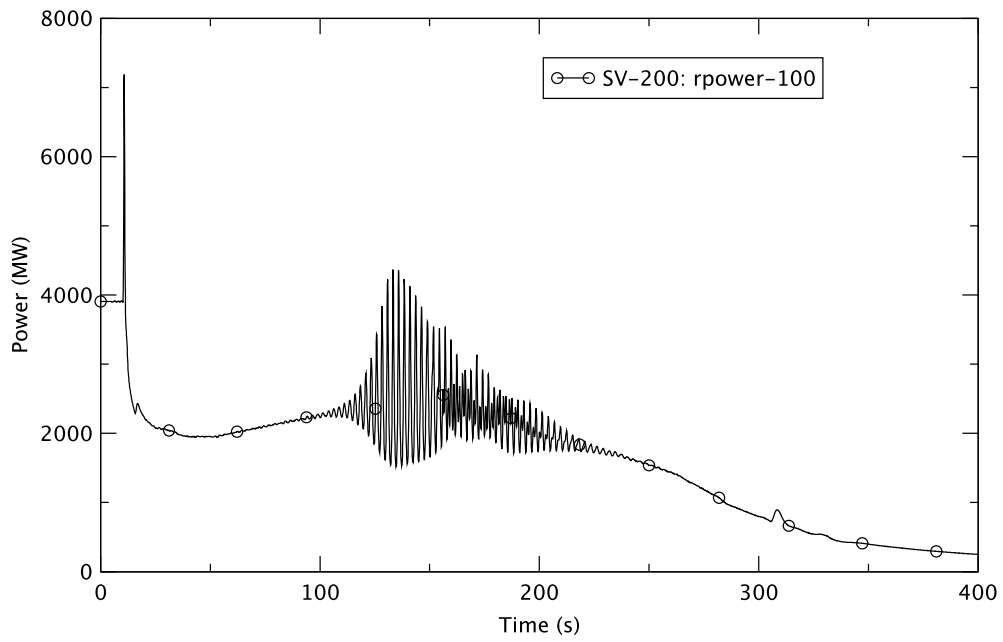


Figure 4.30 Reactor Core Power at BOC with 50% Bypass Fraction (Case 1F)

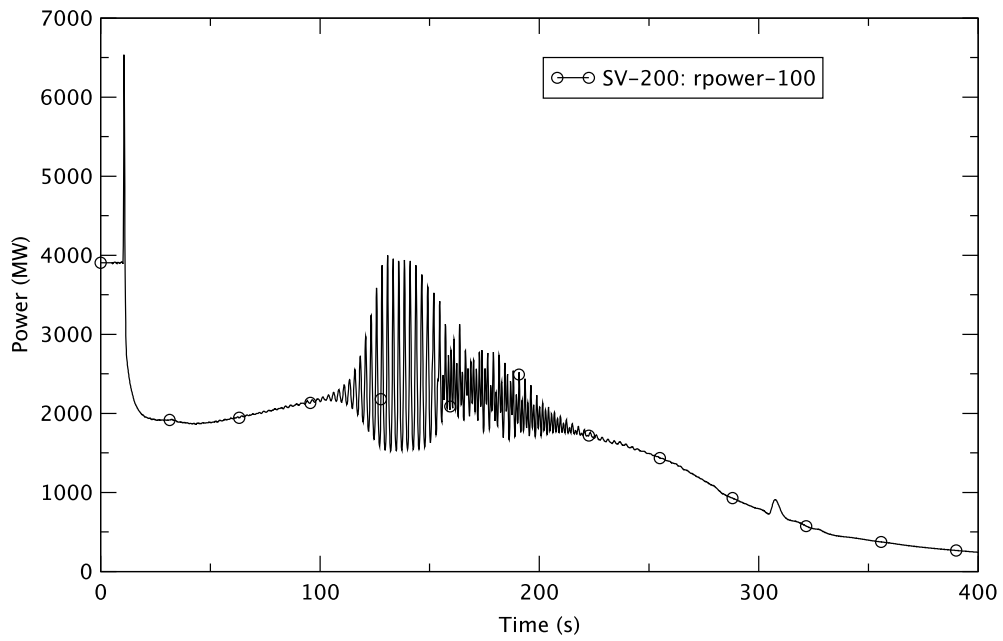


Figure 4.31 Reactor Core Power at BOC with 100% Bypass Fraction (Case 1)

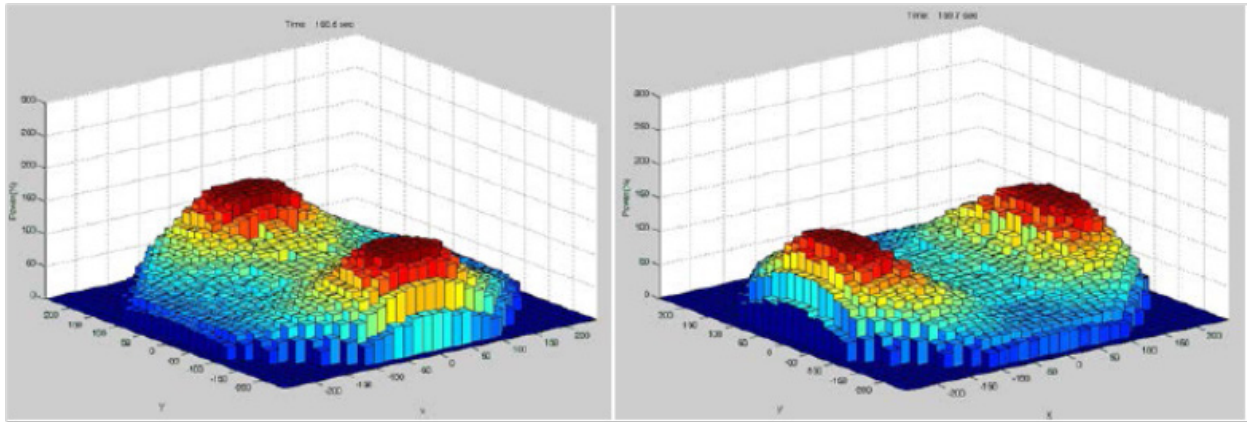


Figure 4.32 Example of Non-Linear Oscillation Contour for BOC Cases

4.3.6 Core Flow

The core flow rates are compared in Figure 4.33. Their behavior is very similar except for some oscillatory behavior from around 40 s to 200 s with small bypass fractions (10% and 25%). The general behavior is described in Section 4.2.4.

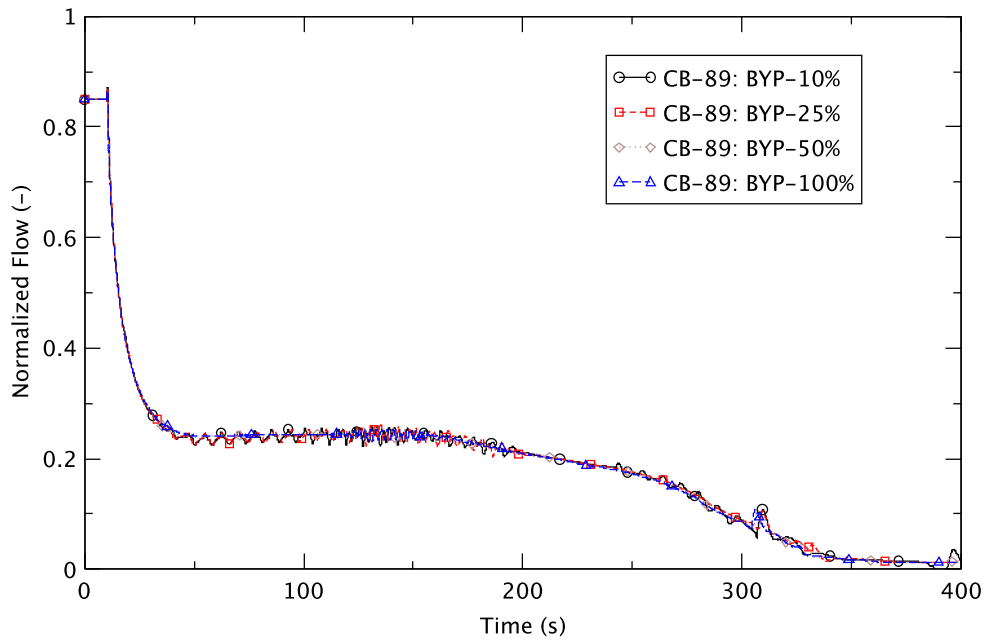


Figure 4.33 Reactor Core Flow Rate in BOC Cases

4.3.7 Feedwater Flow and RPV Water Level

The operator action of reducing the DC water level to TAF is simulated at 120 s by reducing the feedwater flow to lower mass flow into the core. Figure 4.34 compares the feedwater flow rates. As expected, in all cases, the flow rates start decreasing from 120 s. The comparison illustrates that as the turbine bypass fraction becomes smaller, the recovery of the feedwater flow rate also lessens around 14 s when the TBV is open; nevertheless, the flow rate is slightly larger from approximately 23 s until it becomes zero at around 270 s. This larger FW flow is due to the larger steam flow with smaller bypass fraction, as shown in Figure 4.25. However, the general behavior is similar for each case as well as to that of the limiting case (Case 2).

The DC water levels do not drop until around 140 s with 10% and 25 % bypass fractions, and 160 s with 50% and 100% bypass fractions (Figure 4.35). The general behavior of the level is very similar for each case. The delay in the reduction in the level results in late onset of the decrease in core flow (Figure 4.33). The core flow starts declining from around 145 s with 50%, 150 s with 25%, and 155 s with 10% and 100% bypass fractions.

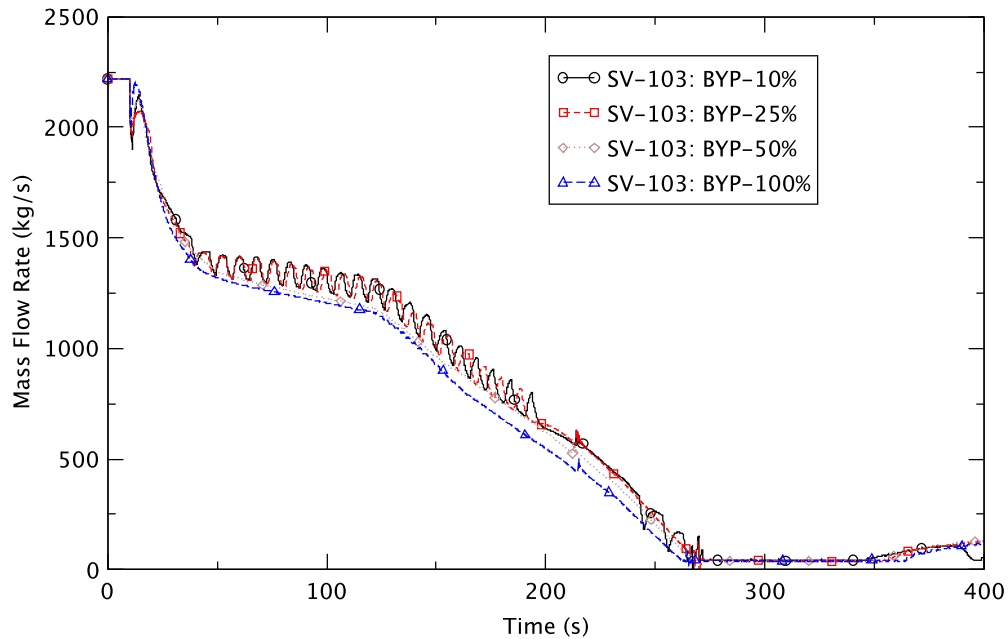


Figure 4.34 Feedwater Flow Rate in BOC Cases

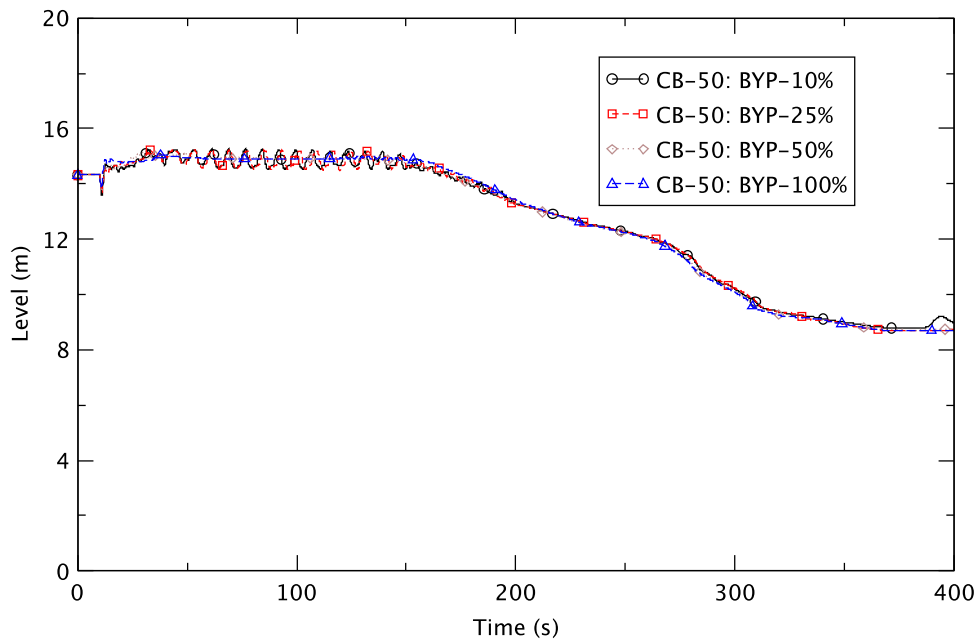


Figure 4.35 Downcomer Water Level in BOC Cases

4.3.8 Boron Inventory in Core

Operation of the SLCS is initiated at 130 s. Figure 4.36 is a comparison of the behavior of the boron inventory in the core. It is almost always the same, until around 260 s, and by then the reactor's instability has almost ended.

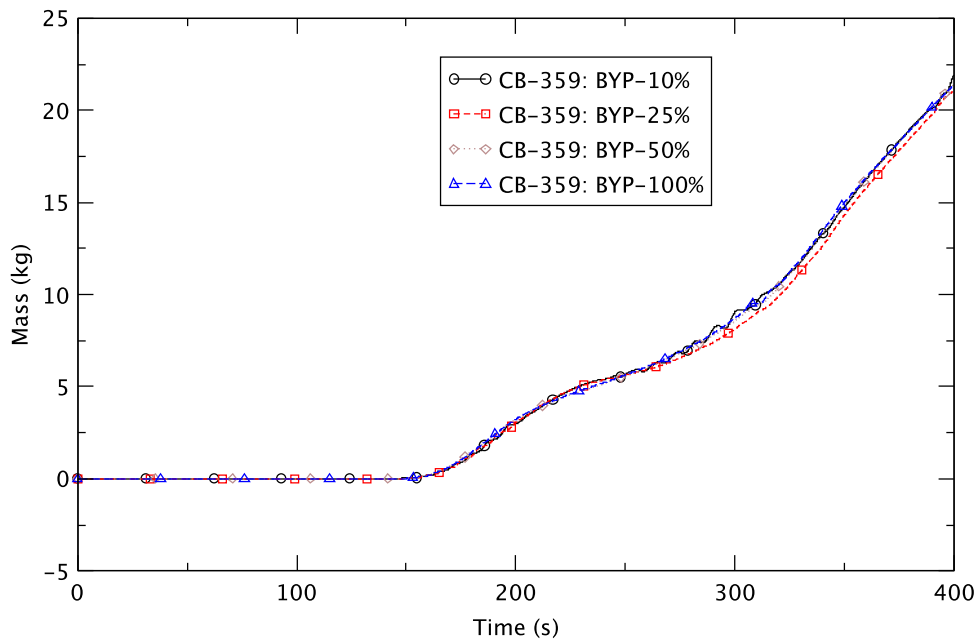


Figure 4.36 Boron Inventory in Core in BOC Cases

4.3.9 Core Inlet Subcooling

Figure 4.37 shows core inlet subcooling in ring 1 that becomes larger as the turbine bypass fraction becomes smaller. This is because the system pressure is higher with smaller bypass fraction (Figure 4.26), so resulting in higher saturation temperature and higher liquid subcooling at the core inlet. As detailed in Section 4.3.5, the amplitude of the power oscillation due to reactor instability is higher in general with smaller bypass fractions (Figure 4.27 through Figure 4.31). For the 10% and 25% bypass cases the amplitude of the power oscillations may be augmented by the pressure perturbations associated with SRV cycling. However, the latter does not occur for the 50% and 100% bypass cases. For them, the parametric effect of system pressure on reactor instability is easier to interpret. Apparently, a high system pressure has two opposing effects on reactor stability, i.e., destabilizing due to higher core inlet subcooling, and stabilizing due to smaller difference between the specific volumes of the liquid and the vapor phase. Results from the studies of bypass cases suggest that core inlet subcooling is the more dominant one in determining the relative stability of two operating conditions. Therefore, the smaller the turbine bypass fraction is, the more unstable the reactor becomes.

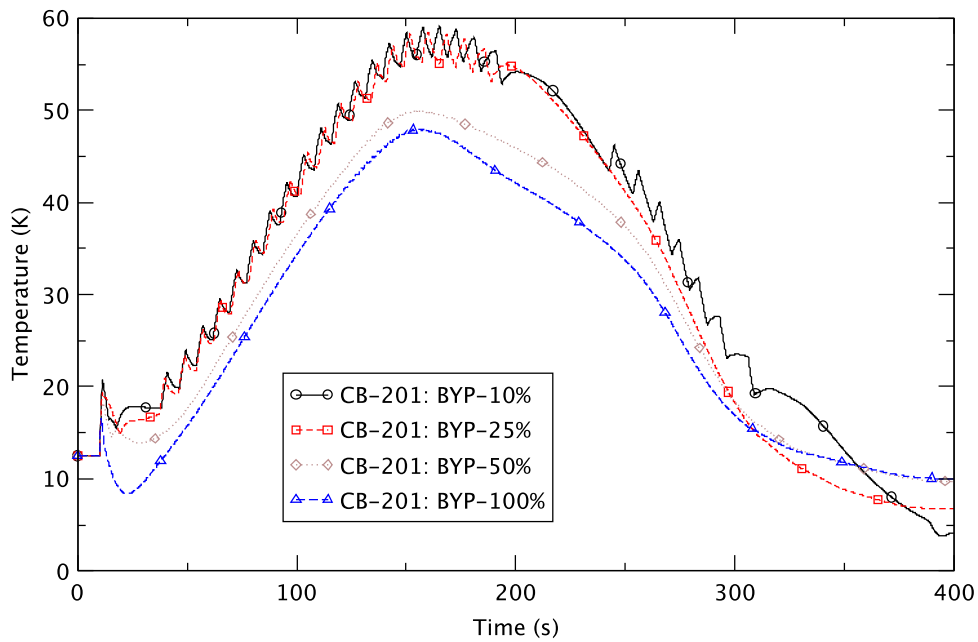


Figure 4.37 Core Inlet Subcooling in BOC Cases

4.3.10 Fuel Cladding Temperature

As discussed in Section 4.2.5, the core power oscillations can affect the temperature of the fuel cladding due to the change in efficiency of the heat transfer from the fuel to coolant because of the continuous change of the void fraction in the core. Figure 4.38 compares the maximum cladding temperature among all bundles in the core. It suddenly increases around 135 s in all cases except for the 10% bypass fraction case where it starts rising at about 120 s. Except for the timing of this sudden rise in the cladding temperature, the 10% and 25% cases show very similar behavior. As is evident from the figure, the peak cladding temperature is higher and occurs earlier with smaller bypass fractions. The highest peaks of 1,489 K and 1,491 K occur at approximately 150 s for the 10% bypass fraction and 168 s for the 25% bypass fraction; they are higher than the cladding temperature limit of 1,478 K (2,200°F).

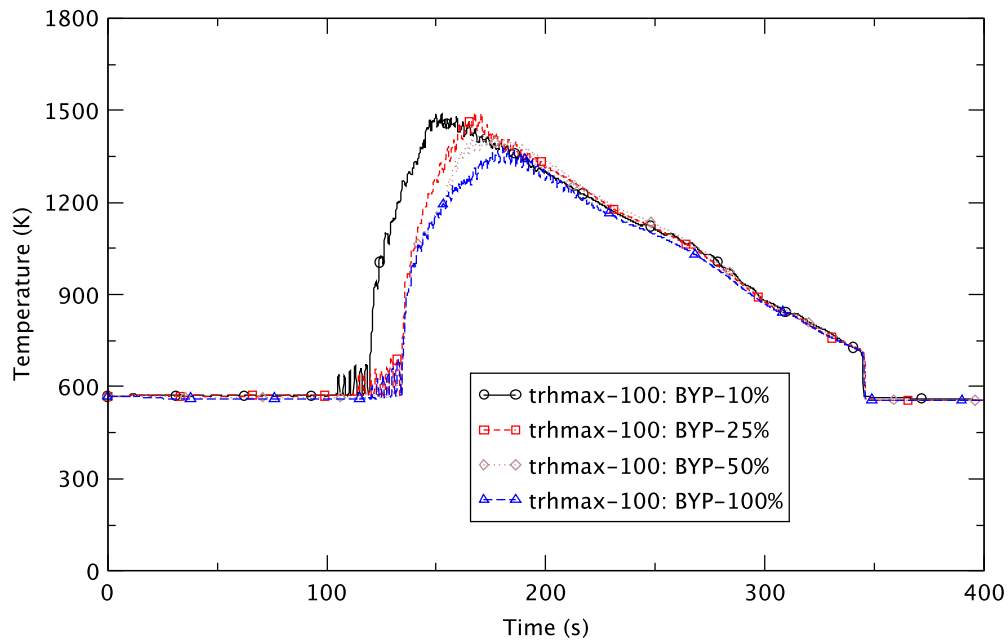


Figure 4.38 Maximum Cladding Temperature in Core in BOC Cases

4.3.11 Summary

We concluded that TRACE predicts unstable reactor conditions in all cases, but the unstable, density wave driven power oscillations in the reactor become more severe as size of the turbine bypass fraction declines. We note that when the bypass fraction is small (10% and 25%) and the system pressure is maintained by the SRVs at the early stage (until around 200 s), the effect of the bypass fraction on the reactor’s instability seems to be the same, regardless of its size. because the system pressure being maintained at the same magnitude entails the same degree of liquid subcooling at the core inlet. However, at a low bypass capacity, the pressure is maintained by the SRVs for longer. Further, based on the power oscillation contours, TRACE predicts higher order harmonic excitation despite the core-wide perturbations imposed by SRV cycling.

4.4 Effect of Time in Cycle

4.4.1 Time in Fuel Cycle

Three cases are considered in the analysis: BOC (Case 1); PHE (Case 2); and, EOFPL (Case 3). All of them have 100% turbine bypass capacity. The TSV is closed in 0.1 s on a turbine trip at 10 s of the simulation time, and then opens in 1.0 s to simulate the bypass paths with flow fractions of 100% turbine bypass. Table 4.7 shows the simulation conditions.

Table 4.7 Simulation Conditions - Effect of Time in Cycle

Case ID	Exposure ¹	Power	Core Flow Rate	Bypass Capacity	Spectral History
1	BOC	100%	85%	100%	UH
2	PHE	100%	85%	100%	UH
3	EOFPL	100%	105%	100%	UH

¹ BOC, PHE, and EOFPL represent beginning-of-cycle, peak-hot-excess-reactivity, and end-of-full-power-life, respectively.

4.4.2 Initial Conditions

The predicted initial values of some key thermal-hydraulic parameters from the TRACE/PARCS null transient calculation for 10 s are compared to reference values in Table 4.8. As shown, the calculated steady-state values generally agree well with the reference ones.

Table 4.8 Comparison of Steady-State Thermal-Hydraulic Parameters - Effect of Time in Cycle

Parameter	BOC (Case 1)		PHE (Case 2)		EOFPL (Case 3)	
	Diff.	Diff. (%)	Diff.	Diff. (%)	Diff.	Diff. (%)
Core Power (MWt)	0	0.0	0	0.0	0	0.0
Steam Dome Pressure (kPa)	7	0.1	5	0.07	5	0.07
Main Steamline Flow (kg/s)	0	0.0	-4	-0.2	-4	-0.2
Total Core Flow ¹ (kg/s)	-10	-0.08	10	0.09	-20	-0.2
Feedwater Flow (kg/s)	2	-0.09	-4	-0.2	-4	-0.2
Feedwater Temperature (K)	0	0.0	0	0.0	0	0.0
Downcomer Level (m)	-0.1	-1	-0.1	-1	-0.1	-1

¹ Simulated initial total core flow rate is 11,620 kg/s (85%) for Cases 1 and 2 and 14,354 kg/s (105%) in Case 3.

4.4.3 Sequence of Events

The timing of the sequence of events is similar at PHE and BOC. However, the case at EOFPL behaves differently. Table 4.9 shows the time sequence for these events and details about the system behavior are presented in the following sections. We note in the table where the sequence differs for different cases.

Table 4.9 Sequence of Events - Effect of Time in Cycle

Time (s)	Event
0.0	<ul style="list-style-type: none"> Null transient simulation starts.
10.0	<ul style="list-style-type: none"> Null transient simulation ends. Turbine trip is initiated by closing the TSV. Recirculation pumps are tripped on the turbine trip. Feedwater temperature starts decreasing.
10.1	<ul style="list-style-type: none"> TSV closes completely and starts opening again to simulate 100% turbine bypass flow.
11.1	<ul style="list-style-type: none"> TSV (bypass) completes opening and its open area provides the predetermined steam flow fraction of 100%.
~11.4	<ul style="list-style-type: none"> Steam flow starts decreasing.
~13.0	<ul style="list-style-type: none"> Feedwater flow starts decreasing.
~95	<ul style="list-style-type: none"> Power oscillation above noise level apparent (instability onset) in Case 1 and Case 2. No power oscillation in Case 3.
120	<ul style="list-style-type: none"> Water level reduction is initiated by reducing the normal water level control system setpoint linearly to TAF over 180 s.
130	<ul style="list-style-type: none"> Boron injection is initiated and linearly ramped to full flow at 190 s.
~147	<ul style="list-style-type: none"> Downcomer water level begins decreasing in Case 3. ~158 s in Case 1 ~163 in Case 2
~143	<ul style="list-style-type: none"> Noticeable bi-modal oscillation of the core power is initiated in Case 1. ~170 s in Case 2. No bi-modal oscillation of the core power in Case 3.
~160	<ul style="list-style-type: none"> Boron starts accumulating in the core.
~163	<ul style="list-style-type: none"> Peak cladding temperature of ~1,691 K occurs in Case 2. ~1,373 K at 181 s in Case 1. No significant increase of cladding temperature in Case 3.
~245	<ul style="list-style-type: none"> Power oscillation ends in Case 1. ~240 s in Case 2. No power oscillation in Case 3.
400	<ul style="list-style-type: none"> Simulation ends.

4.4.4 Steamline Flow

Figure 4.39 compares the steamline flow rates for the three cases. The flow is smaller at EOFPL relative to those at PHE and BOC from approximately 20 s to 330 s. The core flow initially is 105% of normal flow in the former case and 85% in the latter cases. As natural circulation is being established after the dual recirculation pump trip, the rate of core flow rate is determined primarily by the difference in gravity head between the DC and core, and is expected to be almost the same in all cases since this difference will be similar in each case. Among the three cases, the EOFPL case experiences the largest fractional drop in core flow from the initial conditions to natural circulation. This leads to a relatively large negative void reactivity feedback at EOFPL. Therefore, the average core power is relatively small and less steam is generated in the EOFPL case.

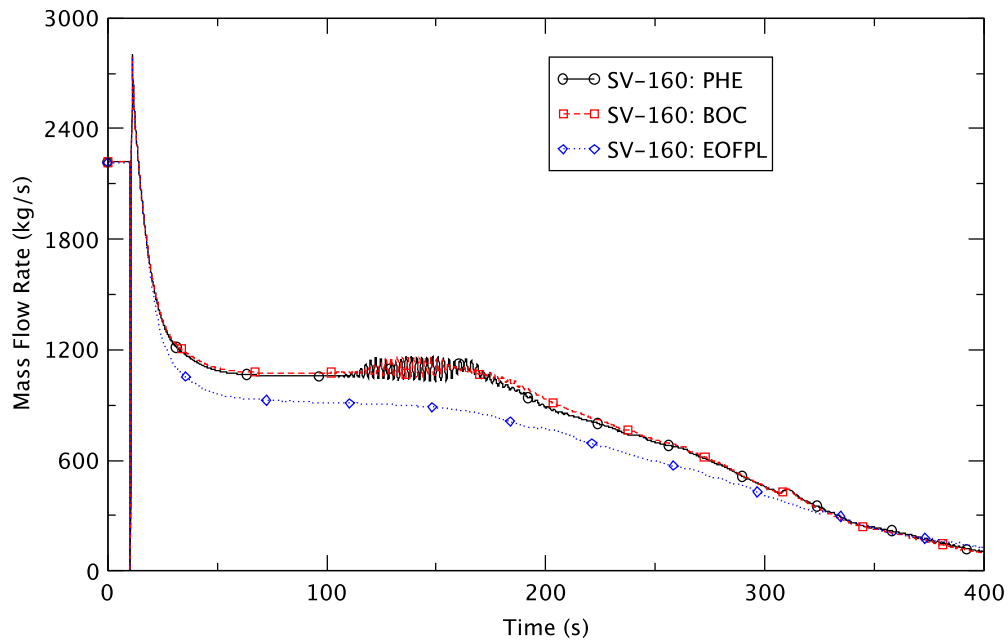


Figure 4.39 Steam Mass Flow Rate in Steamline - Effect of Time in Cycle

4.4.5 Core Power

Figure 4.40 shows reactor core power for each case. The PHE and BOC cases exhibit similar behavior except for the amplitudes and contour of the power oscillations. Very different behavior, however, is evident in the EOFPL case where the power is low compared to the average power in the PHE and BOC cases. While power oscillations are predicted in the latter cases, the reactor is stable in the EOFPL case as shown in Figure 4.41 through Figure 4.43 (power for each case) as well as in Figure 4.40.

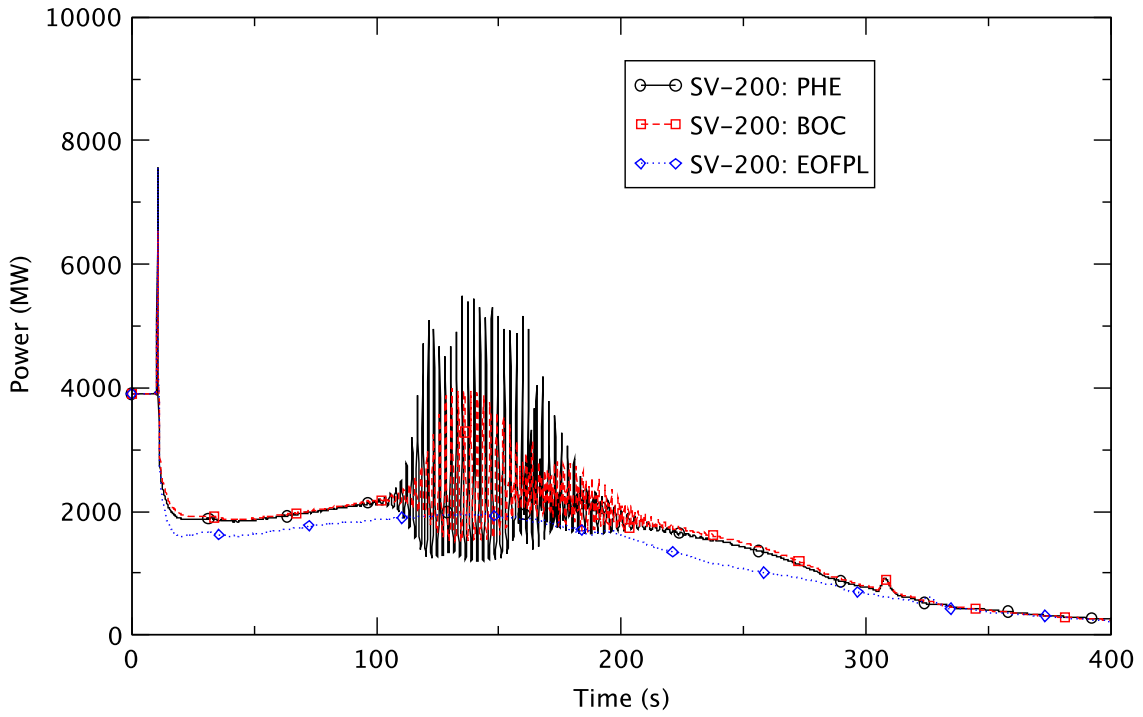


Figure 4.40 Reactor Core Power - Effect of Time in Cycle

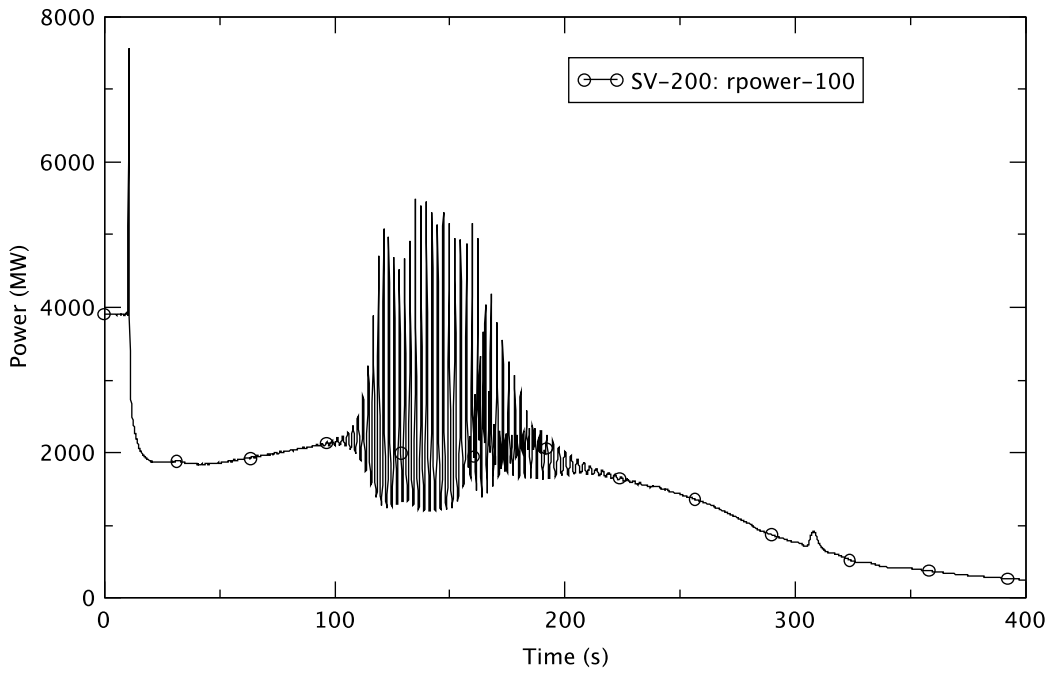


Figure 4.41 Reactor Core Power at PHE (Case 2)

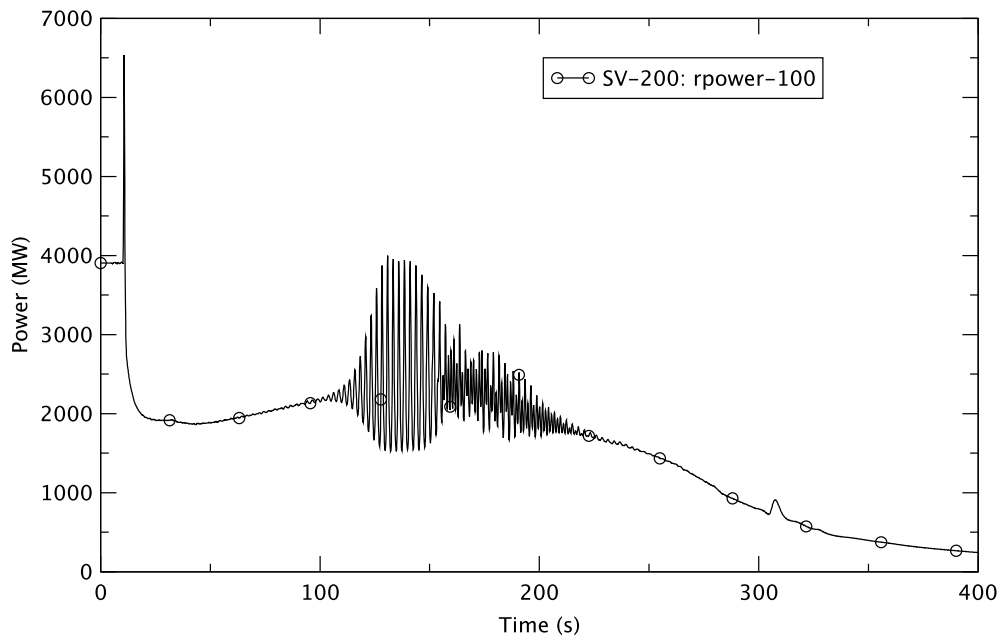


Figure 4.42 Reactor Core Power at BOC (Case 1)

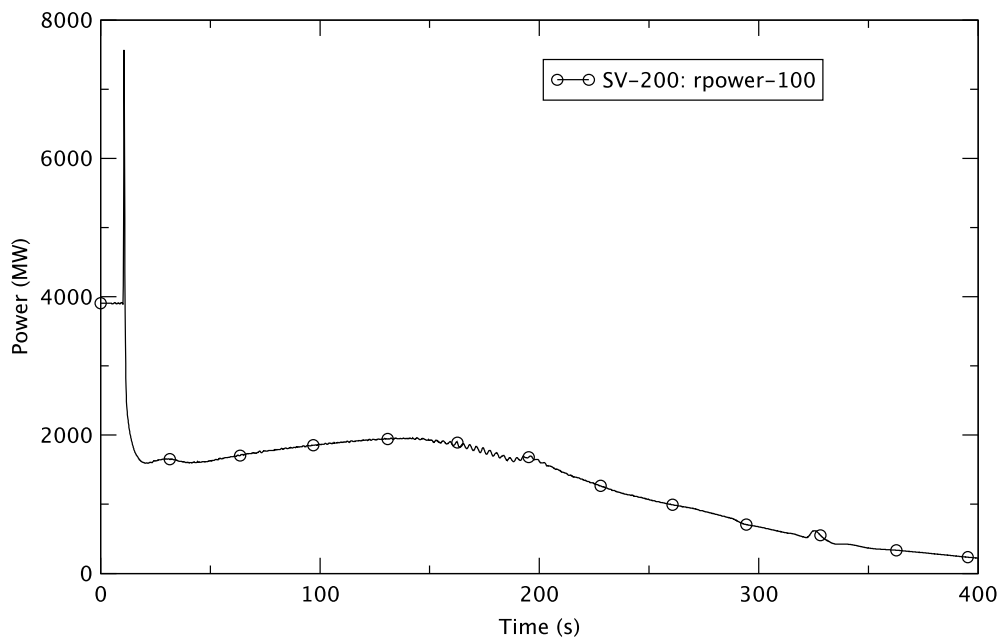


Figure 4.43 Reactor Core Power at EOFPL (Case 3)

The reason for the lower power at EOFPL is that a relatively large negative void reactivity is introduced from around 20 s to 330 s (Figure 4.44), because of the smaller core flow compared

to the initial value. At the EOFPL, the steady-state core power has an axially top-peaked shape whereas it is bottom-peaked in the other cases (Figure 4.45). The combined effect of low core power, top-peaked power shape, and smaller core inlet subcooling (see Section 4.4.8) results in the stable reactor condition and the core power does not oscillate at EOFPL, as shown in Figure 4.43.

As shown in Figure 4.40 through Figure 4.42, TRACE predicts power oscillations at PHE and BOC; in general, the amplitude is larger in the former state. From this observation, we deduce that the PHE condition engenders the most unstable reactor condition among the three simulated points in the fuel cycle.

While both PHE and BOC initially show core-wide oscillations (see top of Figure 4.46 and Figure 4.47), the contours of the oscillations in the non-linear bi-modal stage (after around 144 s for both) are very different. Figure 4.46 shows that for PHE the first harmonic (first azimuthal mode) is excited, while the BOC (Figure 4.47) exhibits higher harmonic excitation (third and higher azimuthal modes).

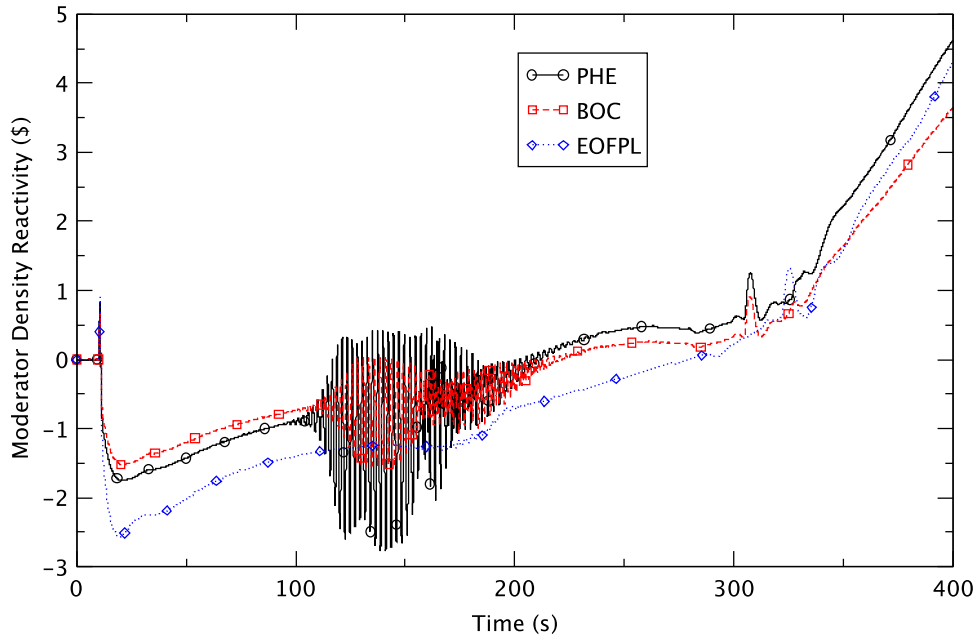


Figure 4.44 Comparison of Void Reactivity - Effect of Time in Cycle

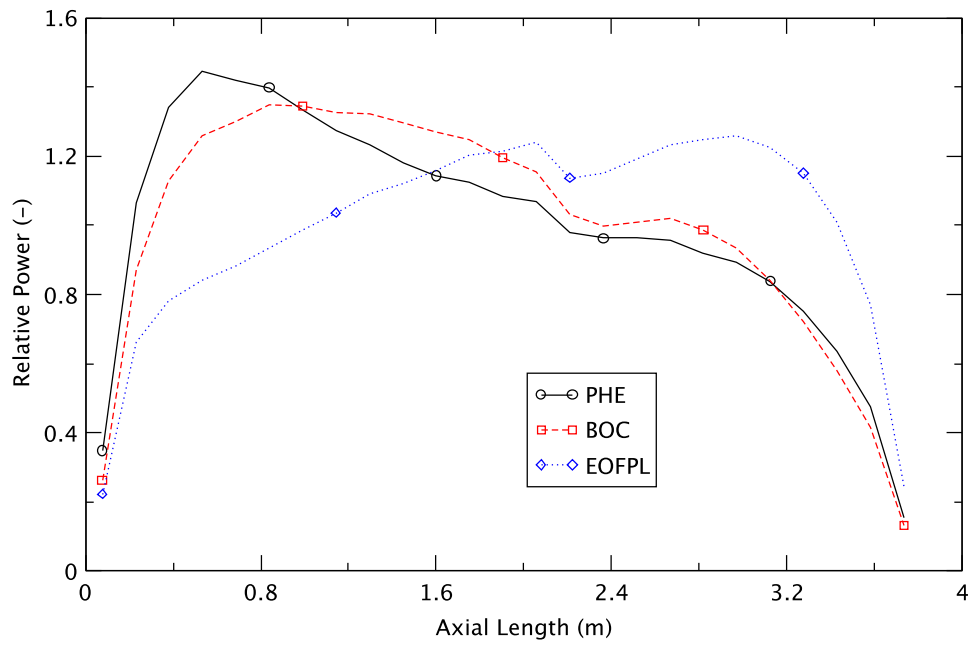


Figure 4.45 Relative Power at Steady-State - Effect of Time in Cycle

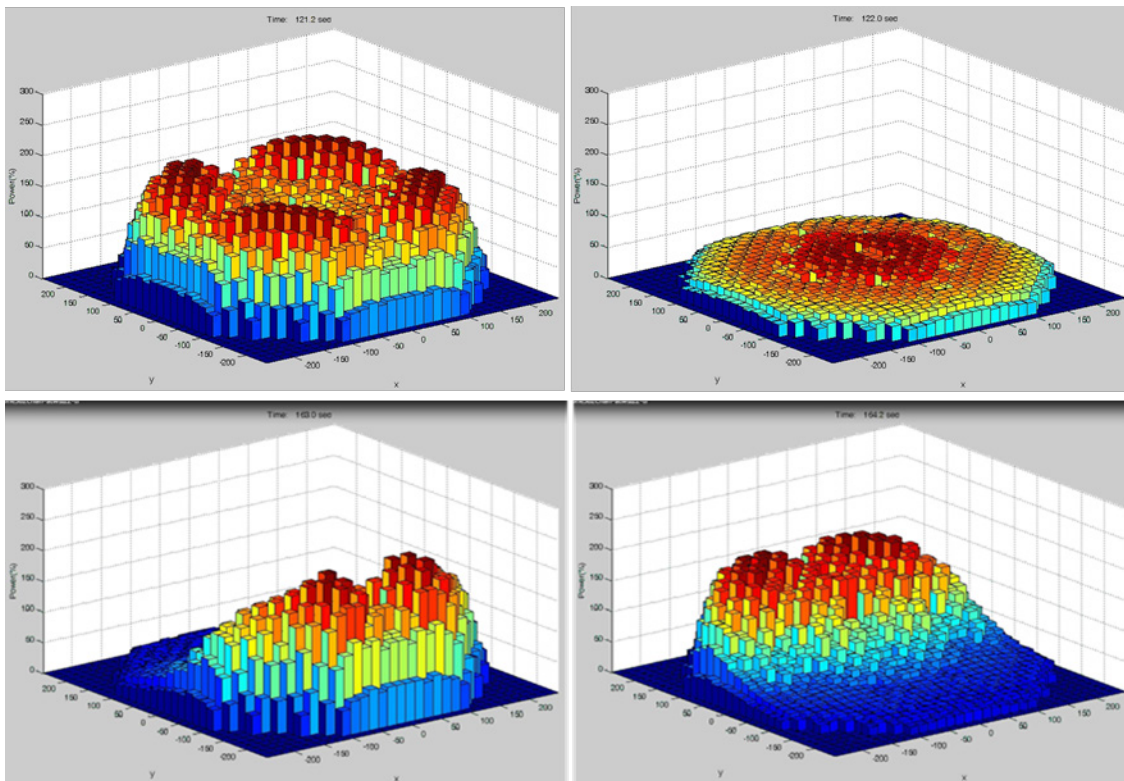


Figure 4.46 Oscillation Contour Showing First Harmonic Excitation for PHE

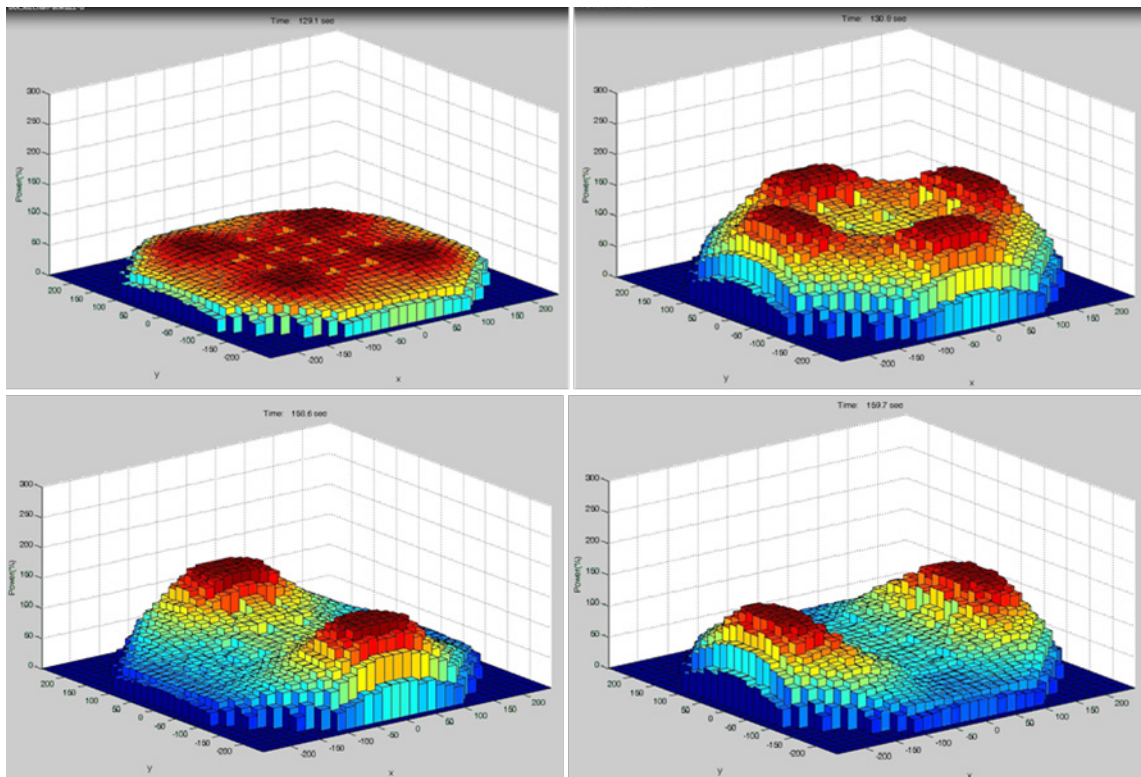


Figure 4.47 Oscillation Contour Showing the Fundamental Mode (Top) and Higher Harmonic Excitation (Bottom) for BOC

Most parameters affecting reactor instability, such as system pressure, core flow, and inlet subcooling, as well as the figure-of-merit for stability, defined as the product of power-peaking factor and power divided by the product of inlet flow rate and enthalpy, $\frac{P_{xyz} \cdot Q}{F \cdot h_{inlet}}$, show very similar behavior in the PHE and BOC cases except that the initial shape of axial power is slightly different. Figure 4.45 compared the initial shapes of axial power, which are radially averaged. As depicted, the power is skewed more toward the bottom of the core at PHE than at BOC, and hence, contributes to the more severe reactor instability in the former.

The general behavior of system pressure is similar to that of the core power (Figure 4.28). The RPV dome pressure is slightly lower at EOFPL than at PHE and BOC, from around 20 s to 300 s, because the core power is lower and less steam is produced in the former scenario.

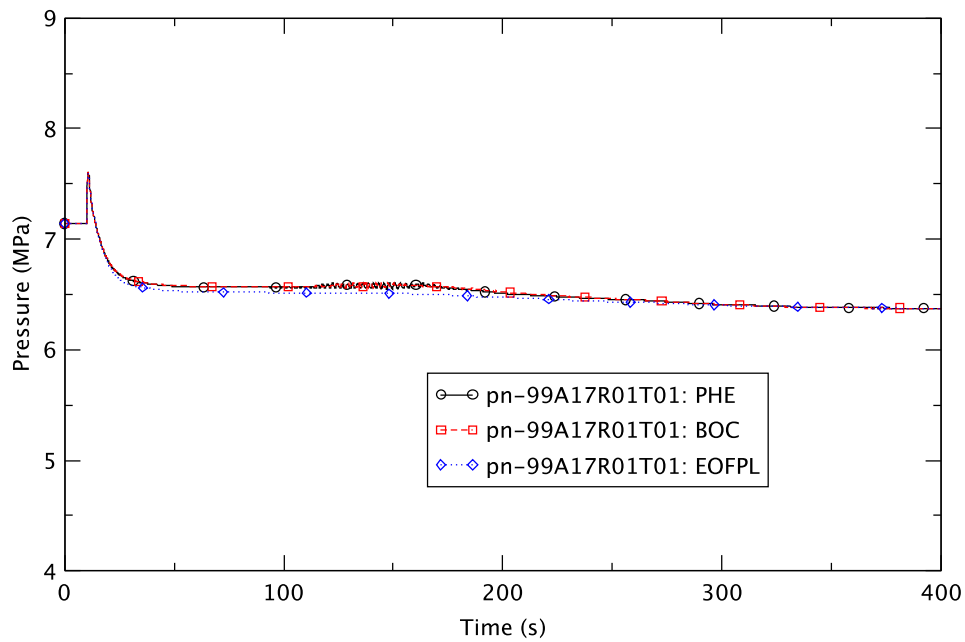


Figure 4.48 RPV Pressure - Effect of Time in Cycle

4.4.6 Core Flow

Core flow rates are compared in Figure 4.49. Initially, the core flow is 105% of normal flow in the EOFPL case, and 85% in the PHE and BOC cases as shown in this figure, and in the fourth column of Table 4.7. As the recirculation pumps coast down from 10 s, the general behavior of the core flow becomes very similar in all cases because it is determined mostly by the difference in the gravity head between the core and downcomer as natural circulation is being established. As Figure 4.49 shows, the flow is slightly larger at EOFPL during the coast-down of the recirculation pump (from about 10 s to 40 s); it seems to be caused by an initially higher pump speed.

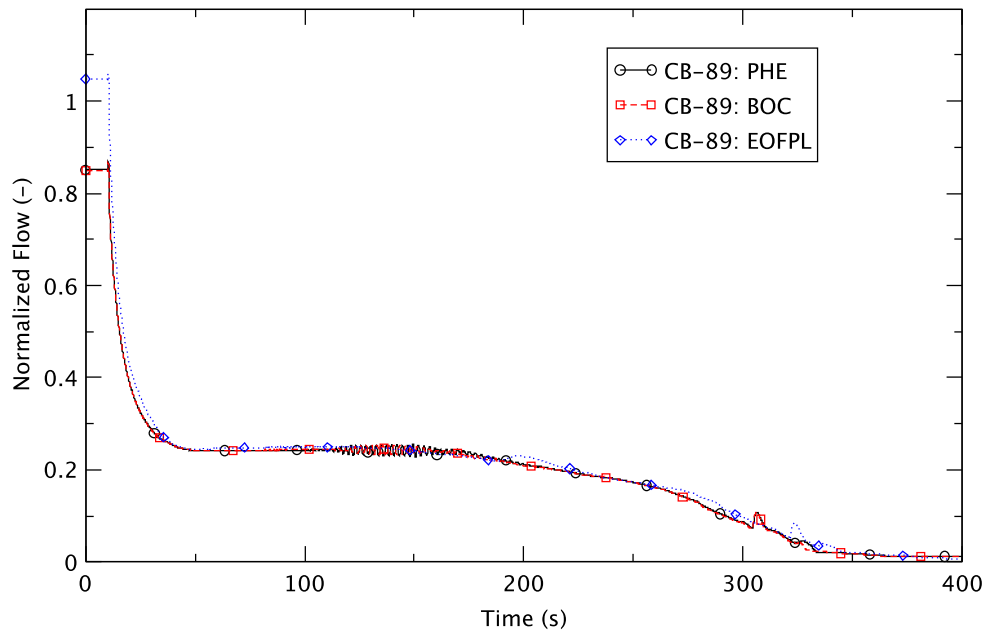


Figure 4.49 Reactor Core Flow Rate - Effect of Time in Cycle

The operator action of reducing the water level to TAF was simulated at 120 s by reducing the feedwater flow to decrease the mass flow into the core. Figure 4.50 compares the rates of flow of the feedwater. As expected, they start decreasing more rapidly after 120 s in all cases. The comparison shows that TRACE predicts smaller FW flow at EOFPL from approximately 20 s because the steam flow rate is smaller (Figure 4.39) and the FW controller tries to match the FW flow with the steam flow so to maintain the DC water level until 120 s, and then the FW flow starts further decreasing. It becomes zero at around 235 s at EOFPL, at 259 s at PHE, and at 262 s at BOC. From those times onward, water flows into the vessel only from the RCIC, and while the FW restarts flowing around 364 s at BOC, and 365 s at PHE, there is no FW flow after it becomes zero at EOFPL.

Figure 4.51 compares the DC water level. The general behavior is similar in all cases. The level does not drop for a relatively long time (about 30 s to 45 s) after the operator action at 120 s. In general, it is slightly higher at EOFPL than at PHE and BOC because in the EOFPL case almost the same or a slightly larger amount of water flows into the core (Figure 4.49) but less steam is produced (Figure 4.39), so more water returns to the DC. The relatively larger recirculation ratio (ratio of total core flow to steam flow) at EOFPL also contributes to a lower demand for feedwater flow and lower core inlet subcooling (Section 4.4.8) as compared to the BOC and PHE cases.

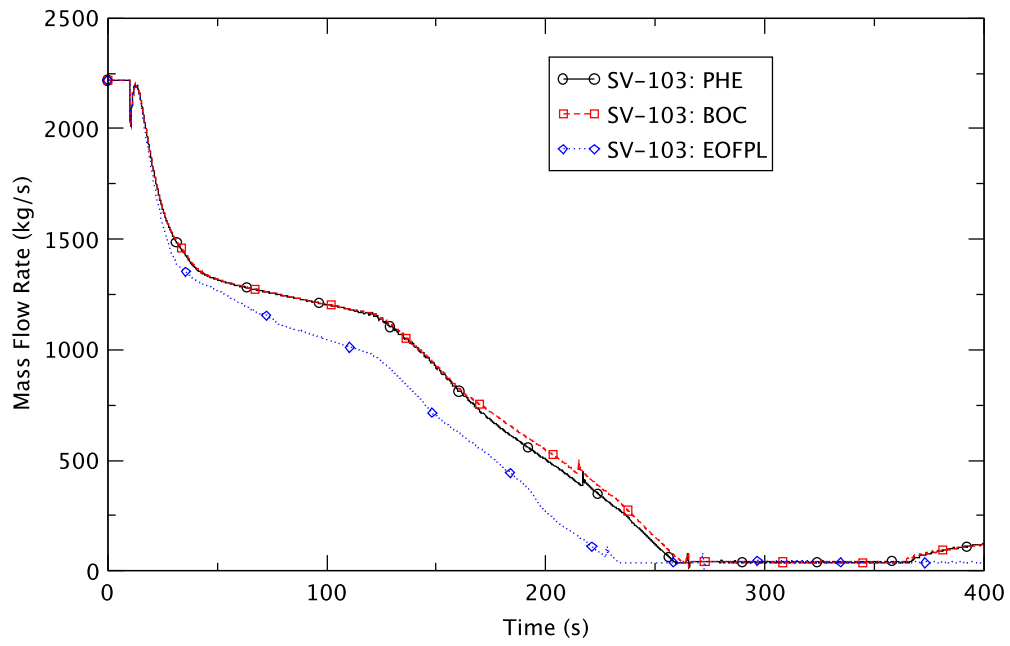


Figure 4.50 Feedwater Flow Rate - Effect of Time in Cycle

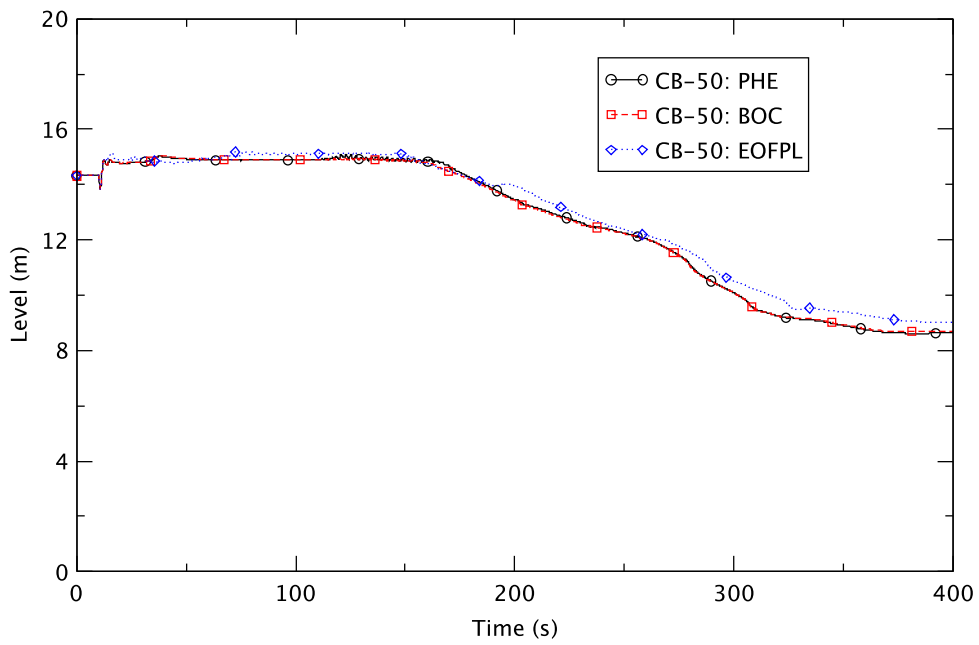


Figure 4.51 Downcomer Water Level - Effect of Time in Cycle

4.4.7 Boron Inventory in Core

The SLCS is initiated at 130 s. Figure 4.52 gives the boron inventory behavior in the core. Its general behavior is almost the same in all cases, especially until 240 s when the core power oscillations cease for the PHE and BOC cases. Hence, boron injection does not contribute to the differences between the cases at different times in the fuel cycle.

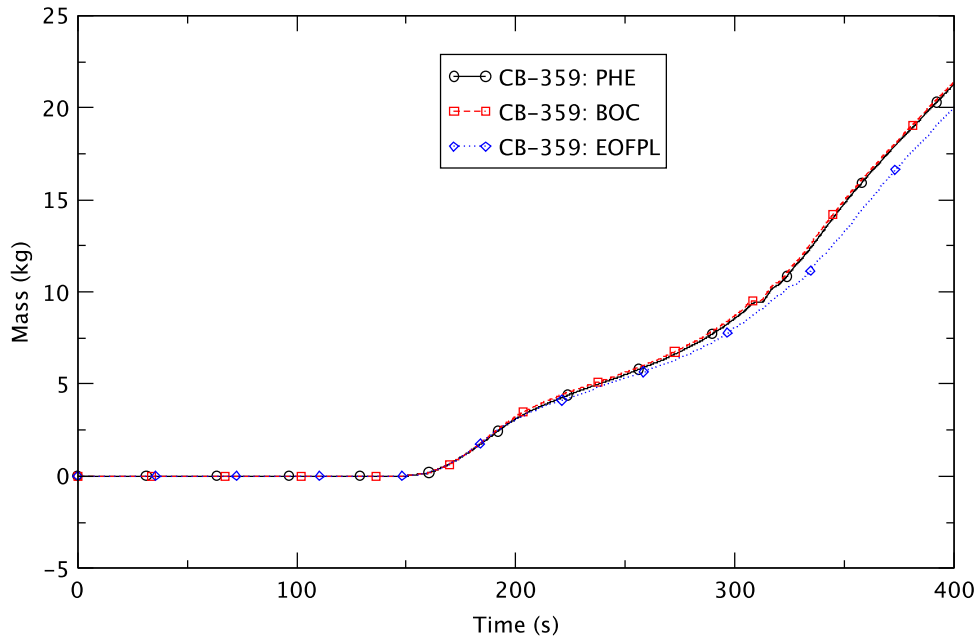


Figure 4.52 Boron Inventory in Reactor Core - Effect of Time in Cycle

4.4.8 Core Inlet Subcooling

Figure 4.53 shows subcooling of the core inlet in ring 1. The general behavior of subcooling is discussed in Section 4.2.4. As the figure shows, subcooling for EOFPL is less for the steady-state and during the transient relative to PHE and BOC. The former, at EOFPL during steady-state, is caused by the large core flow (Figure 4.49) with almost the same amount of steam produced (see Figure 4.39) and the same FW flow (Figure 4.50). This signifies that more hot water returns to the DC from the separators and is mixed with the colder FW, so resulting in smaller subcooling in the DC and at the core inlet in the EOFPL case.

The smaller subcooling during the transient period rests on the fact that the core flow is almost the same for all three cycle times (Figure 4.49) but the steam flow and FW flow are relatively smaller at EOFPL compared to BOC or PHE (see Figure 4.39 and Figure 4.50). Therefore, subcooling is lower at EOFPL since the mixture of the FW and the return flow from the separator includes relatively less feed.

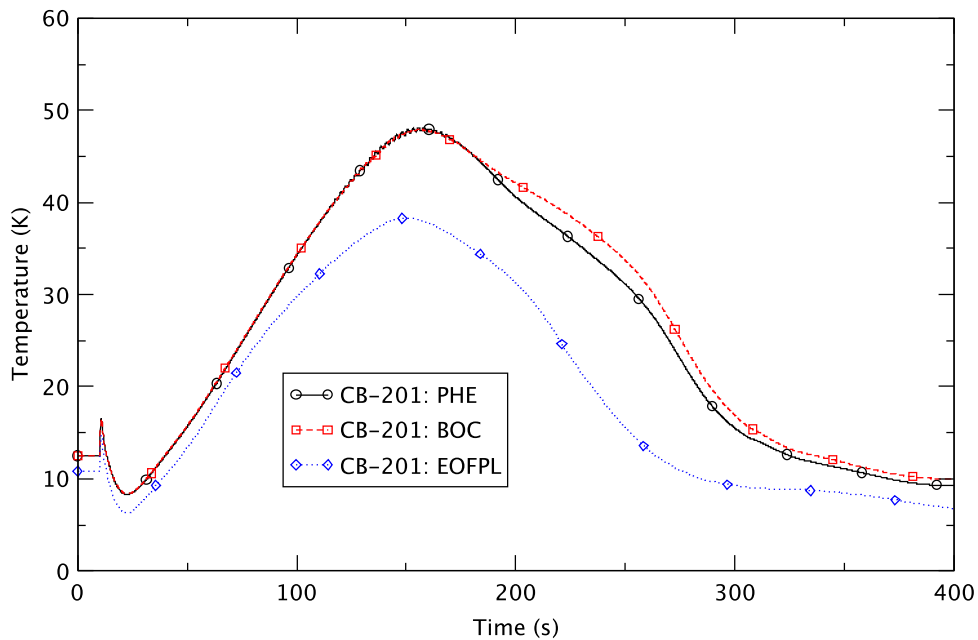


Figure 4.53 Core Inlet Subcooling - Effect of Time in Cycle

Figure 4.53 shows that liquid subcooling becomes slightly larger at BOC than at PHE from about 182 s. This reflects a slightly larger steam flow from around 174 s (Figure 4.39) and the FW flow from about 154 s (see Figure 4.50) at BOC. A lesser amount of hot water returns to the DC and is mixed with more of the colder FW, causing more subcooling in the DC and at the core inlet at BOC than at PHE. This effect is evident in the core power prediction (See Figure 4.40). From around 184 s, the average core power becomes slightly larger in the BOC case than in the PHE case.

From this observation, we consider that the smaller liquid subcooling at the core inlet contributes to the stable reactor condition at EOFPL, while the larger subcooling seems to be one of the reasons for the reactor's instability in the PHE and BOC cases.

4.4.9 Fuel Cladding Temperature

The core power oscillations can affect the temperature of the fuel cladding due to the changes in the power and the efficiency of heat transfer from the fuel to the coolant because of the continuous change of void fraction in the core. The maximum cladding temperature among all bundles in the core is compared in Figure 4.54. It suddenly increases from 122 s at PHE, and 134 s at BOC while it remains almost constant at EOFPL. This observation confirms that if the reactor becomes unstable and the core power oscillates, cladding temperature will increase significantly during the unstable period, while, in contrast, there is no noticeable increase of cladding temperature when the reactor is stable.

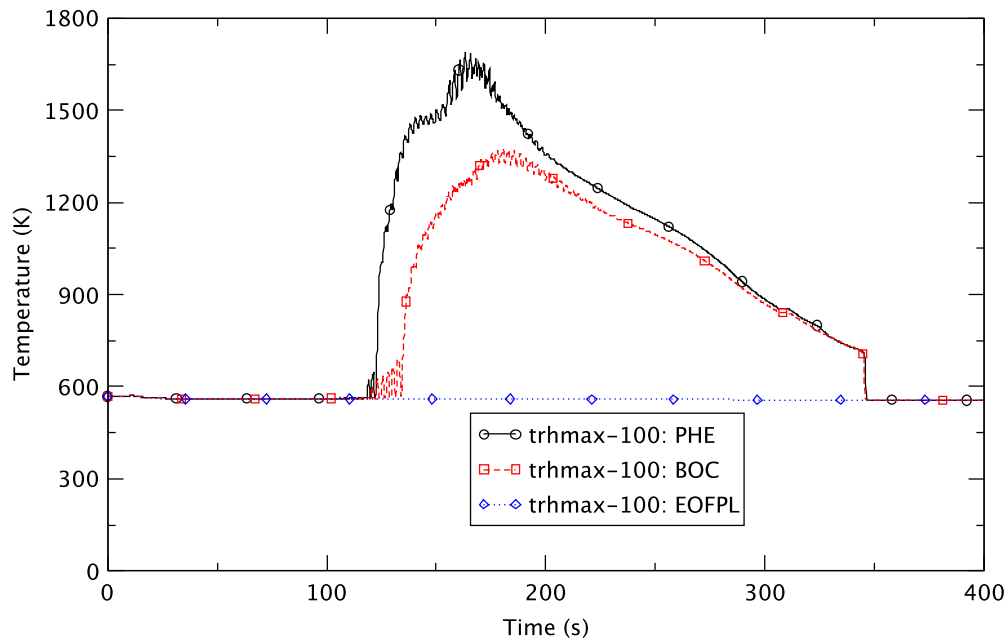


Figure 4.54 Maximum Cladding Temperature in Core - Effect of Time in Cycle

The highest peak cladding temperatures of 1,691 K and 1,373 K occur at approximately 163 s at PHE and 181 s at BOC. For PHE, the cladding temperature becomes higher than its limit of 1,478 K (2,200°F) [32]. These observations imply that at PHE the reactor is the most unstable in terms of peak cladding temperature and the amplitude of power oscillation, while at BOC it is in an intermediate state, and at EOFPL it is stable.

4.4.10 Summary

TRACE predicts that the reactor is most unstable at PHE, intermediately unstable at BOC, and stable at EOFPL. The difference in the degree of instability seems caused by the difference in the initial shapes of the axial power (most bottom-peaked at PHE and top-peaked at EOFPL) and relative rates of core flow. The relative core flow at EOFPL becomes the smallest during the transient, engendering a very large negative void reactivity and a stable reactor configuration.

The operator actions do not seem to impact the reactor's instability differently for the three cycle times we considered. The general behavior of the boron inventory is almost the same in all cases, especially until 240 s when core power oscillations are over. The behavior of the downcomer water levels is also similar in all cases.

The smaller liquid subcooling at the core inlet contributes to the stable reactor condition at EOFPL, while the larger subcooling seems to be one of the reasons for the reactor's instability in the PHE and BOC cases.

4.5 Effect of Void History Modeling

4.5.1 Void History Modeling

To understand the effect of including spectral history in the void history, we consider two cases: PHE with void history (UH) and no spectral history correction (Case 2), and PHE with void history having a spectral history correction (UHSPH) (Case 2G). An explanation of the difference between UH and UHSPH is presented in Section 3.2.5. Both cases have 100% turbine bypass capacity. The TSV is closed in 0.1 s on a turbine trip at 10 s into the simulation time and then opens in 1.0 s to simulate the bypass paths with 100% turbine bypass. Table 4.10 shows the simulation conditions.

Table 4.10 Simulation Conditions - Effect of Void History

Case ID	Exposure	Power, %	Core Flow Rate, %	Bypass Capacity, %	Void History ¹
2	PHE	100	85	100	UH
2G	PHE	100	85	100	UHSPH

¹ UH and UHSPH stand, respectively, for void history and spectrally corrected void history.

4.5.2 Initial Conditions

Predicted initial values of some key thermal-hydraulic parameters from the TRACE/PARCS null transient calculation up to 10 s are compared to the reference values in Table 4.11. As is evident, the calculated steady-state values agree well with the reference ones.

Table 4.11 Comparison of Steady-State Thermal-Hydraulic Parameters - Effect of Void History

Parameter	PHE with UH (Case 2)		PHE with UHSPH (Case 2G)	
	Diff.	Diff. (%)	Diff.	Diff. (%)
Core Power (MWt)	0	0.00	0	0.00
Steam Dome Pressure (kPa)	5	0.07	5	0.07
Main Steamline Flow (kg/s)	-4	-0.2	-4	-0.2
Total Core Flow (kg/s)	10	0.09	10	0.09
Feedwater Flow (kg/s)	-4	-0.2	-4	-0.2
Feedwater Temperature (K)	0	0.00	0	0.00
Downcomer Level (m)	-0.1	-1.	-0.1	-1.

4.5.3 Sequence of Events

The timing of the sequence of events is generally similar for both cases. Table 4.12 shows the time sequence for the events; details about system behavior are presented in the following sections. We note in the table where the sequence differs for different cases.

Table 4.12 Sequence of Events - Effect of Void History

Time (s)	Event
0.0	<ul style="list-style-type: none"> Null transient simulation starts.
10.0	<ul style="list-style-type: none"> Null transient simulation ends. Turbine trip is initiated by closing the TSV. Recirculation pumps are tripped on the turbine trip. Feedwater temperature starts decreasing.
10.1	<ul style="list-style-type: none"> TSV closes completely and starts opening again to simulate 100% turbine bypass flow.
11.1	<ul style="list-style-type: none"> TSV (bypass) completes opening and its open area provides the predetermined steam flow fraction of 100%.
~11.4	<ul style="list-style-type: none"> Steam flow starts decreasing.
~12.3	<ul style="list-style-type: none"> Feedwater flow starts decreasing.
~95	<ul style="list-style-type: none"> Power oscillation above noise level apparent (instability onset).
120	<ul style="list-style-type: none"> Water level reduction is initiated by reducing the normal water level control system setpoint linearly to TAF over 180 s.
130	<ul style="list-style-type: none"> Boron injection is initiated and linearly ramped to full flow at 190 s.
~144	<ul style="list-style-type: none"> Noticeable bi-modal oscillation of the core power is initiated: <ul style="list-style-type: none"> ○ Fundamental to first harmonic for UH ○ Fundamental to higher harmonic for UHSPH
~160	<ul style="list-style-type: none"> Boron starts accumulating in the core.
~163	<ul style="list-style-type: none"> Downcomer water level begins decreasing in Case 2. Peak cladding temperature of ~1,691 K occurs in Case 2. ~1,606 K at 175 s in Case 2G.
~164	<ul style="list-style-type: none"> Downcomer water level begins decreasing in Case 2G.
~170	<ul style="list-style-type: none"> Higher harmonic to first harmonic transition for UHSPH.
~240	<ul style="list-style-type: none"> Power oscillation ends.
400	<ul style="list-style-type: none"> Simulation ends.

4.5.4 Steamline Flow

Figure 4.55 compares the steamline flow rates for the two cases; the behavior is almost identical in each. However, closer observation of Figure 4.55 reveals that the steam flow is almost the same until around 155 s, from then till 172 s it is slightly higher in the UH case than in the UHSPH case, then slightly higher in the latter than in the former until about 210 s; thereafter, both are the same. This behavior is strongly related to core power. Specifically, the magnitude of steam flow is higher when average core power is higher. The core power is discussed in the following section.

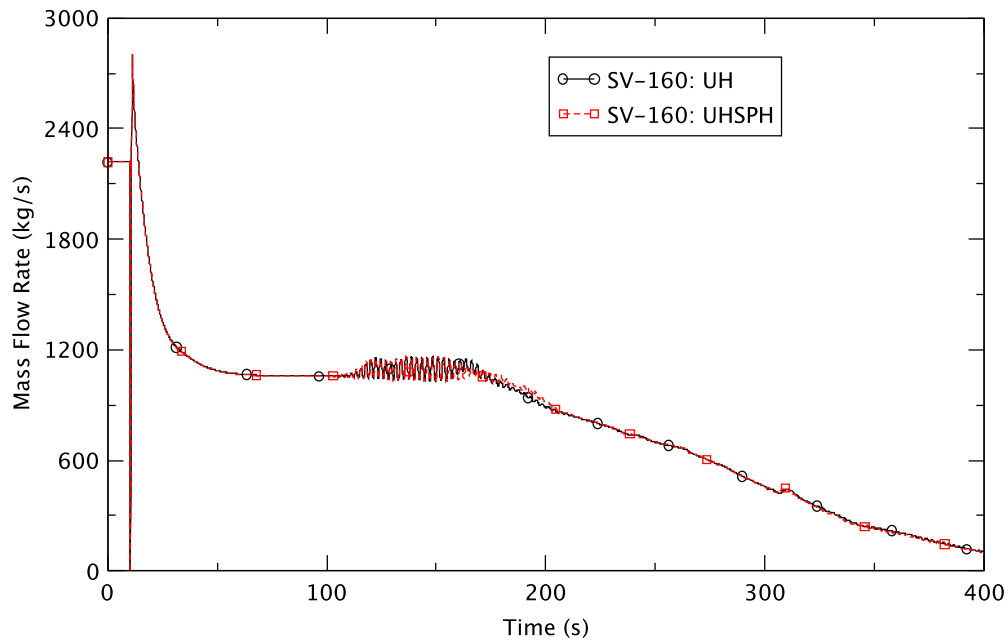


Figure 4.55 Steam Mass Flow Rates in Steamline - Effect of Void History

4.5.5 Core Power

Figure 4.56 compares reactor core power. The UH and UHSPH cases show very similar general behavior. Figure 4.57 depicts the core power in a narrow range. As shown, the amplitude of the power oscillation and the average power become higher in the UH case than in the UHSPH case from approximately 152 s to 173 s; then, they are higher in the latter case until about 210 s. For other periods, the power behavior is almost the same.

It is difficult to pinpoint the reason for the difference in the amplitudes of the power oscillations from 155 s to 210 s. The important parameters affecting reactor instability, such as core flow, system pressure, boron concentration, and core inlet subcooling show very similar or almost identical behavior. But the differences, although subtle, are sufficient to impact the evolution of the axially averaged bundle power shown in the movies prepared from PARCS output. For both cases, the power oscillations initially are core-wide, and around 144 s evolve into a bimodal mode with both a core-wide component and a regional one. But, for the UH case, the oscillation contour shows an excitation of the first harmonic (Figure 4.6 and Figure 4.7 in Section 4.2), while for the UHSPH case a higher harmonic mode is observed (Figure 4.58) until around 170 s, when it decays to the first harmonic (Figure 4.59). As mentioned earlier, however, the general behavior of the core power is very similar in both cases.

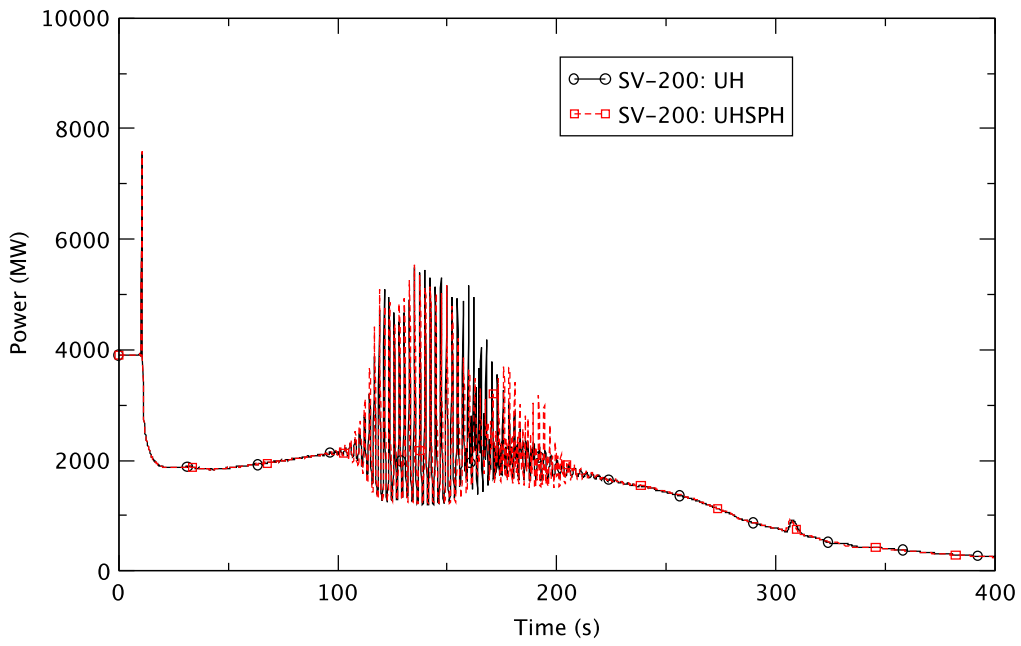


Figure 4.56 Reactor Core Power - Effect of Void History

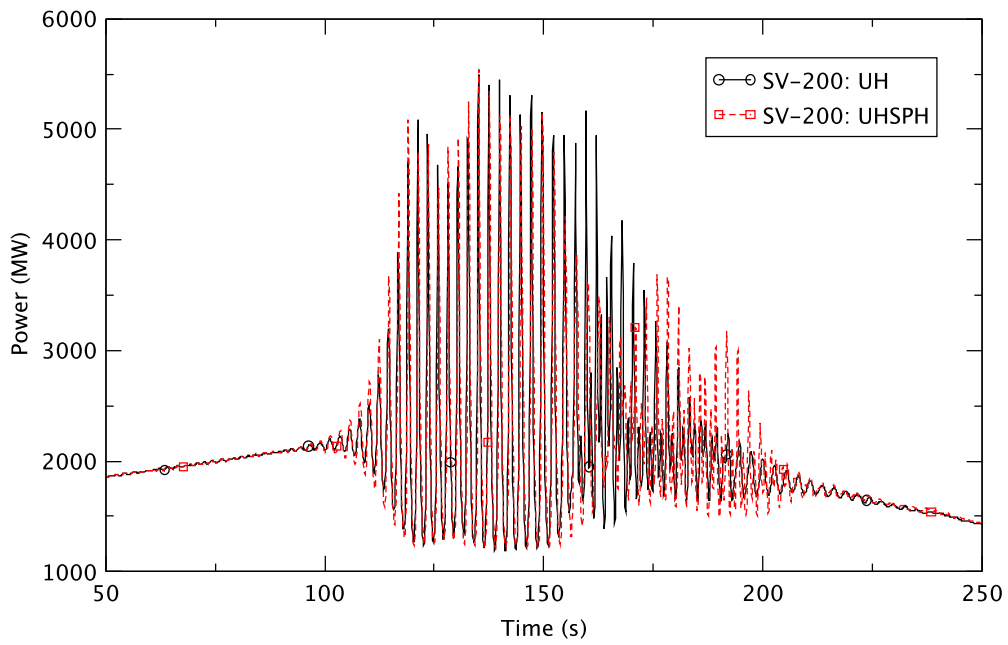


Figure 4.57 Core Power in a Narrow Range - Effect of Void History

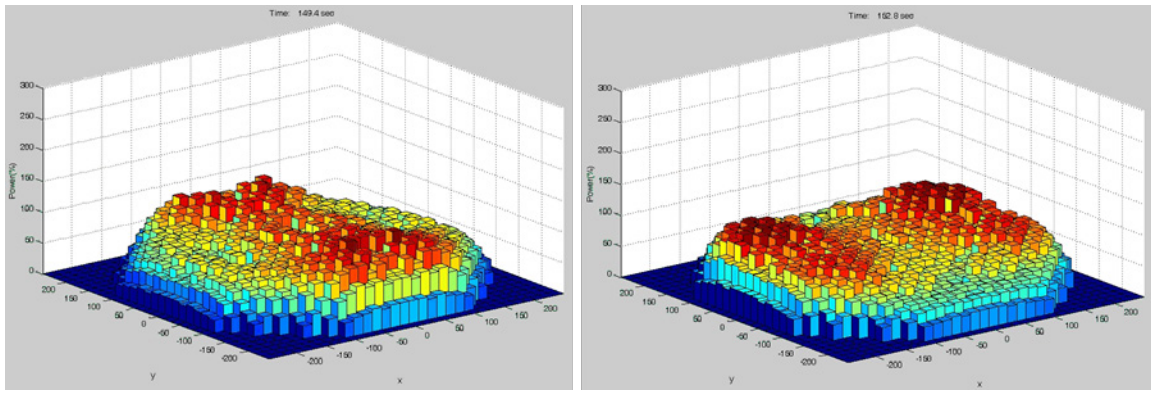


Figure 4.58 Example of Non-Linear Oscillation Contour Showing Higher Harmonic Mode - PHE, UHSPH Void History

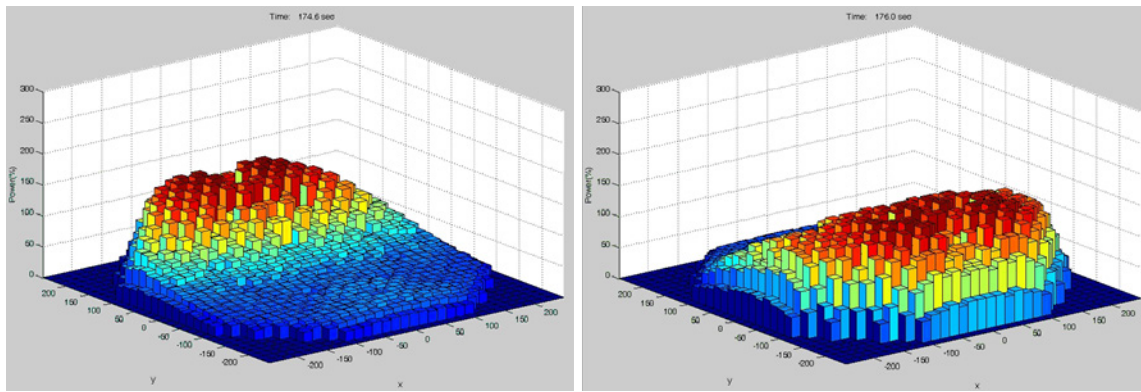


Figure 4.59 Example of Non-Linear Oscillation Contour Showing First Harmonic Mode - PHE, UHSPH Void History

The general system pressure behavior is very similar in each case (Figure 4.60). A close examination illustrates that the pressure is slightly higher for the UH case than for UHSPH from around 155 s to 172 s, and then higher in the latter until about 210 s, although the difference between them is almost negligible.

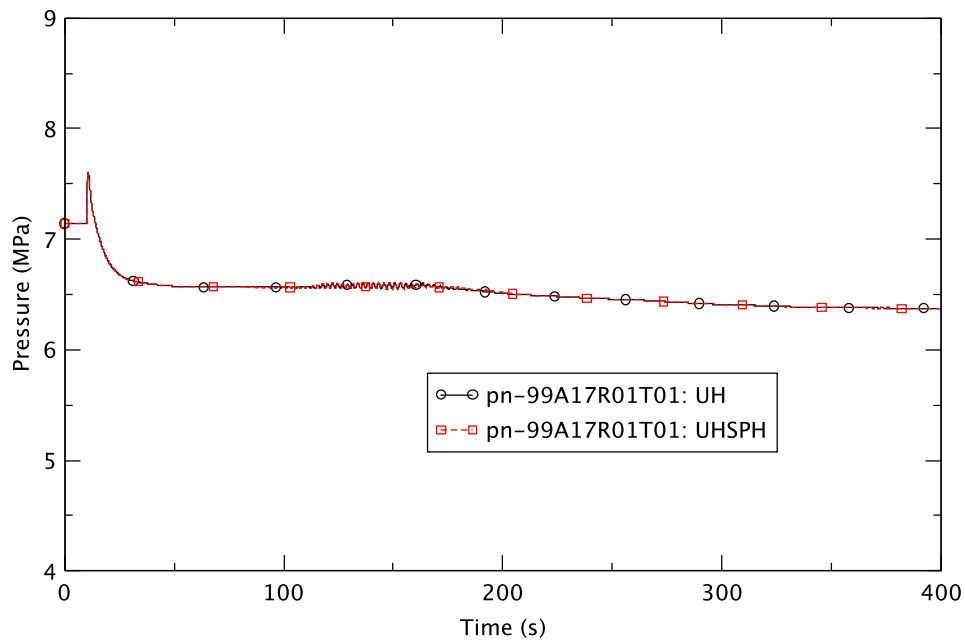


Figure 4.60 RPV Pressure - Effect of Void History

4.5.6 Core Flow

Core flow rates are compared in Figure 4.61. Their behavior basically is identical. This is because, under two-phase natural circulation, the rate of core flow is quite insensitive to the changes in the reactor's power level (Figure 1.3 illustrates the natural circulation line on the power/flow map of a typical BWR/5). Our study suggests that the sensitivity of the core flow rate to the exposure history has little bearing on the overall effect of void history on the reactor's stability characteristics.

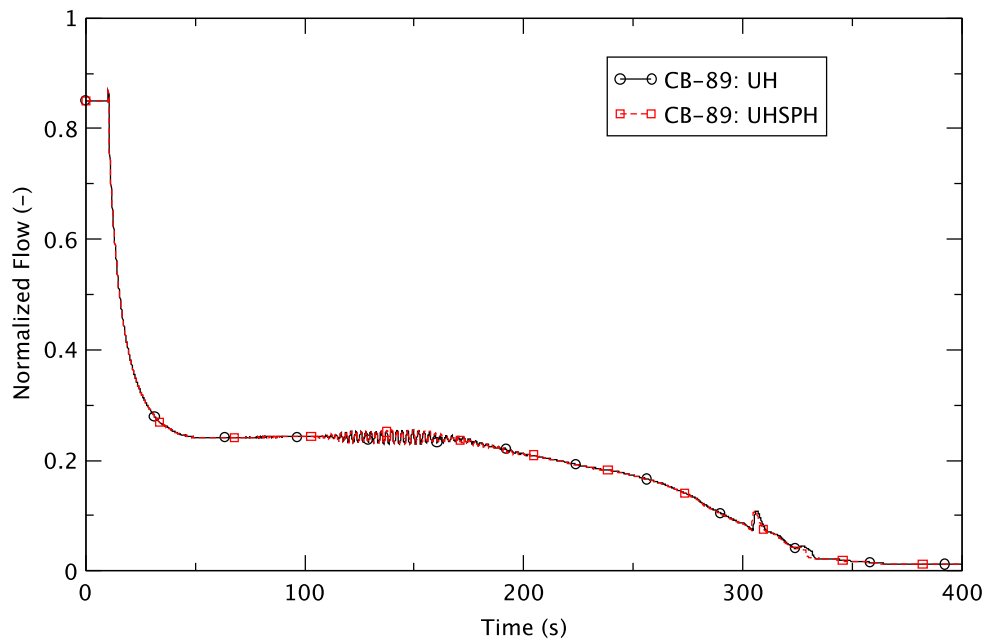


Figure 4.61 Reactor Core Flow Rate - Effect of Void History

The operator's action for reducing the water level to TAF is simulated at 120 s by lowering the feedwater flow to decrease the mass flow into the core. Figure 4.62 compares the feedwater flow rates. As expected, the rates start decreasing faster from 120 s in both cases; also, the behavior of the FW water flow is almost identical. In both cases, the FW flow becomes zero at around 259 s. At that point only water from the RCIC flows into the vessel until the FW starts flowing again at about 365 s.

Figure 4.63 compares the behavior of DC water level. For both, the general pattern is almost identical and it causes identical behavior of the core flow, especially after natural circulation is established (Figure 4.61). As discussed in previous sections, the DC level does not drop for about 43 s (a relatively long time) after the operator action at 120 s.

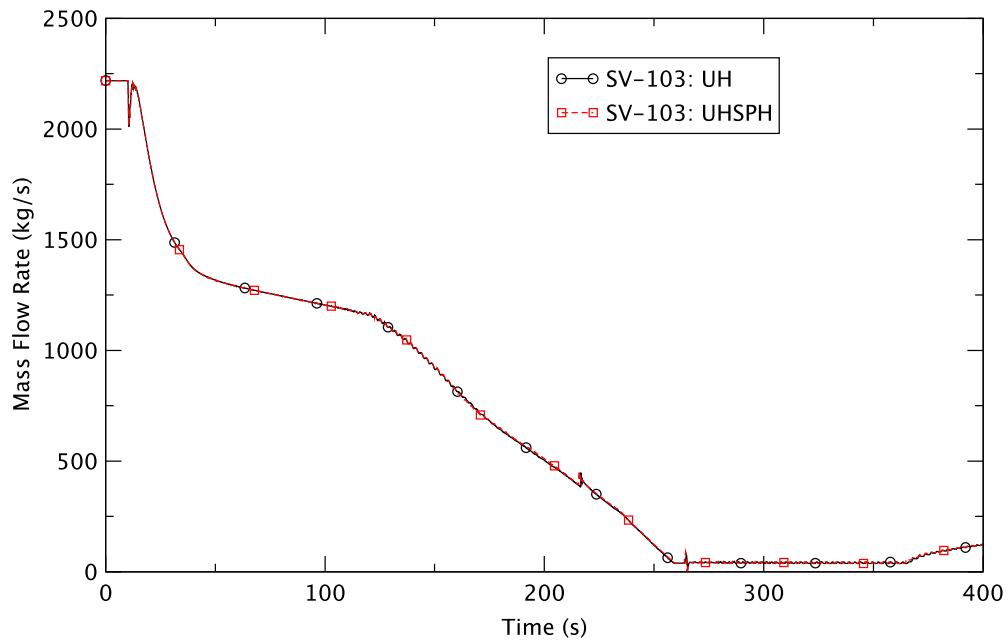


Figure 4.62 Feedwater Flow Rate - Effect of Void History

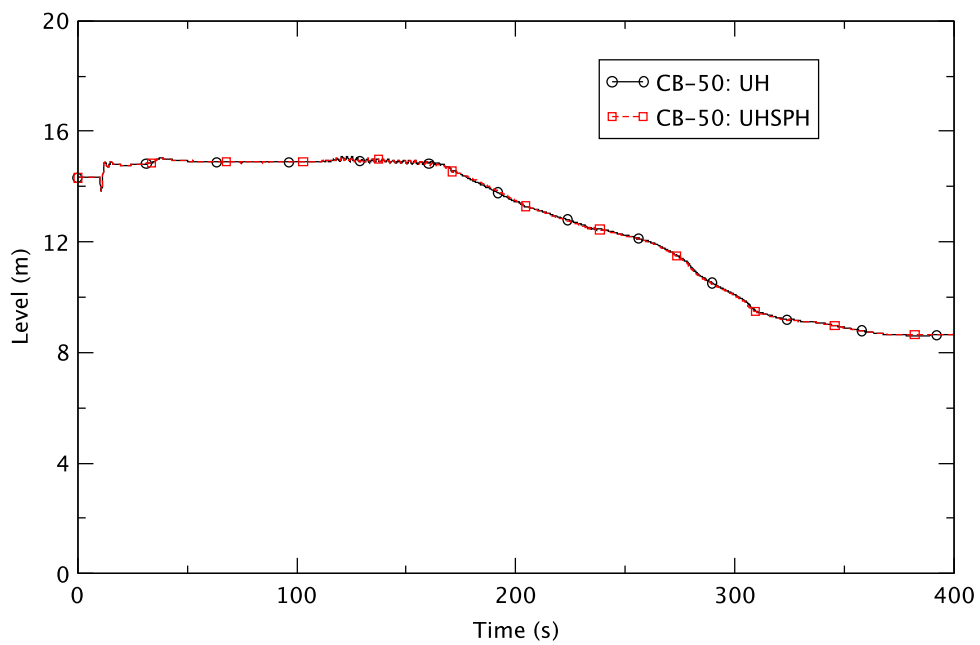


Figure 4.63 Downcomer Water Level - Effect of Void History

4.5.7 Boron Inventory in Core

SLCS is initiated at 130 s and Figure 4.64 compares the boron inventory in the core; it is the same in both cases. This means that the different modeling of void history does not affect the reactor's stability due to boron injection.

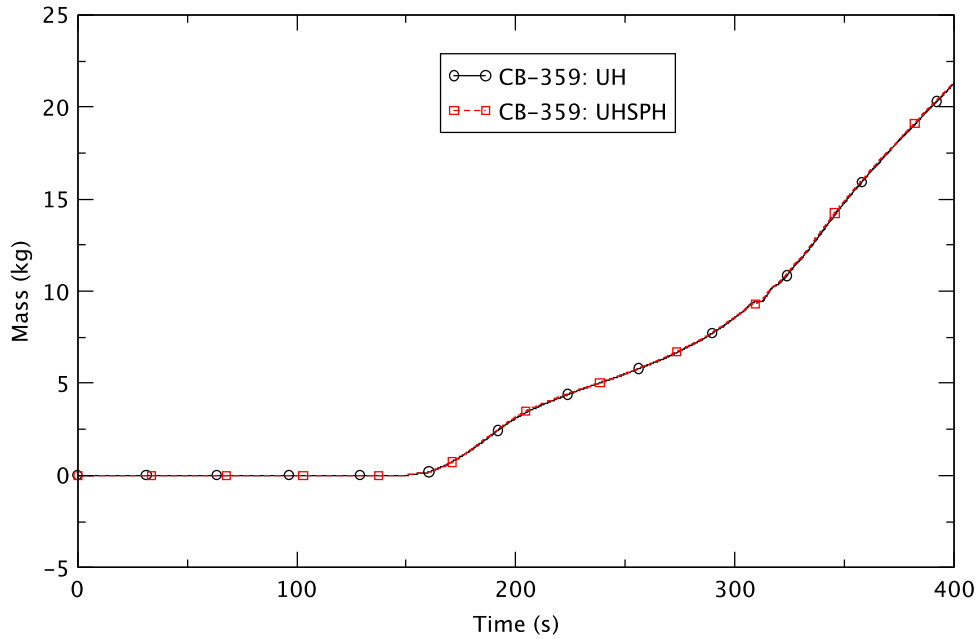


Figure 4.64 Boron Inventory in Core - Effect of Void History

4.5.8 Core Inlet Subcooling

Figure 4.65 shows the behavior of the core inlet subcooling in ring 1 that is almost identical in both cases, implying that the modeling of the void history does not significantly affect reactor stability due to inlet subcooling.

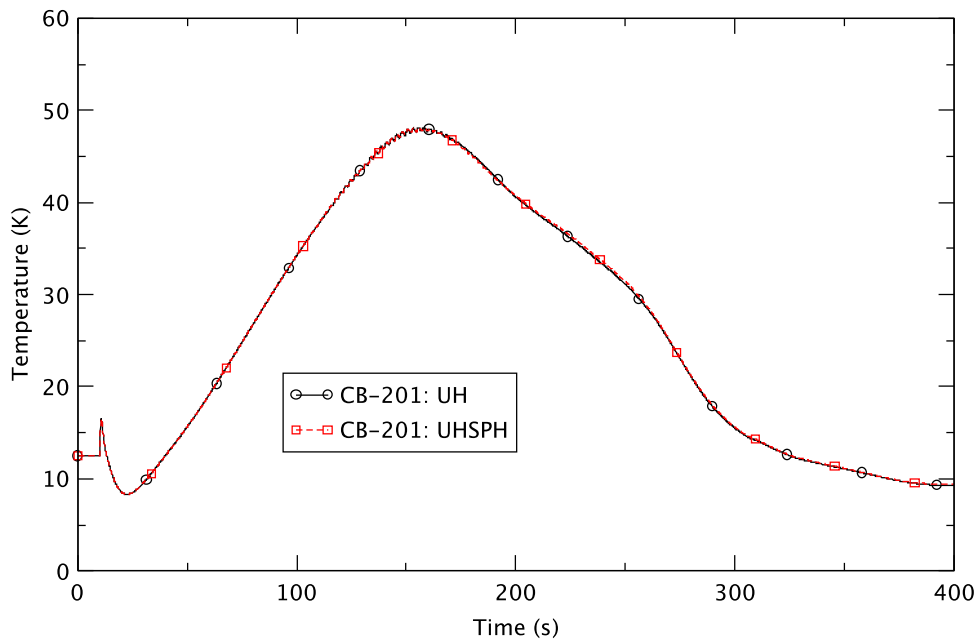


Figure 4.65 Core Inlet Subcooling - Effect of Void History

4.5.9 Fuel Cladding Temperature

The core power oscillations can affect the fuel cladding's temperature due to the changes in the power and efficiency of heat transfer from the fuel to coolant, because of the continuous change of the core's void fraction. Figure 4.66 compares the maximum cladding temperature among all bundles in the core. It suddenly increases around 122 s in both cases, and the increasing trend is almost identical until approximately 155 s. From that point, the rod temperature suddenly rises in the UH case, while it continues increasing gradually in the UHSPH case. From around 177 s, the cladding temperature becomes slightly higher in the UHSPH case than in the UH case until about 300 s.

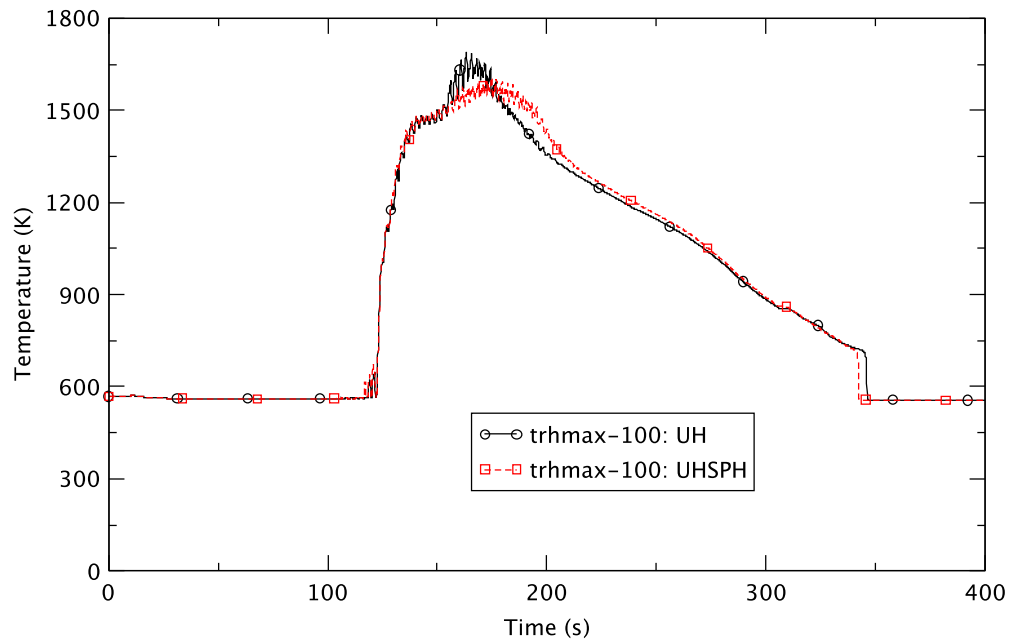


Figure 4.66 Maximum Cladding Temperature in Core - Effect of Void History

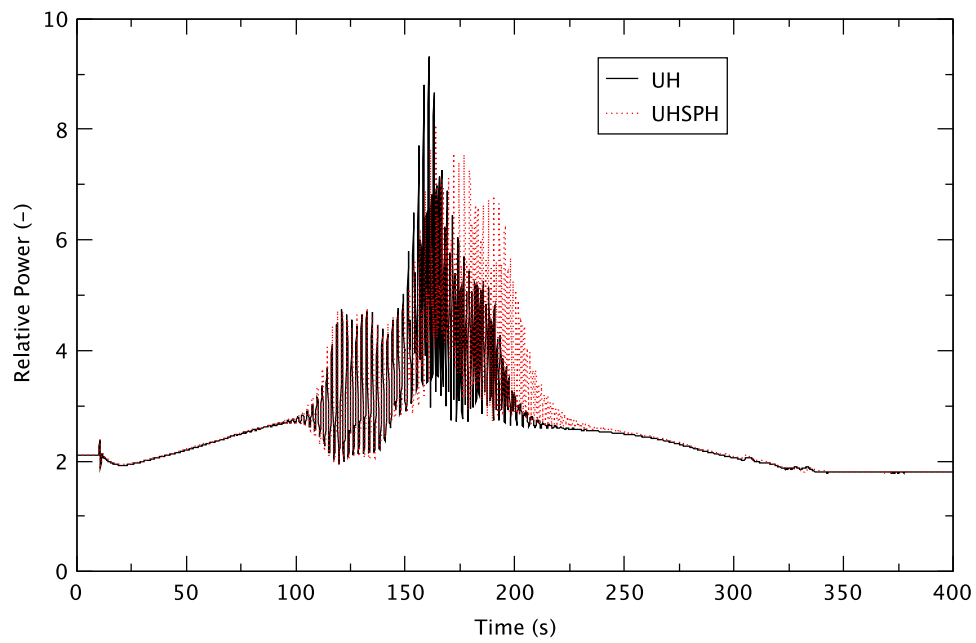


Figure 4.67 Local Peak Power for PHE Cases - Effect of Void History

The highest peak cladding temperatures of 1,691 K and 1,606 K are evident at approximately 163 s in the UH case and 175 s in the UHSPH case. In both cases, the cladding temperature becomes higher than its limit of 1,478 K (2,200 °F) [32]. The highest cladding temperature is closely related to the peak relative local power (and not the total power) shown in Figure 4.67. The relative local peak power for the UH case is around 9.3, while it is around 8.1 for the UHSPH case, which explains the lower peak clad temperature. The general behavior of the cladding temperature is similar in both cases.

4.5.10 Summary

The general behavior of the reactor core power is very similar at PHE with UH or UHSPH void history. However, the amplitude of the power oscillation and the average power become higher in the UH case than in the UHSPH case from approximately 152 s to 173 s and then they are higher in the latter until about 210 s. This difference is caused by a different evolution in the non-linear bi-modal stage, showing the excitation of the first harmonic mode for the former and of the higher harmonic(s) for the latter. This difference is reflected in the peak local power after bifurcation, which, in turn, impacts the peak cladding temperatures. The other behaviors including the downcomer water level, core inlet subcooling, and boron inventory in the core are predicted to be very similar in both cases.

4.6 Stability Figures-of-Merit

The concern in the ATWS-I events described above is both the efficacy of operator actions to reduce power to compensate for the failure of reactor trip, and the impact of instability and the resulting power oscillations. Power oscillations, if unmitigated, may damage the fuel and hamper the effectiveness of the operator's mitigation strategies. Therefore, in this section, the focus is on the behavior during the period of instability. Here, it is convenient to separate the period of instability into different stages and analyze behavior according to figures-of-merit that are traditionally used for this purpose. Table 4.13 summarizes the different ATWS-I stages and figures-of-merit (FOM) for comparing and analyzing the results of simulation, and identifies key figures and tables used in developing and analyzing the FOMs.

Table 4.13 Characterization of ATWS-I Phases and Figures-of-Merit [15]

Stage	Description	Figure-of-Merit (FOM)	Effect of FOM	Reference
1	Initial	Ratio of vapor production rate (or power) following dual recirculation pump trip to turbine bypass system (TBS) capacity or RPV dome pressure	The higher this figure, the more stable the reactor is expected to be.	Figure 4.68
2	Natural circulation (approach to onset)	$FOM1 = \frac{P_{xyz} \cdot Q}{\dot{m} \cdot h_{inlet}}$	The lower this figure, the more stable the reactor is expected to be.	Figure 4.69
3	Onset through normal growth	Growth ratio	The lower this figure, the less unstable the reactor is.	Table 4.14
4	Large amplitude limit cycle oscillations	RPV downcomer level	The maximum power is constrained by the available head to drive flow (which dictates average power).	Figure 4.76
5	Bi-modal power oscillations	Instantaneous modal reactivity less modal eigenvalue difference	Higher mode excitation occurs when the modal reactivity exceeds the eigenvalue separation.	Table 4.15
6	Non-linear bi-modal power oscillations	Frequency	Incidence of frequency doubling indicates a highly unstable condition	Table 4.16
7	Decay	Decay ratio	The lower this figure, the more stable the reactor is.	Table 4.17
8	Long-term (approach to cold shutdown)	Ratio of single-phase to two-phase average channel pressure drop, $FOM2 = \frac{\Delta P_{LIQ}}{\Delta P_{2-\Phi}}$	The higher this figure, the more stable the reactor is expected to be.	Figure 4.85

4.6.1 Initial Stage

During the initial stage, a key figure-of-merit that indicates the reactor's relative stability is the RPV dome pressure following the rapid power reduction from the dual recirculation pump trip. When the reactor pressure is relatively low with the same liquid temperature at the core inlet, its power response generates an exacerbated transient void relative to a higher pressure scenario. Two facts can explain this behavior. The first is that vapor starts being generated earlier when the system pressure is lower because of lower saturation temperature. The second is that the specific volume of vapor is larger at lower system pressure. Together, they result in the vapor occupying more space in the core region. Therefore, the expectation is that at a lower reactor pressure, the core will be more unstable.

Figure 4.68 compares the system pressures for all simulation cases at the early stage (until 120 s). It shows that system pressure can be categorized in three groups. TRACE predicts the highest pressure in the cases at BOC with 10% and 25% turbine bypass fractions; that with the 50% bypass fraction shows intermediate system pressure. The lowest pressure is predicted in the remaining four cases. However, the relative instability of the reactor differs from that expected when the parametric effect is based on pressure alone. As discussed earlier, the reactor is most unstable in the PHE cases, intermediately unstable in the BOC cases, and stable in the case of EOFPL. Therefore, it is difficult to directly correlate the behavior of this figure-of-merit to reactor instability without considering some other important parameters, for example, axial power shape. If the time during the fuel cycle is kept constant, for example, for the four cases at BOC, the effect of high system pressure on reactor instability was observed to be opposite to expectation. In other words, when the pressure is higher, TRACE generally predicts more severe instability in the reactor. This behavior is caused by the system pressure affecting the magnitude of liquid subcooling at the core inlet that becomes larger as the pressure becomes higher (Section 4.3).

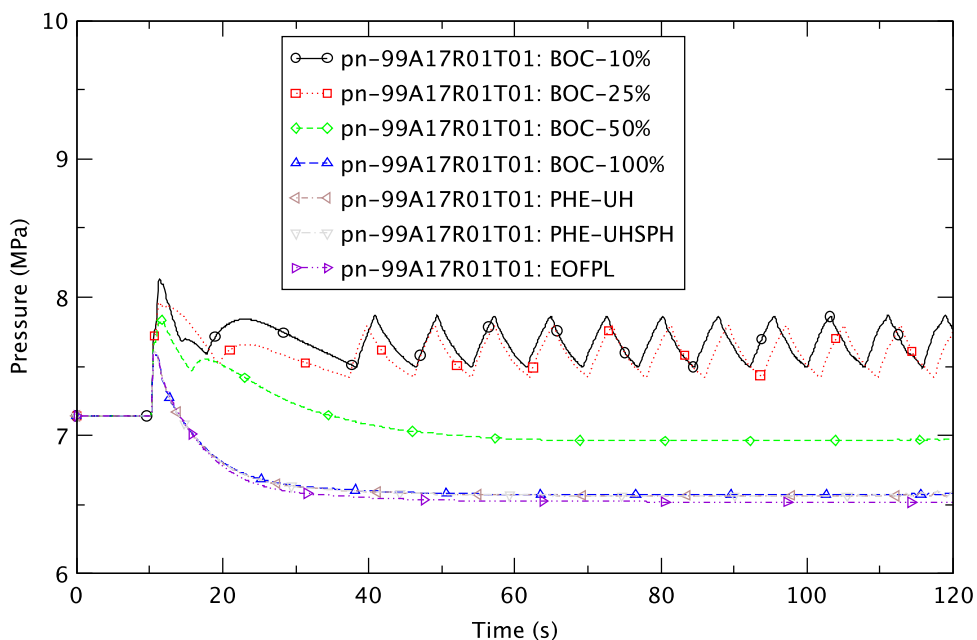


Figure 4.68 Comparison of System Pressures

4.6.2 Natural Circulation Stage

Another FOM in the initial phase of an event, is the ratio

$$\frac{P_{xyz} \cdot Q}{\dot{m} \cdot h_{inlet}}$$

where P_{xyz} , Q , \dot{m} , and h_{inlet} , respectively represent power peaking factor, total power, core inlet flow rate, and inlet enthalpy. After the recirculation pumps fully coast down, natural circulation dictates the reactor core's flow rate. However, the turbine trip isolates extraction steam flow from the feedwater heater cascade, and the temperature of the feedwater slowly begins to decrease. This second stage of the event is natural circulation and approaches the onset of instability. As the feedwater temperature slowly decreases, the reactor power rises in response to maintain a critical void fraction in the core. The colder feedwater increases the inlet subcooling so causing a shift of the reactor power downward in the core and an overall increase in reactor thermal power. The low flow condition, coupled with increased power, and the downward shift in axial power shape bring the reactor into an unstable condition. Therefore, the figure-of-merit shown above can indicate the relative degree of instability into which the reactor is brought.

In the analysis, this figure-of-merit was slightly modified because of the difficulty in locating the specific bundle with the highest local power peaking factor. This location varies depending upon the thermal-hydraulic and kinetic conditions. For simplicity, a limiting bundle has been chosen to evaluate this figure-of-merit:

$$FOM1 = \frac{Q_{LIMT-BNDL}}{\dot{m}_{LIMT-BNDL} \cdot h_{LIMT-BNDL-inlet}}$$

where $Q_{LIMT-BNDL}$, $\dot{m}_{LIMT-BNDL}$, and $h_{LIMT-BNDL-inlet}$ represent power, inlet flow rate, and inlet enthalpy in the limiting bundle, respectively. The lower this figure is, the more stable the reactor is expected to be.

It was found that the threshold of (linear) stability for a natural circulation system is most efficiently represented as a function of the dimensionless Zuber number, N_{Zu} , and subcooling number, N_{sub} [33]:

$$N_{Zu} = (q/(w \cdot h_{fg}))^* (\rho_l - \rho_g) / \rho_g$$

$$N_{sub} = (h_{sub}/h_{fg})^* (\rho_l - \rho_g) / \rho_g$$

where q is the power in a heated channel, w is the inlet mass flow rate, h_{sub} is the inlet subcooling, h_{fg} is the latent heat of vaporization of the coolant, ρ_l is the saturated liquid density of the coolant, and ρ_g is the vapor density of the coolant.

It is observed that FOM1 is related to N_{Zu} and N_{sub} for the limiting bundle,

$$FOM1 = \frac{N_{Zu}}{N_{sub}} \left(\frac{h_{sub}}{h_{LIMT-BNL-inlet}} \right)$$

and it may be correlated with the onset of density-wave instabilities.

Figure 4.69 compares the behavior of $FOM1$ in the limiting bundles where the highest peak cladding temperature seems to be predicted. The reactor begins to become unstable between 70 s and 100 s in all cases except for the EOFPL case where no power oscillation is predicted. From the figure, we observed that this figure-of-merit continues increasing with time in all cases, and is large in the cases at BOC with 10% turbine bypass fraction and BOC with 25% turbine bypass fraction especially between 70 s and 100 s. In those cases, the reactor becomes relatively very unstable. For BOC with 50% turbine bypass fraction, BOC with 100% bypass fraction, PHE with UH void history, and PHE with UHSPH void history, TRACE predicts intermediate magnitudes of this figure-of-merit and the smallest one at EOFPL. This observation confirms that, in general, the reactor's instability becomes more severe when this figure-of-merit is higher. In the figure the large oscillatory behavior in $FOM1$ is caused by oscillatory bundle flow that correlates with unstable reactor power.

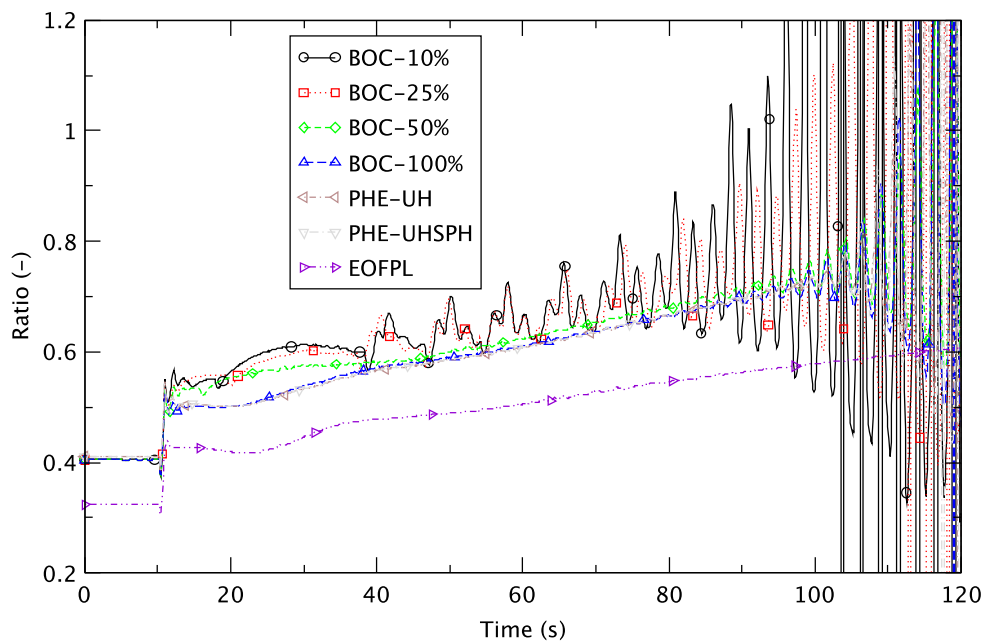


Figure 4.69 Power Ratio FOMs in Limiting Bundles

4.6.3 Stage of Onset through Normal Growth

The next important figure-of-merit is the timing of instability onset. It reasons that a more limiting reactor configuration in terms of stability would exhibit the earlier onset of unstable power oscillations. Therefore, the onset timing is a relative figure-of-merit for assessing the limiting nature of any particular analysis condition.

Following the onset of instability, the magnitude of the oscillation begins to increase. Once the reactor reaches an unstable condition, the background transient conditions suffice to excite unstable power oscillations. During the third (or normal growth) stage, a recommended figure-of-merit is the growth ratio (or a decay ratio with magnitude greater than unity). The growth ratio refers to the relative magnitude of the amplitude of the power in successive oscillations. The larger the growth ratio, the more rapidly the oscillation magnitude rises. A high growth ratio indicates a highly unstable reactor condition. Table 4.14 illustrates the times of onset of reactor instability and growth ratios of power oscillations.

Table 4.14 Times of Reactor Instability Onset and Growth Ratios

Case	Time of Onset of Reactor Instability (s)	Growth Ratio of Power Oscillation
BOC-10% (Case 1A)	75	Overall growth of power oscillation can be observed but it is difficult to determine the growth ratio due to SRVs opening/closing.
BOC-25% (Case 1B)	75	Overall growth of power oscillation can be observed but it is difficult to determine the growth ratio due to SRVs opening/closing.
BOC-50% (Case 1F)	95	Three points are selected to evaluate the growth ratio from Figure 4.72 and they are (125.8, 3435.8), (128.3, 3839.4), and (130.8, 4223.0). The average growth ratio is 1.11.
BOC-100% (Case 1)	95	Three points are selected to evaluate the growth ratio from Figure 4.73 and they are (125.8, 3587.1), (128.3, 3872.9), and (130.8, 3999.6). The average growth ratio is 1.06.
PHE-UH (Case 2)	95	Three points are selected to evaluate the growth ratio from Figure 4.74 and they are (116.8, 3885.7), (119.0, 4711.8), and (121.2, 5082.2). The average growth ratio is 1.15.
PHE-UHSPH (Case 2G)	95	Three points are selected to evaluate the growth ratio from Figure 4.75 and they are (114.7, 3673.3), (116.9, 4424.4), and (119.1, 5090.3). The average growth ratio is 1.18.
EOFPL (Case 3)	Reactor is stable.	

The times of instability onset and the growth ratios were determined based on the total power behavior shown in Figure 4.70 through Figure 4.75. These figures depict the total power behavior with indications of onsets of several important transitions in all cases except for the EOFPL case, where the reactor is predicted to be stable. For evaluating the growth ratios, three points are selected from these figures, viz., three consecutive power peaks and the last one is considered to represent the highest caused by the limit cycle.

We note that in the cases of BOC with bypass fractions of 10% and 25%, an overall growth of power oscillation was observed but it is difficult to determine the growth ratio due to the continuous disturbances resulting from the repeated cycling of the SRVs.

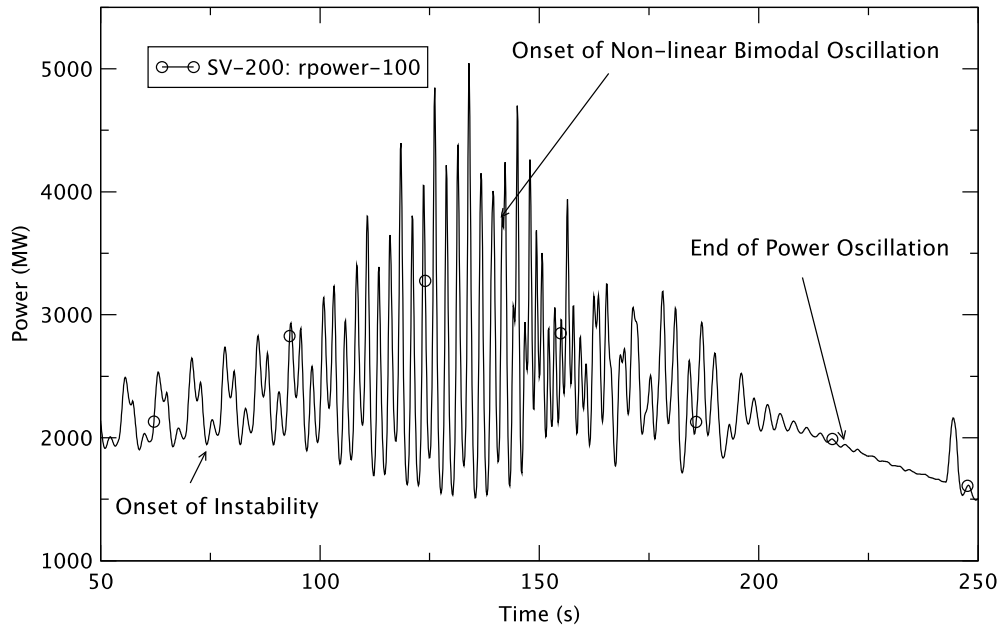


Figure 4.70 Core Power - BOC, 10% Bypass (Case 1A)

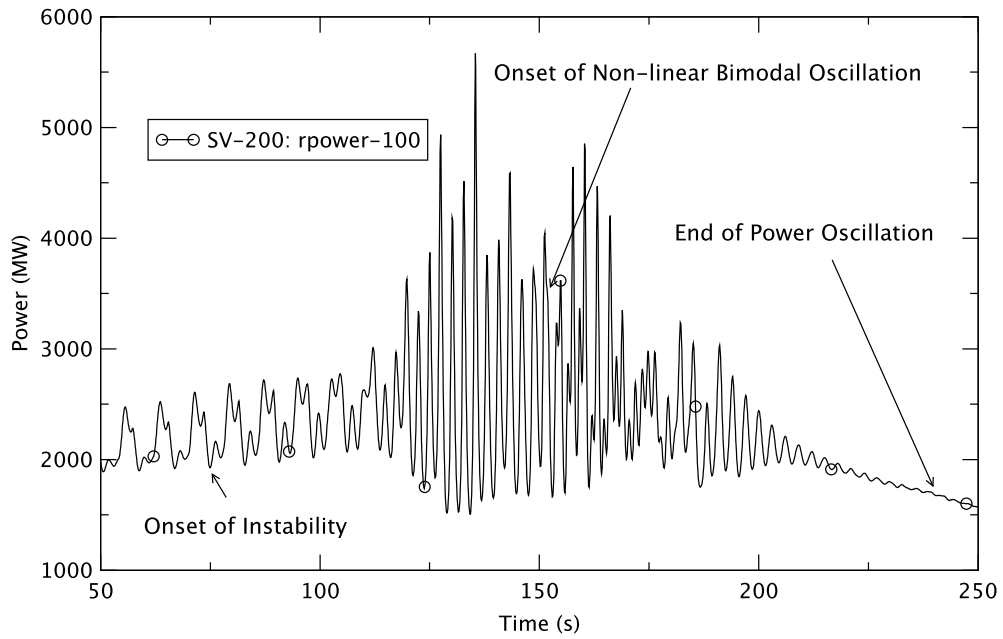


Figure 4.71 Core Power - BOC, 25% Bypass (Case 1B)

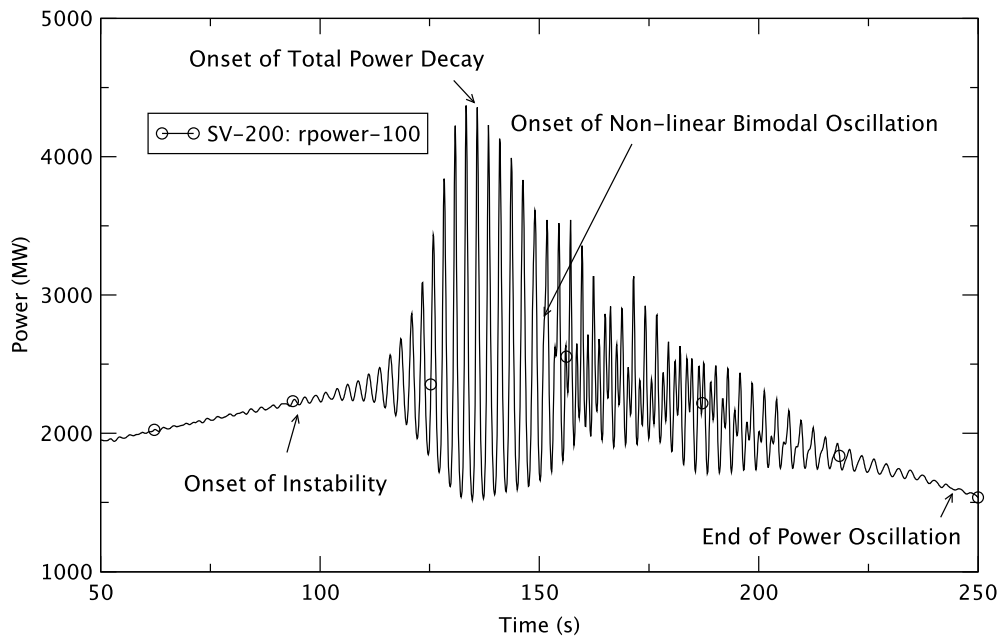


Figure 4.72 Core Power - BOC, 50% Bypass (Case 1F)

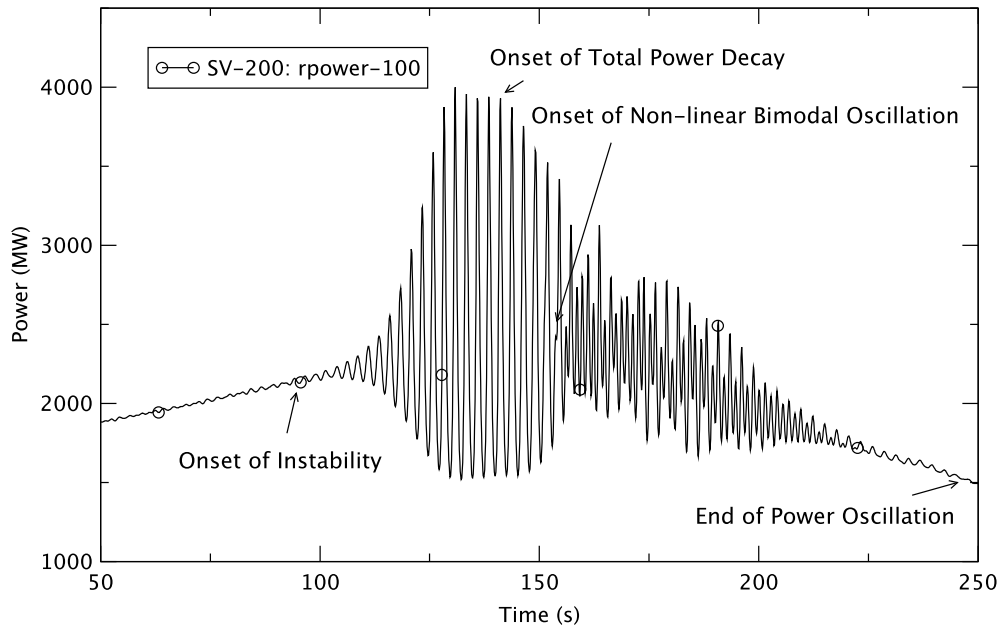


Figure 4.73 Core Power - BOC, 100% Bypass (Case 1)

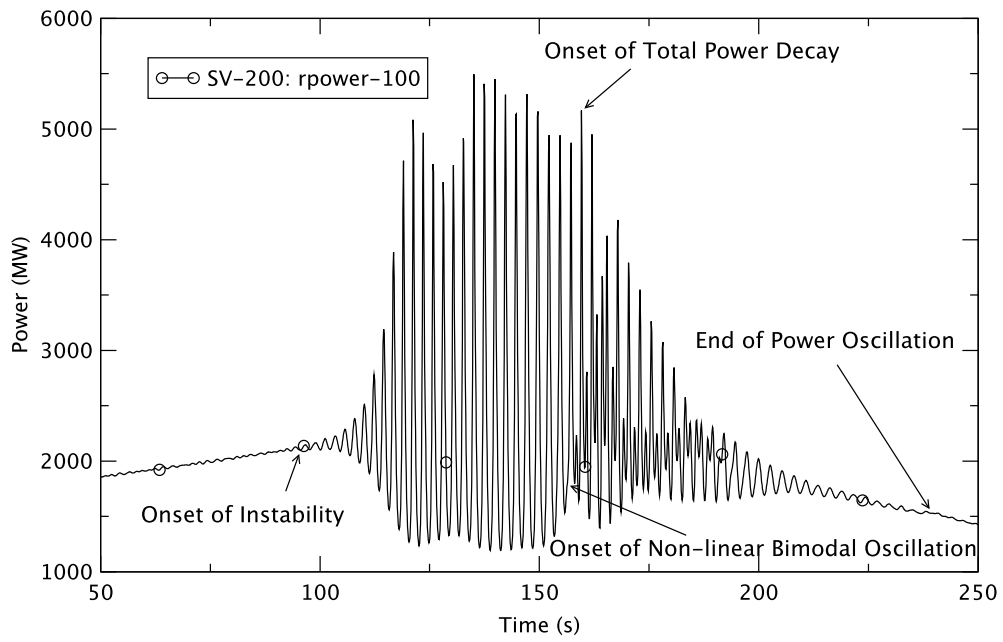


Figure 4.74 Core Power - PHE, UH Void History (Case 2)

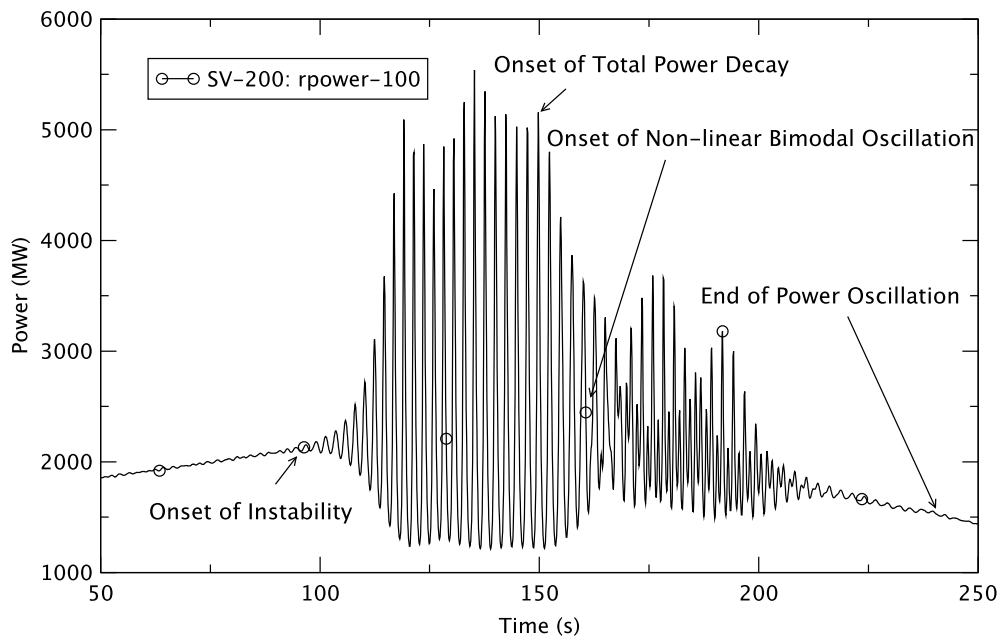


Figure 4.75 Core Power - PHE, UHSPH Void History (Case 2G)

As Table 4.14 shows, the onset of the reactor's instability occurs at around 75 s at BOC with bypass fractions of 10% and 25%, and around 95 s in the other cases. As discussed above, we expected an earlier onset of unstable power oscillations with a more limiting reactor configuration in terms of stability. When comparing the timings of the instability onset, it is difficult to derive a good correlation between this figure-of-merit and the severity of reactor instability because the PHE cases show the most severe reactor instability (Section 4.4) but the power oscillation starts later in them. However, if we consider only BOC cases, then in those with 10% and 25% bypass fractions, the reactor becomes more unstable and power oscillation starts sooner (Section 4.3). This behavior is consistent with that expected.

By comparing the evaluated growth ratios, we find, as expected, generally a high growth ratio engenders more severe power oscillations.

4.6.4 Stage of Large Amplitude Limit Cycle Oscillations

The growth in magnitude of the power oscillation ultimately is limited, and during, the fourth (or large amplitude) stage it achieves a limit cycle and normal growth has ceased. Depending on the core loading and other factors, the dominant oscillation mode may be core wide (CW) or out-of-phase (OOP). The maximum pulse height for the power oscillations ultimately is dictated by the maximum natural circulation flow achievable with the available downcomer level and associated density head. Therefore, the power response largely is governed by downcomer level. During this stage, this level would serve as a relative figure-of-merit.

Figure 4.76 compares the DC levels. The highest amplitude of power oscillation is usually observed before the DC level starts dropping. It is relatively high in the case of EOFPL in which the reactor remains stable while TRACE predicts very similar DC water levels in the other cases. From these observations, it was hard to draw a reasonable relationship between the DC water level and magnitude of power oscillations. In general, their magnitude is the highest in the PHE cases and smallest in the cases of BOC with 50% and 100% bypass fractions (Figure 4.70 through Figure 4.75) while the DC water levels are very similar in all cases. The EOFPL case is not considered in this analysis.

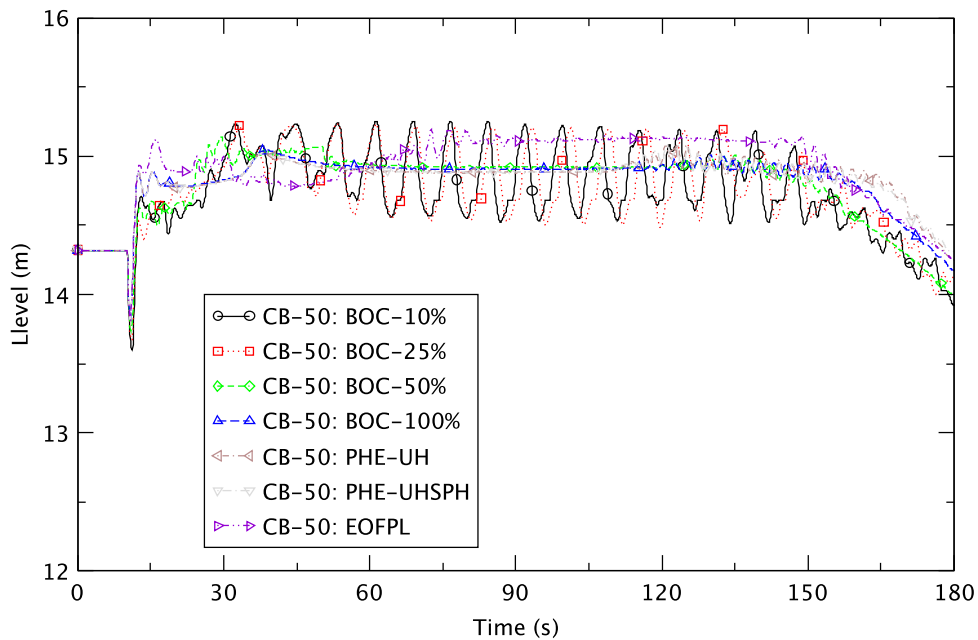


Figure 4.76 Comparison of Downcomer Water Level

4.6.5 Stage of Bimodal Power Oscillations

As the power oscillations continue, they become large and irregular. Their irregularity is a function of bifurcation. The first bifurcation occurs when the pulse height between successive peaks changes. When the response first bifurcates, a high peak and lower peak are observed in the power response with regular periodicity, and at a frequency that is half the natural one. The response may further bifurcate into four unique peak pulse heights, and so forth. While power will still pulse at the same frequency once bifurcated, the period of the oscillation doubles, such that it takes more pulses before the peak achieves the same value. Successive bifurcations result in additional maxima amplitudes. If bifurcation occurs to a large extent, the power pulse heights appear irregular. An approach to study the bifurcation phenomenon in BWRs is to treat the mathematical model of the reactor as a dynamical system [34]. Its resolution when displayed in the phase-space enables us to learn if a system predicted to be stable by the linear (frequency domain) analysis would become unstable if a sufficiently large perturbation were applied. The bifurcation analysis [34] indicates that if a positive perturbation is imposed on a limit cycle oscillation, the system's nonlinearities create a positive increase in average power that, through its reactivity effect, damps out the disturbance. The study further points out that instability in this mechanism (pitchfork bifurcations [35]) can occur if the average power increases too much during a power peak, causing the next peak to decrease by an amount larger than the original disturbance. Thus, if the limit cycle should become unstable, an oscillation of double the original period will be established because the mechanism involves two full oscillation periods. A further increase in the reactivity effect can produce a cascade of period-doubling bifurcations, leading to an aperiodic (chaotic) regime [36].

During the large-amplitude power oscillations, large amplitude reactivity pulses may be sufficient to excite the higher harmonic modes of the flux. The instantaneous modal reactivity pulses may suffice to overcome the eigenvalue difference between the fundamental and higher mode

harmonics. When these reactivity spikes are large enough, the higher harmonic modes may be excited, and potentially, may also be unstable (i.e., not rapidly decay). The oscillation could become bi-modal or even poly-modal depending on the magnitude of the reactivity pulses and the modal adjoint. The fifth stage of the event is characterized by the excitation of higher harmonic modes in the transient response.

The bi-modal characteristics would be most easily analyzed by evaluating modal kinetic parameters, such as mode reactivity and eigenvalue separation. However, at the current time, PARCS does not calculate modal kinetic parameters nor has it been used to calculate higher harmonic mode eigenvalues besides the first harmonic. As figures-of-merit in this stage, the times of onset of bi-modal power oscillation are examined, based on the power-contour movies generated using the detailed PARCS results of bundle powers.

Table 4.15 illustrates the times of onset of bi-modal power oscillation. TRACE predicts that power oscillations first evolves into a higher harmonic mode from the fundamental mode at similar times in all cases (except for BOC with 10% bypass fraction in which it occurs around 10 s earlier than the other cases). Then, the higher harmonic mode oscillations evolved into first harmonic mode oscillations at 154 s and 170 s for, respectively, the cases of PHE with UH and UHSPH void histories; the higher harmonic mode oscillations last until the end of the simulations in the all BOC cases.

Table 4.15 Times of Onset of Bi-Modal Power Oscillation

Case	Bi-Modal Power Oscillation	
	Onset Time (s)	Mode of Oscillation
BOC-10% (Case 1A)	132	From fundamental to higher harmonic
BOC-25% (Case 1B)	141	From fundamental to higher harmonic
BOC-50% (Case 1F)	141	From fundamental to higher harmonic
BOC-100% (Case 1)	143	From fundamental to higher harmonic
PHE-UH (Case 2)	144	From fundamental to higher harmonic
	154	From higher harmonic to first harmonic
PHE-UHSPH (Case 2G)	144	From fundamental to higher harmonic
	170	From higher harmonic to first harmonic
EOFPL (Case 3)	Reactor is stable.	

4.6.6 Stage of Non-Linear Bi-Modal Power Oscillations

Large reactivity oscillations within a dominant oscillation mode may be sufficient to drive yet another oscillation mode via non-linear dynamic reactivity coupling. For example, the modal reactivity oscillation within an unstable CW power oscillation may excite and drive an OOP harmonic oscillation at double the frequency (or vice-versa). Unstable bi-modal oscillation of this type with frequency doubling is referred to as non-linearity. Therefore, the sixth stage is characterized by the onset of non-linear power oscillation with frequency doubling. The timings of this onset are determined based on the total power behavior as shown in Figure 4.70 through Figure 4.75; Table 4.15 illustrates those onset times. The change of the frequency was obtained by performing Fast Fourier Transforms of the total power oscillations (Figure 4.77). The results are given in Table 4.16. From the observation of the frequency doubling, we confirmed that the reactor evolves non-linear, large amplitude power oscillations in all cases except EOFPL.

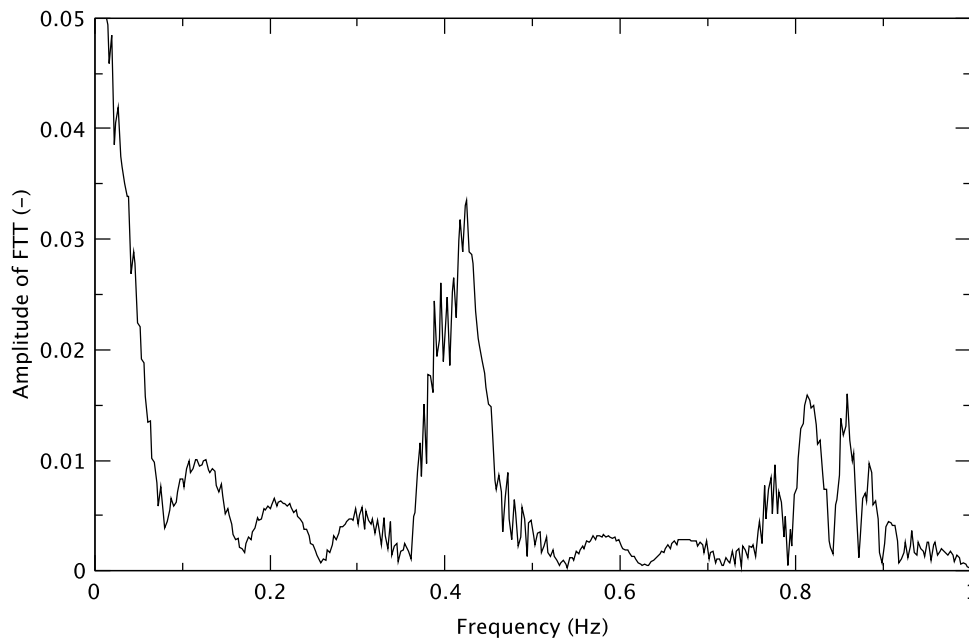


Figure 4.77 Amplitude of Fast Fourier Transform of Power for PHE-UH Case

Table 4.16 Times of Frequency Change and Frequencies

Case	Time of Frequency Change (s)	Frequency Change
BOC-10% (Case 1A)	142	From 0.39 to 0.78
BOC-25% (Case 1B)	152	From 0.39 to 0.76
BOC-50% (Case 1F)	151	From 0.39 to 0.75
BOC-100% (Case 1)	154	From 0.39 to 0.77
PHE-UH (Case 2)	157	From 0.42 to 0.79
PHE-UHSPH (Case 2G)	162	From 0.41 to 0.84
EOFPL (Case 3)	Reactor is stable.	

4.6.7 Decay Stage

During the event, the operator undertakes manual actions, such as injecting boron and lowering the water level to suppress the oscillation. Depending on their effectiveness, the transient response may not exhibit bi-modal oscillation or bifurcation. Once the reactor operators are successful in restoring a stable configuration, the amplitude of the power oscillations should decrease. Such behavior would show a decay of the magnitude of oscillation with time. Once the oscillations indicate decay, the instability has been mitigated and the reactor is stable. This stage could be referred to as the approach to full suppression. When significant power oscillations cease, the instability is said to have been fully suppressed. Therefore, the seventh stage is the decay stage that occurs once the mitigating actions have established a relatively stable condition; here, the decay ratio would serve as a figure-of-merit.

However, in the analysis, we found that the power oscillations do not show an idealized textbook behavior as is apparent in Figure 4.70 through Figure 4.75. This makes it difficult to determine onset of decay based on the evolution of the total power. Figure 4.78 shows the relative peak bundle and total powers for the BOC, 100% bypass case, demonstrating that the local power can oscillate severely even after the amplitude of oscillation of the total power starts decreasing (an indication that the oscillations have become bimodal). We note that the peak bundle powers (F_{xy}) are obtained from the PARCS summary file. For the reduced bypass cases, the behavior of the total power is very irregular (Figure 4.70 and Figure 4.71) because of the perturbation added by the cycling of the SRVs. In those cases, it is useful to look at other parameters like bundle mass flow rate (shown in Figure 4.79 for a limiting channel in the BOC, 10% bypass case). While the power is instantly perturbed by the opening/closing of the SRVs, it is not the case with the flow because of its inertia, on one hand, and also because in a BWR the top of the downcomer is open to the steam dome, so that pressure change occurs not only in the core region but simultaneously in the DC. Therefore, we can determine the onset of decay of oscillations by looking at different figures, choosing in each case one suitable for that particular case.

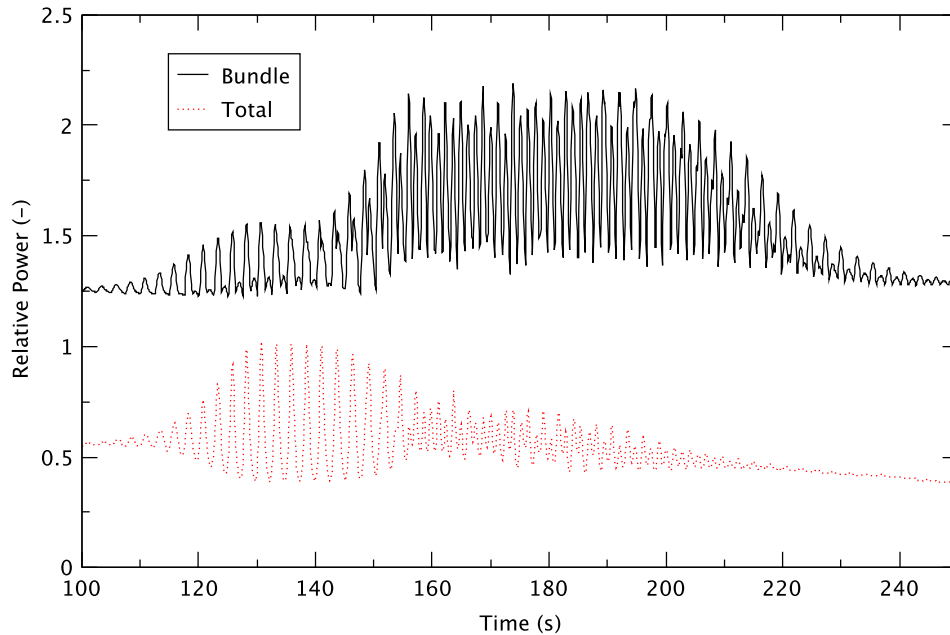


Figure 4.78 Total vs Local Power at BOC, 100% Bypass

Figure 4.79 to Figure 4.84 depict the local power peaking factors, or peak relative nodal power (F_q) obtained from the PARCS summary file. The timings of onset of decay of oscillations were determined from these figures and are shown in Table 4.17. For completeness, we also show therein the timings of onset of decay of total power obtained from Figure 4.70 to Figure 4.75. The difference of timings between the onset of decay of total power and the onset of decay of oscillations can be interpreted as evidence of non-linear coupling. For evaluating the decay ratios, three points are selected from those figures; they are three consecutive power peaks from the onset point as described in Table 4.17.

Table 4.17 Time of Onset of Decay of Power Oscillation and Decay Ratio

Case	Time of Onset of Total Power Decay (s)	Time of Onset of Oscillation Decay (s)	Decay Ratio of Power Oscillation
BOC-10% (Case 1A)	N/A	146	N/A
BOC-25% (Case 1B)	N/A	167	N/A
BOC-50% (Case 1F)	136	177	Three points are selected to evaluate the decay ratio from Figure 4.81 and they are (176.5, 5.2301), (179.2, 5.1047), and (182.1, 5.0219). The average decay ratio is 0.98.
BOC-100% (Case 1)	141	189	Three points are selected to evaluate the decay ratio from Figure 4.82 and they are (189.2, 5.3934), (191.9, 5.3136), and (194.5, 5.1008). The average decay ratio is 0.97.
PHE-UH (Case 2)	160	167	Three points are selected to evaluate the decay ratio from Figure 4.83 and they are (166.6, 7.2621), (169.0, 6.9010), and (171.6, 6.4356). The average decay ratio is 0.94.
PHE-UHSPH(Case 2G)	150	190	Three points are selected to evaluate the decay ratio from Figure 4.84 and they are (190.4, 6.7891), (192.9, 6.6598), and (195.4, 6.2236). The average decay ratio is 0.96.
EOFPL (Case 3)		Reactor is stable.	

It is difficult to determine the decay ratio for BOC with 10% and 25% bypass fractions because of the constant interruption caused by the SRVs opening and closing. Hence, those two cases were excluded.

As discussed above, when operator action is taken at 120 s, the DC water levels do not drop immediately but after a 30 s to 45 s delay (Figure 4.76). Also, when the operator initiates boron injection at 130 s, TRACE predicts that the boron starts arriving and being accumulated in the core from about 160 s. However, in all four cases, the decay of the amplitude of total power oscillation occurs before the noticeable reduction of the DC level and the boron accumulation in the core. Therefore, it seems that the decay of the total power oscillation is associated more with its modal transition than effectiveness of the operator's actions in reducing the DC level and/or injecting boron.

Again, we note that we excluded BOC with 10% and 25% bypass fractions from this analysis because of the constant interruption resulting from the cycling of the SRVs.

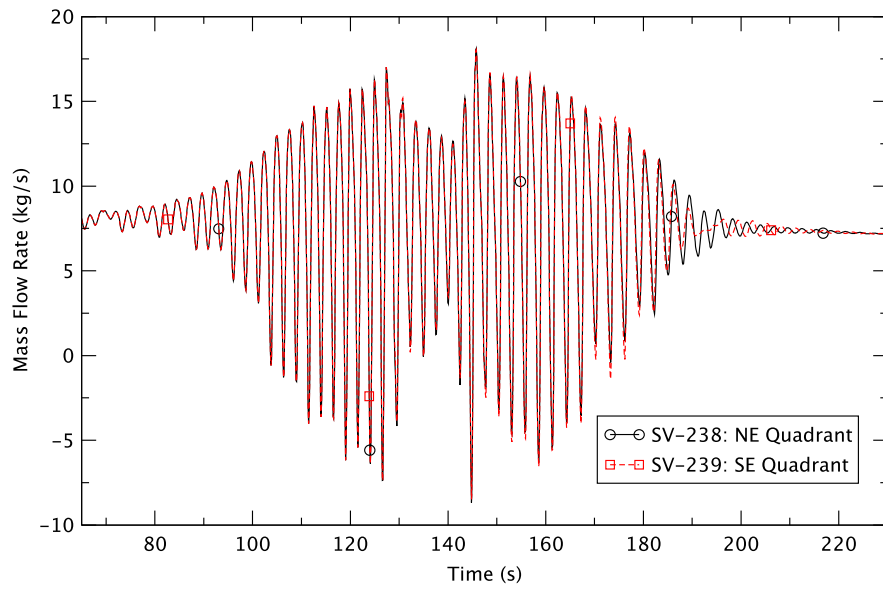


Figure 4.79 Limiting Channel Inlet Mass Flow Rate at BOC, 10% Bypass

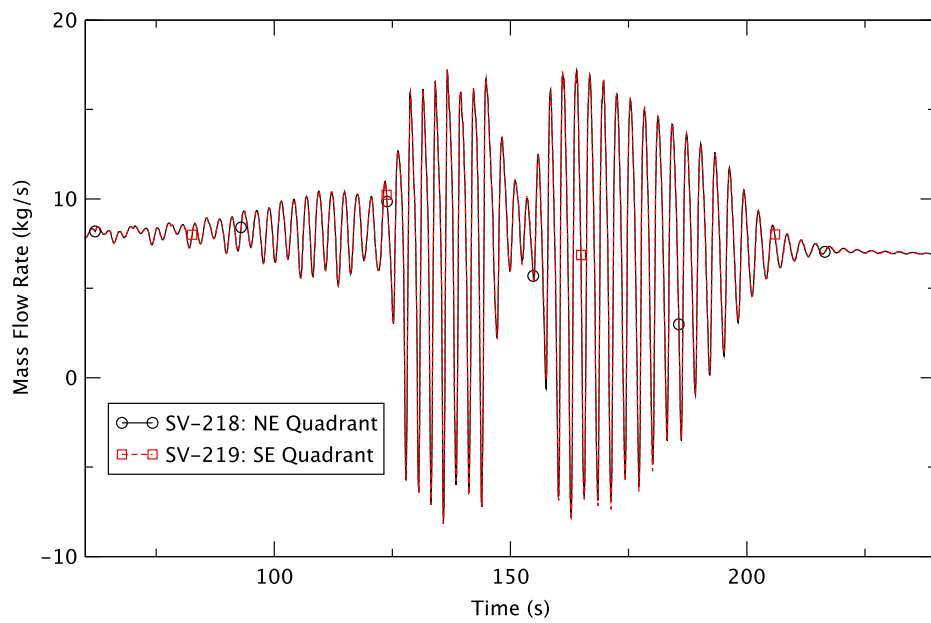


Figure 4.80 Limiting Channel Inlet Mass Flow Rate at BOC, 25% Bypass

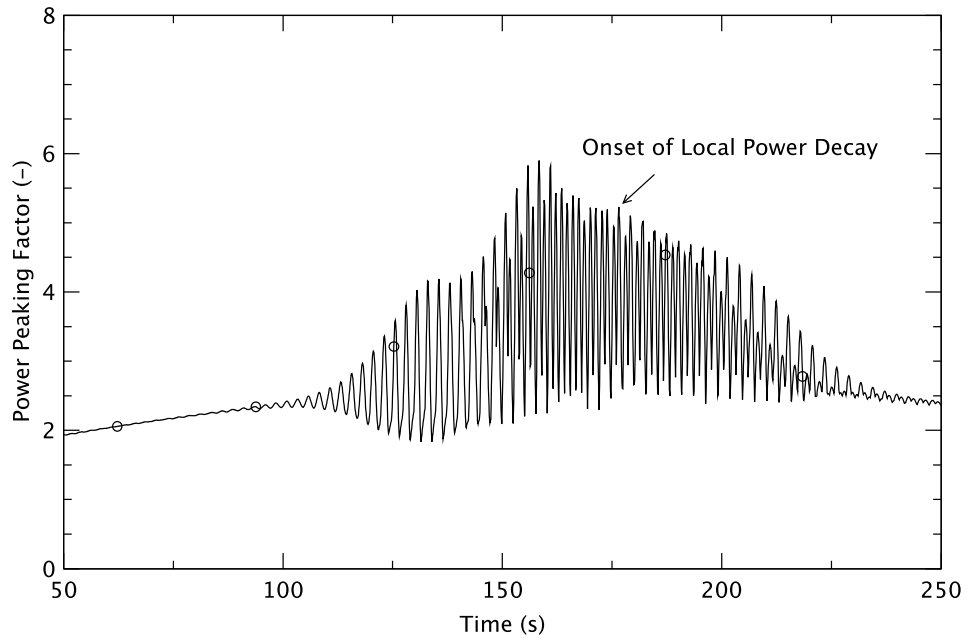


Figure 4.81 Highest Local Power Peaking Factor - BOC, 50% Bypass (Case 1F)

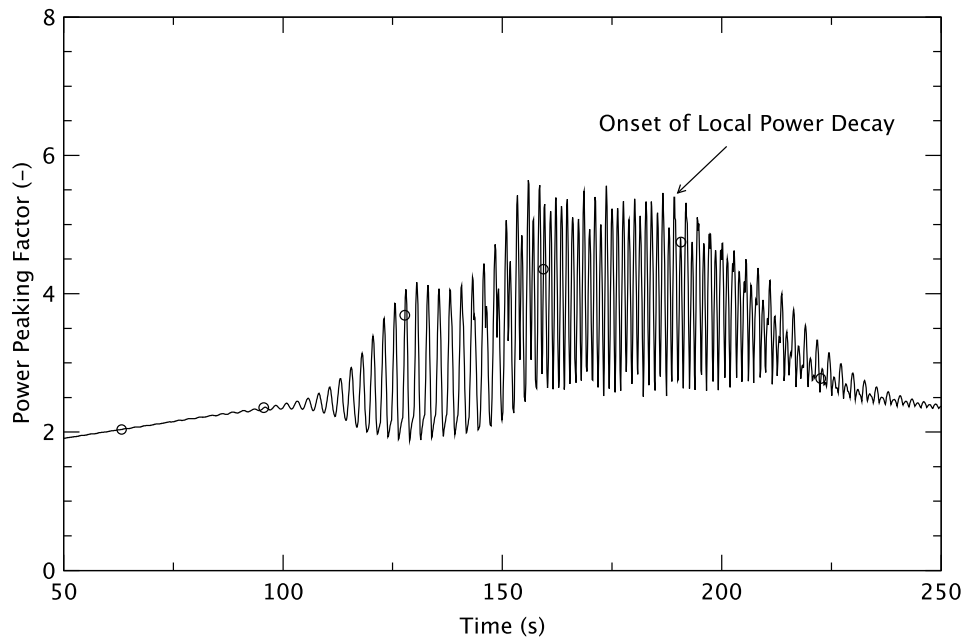


Figure 4.82 Highest Local Power Peaking Factor - BOC, 100% Bypass (Case 1)

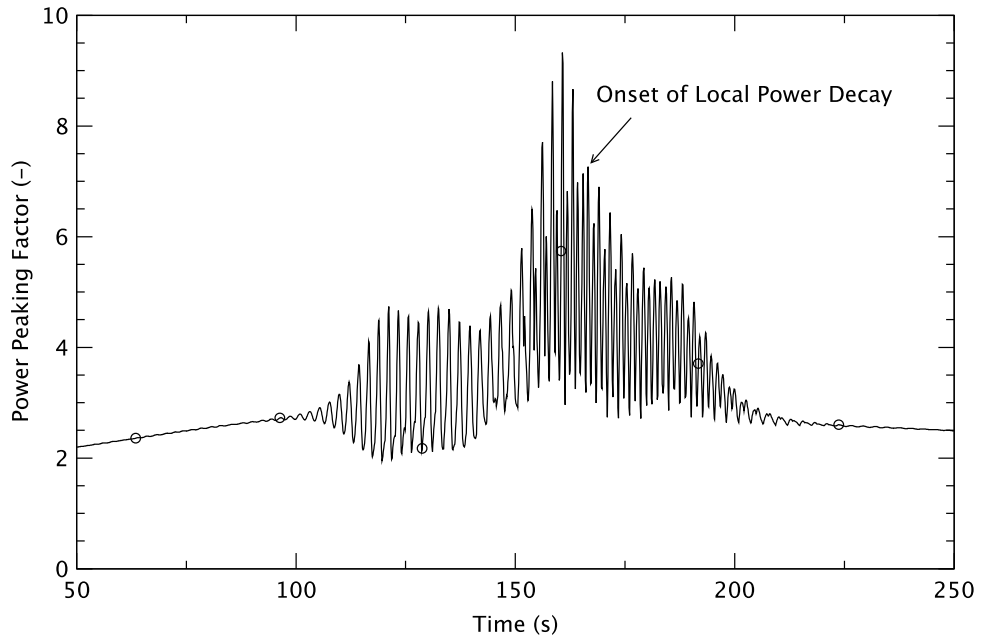


Figure 4.83 Highest Local Power Peaking Factor - PHE, UH Void History (Case 2)

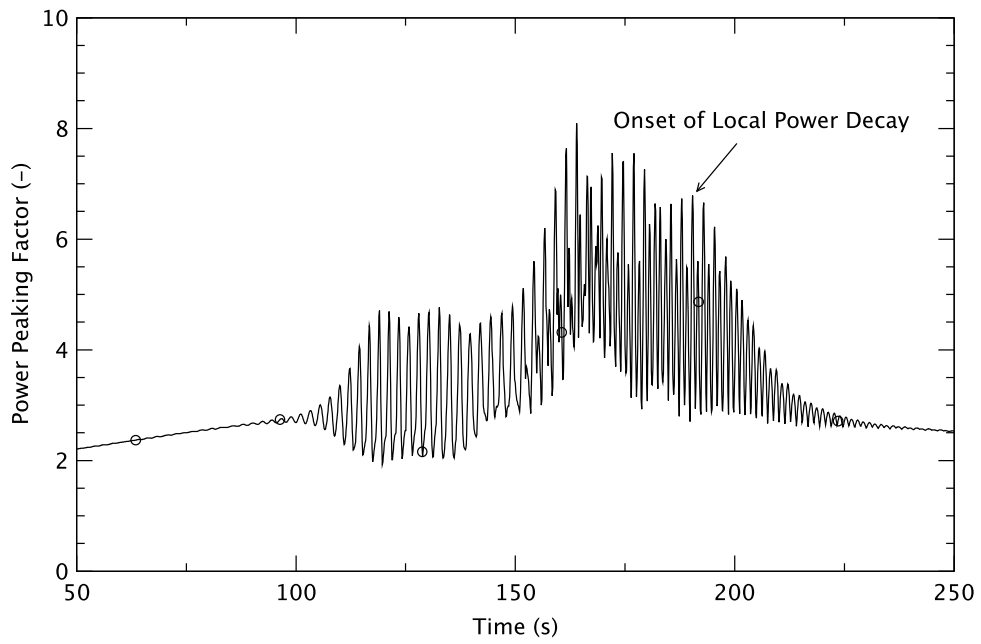


Figure 4.84 Highest Local Power Peaking Factor - PHE, UHSPH Void History (Case 2G)

The onset of decay of the power oscillations occurs in all cases after the effect of the operator's actions in lowering the DC level (accomplished through FW reduction and also leads to reducing the core inlet subcooling) and boron injection. Unfortunately, however, based on the determined onset times and decay ratios, it is difficult to draw any reasonably good relationships between the severity of power oscillation and the onset of decay, and between the severity of power oscillation and the decay ratio. The most severe power oscillations are observed in the PHE cases and the onset of power decay takes place at approximately 167 s for PHE with UH void history and at about 190 s for PHE with UHSPH void history while it happens at 177 s and 189 s in the BOC cases. The decay ratios have similar values in all four cases. Therefore, it is problematic to determine quantitatively or qualitatively, a correlation between the effectiveness of the operator actions to bringing the reactor into a stable configuration and these FOMs.

4.6.8 Long-Term Stage

The last stage, or long-term stage, is characterized by a slow decrease in power and an approach to a stable configuration. The scope of the calculations is to determine the effectiveness of the manual operator actions to suppress the power oscillations, and that the plant trajectory is evolving towards a cold shutdown condition.

A recommended figure-of-merit in this stage is the ratio of single-phase pressure drop to two-phase pressure drop:

$$FOM2 = \frac{\Delta P_{LIQ}}{\Delta P_{2-\Phi}}$$

where ΔP_{LIQ} and $\Delta P_{2-\Phi}$, respectively are the pressure drops due to the single-phase liquid and two-phase in the limit bundle (see Table A.28 in Appendix A for an explanation of how these pressure drops are obtained). This ratio can indicate a growing stability margin when the reactor approaches or reaches a stable condition. The higher that this figure-of-merit is, the more stable the reactor is expected to be. Figure 4.85 compares this figure-of-merit in the limiting bundles. As shown therein, the ratios of single-phase pressure drop to two-phase pressure drop are almost the same after around 240 s in all cases. This means that this figure-of-merit has almost the same universal effect on reactor stability when the reactor approaches a stable condition. Figure 4.85 also shows that FOM2 decreases slightly with time for all cases. This may indicate that the reactor is approaching a less stable configuration. This unexpected trend suggests that the assumption of approximating the single-phase pressure drop by the fall in the core inlet pressure may not be satisfactory at lower power levels; however, a low power level is indicative of the effectiveness of boron accumulation in suppressing reactor power (and oscillations). We note that, as discussed in the previous sections, boron starts accumulating in the core from around 160 s and its concentration continues increasing, so the reactor is observed to remain stable after ~240 s.

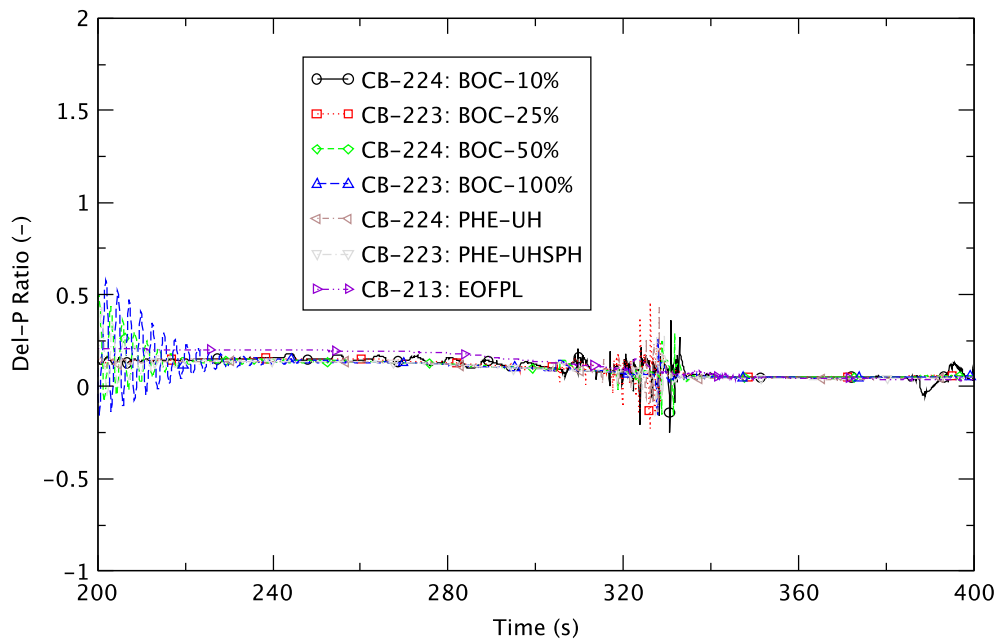


Figure 4.85 Pressure Drop Ratios in Limiting Bundles

4.6.9 Summary

TRACE predicts that the reactor's instability can be classified into four groups. It becomes the most unstable at PHE (with UH and UHSPH void histories), intermediately unstable at BOC with 10% and 25% turbine bypass fractions, less unstable at BOC with 50% and 100% bypass fractions, and stable at EOFPL. The figures-of-merit that show the expected behaviors are *FOM1* and the growth ratio. In general, the reactor instability becomes severe when *FOM1* is high, and the higher growth ratio leads the reactor into more severe power oscillations. It is difficult to draw reasonably good relationships between the other figures-of-merit and the behavior of power oscillations.

The operator's actions are simulated to reduce the DC water level at 120 s and to inject boron into the core through the SLCS at 130 s. Unfortunately, the figures-of-merit we identified in this study do not offer a consistent trend for predicting the stability outcome of the ATWS-I cases analyzed. This leads to difficulty in using the FOMs to identify the particular ATWS-I cases or scenarios that present the greatest inherent challenge to the effectiveness of the manual operator actions to bring the reactor to a stable configuration.

4.7 Summary and Conclusions

This study analyzed the BWR/5 response to an ATWS initiated by a turbine trip while operating at MELLLA+ conditions. Seven ATWS-I cases were considered using the coupled code system TRACE/PARCS to investigate the effectiveness of important parameters, such as turbine bypass fraction, time in fuel cycle, void history, manual operator actions, on reactor instability and the ability to cope with the failure of a reactor trip. The findings from the simulation were examined carefully and our conclusions from the analysis are summarized below.

- The most severe reactor instability is predicted at PHE with UH void history. This is based on using the peak clad temperature as the metric for the margin to safety for an ATWS event.
- TRACE predicts that the operator's manual actions recommended by the EPGs (namely reducing water level and injecting boron) are effective in suppressing unstable power oscillations that develop during the ATWS-I event. The action to reduce level is effective insofar as lowering the FW flow contributes to limiting the increase in core-inlet subcooling.
- TRACE predicts that the PCT exceeds the limit of 2,200°F (1,478 K) in the limiting cases. This prediction is consistent with the TRACE models and constitutive relationships. The PCT excursion is due to a failure to rewet once local power oscillations have resulted in the temperature of the cladding exceeding the minimum stable film boiling temperature.
- In all cases, the effect of the operator's action of level reduction to the TAF at 120 s starts after a relatively long delay of 20 s to 45 s. The onset of core power oscillations occurs earlier than the time of the decrease in downcomer water level in all cases. The onset of decay of the power oscillations, in terms of the highest local power peaking factor, takes place in all cases after the DC level has dropped and boron has built up in the core. However, based on the determined onset times and decay ratios, it is difficult to draw any reasonably good relationship between the severity of power oscillation and the onset of decay or the decay ratio.
- TRACE calculates a 30 s delay for the boron to reach the core after injection into the RPV that starts at 130 s. Boron contributes to suppressing power oscillations in the reactor, and maintains the core in cold shutdown over the long term.
- TRACE predicts larger oscillations when smaller turbine bypass fraction is considered. The reason is that when turbine bypass capacity is less than the reactor power, the RPV pressurizes until the pressure reaches the SRV's lift pressure. At a higher RPV pressure, given the same FW injection enthalpy, the coolant's subcooling increases. We note that when the bypass fraction is very small (10% and 25%) and the system pressure is maintained by the same SRV banks in the early stages of the transient, the reactor instability appears insensitive to the actual size of the bypass because the system pressure is similar, so leading to the same degree of liquid subcooling at the core inlet.
- The time in a fuel cycle has an impact on reactor instability. The most unstable reactor condition is predicted at PHE and intermediate reactor instability at BOC, even though the general behavior of the important parameters affecting reactor instability is very similar for both. The reactor does not develop any significant power oscillations at EOFPL. The relative stability therein is attributed to a combination of factors: a relatively lower core power after the 2RPT, a lower liquid subcooling at the core inlet, and an axially top-peaked core power shape.
- Basically no difference is observed of the effect of spectral history on reactor instability except for the core power behavior for a certain period when different modes of oscillation are observed for the two cases with different spectral history.

- The figures-of-merit that show expected behavior are *FOM1* and the growth ratio. In general, reactor instability becomes more severe when *FOM1* is higher and a higher growth ratio leads the reactor to more severe power oscillations. On the other hand, it is difficult to draw reasonably good relationships between the other figures-of-merit analyzed and the behavior of power oscillations because the other FOMs do not consistently predict the evolution of the reactor instability.
- Different cases exhibit different transitions from the fundamental to the harmonic modes of oscillation. In all cases at BOC, TRACE predicts the evolution of the core power oscillation from fundamental mode to higher harmonic modes, while at PHE with a UH or UHSPH void history, the core power oscillations evolve first from the fundamental mode to higher harmonic mode (though less obvious in the UH case) and then to the first harmonic mode.
- It is evident from the ATWS-I results that determining core stability cannot be based on the core average power alone. In analyzing the power oscillations, the transition from the fundamental to the harmonic modes may result in a decrease in the average core power, suggesting an approach to a more stable state. However, higher mode oscillations, the first harmonic in particular, were observed to exhibit sustained oscillations in individual channels (or fuel bundles) with growing amplitude. The space-time kinetics analysis conducted with the TRACE/PARCS code system provides the additional spatial element to delineate the effects of out-of-phase oscillations.
- The current assumption of half-core symmetry in the mapping of hydraulic channels may be inadequate to resolve higher harmonic modes in the core response. This is particularly true for regional oscillations where the axis of symmetry may rotate in the core.
- There are thermal-hydraulic parameters other than the channel power, such as the channel mass flow, that afford supplementary information useful in analyzing the density wave-driven instability. For example, SRV cycling can cause power oscillations that are not due to the reactor's instability. For the cases of reduced turbine bypass (10% and 25%), the channel mass flow seemingly is not sensitive to the perturbations in system pressure caused by the cycling of the SRVs, and so can be used to differentiate between these two types of oscillations.

In analyzing the ATWS-I results, some code issues and limitations were identified. They are discussed in Chapter 5. In certain instances, these issues impacted predictions of specific parameters; however, they do not impact the conclusions of this work.

5 CONCLUSIONS AND RECOMMENDATIONS

The objective of this work was to develop TRACE/PARCS models supporting ATWS confirmatory analyses at MELLLA+ operating conditions for two specific scenarios, ATWS initiated by a turbine trip that leads to large-amplitude core instability, and ATWS initiated by closure of main steam isolation valves (MSIVs) that leads to emergency depressurization once the heat capacity temperature limit (HCTL) of the suppression pool is exceeded.

We followed our development of the models by analyzing ATWS events with different assumptions about plant conditions and/or modeling. The events that are documented in this report are those that are initiated by a turbine trip and lead to instability (ATWS-I cases). Analysis of events that lead to emergency depressurization will be documented separately.

Equally important, another objective was to assess the capabilities of the TRACE/PARCS code to calculate the thermal-hydraulic and neutronic phenomena associated with BWR ATWS and reactor stability events.

These objectives were met and this report provides the details. In this chapter, the most significant conclusions are provided. The chapter is divided into a section on how the study has generally met the objectives, a section on what has been learned about ATWS-I events for a BWR/5 reactor design, a section related to the calculation tool that was used, namely TRACE/PARCS, and the BWR/5 model that was developed for the ATWS application, and a section on the future use of this analysis.

5.1 TRACE/PARCS Application to ATWS Events

BWR/5 models for use with TRACE/PARCS were developed for application to ATWS. The models are used at different times during a fuel cycle and include all systems needed for events initiated by turbine trip or the closure of main steamline isolation valves. It includes the standby liquid control system (SLCS), recirculation pumps, feedwater and water-level control, reactor core isolation cooling system (RCIC), safety and relief valves (SRVs), and the suppression pool cooling. The modeling in the core is detailed relative to state-of-the-art models with four different fuel rod types included in each fuel assembly, and 382 channels to represent all assemblies taking into account half-core symmetry for the cases of turbine trip. The models developed can be used for many ATWS applications and for many transients with the reactor trip operational.

A MATLAB script was developed for generating input for the CHAN components in TRACE. The script includes a feature to use FRAPCON results to develop inputs for the dynamic gap model of TRACE. This script has general application and can be used by the larger community of TRACE users.

5.2 ATWS Events Initiated by Turbine Trip

Results were calculated for ATWS events initiated by turbine trip in a BWR/5 with GE14 fuel. The calculations were done at nominal initial conditions and assumptions for three times during an equilibrium fuel cycle; beginning-of-cycle (BOC), peak-hot-excess-reactivity (PHE, close to the middle of the cycle), and end-of-full-power-life (EOFPL, near end of cycle). Sensitivity calculations were done at BOC to determine the effect of the bypass fraction (10, 25, 50, and 100%), and at PHE to determine the effect of including a spectral history correction on the void density. The results show the following:

- Power oscillations are more severe at PHE relative to BOC and non-existent at EOFPL.
- The relative stability at EOFPL is attributed to several factors: a relatively lower core power after the 2RPT, a lower liquid subcooling at the core inlet, and an axially top-peaked core power shape.
- In the BOC cases, the core becomes more unstable as the turbine bypass fraction becomes smaller.
- When the bypass fraction is small (10% and 25%) and the system pressure is maintained by the SRV banks during the early stage (until around 200 s), reactor instability appears not to be sensitive to the actual size of the bypass fraction because the system pressure is similar in both cases, leading to the same degree of liquid subcooling at the core inlet.
- The operator's actions to reduce water level and start the SLCS to get soluble boron into the core are effective in mitigating power oscillations in ATWS-I transients, help to keep power low, and eventually, shut down the core.
- The TRACE results indicate some time delay in the realization of the operator actions to reduce power oscillations. It is difficult to correlate the severity of power oscillation with either the time of onset of decay, or the decay ratio.
- The effect of adding a spectral correction to the void history cannot be seen in the steady-state conditions; however, it does impact the transient. Although downcomer water level, core inlet subcooling, and boron inventory in the core are very similar with and without the correction, during the period with oscillations, the timing of the transitions from the higher harmonic modes to the first harmonic is different, and as a result, the peak cladding temperatures differ.
- Different cases exhibit different transitions from the fundamental to the harmonic modes of oscillation. In all cases at BOC, TRACE predicts the evolution of the core power oscillation from fundamental mode to higher harmonic modes. At PHE with a UH or UHSPH void history, the core power oscillations evolve first from the fundamental mode to higher harmonic modes (although less obvious in the UH case) and then to first harmonic mode.
- It is evident from the ATWS-I results that determining core stability cannot be based on the core's average power alone. In analyzing the power oscillations, the transition from fundamental to harmonic modes may result in a decrease in the average core power, suggesting approach to a more stable state. However, higher mode oscillations, the first harmonic in particular, were observed to exhibit sustained oscillations in individual channels (or fuel bundles) with growing amplitude. The space-time kinetics analysis conducted with the TRACE/PARCS code system provides the additional spatial element to delineate the effects of regional and out-of-phase oscillations. Visualization tools, such as computer animation, are best suited to analyze the complex spatial detail of the calculations.
- The current assumption of half core symmetry in mapping of hydraulic channels may not be adequate to resolve higher harmonic modes in the core's response. This is particularly true for regional oscillations that are manifest in different azimuthal modes that were observed in plant events and other calculations [37].

- There are thermal-hydraulic parameters other than the channel power, such as the channel mass flow, that can provide supplementary information on the state of the core's stability. For the cases with reduced turbine bypass fraction (10% and 25%), the channel mass flow does not appear to be sensitive to the perturbations in system pressure caused by cycling of the SRVs.
- The figures-of-merit that show expected behavior are $FOM1$ (essentially power to flow), and the growth ratio. In general, reactor instability becomes more severe when $FOM1$ is higher and a higher growth ratio leads to more severe power oscillations. It is difficult to correlate the other figures-of-merit with the behavior of power oscillations because they do not consistently predict the evolution of the reactor's instability.
- The calculated peak clad temperature (PCT) for several cases was greater than the acceptance criterion (1,478 K). If further study (see Section 5.3) confirms this number, this finding would have to be factored into any ongoing review of MELLLA+ operation. Furthermore, it would then be important to see if this result also applied under other (more prevalent) operating conditions.

Additional sensitivity studies are recommended with the following assumptions:

- fixed gap conductance (low value) at BOC
- fixed gap conductance (high value) at PHE
- 10% turbine bypass at PHE
- 25% turbine bypass at PHE
- reduced core flow (75% rated) with no change in the control-rod pattern at PHE

5.3 Modeling in TRACE/PARCS

This study examined the ability of the TRACE/PARCS code system to calculate the complex phenomena during ATWS events. TRACE/PARCS was shown to be an extremely useful tool for analyzing these events. We also gained insights into effective modeling of those phenomena. First for TRACE then for PARCS, this section describes our user experience related to relevant, important phenomena. Hence, this section may be used to further develop rigorous modeling and user guidance for similar application.

5.3.1 TRACE

Clad Temperature

The initial steady-state profile of the axial clad temperature appears to be different depending on the critical heat flux (CHF) option selected for the CHAN component. This is observed in the results of a sensitivity study conducted with an earlier version of TRACE (V5.354-fix2). Before determining the applicability of TRACE to predict the onset of CHF heat transfer for BWR rod bundles, the NRC staff had recommended using various features in TRACE to suppress the onset of CHF. Once TRACE was found applicable on the basis of various steady-state and transient assessments, the staff recommended using the Biasi correlation. The transient clad temperature for the ATWS-I calculations, however, exhibits trends that are indicative of some limitations or deficiencies in determining clad temperature during oscillatory conditions where the heat transfer may rapidly vary between pre- and post-CHF regimes.

A significant increase in clad temperature is first predicted when the coolant void fraction grows beyond 0.9. Seemingly, once the cladding temperature, as predicted by TRACE, has exceeded the minimum stable film-boiling temperature (T_{min}), the existing post-CHF heat transfer model in TRACE will not predict the rewetting of the cladding surface until the clad temperature is reduced below a rewet temperature, even though the coolant void has neared zero. The prediction of rewet thus is contingent on the ability of TRACE to accurately calculate the clad temperature. Some inconsistency in predicting clad temperature by TRACE was observed. For very similar coolant thermal-hydraulic conditions (void fraction close to zero), TRACE predicts different trends for the clad temperature, oscillatory without increase in some nodes, and continuous increase in nodes close by. In evaluating this behavior in the calculated clad temperature the analyst should consider the following:

- the logic and process of switching the heat transfer regime into and out of the post-CHF region
- pre- and post-CHF heat transfer model and quenching of fuel rods (e.g., models for T_{min} and IAFB (inverted annular film boiling)) in oscillatory flow field (mass flow and void fraction)
- fine-mesh re-zoning for the fuel rods

Owing to the oscillations of the core conditions in an ATWS-I event, the fuel rods are exposed to periodic high void and low void conditions similar to core uncover and reflood in a loss-of-coolant accident (LOCA). Implementation of fine-mesh rezoning will result in a more realistic prediction of clad temperature by providing an additional mechanism (axial heat conduction) for energy removal from the location of the peak clad temperature.

Level Tracking

Both one-dimensional (1-D) and three-dimensional (3-D) level tracking appear to significantly impact the TRACE results. Preliminary calculations suggested that 1-D level tracking was not effective in damping pressure spikes in the SRV discharge pipes that are partially submerged in the suppression pool. To overcome the failure of TRACE execution due to pressure convergence in the SRV discharge pipe, we replaced the valve-pipe combination by a single-junction valve connected to the suppression pool via a BREAK component. 3-D level tracking in the VESSEL component also proved to be problematic for the ATWS calculations. Early evaluations indicated that TRACE failed to approach an initial steady-state when the 3-D level tracking was turned on only for some of the nodes in the upper downcomer. Eventually steady-state is achieved using a 3-D level tracking scheme that is active only in fluid regions that can sustain a liquid column with a free surface on top. However, with early versions of the TRACE executable we encountered other difficulties in analyzing an ATWS transient. When the level of the downcomer water dropped below the feedwater sparger, pressure convergence failed in the VESSEL node with the free surface (interface between steam and water). This finding suggests the 3-D level tracking logic has deficiencies in the modeling of heat transfer with a free surface. Another problem potentially related to the 3-D level tracking is the observed sudden change in core flow when the water level reaches the top face of the downcomer node that sits directly above the top (inlet) of the jet pump.

These TRACE difficulties are all related to implementing level tracking. The experience of applying TRACE to the ATWS-I analysis provides valuable insights that could be used if needed to further develop rigorous guidance for applying 1-D and 3-D level tracking. For example, in implementing 1-D and 3-D level tracking the analyst should pay attention to their interfaces with the momentum and energy balances of the hydraulic components

Steam Separator

We observed in the ATWS-I results that the effect of the operator's action to lower the reactor's water level was delayed by about 40 s. Two factors seem to cause this:

- release of water accumulated in the separator to the downcomer
- downcomer water level remaining unchanged while water was being accumulated in the steam separator during the early part of the transient

The mechanisms leading to the accumulation of water in the separator and the relatively constant water level in the downcomer have not been established. The causes are likely related to the modeling assumptions of the SEPD component and the momentum balance for the flow paths between the separator and the VESSEL component. 3-D level tracking also may play a role in the behavior of the water level in the downcomer. The TRACE results suggest that the release of saturated water from the separator directly impacts the reduction in the core inlet's subcooling.

Fixes have been incorporated in the TRACE code to resolve the following problems encountered in the early analysis of the ATWS transient:

- excessive mass error in the SEPD component
- pressure and temperature spikes in the SEPD component

A sensitivity study on the modeling of the SEPD component was performed with a simplified VESSEL with initially stagnant flow condition. The results revealed several puzzling trends:

- unexpectedly high mass flow through the SEPD
- unexpected pressure distribution in the VESSEL
- unphysical void distribution inside the VESSEL

Given the sensitivity of the results to SEPD modeling, future analysts should pay special attention to: the SEPD modeling assumptions and their implementation in TRACE, the thermal-hydraulic coupling between the SEPD and the VESSEL component, and the role of 3-D and 1-D level tracking in this coupling.

Boron Mixing

TRACE does not have a built-in model for boron mixing in the reactor vessel. An ad hoc approach is used in the ATWS analysis to simulate the settlement and remixing of boron in the lower plenum of the VESSEL component. The opening and closing of a valve in the lower plenum, based on reactor flow, simulated the effect of boron mixing and settlement. The existence of the flow valve has perceivable effects on the TRACE thermal-hydraulic calculations. It adds more volume to the lower plenum and when closed diverts the core flow from the lower plenum. The cycling of the flow valve perturbs the core flow.

Our study indicates that the preferred method for treating boron mixing and remixing would be implementing a control logic to introduce the boron solution into the core flow so as to emulate the effect of boron mixing and settlement.

5.3.2 PARCS

Xenon and Samarium

Equilibrium concentrations of xenon and samarium are calculated during the steady-state and then used (without change) in the transients. Not taking into account the transient evolution of their concentrations could impact long transients (e.g., ATWS-ED). PARCS has a Xe/Sm transient option that could not be used because of a deficiency in the code. When this option is engaged in a transient calculation, the code initialized with a large negative reactivity from Xe/Sm.

TRACE/PARCS Mapping

The convenience of using the Automapping feature ought to be weighed against its drawbacks. With Automapping, the reflector has constant properties defined in the mapping file. This becomes problematic when the boron concentration in the core is high, because then, there is a huge gradient between the core and the reflector. This gradient was identified as the cause of code crash (because of negative flux), and is the reason why ANM cannot be used for ATWS-ED. As per the guidance from the NRC staff, FDM (finite difference method) is used instead.

The mapping between PARCS and TRACE used for these calculations was based on the symmetry of the first harmonic calculated by PARCS. However, it was found that higher harmonic modes are excited during the power oscillations. A more rigorous approach would be a one-to-one correspondence between PARCS and TRACE (i.e., same number of TRACE channels and PARCS fuel assemblies).

PARCS Outputs

This section describes our experience interpreting the PARCS output files. We observed that the information provided in the output files, in many instances, was confusing or insufficiently clear. These observations, however, have no impact on the calculation results

- There are some spurious/misleading/confusing outputs in the PARCS main output file (*.parcs_out):
 - Header lists PARCS version as “NRC - V3.00”. The version number in the PARCS output is not correct.
 - When card XS_EXTRAP is not used, the output reads “Caution: instantaneous variables out of range!” This message is misleading because it is printed whenever any of the possible instantaneous variables is not considered. For instance, the cross sections used for this ATWS analysis do not have control rod or moderator temperature branches, and that prompts this message. It would be more useful if details were also included (e.g. “No Tm branches found”, or “Tf=5000°C is out of range”).
 - “Warning: negative flux has been corrected!” appears throughout the main output file. This message is incorrect.
 - In the steady-state output, there is a series (thousands) of lines with the message: “Maximum Doppler Change 65761.4765354191 Kelvin/Second,” where the maximum Doppler change decreases. This information is not very useful, but indicates some kind of metrics for convergence. In the transient output, under “Steady-State Eigenvalue Calculation Results,” only the first line is

output: "Maximum Doppler Change 65761.4765354191 Kelvin/Second," and is immediately followed by k-eff. It would be better to output the whole series to indicate convergence, or (preferably) bypass this altogether.

- PARCS generates output files not described in the manual (Section II.D.2 of the user guide). Information on the contents of ALL output files would be useful.
- Better identification of the information in the output files themselves would also be valuable, for example:
 - the *.plt file has no headers
 - the headers in the *.sum file are misaligned, making it difficult to interpret the information therein
- One of the PARCS output files (*.bpf) is readable by AptPlot. It includes time-dependent node-by-node information of variables, such as boron concentration, density, and fuel temperature. It would be useful if it also had other time-dependent information, in particular, core-averaged information (e.g. core-averaged boron concentration, which currently is output in the *.sum file).
- PARCS does not output useful modal kinetics parameters, such as mode reactivity and eigenvalue separation. It only gives the first harmonic shape (but not the eigenvalue).

PARCS Documentation

PARCS has the capability of calculating the first harmonic and simulating noise; however:

- Currently available PARCS code documentation does not describe:
 - The implementation of noise in the PARCS calculation.
 - The calculation of the first harmonic.
- There is no current generic user guidance for the noise feature.

SNAP for PARCS

We found that SNAP is not very useful for building PARCS models or mapping files. It is much easier to prepare the ASCII files directly.

PARCS Stand-Alone Calculations

When running PARCS in stand-alone mode, a segmentation fault occurs if there is a file called "tracin" in the same directory.

When a DEP file produced from a coupled calculation is used to drive a stand-alone PARCS calculation a EXT_TH card must be supplied.

If harmonic output is requested in a stand-alone calculation, it may impact other requested outputs, e.g., point kinetics data.

5.3.3 Use of Analysis Results

The NRC undertook the current study to demonstrate the application of TRACE/PARCS to evaluate the consequences of ATWS with instability events for BWRs operating under MELLLA+ conditions. While the results of the current analysis are applicable only to the generic BWR/5 plant modeled; the calculations and sensitivity studies herein have provided insight into the importance of certain phenomena affecting the prediction of oscillations and fuel damage consequences. Of key importance, and consistent with the NRC staff's PIRT [2], are those phenomena affecting the prediction of dryout and rewet. Fuel damage may occur due to a failure of the cladding surface to rewet during periods of large amplitude oscillation. These results can be used by the NRC staff in reviewing the results of any plant-specific analyses submitted by potential MELLLA+ applicants insofar as they demonstrate certain sensitivities of the consequences to models of highly important phenomena.

Further, in the course of this work, some minor code errors were discovered. Given that the errors identified in this report do not have a significant impact on the capability of TRACE/PARCS to analyze these kinds of events, their correction has been deemed a low priority by the NRC staff.

6 REFERENCES

1. J. Harrison, GE Hitachi, letter to U.S. Nuclear Regulatory Commission, "Accepted Version of GE Licensing Topical Report NEDC-33006P-A, Revision 3 (TAC No. MD0277)," MFN 09-362, June 19, 2009, ADAMS Accession No. ML091800512.
2. P. Yarsky, "Applicability of TRACE/PARCS to MELLLA+ BWR ATWS Analyses, Revision 1," U.S. Nuclear Regulatory Commission, Office of Nuclear Regulatory Research, November 18, 2012, ADAMS Accession No. ML113350073.
3. "TRACE V5.0 Theory Manual," U.S. Nuclear Regulatory Commission, June 4, 2010, ADAMS Accession No. ML120060218.
4. T. Downar et al., "PARCS: Purdue Advanced Reactor Core Simulator," Proceedings of Reactor Physics Topical Meeting, PHYSOR 2002, Seoul, Korea, October 7-10, 2002.
5. "TRACE V5.0 Assessment Manual," U.S. Nuclear Regulatory Commission, 2007, ADAMS Accession No. ML120060403.
6. T. Kozlowski et al., "TRACE/PARCS Validation for BWR Stability Based On OECD/NEA Oskarshamn-2 Benchmark," The 14th International Topical Meeting on Nuclear Reactor Thermal Hydraulics, NURETH-14, Toronto, Canada, September 25-30, 2011.
7. J. Gehin et al., "TRACE-PARCS Testing for BWR Stability Analysis," January 31, 2007, ADAMS Accession No. ML070380086.
8. Y. Xu et al., "Multi-Physics Coupled Code Reactor Analysis with the U.S. NRC Code System TRACE/PARCS," ANS Topical Meeting on Reactor Physics, PHYSOR-2006, Vancouver, Canada, September 10-14, 2006.
9. U.S. Nuclear Regulatory Commission, "Safety Evaluation by the Office of Nuclear Reactor Regulation Related to Amendment No. 140 to Facility Operating License No. NPF-69 Nine Mile Point Nuclear Station, LLC, Nine Mile Point, Unit No. 2, Docket No. 50-410," December 22, 2011, ADAMS Accession No. ML113560333.
10. J. Harrison, GE Hitachi, letter to U.S. Nuclear Regulatory Commission, "Response to NRC's Data Request to Support Confirmatory ATWS Calculations Regarding MELLLA Plus," MFN 09-681, November 4, 2009, ADAMS Accession No. ML093170371.
11. U.S. Nuclear Regulatory Commission, "Summary of Trip Report for Site Visit to Brookhaven National Laboratory August 2010," February 12, 2015, ADAMS Accession No. ML15043A802.
12. U.S. Nuclear Regulatory Commission, "Summary of Trip Report for Site Visit to Brookhaven National Laboratory October 2010," February 12, 2015, ADAMS Accession No. ML15043A803.
13. U.S. Nuclear Regulatory Commission, "Summary of Trip Report for Site Visit to Brookhaven National Laboratory February 2011," February 12, 2015, ADAMS Accession No. ML15043A804.
14. U.S. Nuclear Regulatory Commission, "Summary of Trip Report for Site Visit to Brookhaven National Laboratory April 2011," February 12, 2015, ADAMS Accession No. ML15043A805.

15. U.S. Nuclear Regulatory Commission, "Summary of Trip Report for Site Visit to Brookhaven National Laboratory August 2011," February 12, 2015, ADAMS Accession No. ML15043A806.
16. U.S. Nuclear Regulatory Commission, "Summary of Trip Report for Site Visit to Brookhaven National Laboratory October 2010," February 12, 2015, ADAMS Accession No. ML15043A803.
17. L-Y. Cheng et al., "TRACE/PARCS Core Modeling of a BWR/5 for Accident Analysis of ATWS Events," *Trans. Am. Nucl. Soc.* 109, pp 979-982, November 2013.
18. A. Lingenfelter, Global Nuclear Fuels, letter to U.S. Nuclear Regulatory Commission, "NEDE-31152P, Global Nuclear Fuels, Fuel Bundle Designs, Revision 9 and Supplements 5 and 6, May 2007," FLN-2007-019, May 25, 2007, ADAMS Accession No. ML071510285.
19. L-Y. Cheng et al., "TRACE Assessment for BWR ATWS Analysis," BNL-91311-2010-IR, Brookhaven National Laboratory, April 22, 2010.
20. J. Harrison, GE Hitachi, letter to U.S. Nuclear Regulatory Commission, "Accepted Version of GE Licensing Topical Report NEDC-33006P-A, Revision 3 (TAC No. MD0277)," MFN 09-362, June 19, 2009, ADAMS Accession No. ML091800512.
21. J. Harrison, GE Hitachi, letter to U.S. Nuclear Regulatory Commission, "Response to Supplemental NRC Information Requests 8 through 14 – Confirmatory ATWS Calculations Regarding MELLLA+," MFN10-213, July 29, 2010.
22. L-Y. Cheng et al., "TRACE/PARCS Core Modeling of a BWR/5 for Accident Analysis of ATWS Events," *Trans. Am. Nucl. Soc.* 109, pp 979-982, November 2013.
23. T. Downar and D. Barber, "Final Technical Report," Task 3 of Task Order No. 8, Rev. 1, ESBWR Upgrades to TRAC-M, Under Contract NRC-04-02-054, Subtasks 3.1 and 3.2, University of Michigan, February 2003.
24. U.S. Nuclear Regulatory Commission, "Summary of Trip Report for Site Visit to Brookhaven National Laboratory October 2010," February 12, 2015, ADAMS Accession No. ML15043A803.
25. P. Yarsky, "TRACE/PARCS Evaluation of Potentially Limiting ATWS Events with Core Instability for the ABWR," Proceedings of ICAPP 2013, paper F-010, Jeju Island, Korea, April 14-18, 2013.
26. GE Hitachi Nuclear Energy, "Safety Analysis Report for Nine Mile Point Nuclear Station Unit 2 Constant Pressure Power Uprate (PUSAR)," NEDO-33351P, Rev. 0, May 31, 2009, ADAMS Accession No. ML091610104.
27. J. Harrison, GE Hitachi, letter to U.S. Nuclear Regulatory Commission, "Accepted Version of GE Licensing Topical Report NEDC-33173P, Applicability of GE Methods to Expanded Operating Domains, (TAC No. MD0277)," October 5, 2010, ADAMS Accession No. ML102920131.
28. B. Ade et al, "SCALE/TRITON-PARCS Code Validation with BWR Steady-State Plant Operating Data", ORNL/TM-2011/256, Oak Ridge National Laboratory, November 2011.

29. J. Harrison, GE Hitachi, letter to U.S. Nuclear Regulatory Commission, "Response to Supplemental NRC Information Requests 8 through 14 – Confirmatory ATWS Calculations Regarding MELLLA+," MFN10-213, July 29, 2010.
30. T. Zaki et al., "Use of White Noise in TRACE/PARCS Analysis of ATWS with Instability," Proceedings of NURETH-16, Chicago, IL, August 30-September 4, 2015 (to be published).
31. U.S. Nuclear Regulatory Commission, "Summary of Trip Report for Site Visit to Brookhaven National Laboratory January 2012," February 12, 2015, ADAMS Accession No. ML15043A807.
32. U.S. Nuclear Regulatory Commission, "Standard Review Plan," NUREG-0800, Chapter 15, 2007.
33. D. D. B. van Bragt and T. H. J. J. van der Hagen, "Stability of Natural Circulation Boiling Water Reactors: Part I – Description Stability Model and Theoretical Analysis in Terms of Dimensionless Groups," *Nucl. Technol.*, 121, 40, January 1998.
34. J. March-Leuba, "Density-Wave Instabilities in Boiling Water Reactors," NUREG/CR-6003, U.S. Nuclear Regulatory Commission, September 1992.
35. M. J. Feigenbaum, "The Transition to Aperiodic Behavior in Turbulent Systems," *Commun. Math. Phys.* 77, 65, 1980.
36. J. March-Leuba, D. G. Cacuci, and R. B. Perez, "Nonlinear Dynamics and Stability of Boiling Water Reactors: Part 1 – Qualitative Analysis," *Nucl. Sci. Eng.*, 93, 111, 1986.
37. "Neutronics/Thermal-Hydraulics Coupling in LWR Technology: State-of the-art Report (REAC-SOAR)," CRISSUE-S-WP2, ISBN 92-64-02084-5, NEA No. 5436, Nuclear Energy Agency, OECD, 2004.

APPENDIX A

TRACE Calculation Notebook: BWR/5 Model for ATWS Analysis

TABLE OF CONTENTS

1	TRACE MODEL	A-9
1.1	System Model.....	A-10
1.2	Vessel Model.....	A-19
1.3	Vessel Heat Structures	A-21
1.4	CHAN Model	A-22
1.5	Guidetubes	A-25
1.6	Core Bypass Flow	A-25
1.7	Jet Pump	A-27
1.8	Steam Separator	A-27
1.9	Recirculation Loop.....	A-27
1.10	Main Steamline.....	A-29
1.11	Turbine Control/Bypass Valve	A-31
1.12	SRV/ADS.....	A-33
1.13	Feedwater and Reactor Water Level Control	A-37
1.14	Reactor Core Isolation Cooling System	A-42
1.15	Standby Liquid Control System.....	A-54
1.16	Lower Plenum Flow Valve	A-55
1.17	Containment.....	A-57
1.18	Boron Inventory in the Core.....	A-60
1.19	Signal Variables and Control Blocks for the VESSEL Component	A-65
1.20	Signal Variables and Control Blocks for the Representative Channels	A-66
2	REFERENCES	A-74

LIST OF FIGURES

Figure A.1	Component View of the BWR/5 Plant	A-11
Figure A.2	TRACE VESSEL Model	A-20
Figure A.3	GE14 Rod Layout	A-23
Figure A.4	Core Bypass Flow Paths.....	A-26
Figure A.5	Recirculation Loop	A-29
Figure A.6	Main Steamline	A-30
Figure A.7	Turbine Control/Bypass Valve Control Logic.....	A-32
Figure A.8	Model for Determining Turbine Bypass Valve Flow Areas.....	A-33
Figure A.9	SRV and ADS Control Logic	A-35
Figure A.10	Feedwater Line	A-38
Figure A.11	Feedwater Flow Control Logic	A-38
Figure A.12	Water Level Control Logic.....	A-39
Figure A.13	Feedwater Temperature Control Logic.....	A-42
Figure A.14	NPSH Limit [5]	A-43
Figure A.15	RCIC Flow vs. Reactor Pressure [5]	A-44
Figure A.16	Control System for Stopping Feedwater.....	A-46
Figure A.17	Control System for RCIC Flow from CST	A-48
Figure A.18	Control System for RCIC Flow from SP	A-51
Figure A.19	Lower Plenum Flow Valve Control Logic.....	A-56
Figure A.20	Containment and Suppression Pool Cooler System.....	A-58
Figure A.21	Control Logic for the Suppression Pool Cooler.....	A-59
Figure A.22	Control System Diagram for Calculating Boron Inventory.....	A-64
Figure A.23	Control Logic for the Calculation of Pressure Losses in a Channel	A-73

LIST OF TABLES

Table A.1	Summary of TRACE Components.....	A-12
Table A.2	Component Nodalization and Orientation.....	A-15
Table A.3	Component Connections.....	A-16
Table A.4	3D Level Tracking Option for the VESSEL.....	A-21
Table A.5	Location of Heat Structures.....	A-22
Table A.6	Characteristics of Rod Groups in Bundles.....	A-23
Table A.7	Material Composition of the Fuel Rod.....	A-24
Table A.8	Core Bypass Flow Paths for a BWR/5.....	A-26
Table A.9	Signal Variables for the Steamline Components.....	A-31
Table A.10	Equivalent Turbine Control Valve Area for Different Bypass Capacities.....	A-33
Table A.11	ADS/SRV Valve Setpoints.....	A-34
Table A.12	Signal Variables, Control Blocks, and Trips Used in Control Logic for.....	A-36
Table A.13	SRV/ADS Valve Flow Area Fraction.....	A-37
Table A.14	Trips, Signal Variables (SV) and Control Blocks (CB) for.....	A-40
Table A.15	Functional Form of CBs 43, 44, 45 and 42.....	A-41
Table A.16	Pressure and Temperature Values shown in Figure A.14.....	A-43
Table A.17	RCIC Flow vs. Reactor Pressure Shown in Figure A.15.....	A-45
Table A.18	CST Capacities.....	A-45
Table A.19	Signal Variables, Control Blocks, and Trips Used in.....	A-47
Table A.20	Signal Variables, Control Blocks, and Trips Used in Control Logic.....	A-49
Table A.21	Input Information for FILL-92.....	A-50
Table A.22	Signal Variables, Control Blocks, and Trips Used in Control Logic.....	A-52
Table A.23	Input Information for FILL-91.....	A-54
Table A.24	Control Components for Valve 34.....	A-56
Table A.25	Control Components for the Suppression Pool Cooler.....	A-59
Table A.26	Control Components for Calculating the Boron Inventory.....	A-61
Table A.27	Signal Variables and Control Blocks Identified.....	A-65
Table A.28	Control Components for the Representative Channels.....	A-67

Nomenclature

Acronym	Definition
ADS	Automatic Depressurization System
ATWS	Anticipated Transient Without SCRAM
ATWS-ED	Anticipated Transient Without SCRAM with Emergency Depressurization
ATWS-I	Anticipated Transient Without SCRAM with Instability
BWR	Boiling Water Reactor
BYP	Bypass Capacity
CB	Control Block in TRACE Input
CHAN	Channel Component in TRACE Input
CONTAN	Containment Component in TRACE Input
CRGT	Control Rod Guide Tube
CST	Condensate Storage Tank
ECCS	Emergency Core Cooling System
FW	Feedwater
FWH	Feedwater Heater
FWTR	Feedwater Temperature Reduction
GE	General Electric
GEH	GE Hitachi
GNF	General Nuclear Fuel
HCTL	Heat Capacity Temperature Limit
HPCS	High Pressure Core Spray
HTSTR	Heat Structure in TRACE Input
HSBW	Hot Shutdown Boron Weight
ISL	Information Systems Laboratories, Inc.
JUN	Junction in TRACE Input
LOCA	Loss-of-Coolant Accident
LP	Lower Plenum
LPV	Lower Plenum Valve
LPCI	Low Pressure Core Injection
LPCS	Low Pressure Core Spray
LTP	Lower Tie Plate
MELLLA	Maximum Extended Load Line Limit Analysis
MELLLA+	Maximum Extended Load Line Limit Analysis Plus
MSIV	Main Steam Isolation Valve
NFI	Nuclear Fuels Industries
NPSH	Net Positive Suction Head
OOS	Out-of-Service
OPRM	Oscillation Power Range Monitor
PARCS	Purdue Advanced Reactor Core Simulator
RCIC	Reactor Core Isolation Cooling System
RHR	Residual Heat Removal System
RPT	Recirculation Pump Trip
RPV	Reactor Pressure Vessel
RWL	Reactor Water Level
RWLRS	Reactor Water Level Recovery Strategy
SBLOCA	Small-Break Loss-of-Coolant Accident

Acronym	Definition
SEPD	Steam Separator/Dryer Component in TRACE Input
SJC	Single-Junction Connection in TRACE Input
SLCS	Standby Liquid Control System
SNAP	Symbolic Nuclear Analysis Package
SP	Suppression Pool
SPCM	Suppression Pool Cooling Mode
SRV	Safety Relief Valve
SRVOOS	Safety Relief Valve Out of Service
SV	Signal Variable in TRACE Input
TAF	Top-of-ActiveFuel
TAF+5	Top-of-Active-Fuel Plus Five Feet
TAF-2	Top-of-Active-Fuel Minus Two Feet
TBS	Turbine Bypass System
TBV	Turbine Bypass Valve
TCV	Turbine Control Valve
TRACE	TRAC-RELAP Advanced Computational Engine
TRACG	Transient Reactor Analysis Code (GE version)
TSV	Turbine Stop Valve
TT	Turbine Trip
WLEN	TRACE Built-in Water Level Controller

1 TRACE MODEL

This notebook describes the development of a TRACE BWR/5 model for TRACE/PARCS coupled analysis of BWR ATWS events. The appendix is limited to non-proprietary aspects of the model and includes how the model is used to emulate a BWR/4. It summarizes user experience and provides feedback on the suite of computer codes utilized in the ATWS calculations: TRACE/PARCS, SNAP, and AptPlot. The ATWS calculations are to confirm results at MELLLA+ operating conditions for two specific plant scenarios: ATWS-I, initiated by a turbine trip and leading to large-amplitude core oscillations (both core-wide and regional), and ATWS-ED, initiated by closure of main steam isolation valves (MSIVs) and leading to emergency depressurization once the heat capacity temperature limit (HCTL) of the suppression pool is exceeded. In addition the analyses are to assess the capabilities of TRACE/PARCS to calculate the thermal-hydraulic and neutronic phenomena associated with BWR ATWS and reactor stability events. The development of the TRACE BWR/5 model evolved over months with changes and modifications due to either code fixes or new information/guidance from the NRC staff. That guidance pertains to the applications in this project and does not represent any NRC policy or acceptable method for any other applications.

The TRACE BWR/5 model builds on a small-break loss-of-coolant accident (SBLOCA) input model from ISL [1], herein referred to as the base reference model, supplemented by information derived from TRACG input decks and results of the TRACG analyses from GEH [2]. The following is a summary of modifications to the ISL SBLOCA model [1] (i.e. the base reference model).

1. Increased the number of CHANs from three in the base reference model to 27 and 382 for the ATWS-ED and the ATWS-I cases, respectively.
2. Merged two recirculation loops into one.
3. Adjusted jet pump inlet flow area to reduce steady-state core flow from 119% to 100%.
4. Merged two main steamlines to one.
5. Adjusted the steamline pressure loss coefficient to reduce vessel dome pressure to rated value.
6. Eliminated emergency core cooling system (ECCS) PIPEs and FILLs – low pressure core spray (LPCS) and low pressure coolant injection (LPCI).
7. Implemented safety/relief valve (SRV) and automatic depressurization system (ADS) control logic with two SRVs assumed out of service.
8. Simplified the SRV discharge line by modeling the SRV as a single-junction valve discharging to a BREAK volume that is connected to the wetwell.
9. Implemented turbine control valve logic to emulate the turbine bypass system with different bypass capacity.
10. Implemented the standby liquid control system (SLCS) with two injection paths – upper plenum and lower plenum.
11. Segmented the bottom volume of the VESSEL into three axial volumes.
12. Modified free volumes in rings 2 and 3 of the VESSEL at axial levels 11 and 12. Also minor axial height adjustments in axial levels 8, 9 and 10.
13. Implemented a flow valve in the lower plenum to simulate boron remixing.
14. Implemented new feedwater (FW) control logic to enable level regulation in a transient and termination of FW flow when the condensate storage tank (CST) is depleted.
15. Implemented a FW temperature controller to emulate a reduction in FW temperature associated with a loss of extraction steam after MSIV/turbine trip.

16. Implemented injection points and control logic for the RCIC, switching suction from the CST to the suppression pool when the CST reserve for the reactor core isolation cooling system (RCIC) is depleted.
17. Implemented CHAN geometry from the TRACG model.
18. Incorporated relative assembly power and radially averaged relative axial power in the CHAN components using data from the GEH analyses.
19. Incorporated a dynamic gap model in the four rod groups (for the fuel) in each CHAN.
20. Developed inputs for the dynamic gap model using results from FRAPCON calculations.
21. Enabled the use of the modified NFI correlation for fuel thermal conductivity.
22. Modified inputs for guidetubes, CHAN and VESSEL to model core bypass flow.
23. Modified inlet loss coefficients for peripheral fuel assemblies.
24. Updated the model for the channel leakage flow through the lower tie plate.
25. Created a model for the suppression pool cooler that emulates the suppression pool cooling mode of the residual heat removal system.
26. Implemented three dimensional (3D) level tracking for the VESSEL.
27. Implemented coupling between the TRACE stand-alone models and the PARCS module.
28. Implemented various model changes to work around code limitations.
29. Defined various signal variables and control blocks for trips (e.g. recirculation pump trip), controls (e.g. water level control), and outputs (e.g. boron inventory in the core region).
30. Implemented steady-state controllers to initialize recirculation flow and turbine inlet pressure.

1.1 System Model

The TRACE model of the BWR/5 plant consists of a number of hydraulic components and heat structures. There is also a POWER component (to define 100% power for the TRACE stand-alone steady-state initialization), signal variables, control blocks and trips. BWR/4 plant configuration options are included to allow the model to simulate BWR/4-like conditions (specifically the location of the SLCS injection into the vessel).

Figure A.1 is a node diagram providing the component view of the complete model. The model consists of a BWR vessel (with internals consisting of one jet pump, a lower plenum flow control valve, two control rod guidetubes, fuel assembly CHANs, and two steam separators), one recirculation loop with recirculation pump and flow control valve, a feedwater line, a RCIC line (the current model has the RCIC injecting into the FW line but the actual injection location can also be changed depending on plant configuration) with option to draw from the CST or the suppression pool, two SLCS lines (for lower plenum and upper plenum injection), a main steamline with in-board and out-board MSIVs and a branch to SRV/ADS valves, turbine control valve, and a primary containment (drywell and wetwell) with suppression pool cooler. The model also has a BREAK junction in the recirculation line and a HPCS system; they are for future applications. The core is modeled by either 27 or 382 CHAN components, each representing two or more GE14 fuel assemblies. Table A.1 summarizes the hydraulic components and heat structures included in the 27-channel TRACE model. It is noted that the component numbers do not necessarily correspond to the original SBLOCA deck [1].

The TRACE model described in this notebook is applicable in general to both the 27-channel and the 382-channel model. The most distinguishing difference between the two models is the mapping of fuel assemblies to channel components. The 382-channel model is for the ATWS-I

analysis (assuming a half-core symmetry in the TRACE thermal-hydraulic calculations) while the 27-channel model is for the ATWS-ED analysis. Planned changes and new features to be implemented in the ATWS-ED model are summarized by footnotes in this notebook.

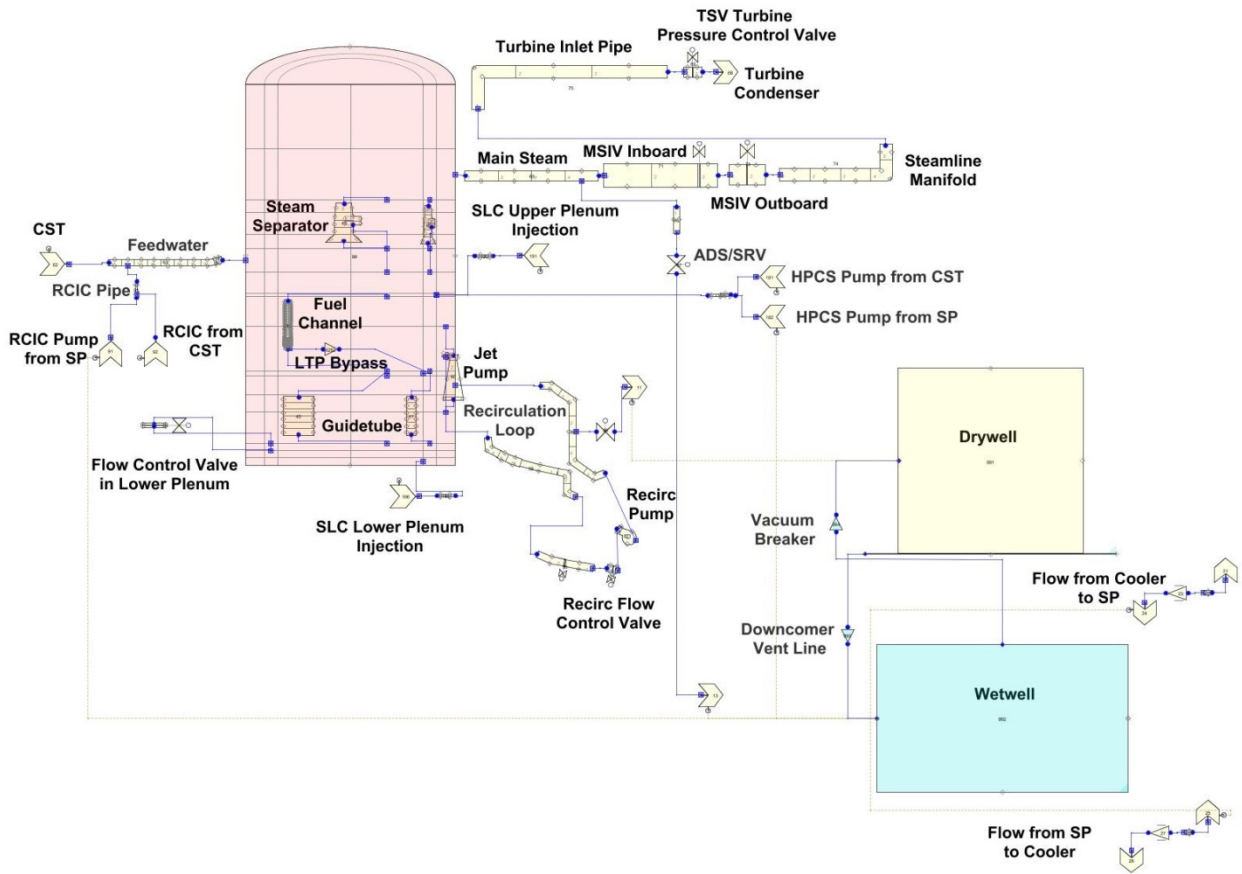


Figure A.1 Component View of the BWR/5 Plant

Table A.1 Summary of TRACE Components

Type	Comp #	Name	Junctions
BREAK	11	\$11\$ bkn-loop contain. break 1	71150
BREAK	13	\$13\$ SRV/ADS break 1	71207
BREAK	21	Cooler to SP	71195
PIPE	22	Cooler to SP	71195 71196
PUMP	23	SJC pump - flow to SP	71196 71194
BREAK	24	Break connection (to SP)	71194
BREAK	25	Break connection (from SP)	71197
PIPE	26	SP to Cooler	71197 71198
PUMP	27	SJC pump - flow from SP	71198 71199
BREAK	28	SP to Cooler	71199
VALVE	34	Valve 34 Lower Plenum	33 35
VALVE	36	Recir-Break-1	71164 71150
PIPE	40	\$40\$ Guidetube1	5 14
PIPE	41	\$41\$ Guidetube2	23 32
SEPD	45	\$45\$ Separator1	41 50 59
SEPD	46	\$46\$ Separator2	68 77 86
PIPE	50	\$50\$ Recirculation1	71162 71163
PUMP	52	\$52\$ Recircpump1	71163 113
VALVE	54	\$54\$ Recirc Flow Control Valve	113 122
VALVE	56	\$56\$ Recirc Discharge Valve1	122 131
PIPE	58	\$58\$ Recirc Discharge1	131 140
JETP	60	\$60\$ Jetpump1	149 158 140
FILL	62	\$62\$ Feedwater	1
PIPE	63	\$63\$ Feedwater Piping	1 163
PIPE	65	\$65\$ Steamlineoutlet1	29 21
PIPE	66	\$66\$ Standpipe for SRV	71155 71206
VALVE	67	\$67\$ ADS/SRV1	71206 71207
BREAK	68	\$68\$ turbine 1st stage inlet	71185
VALVE	69	Valve 69 TSV	71205 71185
VALVE	71	\$71\$ MSIVinboard1	21 22
VALVE	73	\$73\$ MSIVoutboard1	22 25
PIPE	74	\$74\$ Steamline Manifold	25 71204
PIPE	75	\$75\$ Turbineinletpiping	71204 71205
PIPE	81	\$81\$ RCIC Pipe	71178 71179
FILL	91	\$91\$ RCIC from SP	71178
FILL	92	\$92\$ RCIC from CST	71186
VESSEL	99	\$99\$ RPV2D	
POWER	100	Power	
FILL	181	\$181\$ HPCS from CST	71165

Type	Comp #	Name	Junctions
FILL	182	\$182\$ HPCS from SP	71166
TEE	183	\$183\$ HPCS Injection Pipe	71167 71166 71165
PIPE	190	\$190\$SLCS Injection Pipe	192 193
FILL	191	\$191\$ SLC FILL	192
PIPE	195	\$195\$SLCS Injection to LP	197 198
FILL	196	\$196\$ SLC FILL	197
CHAN	251	\$251\$	1251 2251
CHAN	252	\$252\$	1252 2252
CHAN	261	\$261\$	1261 2261
CHAN	262	\$262\$	1262 2262
CHAN	271	\$271\$	1271 2271
CHAN	272	\$272\$	1272 2272
CHAN	281	\$281\$	1281 2281
CHAN	282	\$282\$	1282 2282
CHAN	291	\$291\$	1291 2291
CHAN	292	\$292\$	1292 2292
CHAN	351	\$351\$	1351 2351
CHAN	352	\$352\$	1352 2352
CHAN	361	\$361\$	1361 2361
CHAN	362	\$362\$	1362 2362
CHAN	371	\$371\$	1371 2371
CHAN	372	\$372\$	1372 2372
CHAN	451	\$451\$	1451 2451
CHAN	452	\$452\$	1452 2452
CHAN	461	\$461\$	1461 2461
CHAN	462	\$462\$	1462 2462
CHAN	551	\$551\$	1551 2551
CHAN	552	\$552\$	1552 2552
CHAN	651	\$651\$	1651 2651
CHAN	652	\$652\$	1652 2652
CHAN	751	\$751\$	1751 2751
CHAN	752	\$752\$	1752 2752
CHAN	753	\$753\$	1753 2753
CONTAN	999	Containment	
PIPE	6251	\$6251\$	5251 7251
PIPE	6252	\$6252\$	5252 7252
PIPE	6261	\$6261\$	5261 7261
PIPE	6262	\$6262\$	5262 7262
PIPE	6271	\$6271\$	5271 7271
PIPE	6272	\$6272\$	5272 7272

Type	Comp #	Name	Junctions
PIPE	6281	\$6281\$	5281 7281
PIPE	6282	\$6282\$	5282 7282
PIPE	6291	\$6291\$	5291 7291
PIPE	6292	\$6292\$	5292 7292
PIPE	6351	\$6351\$	5351 7351
PIPE	6352	\$6352\$	5352 7352
PIPE	6361	\$6361\$	5361 7361
PIPE	6362	\$6362\$	5362 7362
PIPE	6371	\$6371\$	5371 7371
PIPE	6372	\$6372\$	5372 7372
PIPE	6451	\$6451\$	5451 7451
PIPE	6452	\$6452\$	5452 7452
PIPE	6461	\$6461\$	5461 7461
PIPE	6462	\$6462\$	5462 7462
PIPE	6551	\$6551\$	5551 7551
PIPE	6552	\$6552\$	5552 7552
PIPE	6651	\$6651\$	5651 7651
PIPE	6652	\$6652\$	5652 7652
PIPE	6751	\$6751\$	5751 7751
PIPE	6752	\$6752\$	5752 7752
PIPE	6753	\$6753\$	5753 7753

Component numbers between 201 and 964 have been reserved for the CHAN components and component numbers between 6201 and 6964 have been reserved for the single-junction connection (SJC), modeled as PIPE with zero volume, representing the bypass orifice in the lower tie plate (LTP) of a fuel assembly. Each CHAN XXX then has a corresponding SJC PIPE 6XXX. In addition the following junction numbers have been reserved for connection junctions associated with the CHAN components:

- Junctions 1201 to 1964 for CHAN inlet junction
- Junctions 2201 to 2964 for CHAN outlet junction
- Junctions 3201 to 3964 for water rod inlet junction
- Junctions 4201 to 4964 for water rod outlet junction
- Junctions 5201 to 5964 for junction between the CHAN and the SJC in the LTP
- Junctions 7201 to 7964 for junction between the SJC in the LTP and the VESSEL

It is noted that the reserved component/junction numbers allow the TRACE model to simulate a core with up to 764 individual CHANs. Table A.1 lists the CHANs for the 27-channel model. For the 382-channel model the channel numbers (XXX) run consecutively from 201 to 582.

Component nodalization and connections are summarized in Table A.2 and Table A.3, respectively and in these tables only one CHAN is shown for illustration because the geometric dimensions of all CHANs are identical. The two tables are extracted from the results of running a SNAP model closure check and it confirms that the TRACE model satisfies loop closure.

Table A.2 Component Nodalization and Orientation

Component	Node	Inlet Angle (deg)	Outlet Angle (deg)	Component	Node	Inlet Angle (deg)	Outlet Angle (deg)
Vessel 99	1-17	90	90	Pipe 190	1-2	0	0
Channel 252	1-40	90	90	Pipe 63	1-7	0	0
Tee 183	1-4	0	0	Pipe 63	8	0	10.043
Pipe 50	1	0	-34.377	Pipe 63	9	10.043	22.024
Pipe 50	2	-34.377	-90	Pipe 63	10	22.024	0
Pipe 50	3	-90	-90	Pipe 81	1-2	90	90
Pipe 50	4	-90	-34.377	Separator 46	1-5	90	90
Pipe 50	5	-34.377	19.194	Separator 46	6-7	-90	-90
Pump 52	1	19.194	46.352	Separator 45	1-5	90	90
Pump 52	2	46.352	35.523	Separator 45	6-7	-90	-90
Valve 54	1	35.523	9.568	Valve 34	1-2	-90	-90
Valve 54	2	9.568	9.568	Pipe 41	1-6	90	90
Valve 56	1	9.568	11.459	Pipe 65	1-4	0	0
Valve 56	2	11.459	24.122	Valve 71	1-3	0	0
Pipe 58	1	24.122	90	Valve 73	1-2	0	0
Pipe 58	2	90	11.459	Pipe 74	1-3	0	0
Pipe 58	3	11.459	15.756	Pipe 74	4	0	90
Pipe 58	4	15.756	22.918	Pipe 74	5	90	90
Pipe 58	5	22.918	28.648	Pipe 75	1	90	0
Pipe 58	6	28.648	82.391	Pipe 75	2-3	0	0
JetPump 60	1-3	-90	-90	Valve 69	1-2	0	0
JetPump 60	4	90	0	Pipe 66	1	-90	-90
JetPump 60	5	0	82.391	Pipe 40	1-6	90	90
Pipe 195	1-2	0	0				

Table A.3 Component Connections

Component	Connection Location
Vessel 99	Root Component (Reference 0.0 is at the bottom of the VESSEL)
Vessel 99	Jun 7252 To Single Junction 6252
Vessel 99	Jun 2252 To Channel 252
Vessel 99	Jun 71167 To Tee 183
Vessel 99	Jun 71162 To Pipe 50
Vessel 99	Jun 198 To Pipe 195
Vessel 99	Jun 193 To Pipe 190
Vessel 99	Jun 163 To Pipe 63
Vessel 99	Jun 158 To JetPump 60
Vessel 99	Jun 149 To JetPump 60
Vessel 99	Jun 1252 To Channel 252
Vessel 99	Jun 86 To Separator 46
Vessel 99	Jun 77 To Separator 46
Vessel 99	Jun 68 To Separator 46
Vessel 99	Jun 59 To Separator 45
Vessel 99	Jun 50 To Separator 45
Vessel 99	Jun 41 To Separator 45
Vessel 99	Jun 35 To Valve 34
Vessel 99	Jun 33 To Valve 34
Vessel 99	Jun 32 To Pipe 41
Vessel 99	Jun 29 To Pipe 65
Vessel 99	Jun 23 To Pipe 41
Vessel 99	Jun 14 To Pipe 40
Vessel 99	Jun 5 To Pipe 40
Single Junction 6252	Source: Jun 7252 From Vessel 99
Single Junction 6252	Jun 5252 To Channel 252
Single Junction 6252	Jun 7252 To Vessel 99
Channel 252	Source: Jun 5252 From Single Junction 6252
Channel 252	Jun 1252 To Vessel 99
Channel 252	Jun 2252 To Vessel 99
Channel 252	Jun 5252 To Single Junction 6252
Tee 183	Source: Jun 71167 From Vessel 99
Tee 183	Jun 71167 To Vessel 99
Tee 183	Jun 71166 To Fill 182
Tee 183	Jun 71165 To Fill 181
Pipe 50	Source: Jun 71162 From Vessel 99
Pipe 50	Jun 71162 To Vessel 99
Pipe 50	Jun 71163 To Pump 52
Pipe 50	Jun 71164 To Valve 36

Component	Connection Location
Pump 52	Source: Jun 71163 From Pipe 50
Pump 52	Jun 71163 To Pipe 50
Pump 52	Jun 113 To Valve 54
Valve 54	Source: Jun 113 From Pump 52
Valve 54	Jun 113 To Pump 52
Valve 54	Jun 122 To Valve 56
Valve 56	Source: Jun 122 From Valve 54
Valve 56	Jun 122 To Valve 54
Valve 56	Jun 131 To Pipe 58
Pipe 58	Source: Jun 131 From Valve 56
Pipe 58	Jun 131 To Valve 56
Pipe 58	Jun 140 To JetPump 60
JetPump 60	Source: Jun 140 From Pipe 58
JetPump 60	Jun 149 To Vessel 99
JetPump 60	Jun 158 To Vessel 99
JetPump 60	Jun 140 To Pipe 58
Valve 36	Source: Jun 71164 From Pipe 50
Valve 36	Jun 71164 To Pipe 50
Valve 36	Jun 71150 To Break 11
Pipe 195	Source: Jun 198 From Vessel 99
Pipe 195	Jun 197 To Fill 196
Pipe 195	Jun 198 To Vessel 99
Pipe 190	Source: Jun 193 From Vessel 99
Pipe 190	Jun 192 To Fill 191
Pipe 190	Jun 193 To Vessel 99
Pipe 63	Source: Jun 163 From Vessel 99
Pipe 63	Jun 1 To Fill 62
Pipe 63	Jun 163 To Vessel 99
Pipe 63	Jun 71179 To Pipe 81
Pipe 81	Source: Jun 71179 From Pipe 63
Pipe 81	Jun 71178 To Fill 91
Pipe 81	Jun 71179 To Pipe 63
Pipe 81	Jun 71186 To Fill 92
Separator 46	Source: Jun 86 From Vessel 99
Separator 46	Jun 68 To Vessel 99
Separator 46	Jun 77 To Vessel 99
Separator 46	Jun 86 To Vessel 99
Separator 45	Source: Jun 59 From Vessel 99
Separator 45	Jun 41 To Vessel 99
Separator 45	Jun 50 To Vessel 99
Separator 45	Jun 59 To Vessel 99

Component	Connection Location
Valve 34	Source: Jun 35 From Vessel 99
Valve 34	Jun 33 To Vessel 99
Valve 34	Jun 35 To Vessel 99
Pipe 41	Source: Jun 32 From Vessel 99
Pipe 41	Jun 23 To Vessel 99
Pipe 41	Jun 32 To Vessel 99
Pipe 65	Source: Jun 29 From Vessel 99
Pipe 65	Jun 29 To Vessel 99
Pipe 65	Jun 21 To Valve 71
Pipe 65	Jun 71155 To Pipe 66
Valve 71	Source: Jun 21 From Pipe 65
Valve 71	Jun 21 To Pipe 65
Valve 71	Jun 22 To Valve 73
Valve 73	Source: Jun 22 From Valve 71
Valve 73	Jun 22 To Valve 71
Valve 73	Jun 25 To Pipe 74
Pipe 74	Source: Jun 25 From Valve 73
Pipe 74	Jun 25 To Valve 73
Pipe 74	Jun 71204 To Pipe 75
Pipe 75	Source: Jun 71204 From Pipe 74
Pipe 75	Jun 71204 To Pipe 74
Pipe 75	Jun 71205 To Valve 69
Valve 69	Source: Jun 71205 From Pipe 75
Valve 69	Jun 71205 To Pipe 75
Valve 69	Jun 71185 To Break 68
Pipe 66	Source: Jun 71155 From Pipe 65
Pipe 66	Jun 71155 To Pipe 65
Pipe 66	Jun 71206 To Valve 67
Valve 67	Source: Jun 71206 From Pipe 66
Valve 67	Jun 71206 To Pipe 66
Valve 67	Jun 71207 To Break 13
Pipe 40	Source: Jun 14 From Vessel 99
Pipe 40	Jun 5 To Vessel 99
Pipe 40	Jun 14 To Vessel 99

The above discussion provides an overview of the layout of the hydraulic components in the TRACE BWR/5 plant model. The following sub-sections provide more detailed description of each hydraulic component including the derivation of some of the input parameters and the trips and controls implemented in the TRACE model to simulate plant behavior in an ATWS transient. The NRC staff has provided a number of guidance documents during the development of the TRACE model and they are cited here as References [3] through [8].

1.2 Vessel Model

Figure A.2 shows the reactor vessel with its internal components and connections to internal and some external components. The VESSEL model is based on the SBLOCA deck [1] with several modifications¹.

1. segmentation of the bottom volume of the vessel into three volumes of equal height
2. addition of a flow control valve in the lower plenum
3. minor axial height adjustments in axial levels 8, 9 and 10 to align the elevations of the axial levels of the VESSEL with the elevations of the cell face of the axial nodes of the CHAN components
4. adjustment of heat structure geometry corresponding to changes in 1) and 3).
5. implementation of 3D level tracking
6. modifications to give more geometrically accurate free volume fractions in rings 2 and 3 at axial levels 11 and 12
7. setting to zero the axial flow areas in rings 1 and 2 at axial level 6 (corresponding to the core support plate elevation)
8. using two guidetubes to model core bypass flow through the core support plate

Modifications 1) and 2) are implemented to enable a more realistic simulation of boron mixing in the lower plenum and modification 3) is needed by TRACE to accurately calculate neutronic nodal average boron concentrations.

¹Items 2) and 5) of the list will be modified for the ATWS-ED analysis.

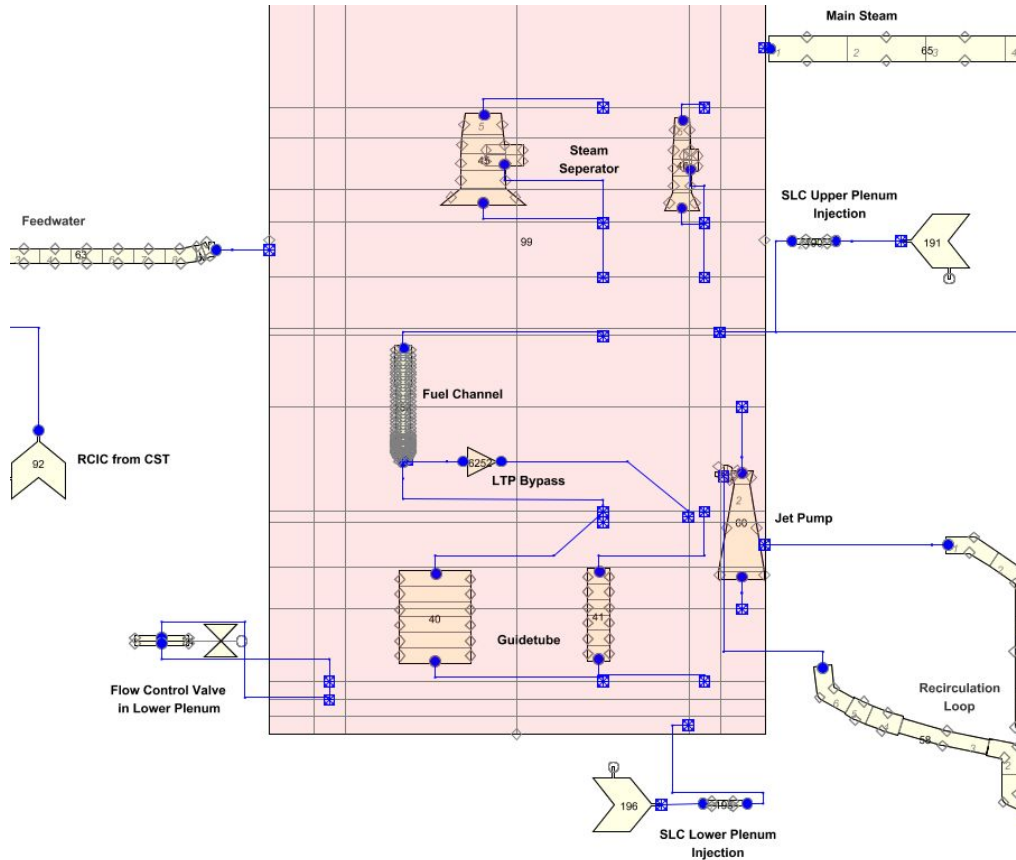


Figure A.2 TRACE VESSEL Model

The VESSEL has 17 axial levels, three radial rings and one azimuthal segment, i.e. a two-dimensional vessel model. The different regions of the reactor vessel are defined as follows:

- Reactor core region occupies the two central radial rings and spans axial levels 7, 8 and 9.
- Upper plenum occupies rings 1 and 2 in axial levels 10 and 11.
- Steam separator spans axial levels 12 through 15.
- Steam dome occupies rings 1 and 2 in level 16 and all 3 rings in level 17.
- Downcomer is in the outermost ring and occupies axial levels 5 through 16.
- Jet pump spans axial levels 5 through 8 and its flow enters ring 3 at axial level 4.
- Axial levels 1 through 3 in ring 3 are dead volumes.
- Lower plenum occupies rings 1 and 2 in axial levels 1 through 4.
- Core inlet region occupies rings 1 and 2 in axial levels 5 and 6.

The VESSEL geometry is based primarily on the SBLOCA input [1] with some modifications highlighted earlier.

Based on user experience stable core flow is achieved when 3D level tracking is turned on only in the downcomer region and the vessel region outside the two steam separators. It is noted that these two regions are the only parts of the VESSEL where a free surface exists and thus it is logical to apply 3D level tracking only in these two regions. The particular 3D level tracking

option for different parts of the VESSEL is demonstrated in Table A.4². In the table a “0” indicates no level; a “-1” indicates level tracking is off; a “1” indicates 3D leveling tracking is on.

Table A.4 3D Level Tracking Option for the VESSEL

Axial Level	Ring 1	Ring2	Ring3
17	-1	-1	-1
16	-1	-1	-1
15	1	1	1
14	1	1	1
13	1	1	1
12	1	1	1
11	-1	-1	1
10	-1	-1	1
9	-1	-1	1
8	-1	-1	1
7	-1	-1	1
6	-1	-1	1
5	-1	-1	1
4	0	0	0
3	0	0	0
2	0	0	0
1	0	0	0

1.3 Vessel Heat Structures

The vessel heat structures are based on the SBLOCA deck [1] with modifications made to reflect changes in the height of the vessel axial levels. The designation (component number) and location of heat structures are shown in Table A.5 . Highlighted entries in the table indicate revisions over the SBLOCA deck.

² For the ATWS-ED analysis 3D level tracking is turned off in ring 3 between axial levels 9 (top-of-active-fuel, TAF) and 12 (feedwater sparger).

Table A.5 Location of Heat Structures

Axial Level	Lumped HS in Ring 1	Lumped HS in Ring 2	Two-Sided HS between Rings 2 & 3	Vessel Wall
17				99041
16	99037	99038	99039	99040
15			99035	99036
14			99033	99034
13				99032
12				99031
11			99029	99030
10			99027	99028
9	99023	99024	99025	99026
8	99019	99020	99021	99022
7	99015	99016	99017	99018
6	99011	99012	99013	99014
5	99007	99008	99009	99010
4	99003	99004	99005	99006
3	99001	99002		
2	98003	98004		
1	98001	98002		

It is noted that the pitch-to-diameter ratio of the heat slabs is set to 1.0 so as to represent slab geometry, a good approximation for the large vessel heat structures.

1.4 CHAN Model

The grouping of fuel assemblies into CHANs and the specialization of each CHAN in a multi-channel model are discussed in Appendices B and C, respectively. The following discussion focuses on the set of common inputs that applies to all CHANs in a multi-channel model.

The current TRACE model retains the ring structure of the VESSEL component from the SBLOCA deck; [1] thus the core size remains at 764 fuel assemblies with 616 assemblies in ring 1 and 148 assemblies in ring 2. Ninety-two of the fuel assemblies in ring 2 are identified as peripheral assemblies because they are located on the outer edge of the core next to the core shroud. The fuel assembly is modeled after a GE14 fuel bundle [2, 9]. Each GE14 fuel assembly has 92 fuel rods and two water rods arranged in a 10x10 array with each water rod occupying four grid positions. There are three types of fuel rods, full length, partial length and gad rod (full-length rods with integral gadolinia burnable poison) and they are grouped together as separate rod groups in the CHAN component. Figure A.3 [10] displays the arrangement of rod types in an assembly. A fourth and fifth rod group represent the hot rod in an assembly and the water rods respectively. Table A.6 summarizes the characteristics of each rod group. The relative rod power values used are based on guidance from the NRC staff [3,7].

Table A.6 Characteristics of Rod Groups in Bundles

Rod Group	Rod Type	Number of Rods
1	Regular full length fuel rod	77
3	Full length rod with gad	
2	Partial length fuel rod	14
4	Hot rod	1
5	Water rod (WR)	2 modeled as 1 WR

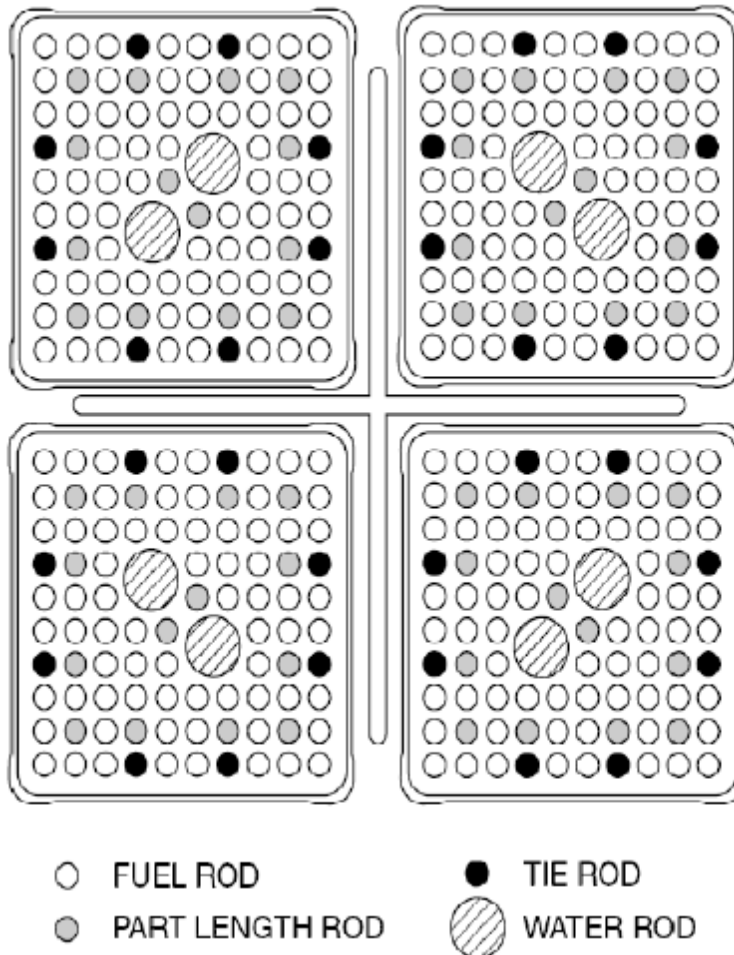


Figure A.3 GE14 Rod Layout

Table A.7 identifies the material composition of the fuel rods; there are nine mesh points that define the boundaries of eight material regions. The fuel pellet is bounded between mesh points 1 and 6. The radial power distribution within the fuel pellet is assumed to be uniform.

Table A.7 Material Composition of the Fuel Rod

Material Region	Material
1	<i>Fuel</i>
2	Fuel
3	Fuel
4	Fuel
5	Fuel
6	Gap Gas
7	Zr Clad
8	Zr Clad

One of the significant changes in modifying the TRACE SBLOCA model [1] is to increase the number of fuel channels to enable the simulation of regional power oscillation in an ATWS. A MATLAB based script has been created to use the input of a single CHAN to generate the required input for a multi-channel TRACE model (see Appendix C). In addition, the MATLAB script automated the preparation of the following parameters in the CHAN component input:

1. junction connections
2. number of fuel assemblies represented by the CHAN component
3. inlet orifice loss coefficient
4. the VESSEL ring where the CHAN is located and thus the interface for the canister wall heat structure
5. core wide radial CHAN-to-CHAN power peaking factor
6. gap gas composition for each fuel rod (group)
7. average burnup in each axial node of a fuel rod (group)
8. reference gap gas temperature for each fuel rod (group)
9. corresponding leakage junction in the lower tie plate

Parameters (6) and (7) are part of the additional inputs required for activating the dynamic gap model in TRACE. The MATLAB script evaluates these parameters from the results of FRAPCON [11] calculations conducted by the NRC staff [12]. The fuel-clad interaction option selected for the current model is a dynamic gas-gap model with elastic cladding deformation and the clad rupture model off (NFCI=2)³. This option is selected because it is the simplest dynamic gap model in TRACE that approximates the phenomena modeled in TRACG. The other input parameters required by the dynamic gap model are:

- UCRPDOWN (cladding deformation due to creepdown) = 0.0 (default value)
- UFSWELL (fuel pin strain due to fission gas induced fuel swelling and densification) = 0.0 (default value)
- RFCLAD (fuel pin surface roughness plus cladding surface roughness) = 0.0 (TRACE resets the value to 1.2×10^{-7} m)

³ For the ATWS-ED analysis a different dynamic gas-gap option is used (NFCI=3) to allow for the modeling of clad rupture. In addition, metal-water reaction and axial conduction (NMWRX=1 and IAXCND=1) are activated for the TRACE calculations.

The burnup information together with the gadolinia content in a fuel rod is used in the evaluation of the fuel thermal conductivity according to the modified NFI correlation (namelist option `USE_MODNFI_K = .TRUE.`). The gad rods are assumed to have a uniform gadolinia content of 7 wt% (`GADC = 0.07`).

The channel geometry retains the basic structure of the SBLOCA deck [1] but with some changes to conform to the TRACG model [2].

Each CHAN has 40 axial nodes and the active fuel occupies nodes 3 through 39. Based on the SBLOCA deck nodes 3 through 18 have one-fourth the axial length of the rest of the heated nodes. The more refined nodalization in the bottom of the fuel is intended to reduce numerical damping due to non-uniform Courant number in the fuel channel. The cell flow areas, volumes and hydraulic diameters are from the TRACG deck (with extrapolation to a 150 inch active fuel vs. the 148 inch fuel modeled in the TRACG deck). The spacer loss coefficients are from the TRACG deck and their axial locations are from a GNF figure provided by the NRC staff [13].

In addition to the fuel rods, the CHAN component also includes representation of the channel box and water rods. The canister walls of the channel box are modeled with information derived from GEH data provided by NRC staff [14]). For the water rod input the staff provided guidance [3,15] on location of the flow holes and the loss coefficients⁴.

1.5 Guidetubes

Rings 1 and 2 of the VESSEL are each modeled with one guidetube. Each guidetube is modeled by a PIPE component penetrating the core support plate with inlet in axial level 3 and outlet in axial level 7. The guidetubes (PIPE 40 and PIPE 41) are used to model core bypass flow (see Section 1.6) through the core support plate and they also provide an alternative flow path for the borated coolant to flow from the core bypass region (volume outside the channel box) allowing the settling (stratification) of the boron solution in the lower plenum of the vessel [3].

1.6 Core Bypass Flow

A number of bypass flow paths exist in a BWR and they are illustrated in Figure A.4 [16] and identified in Table A.8. The steady-state flow through each path for a BWR/5 with 764 fuel assemblies has been calculated by GEH.

The core bypass flow paths can be separated into two groups, a channel bypass group that constitutes flows leaking out of the fuel assembly (paths 6, 8 and 9) and a core support plate bypass group that constitutes flows traversing the core support plate (paths 1a, 1b, 2, 3, 4, and 5). Given the rated total core flow rate of 13671 kg/s (1.085E+08 lbm/hr) the bypass flow fractions for the two groups are derived from the GEH calculation.

TRACG has built-in models to calculate core bypass flows for different core and fuel designs. There is no equivalent model in TRACE and specific flow paths have to be developed to account for core bypass flows. In the current TRACE model the core support plate bypass flow is facilitated by the two guidetubes represented by PIPE 40 and PIPE 41. The channel bypass is facilitated by a side junction in the lower tie plate of a fuel channel. This is the 6XXX PIPE component (zero volume pipe) shown in Table A.1.

⁴ A higher reverse loss coefficient at the entrance flow holes is used in the ATWS-ED model to mitigate negative flow in the water rods.

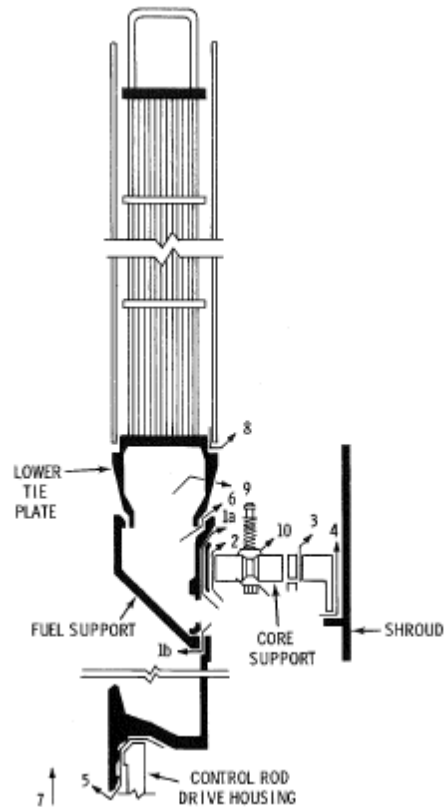


Figure A.4 Core Bypass Flow Paths

Table A.8 Core Bypass Flow Paths for a BWR/5

Path	Flow Path Description
1a	Fuel Sup-CR Guide Tube (Upper)
1b	Fuel Sup-CR Guide Tube (Lower)
2	Core Sup-CR Guide Tube
3	Core Sup-In Core Inst Guide Tube
4	Core Sup-Shroud
5	CR Guide Tube-CR Drive Housing
6	Fuel Sup-Lower Tie Plate Housing
7	CR Drive Cooling Flow
8	Channel bulge
9	Lower Tie Plate Holes
Channel bypass (6, 8 and 9)	
Core plate bypass (1a, 1b, 2, 3, 4, and 5)	

GEH has provided information on the flow area and loss coefficient for the two groups of bypass flows [18]. Some adjustments to the flow areas provided by GEH were necessary in order for the current TRACE model to achieve the desired bypass flow fractions. It is noted that ring 1 in

the current TRACE model is equivalent to the combined rings 1 and 2 of the TRACG model used by GEH to generate the data.

1.7 Jet Pump

It was noted in an early exercise of the SBLOCA deck [1] that the core flow was about 120% of the rated flow (100%) of 13671 kg/s (108.5 Mlbm/hr). With a nominal recirculation flow of 2047 kg/s (16.25 Mlbm/hr) in each of the two loops, the expected jet pump flow ratio is $(108.5/2 - 16.25)/16.25 = 2.34$. The SBLOCA deck, however, produced a flow ratio of slightly greater than three. The over efficiency of the jet pump was corrected by using a more realistic jet pump inlet flow area and it was estimated as follows.

$$\text{jet pump inlet flow area} = (\text{radin1}^2 - (\text{radin2} + \text{th2})^2) * \pi$$

radin1 = inner radius of jet pump main-tube
radin2 = inner radius of jet pump side-tube
th2 = wall thickness of side-tube

Using input values from the SBLOCA deck, the calculated jet pump inlet flow area is 0.047 m² while the SBLOCA deck has a jet pump inlet flow area of 0.054387 m². Results from a series of parametric runs indicate that a jet pump inlet flow area of 0.0452 m² would produce the 100% core flow of 1.367x10⁴ kg/s.

In the current model the jet pump heat structures are thermally connected to the VESSEL component. The additional inputs are:

```
* on card 9*      nhcom = 99
* idrod1 *        3e
* nhcel1 *        8      6      5e
* idrod2 *        3e
* nhcel2 *        9      9e
```

1.8 Steam Separator

A review was done to compare the modeling of steam separators in both TRACG and TRACE. The TRACG ATWS input deck from GEH modeled a 2-stage GE steam separator using a TEE component. The TRACE SBLOCA deck used the SEPD component in TRACE to model the steam separators. For the steam separator geometry the TRACE deck used the same input parameters as in the TRACG model but assumed an ideal separator (zero carryover and carryunder)⁵ with minimum and maximum barrel void of 0.1 and 0.95 respectively. For the current analysis the SEPD component retains the same inputs as in the SBLOCA deck but with one modification, splitting the side arm from a single volume to two nodes of equal volume.

1.9 Recirculation Loop

The recirculation loop, as illustrated in Figure A.5, is modeled with pipe, valve, and pump. The original SBLOCA deck [1] has two recirculation loops of identical geometry. For the current model the two loops have been consolidated into one, consisting of the pump suction line (PIPE 50), the recirculation pump (PUMP 52), recirculation flow control valve (VALVE 54), isolation

⁵ For the ATWS-ED analysis a small amount of carryover (XCO=0.001) and carryunder (XCU=0.0025) will be specified to better emulate the performance of real steam separators.

valve in the pump discharge line (VALVE 56), and the riser pipe that feeds the jet pump drive nozzle (PIPE 58). The consolidation of the two recirculation loops into one loop was carried out in the following steps:

- Deleted components – PIPE 51, PUMP 53, VALVE 55, VALVE 57, PIPE 59, and JETP 61.
- Deleted or modified signal variables and control blocks that receive input from the above deleted components.
- Doubled the target flow value in the control block that regulates the flow control valve (VALVE 54) to initialize the steady-state recirculation flow.
- PIPE 50 – increased the number of pipes represented by the component from 1 to 2.
- PUMP 52 – doubled the value of the following input parameters: cell volume, edge flow area, effective moment of inertia (EFFMI), zero-order coefficient in the PUMP frictional torque correlation (TFR0), zero-order coefficient in the low-speed PUMP frictional torque correlation (TFRL0), rated torque (RTORK), and rated volumetric flow (RFLOW).
- VALVE 54 – doubled cell volume, edge flow area, and valve flow area.
- VALVE 56 – doubled cell volume, edge flow area, and valve flow area.
- PIPE 58 - increased the number of pipes represented by the component from 1 to 2.
- JETP 60 - increased the number of jet pumps represented by the component from 10 to 20.

In Figure A.5 VALVE 36 and BREAK 11 (connected to drywell) are components implemented in the SBLOCA deck [1] to facilitate the simulation of a recirculation line break accident. These two components are retained in the current model to allow the inference of the drywell pressure from the BREAK pressure (currently TRACE does not have a signal variable associated with the CONTAN output variable for the drywell pressure).

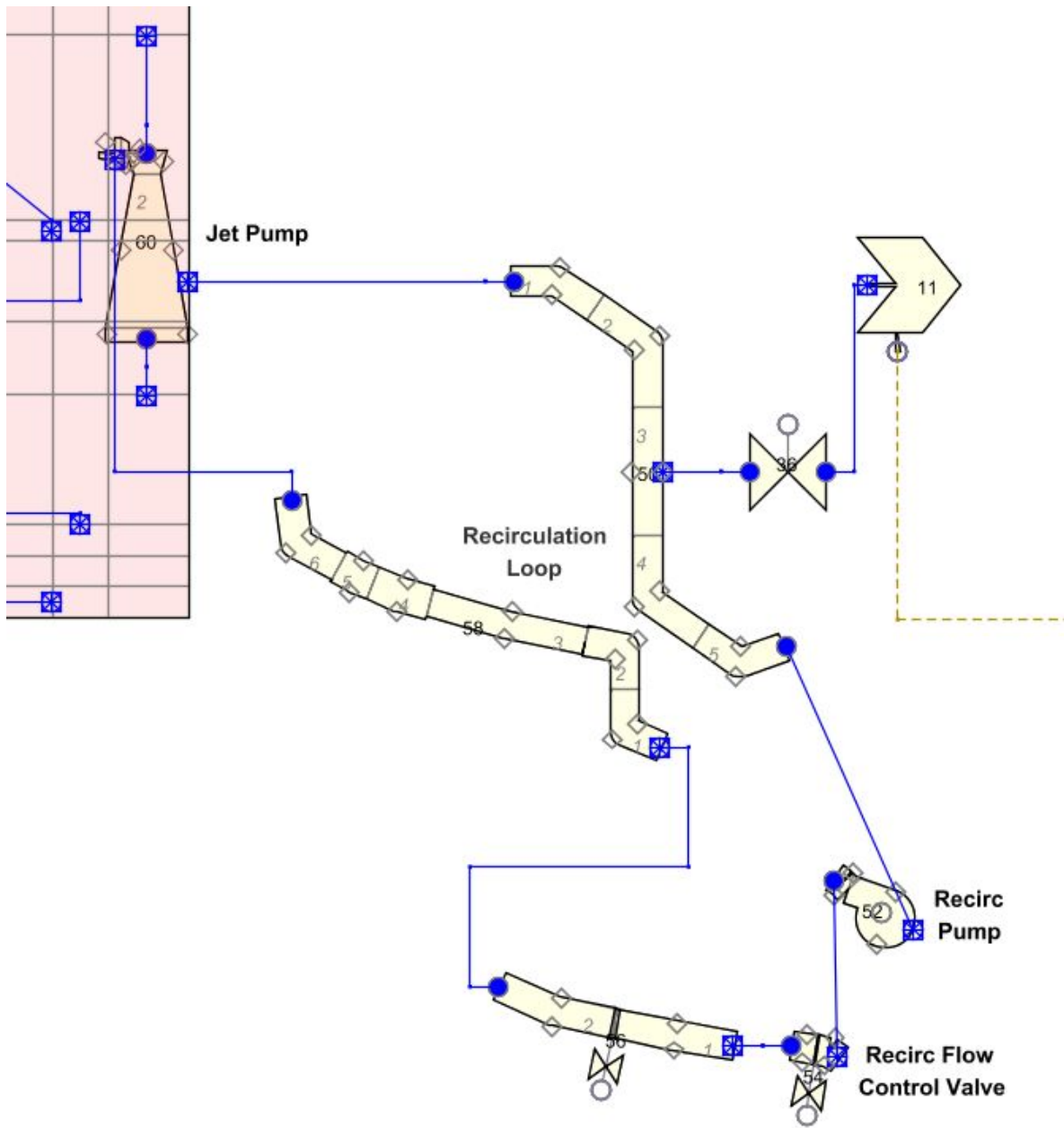


Figure A.5 Recirculation Loop

1.10 Main Steamline

The main steamline, going from the reactor pressure vessel (RPV) to the turbine, consists of several segments: inboard steamline, MSIVs (inboard and outboard), steamline manifold and the turbine inlet pipe. The current model merged the two main steamlines in the base reference model into a single steamline. This was accomplished by summing the volume and flow area of the two lines in the base reference model and replacing all TEES with PIPES. The consolidation of the main steamlines into one single line is consistent with the single azimuthal cell assumption applied to the VESSEL component. It also avoids having to duplicate the main steam components, such as SRVs, MSIVs, and turbine stop/bypass valves, for each main steamline. The reference model included a stub-tube and discharge line for the SRV/ADS. Preliminary test calculations showed that when the SRV/ADS valves were open the valves and

their associated piping became the limiting components to dictate the TRACE time step size. Additionally, the transient nature of the valve opening and closing, along with its junction to the CONTAN wetwell, resulted in oscillatory pressure waves and condensation cycling in the SRV discharge line and these effects led to significant slowdown in the TRACE computation. In order to alleviate these computational difficulties the following changes were made to the SRVs and the discharge line:

- replaced the inboard steamline TEE with a PIPE
- connected the SRVs to the inboard steamline PIPE with a side junction PIPE
- modeled the SRVs as a single junction valve (zero volume)
- removed the SRV discharge line and instead have the SRVs discharge to a BREAK component connected to the wetwell.

Since the primary interest of the calculation is in core response, the simplification of the SRV/ADS is not expected to degrade the overall fidelity of the TRACE transient results. Figure A.6 shows the layout of the main steamline. Table A.9 summarizes signal variables defined for parameters related to the steamline.

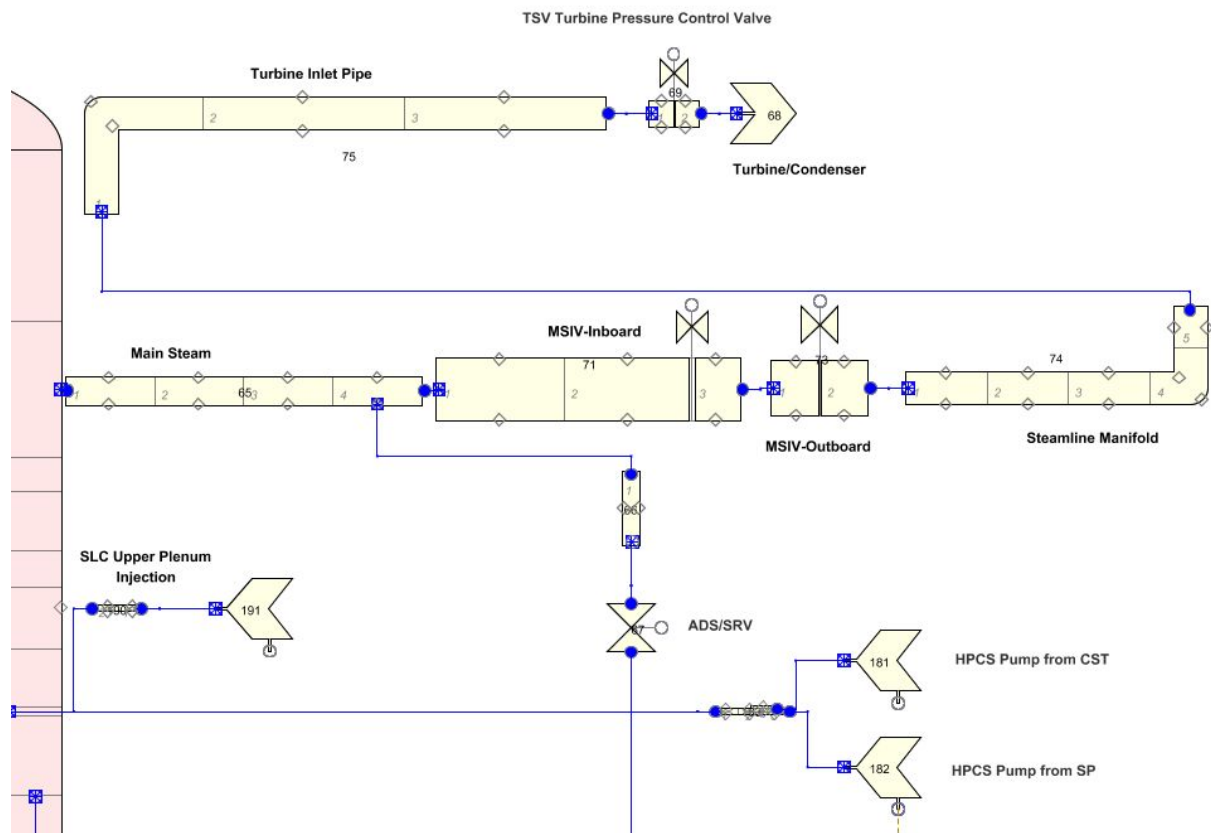


Figure A.6 Main Steamline

Table A.9 Signal Variables for the Steamline Components

Control Component	Function
SV 101	Vapor mass flow in PIPE 75 cell edge 1
SV 104	Pressure in PIPE 75 cell #3 (turbine inlet)
SV 158	Pressure in PIPE 75 cell #1
SV 160 ⁶	Mixed mass flow in PIPE 65 cell #3

Main Steamline Pressure Loss

Preliminary test calculations showed that the reactor pressure vessel (RPV) dome pressure was higher than reference calculations. Since the steamline outlet pressure is controlled by the turbine stop valve (TSV), the dome pressure is related directly to the pressure loss across the steamline. In order to achieve the desired RPV dome pressure, the frictional loss in the main steamline was adjusted. This was done by adjusting local loss coefficients at cell edges (e.g. sudden expansion/contraction losses and valve orifices) in the base input to achieve the desired main steamline pressure drop such that the RPV dome pressure matched reference analysis results. Adjustments to the K-factors were for the main steamline components PIPE 65, VALVE 71, Valve 73, PIPE 74 and PIPE 75.

1.11 Turbine Control/Bypass Valve

The main steamline terminates in a VALVE component representing the turbine control/stop valve that discharges to a BREAK component with a constant pressure condition representing the turbine inlet pressure. The base reference model had the turbine inlet line modeled with a TEE component that included a side arm off-shoot representing the turbine bypass line. The high velocity in this TEE component and the nature of the geometry led to this component not only potentially controlling the Courant limit, but also presented a challenge to the TRACE pressure solution. Test calculations showed that the removal of the side arm significantly reduced the computational expense in resolving the pressure distribution in the main steamline leading to the turbine. In the current model the turbine inlet line is represented by a PIPE component with no side branch, i.e. the turbine bypass line is eliminated. The function of the turbine bypass valve is simulated by re-opening of the turbine control valve after closure to an area equivalent to the desired capacity of the turbine bypass valve (see discussion below).

For steady-state initialization the turbine control valve is regulated by a pressure controller that maintains the upstream pressure to a target value of 6.8327 MPa (991 psia). The downstream pressure at the inlet to the first stage of the turbine is 6.7466 MPa and it represents the constant pressure condition set for the BREAK component downstream of the turbine control valve. The control scheme is show in Figure A.7.

The length of the BREAK component representing the first stage of the turbine was increased to 3 m in an effort to increase the steam transit time such that the component would not be controlling the Courant limited time step.

⁶ A new signal variable for the mass flow in the steamline will be defined for the ATWS-ED analysis. The location of the flow sensor will be downstream of the MSIVs reflecting the instrumentation in the model BWR/5 plant.

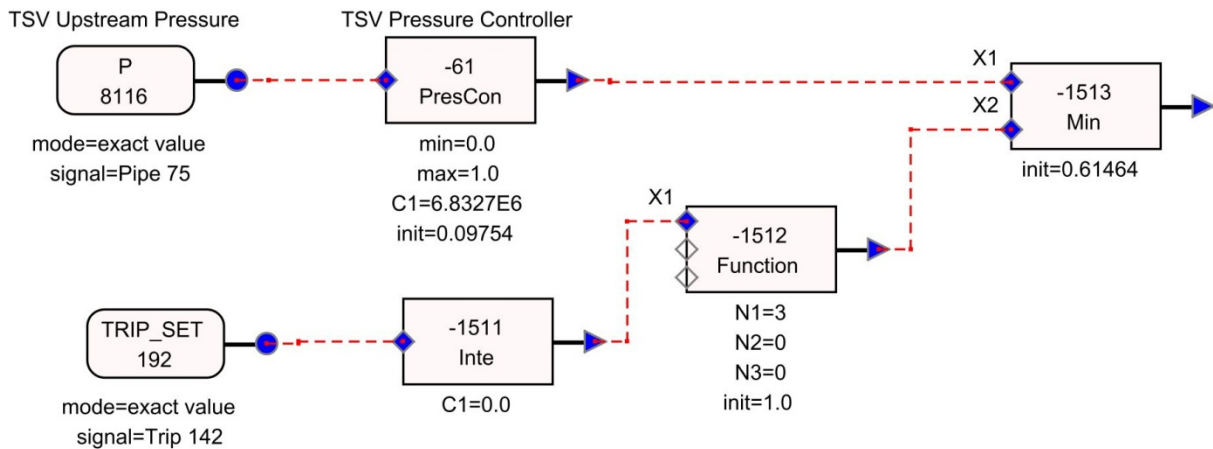


Figure A.7 Turbine Control/Bypass Valve Control Logic

Turbine Bypass Function

In the event of a turbine trip with bypass, the turbine bypass valve will open to relieve the RPV pressure by dumping steam to the condenser. Simply reopening the turbine control valve after closure will not be an accurate representation of the bypass function because it is assumed that the turbine bypass system would strive to maintain reactor pressure at a fixed setpoint to prevent inventory loss, full reactor trip, and ECCS actuation, in a true plant configuration. In light of incomplete information regarding the control system for the turbine bypass valve, a compromise is to apply a back pressure boundary condition to the BREAK downstream of the turbine control valve. The break pressure is set to be equivalent to the long term RPV pressure response predicted by a reference TRACG calculation for an ATWS initiated by turbine trip with bypass. The TRACG calculated RPV pressure response is taken from a data file RAI_I-4.0_Plots-TAF.xls provided (on a CD) in Enclosure 3 to Reference [17]. This back pressure (6.371 MPa or 924 psia) is also used to initialize the steady-state conditions for a transient with turbine bypass actuation.

An auxiliary calculation was performed to determine the appropriate turbine control valve areas to represent 10%, 25%, 50% and 100% bypass scenarios and the model is shown in Figure A.8.

In the auxiliary calculation the combination of the turbine control/stop valve and the BREAK component was connected to the side of the last cell of the turbine inlet pipe. Attached to the end face of the turbine inlet pipe was an identical set of VALVE and BREAK combination. The original set of VALVE/BREAK, attached to a Type 2 CSS controller, performed the intended function of maintaining a constant pressure in the last cell of the turbine inlet pipe. The new set, also attached to a Type 2 CSS controller, was to achieve the desired steam flow through the new valve, i.e. equivalent to 10%, 25% and 100% of the steam flow, respectively. Once a steady-state initialization was achieved, the turbine control valve areas required to accommodate the various bypass fractions were inferred from the valve flow areas of the new valve. Results of the auxiliary calculation that provide the equivalent valve flow area for various bypass fractions are summarized in Table A.10.

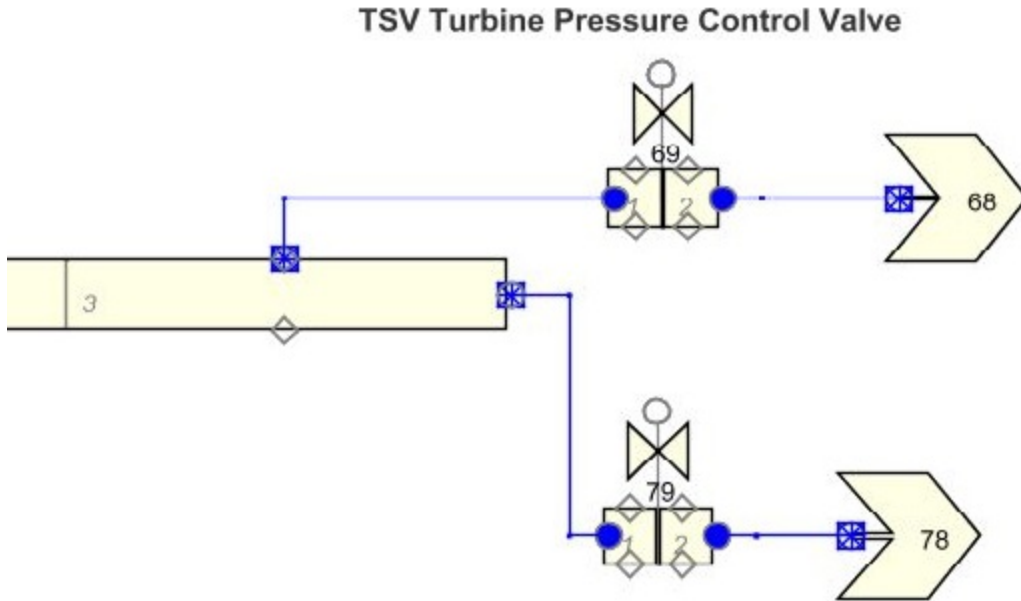


Figure A.8 Model for Determining Turbine Bypass Valve Flow Areas

Table A.10 Equivalent Turbine Control Valve Area for Different Bypass Capacities

Steam Flow Fraction	Turbine Control Valve Area Fraction
100%, Steady-state	0.3915325
100% Bypass	0.3915325
50% Bypass	0.2234803
25% Bypass	0.119331
10% Bypass	0.04885668

The closure and reopening of the turbine control/stop valve is implemented with a table in Control Block 1512. The valve is assumed to move from open to closed in 0.1 s and reopens from closed to its original open position in 1 s.

1.12 SRV/ADS

The model BWR/5 plant has a total of 18 safety relief valves (SRVs) arrayed in five banks. The lowest pressure SRV bank includes two valves. These two valves, however, are assumed out of service (OOS) [3, 5]. The ATWS-ED event sequence calls for manual actuation of the automatic depressurization system (ADS). The manual ADS action takes place once the suppression pool (SP) reaches a temperature equal to the heat capacity temperature limit (HCTL). The SP temperature will rise according to the integrated mass and energy delivered to the SP from reactor steam discharged through the SRVs. Since the reactor power will be elevated at higher reactor pressures, the conservative assumption here is to take the two lowest pressure SRVs as the SRVOOS. Therefore, only four banks are modeled with four SRVs in each bank and the seven ADS valves are associated with the two highest pressure banks.

The lifting of SRVs is dependent on the steamline pressure and the status of the signal to activate the ADS valves. In the current TRACE model the SRVs are modeled using a single lumped valve⁷. This lumped valve represents all available SRVs. An approach for controlling the open fraction of the lumped SRV/ADS uses a control system. The control system features five trips. The first four trips are intended to capture the lift and reset of each bank of SRVs. The steamline pressure is used to determine if any of these individual trips are actuated. These trips are then summed, each with a value of unity. Another trip is present that accounts for the ADS trip. If the ADS trip is TRUE or 1, then a value of 10 is added to the summation of the trips. This means that the output of the sum block has a series of discrete values. These values are then fed into a table that relates the sum block value to the number of open SRVs. For example, if two banks are tripped, a value of two is passed to the table. The table would associate a value of 2 with 2 full banks of open SRVs, or 4+4=8 total SRVs of the 16 available.

Table A.11 shows the number of valves opening based on the steamline pressure and trip status and Figure A.9 shows the control logic for the SRV and ADS valves. Table A.12 shows the signal variables, control blocks, and trips used in this control logic. It is noted that the HCTL is set to 352.59 K (175°F)⁸ and used as the setpoint for the ADS trip (TRIP 6).

Table A.11 ADS/SRV Valve Setpoints

# of SRV Valves	# of ADS Valves	Opening Pressure ¹		Closing Pressure		Remark
		psig	Pa(a)	psig	Pa(a)	
2	0	1103	7.707E+06	1048	7.327E+06	SRV Bank 1: Assumed to be unavailable
4	0	1113	7.775E+06	1048	7.396E+06	SRV Bank 2
4	0	1123	7.844E+06	1058	7.465E+06	SRV Bank 3
4	3 ²	1133	7.913E+06	1068	7.534E+06	SRV Bank 4
4	4 ²	1143	7.982E+06	1078	7.603E+06	SRV Bank 5

¹ The opening and closing pressures are based on values from the Nine Mile Point 2 EPU model analyses. They correspond to the "Relief Mode" nominal trip setpoints. It is noted the opening pressures are identical with the SRV parameters shown in the Nine Mile Point Unit 2 USAR [18] (Table 6A.3-1, USAR Revision 14, February 2001)⁹.

² This is the number of SRVs in the particular bank that also serve the ADS function.

⁷ The modeling of SRV/ADS valves will be modified for the ATWS-ED analysis. The valve loss coefficient, valve delay and valve rate of opening will be revised. In addition individual valves with modified control logic may be used to represent the different banks of SRVs.

⁸ The HCTL limit will be changed to 344.26 K (160°F) for the ATWS-ED analysis.

⁹ For the ATWS-ED analysis the "Relief Mode Analytical Limit" will be used as the setpoints for the opening pressures.

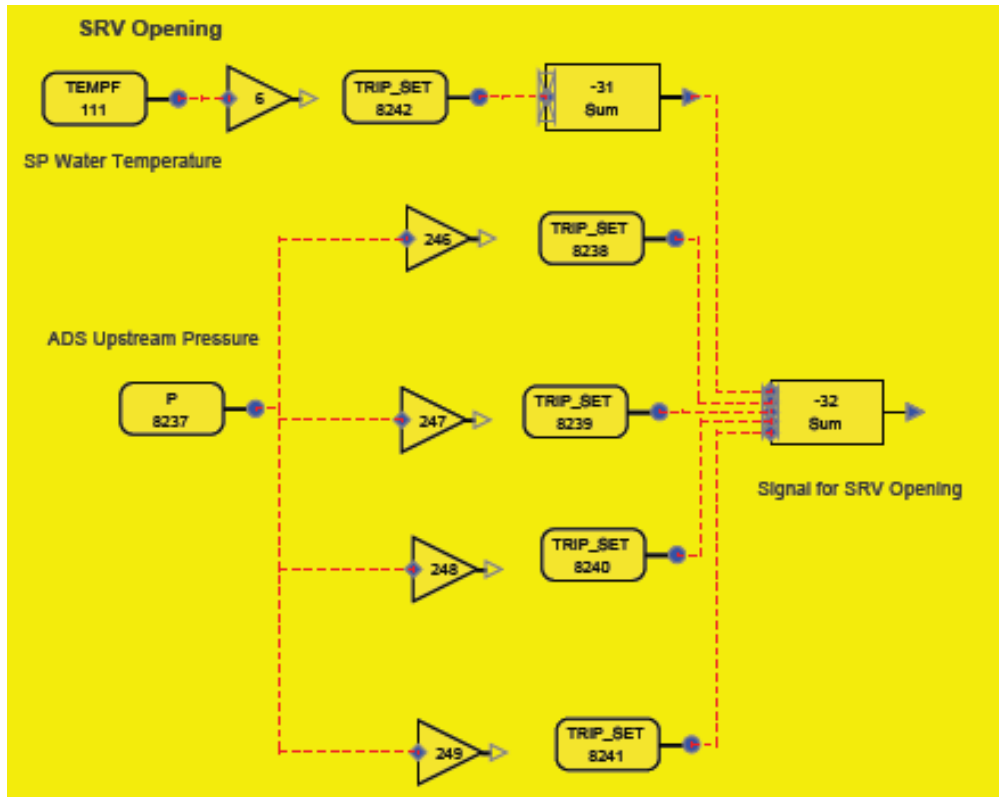


Figure A.9 SRV and ADS Control Logic

Table A.12 Signal Variables, Control Blocks, and Trips Used in Control Logic for SRV and ADS Valves

Trips					
Trip # (IDTD)	Signal range type # (ISRT)	Variable (IDSG)	Setpoint 1 (setp-1)	Setpoint 2 (setp-2)	Remark
6	2	SP liquid temperature (SV-111)	0.0	352.59	To initiate opening of ADS valves
246	2	ADS upstream pressure (SV-8237)	7.396E+06	7.775E+06	To control SRV Bank 2
247	2	ADS upstream pressure (SV-8237)	7.465E+06	7.844E+06	To control SRV Bank 3
248	2	ADS upstream pressure (SV-8237)	7.534E+06	7.913E+06	To control SRV Bank 4
249	2	ADS upstream pressure (SV-8237)	7.603E+06	7.982E+06	To control SRV Bank 5
Signal variables					
SV #	Signal		Parameter type		
111	FILL-182		Liquid temperature: SP temperature		
8237	VALVE-65 Node-4		Pressure: ADS upstream pressure		
8238	TRIP-246		Trip set status value for SRV Bank 2		
8239	TRIP-247		Trip set status value for SRV Bank 3		
8240	TRIP-248		Trip set status value for SRV Bank 4		
8241	TRIP-249		Trip set status value for SRV Bank 5		
8242	TRIP-6		Trip set status value for ADS valve opening		
Control blocks					
CB #	Type	Gain	Inputs		Remark
-31	Sum	10.0	SV-8242		10.0: when $T_{SP} > 352.59$ K (HCTL) 0.0: otherwise
-32	Sum	1.0	SV-8238, SV-8239, SV-8240, and SV-8241		See below.

$CB - 32 = \left\{ \begin{array}{l} 0.0 \text{ when no SRV and ADS need to be opened.} \\ 1.0 \text{ when SRV Bank 2 to be opened.} \\ 2.0 \text{ when SRV Bank 2 and 3 to be opened.} \\ 3.0 \text{ when SRV Bank 2, 3, and 4 to be opened.} \\ 4.0 \text{ when SRV Bank 2, 3, 4, and 5 to be opened.} \\ 10.0 \text{ when only ADS needs to be opened.} \\ 11 \text{ when SRV Bank 2 and ADS need to be opened.} \\ 12 \text{ when SRV Bank 2 and 3 and ADS need to be opened.} \\ 13 \text{ when SRV Bank 2, 3, and 4 and ADS (all SRV) need to be opened.} \\ 14 \text{ when SRV Bank 2, 3, 4, and 5 and ADS (all SRV) need to be opened.} \end{array} \right.$

The output of CB-32 is used as the independent variable of flow area table of the SRV/ADS valve (VALVE-67). Table A.13 shows the SRV/ADS valve flow area fraction depending on the output of CB-32.

Table A.13 SRV/ADS Valve Flow Area Fraction

CB-32 Output	# of SRV/ADS valves open	Valve flow area fraction
0.0	0	0.0
1.0	4	$0.25 = \frac{4}{16}$
2.0	8	$0.5 = \frac{4 + 4}{16}$
3.0	12	$0.75 = \frac{4 + 4 + 4}{16}$
4.0	16	$1.0 = \frac{4 + 4 + 4 + 4}{16}$
10.0	7	$0.4375 = \frac{7}{16}$
11.0	11 (7+4)	$0.6875 = \frac{7 + 4}{16}$
12.0	15 (7+4+4)	$0.9375 = \frac{7 + 4 + 4}{16}$
13.0	16 (7+4+4+1)	$1.0 = \frac{7 + 4 + 4 + 1}{16}$
14.0	16	$1.0 = \frac{7 + 4 + 4 + 1}{16}$

1.13 Feedwater and Reactor Water Level Control

A FILL component representing the condensate storage tank (CST) is used as the source of feedwater (FW). The total capacity of the two CSTs is assumed to be 900,000 gal (3407 m³) and 270,000 gal (1022 m³) of the capacity reserved for RCIC (see Section 2.8.3 of Reference [5]). The depletion of inventory in the CST (and the termination of FW flow) is calculated by a series of control blocks that are part of the control system for RCIC. Details of the RCIC are given in Section 1.14.

The layout of the FW line is shown in Figure A.10. The base reference model utilizes the TRACE built-in level controller (WLEV) to function as the FW controller supplying the FW demand signal so as to maintain the reactor water level (RWL) to a setpoint. The built-in controller requires the following controller inputs: FW flow, steam flow, and reactor water level. The setpoints specified are the nominal FW flow and the desired RWL. The output of the controller is the FW demand that provides a signal to the FILL component simulating the FW system. Preliminary test calculations indicated that the TRACE built-in level controller was incapable of responding to the demand to lower the RWL. For the ATWS analysis, various water level control strategies are under consideration and must be simulated in the transient calculations. In the current model the TRACE built-in level controller is replaced with a three-element FW controller¹⁰ that is known to work from previous applications [19, 20]. The control logic is shown in Figure A.11 and the controller settings are the same as in [19, 20].

¹⁰ Several settings of the FW controller will be modified for the ATWS-ED analysis and among them are the maximum FW flow rate, location of the steam flow sensor, and the proportional gain of the water level differential.

the RWL and the delta and this is the pseudo level or virtual level. Depending on the magnitude of the delta, the FW controller will control RWL to an offset level from its nominal setpoint. Figure A.12 illustrates the control logic used in the calculation of the pseudo or virtual RWL and Table A.14 and Table A.15 summarize the functions of trips, signal variables and control blocks in the figure.

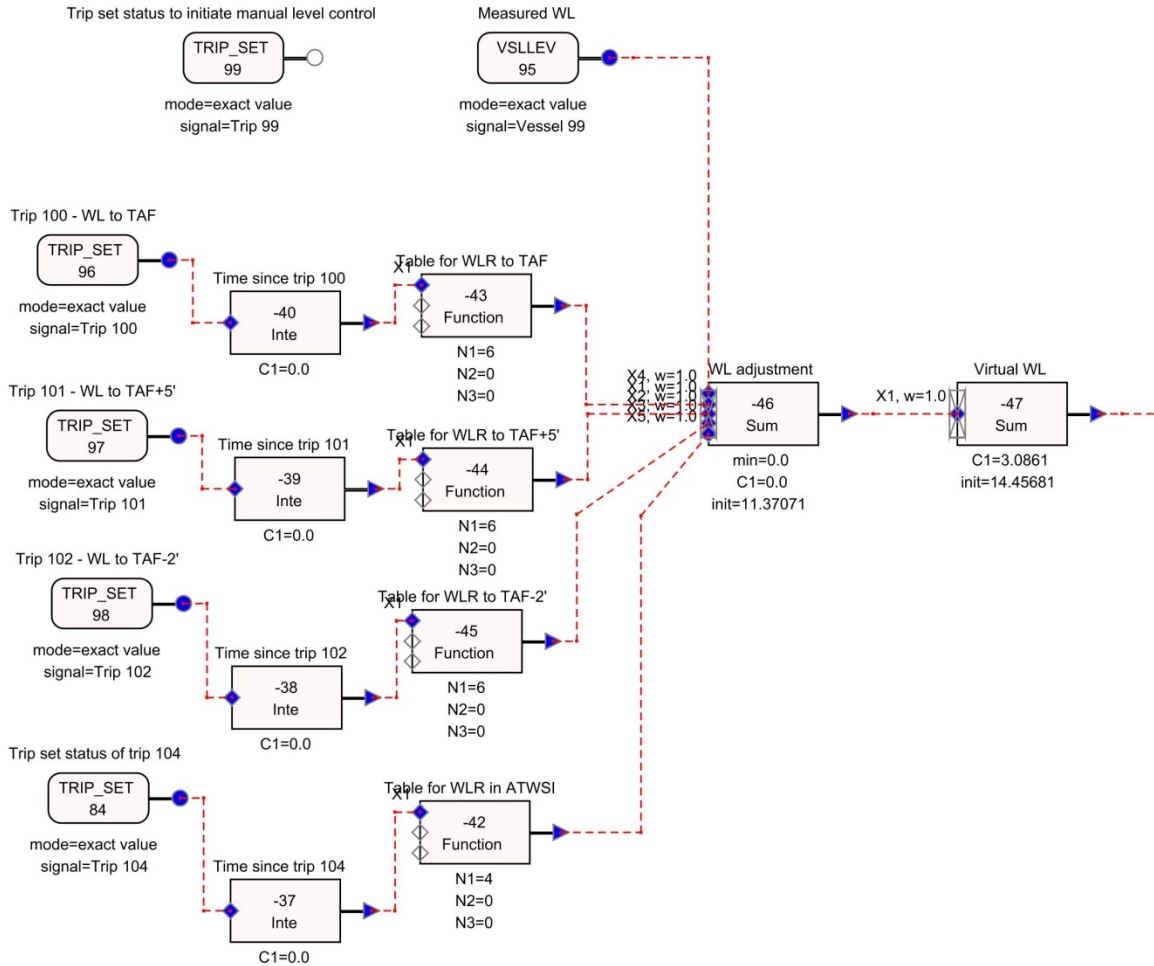


Figure A.12 Water Level Control Logic

**Table A.14 Trips, Signal Variables (SV) and Control Blocks (CB) for
Reactor Water Level Control**

RWLControl Component	Function
Trip 100	A time based trip to initiate RWL control to TAF (for ATWS-ED)
Trip 101	A time based trip to initiate RWL control to TAF+5' (for ATWS-ED)
Trip 102	A time based trip to initiate RWL control to TAF-2' (for ATWS-ED)
Trip 104	A time based trip to initiate RWL control to TAF (for ATWS-I)
SV 96	Trip set status of Trip 100
SV 97	Trip set status of Trip 101
SV 98	Trip set status of Trip 102
SV 84	Trip set status of Trip 104
CB 40	Integrate SV 96 to calculate the time since Trip 100 has become TRUE
CB 39	Integrate SV 97 to calculate the time since Trip 101 has become TRUE
CB 38	Integrate SV 98 to calculate the time since Trip 102 has become TRUE
CB 37	Integrate SV 84 to calculate the time since Trip 104 has become TRUE
CB 43 CB 44 CB 45 CB 42	Look up a table that gives the target delta water level as a function of time. Table A.15 provides the entries in the tables. NWL = 11.37071 m above the bottom of the downcomer, or 14.45681 m above the bottom of the vessel TAF = 9.56971 m above the bottom of the vessel NWL – TAF = 4.8871 m NWL – TAF+5' = 3.3631m NWL –TAF-2' = 5.4967 m
SV 95	Measured water level in the downcomer (isvn=106)
CB 46	Adjusted water level in the downcomer = (SV 95) + (Outputs from CB's 43, 44, 45 and 42)
CB 47	Pseudo or virtual water level that acts as input to the water level controller = (Output from CB 46) + elevation of the bottom of the downcomer (3.0861 m)

Table A.15 Functional Form of CBs 43, 44, 45 and 42

Control Component	Time Since Trip That Activates Level Control (s)	Target Delta Water Level (NWL – Target Water Level) (m)
CB 43	-10.0	0.0
	0.0	0.0
	0.1	4.8871
	2050.0	4.8871
	2150.0	0.0
	1.0E6	0.0
CB 44	-10.0	0.0
	0.0	0.0
	0.1	3.3631
	2050.0	3.3631
	2150.0	0.0
	1.0E6	0.0
CB 45	-10.0	0.0
	0.0	0.0
	0.1	5.4967
	2050.0	5.4967
	2150.0	0.0
	1.0E6	0.0
CB 42	-10.0	0.0
	0.0	0.0
	180.0	4.8871
	1.0E6	4.8871

As shown in Figure A.12 and Table A.14 the reactor water level control includes several trips. These trips will initiate the initial RWL reduction strategy to a desired setpoint. For ATWS-I events, the operators will lower water level to approximately the top of active fuel (TAF). This strategy provides not only the advantage of reducing the reactor core flow, but also, of exposing the feedwater to a steam atmosphere in the downcomer. The mixing of the feedwater with steam in the downcomer above the RWL heats the incoming flow and reduces the inlet subcooling. The reduced inlet subcooling has a stabilizing effect on the reactor.

For the ATWS-ED events, however, the SLCS is aligned to inject into the lower plenum. For this injection point, the operators will eventually pursue a reactor water level recovery strategy (RWLRS). The borated solution is expected to be injected into the lower plenum at low temperature and therefore be subject to stratification in the bottom of the vessel. RWLRS is intended to increase natural circulation flow in the vessel and to provide sufficient flow to remix and entrain the stratified solution. The entrained borated solution may then be delivered to the active core. The RWLRS depends on the event timing as the operators will refrain from recovering the level until the SLCS has had sufficient time to inject the hot shutdown boron weight (HSBW). Since the SLCS flow rate is modeled using a constant flow rate, the timing of HSBW injection is based on this flow rate and the timing of SLCS initiation. Therefore, it is appropriate to use time-based initiating signals to model RWLRS.

The approach to initiate water level reduction and recovery is to use several tables for the controller as shown in Table A.15. The table gives the delta as a function of time after the trip. Different tables are generated depending on the scenario:

ATWS-I: The delta reflects a change in demand to TAF over a period of 180 seconds, starting at 120 seconds (or 110 seconds after turbine trip and this strategy is based on the RAI 10 response [2]). For ATWS-I, the delta is calculated using an integrator that begins to integrate after the trip. The integrator has a gain and a maximum value. This simulates the ramp in the demand change over a period of 180 seconds. The maximum delta is normal WL – TAF (maximum value of delta). No water level recovery is simulated for the ATWS-I.

ATWS-ED: The delta must include the ramp down (over 0.1 second) and the subsequent recovery over a period of 100 seconds. The delta will rapidly increase, be held for a period, and then slowly drop down over 100 seconds to zero (normal water level control re-established; this strategy is based on the RAI 10 response). Since the operators may control the RWL to TAF, TAF-2, or TAF+5, three tables are required.

The feedwater temperature is expected to decrease once the turbine is isolated (by MSIV closure or turbine trip) and the steam flow to the feedwater heater cascade is cut off. The simulation of feedwater temperature ramp-down is done by the use of a feedwater temperature curve provided in NEDC-33006P-A, Rev 3 [20] (the MELLLA+ licensing topical report or M+LTR). The M+LTR curve is based on a similarly sized BWR plant and is appropriate for characterizing the timing and degree of feedwater temperature decrease. The control logic used to model the feedwater temperature ramp-down is shown in Figure A.13. The feedwater temperature ramp down is modeled as a first-order lag with a time constant of 75 s and a temperature decrease from 500.09 K (440.5°F) to 316.48 K (110°F) starting after either a turbine trip or a complete closure of the MSIV.

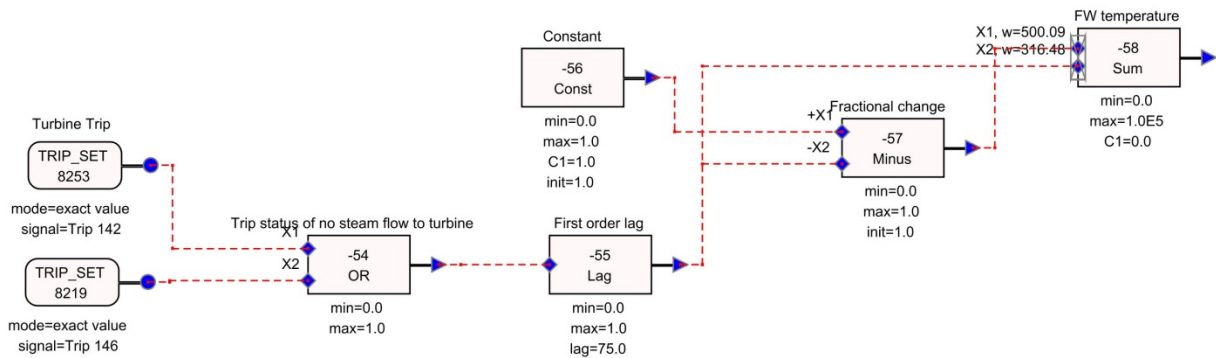


Figure A.13 Feedwater Temperature Control Logic

1.14 Reactor Core Isolation Cooling System

The RCIC is modeled in TRACE using two FILL components (see Figure A.10) and they represent RCIC suction from the CST and the suppression pool (SP) respectively. The RCIC with its steam-driven pump takes suction from either the CST or the SP (source determined by a control system) and injects through a side pipe connection to the FW line. It is noted that the RCIC injection point can be at a different location depending on the plant configuration.

The RCIC is included in the current TRACE model to provide coolant when the reactor is isolated, in particular after the MSIV closure. The system is to supply coolant to maintain the reactor water level between levels L3 and L8 (these are water level setpoints and are different from the axial levels in the VESSEL component). The rated flow of RCIC is 39.414 kg/s [1].

The RCIC will take suction first from the CST until the depletion of the reserve and then from the SP. The following description of the control systems developed for the RCIC has incorporated specific technical information from the NRC staff that includes: net positive suction head, low pressure operation, and condensate storage tank capacity [5].

Net Positive Suction Head

In anticipated transients without scram with emergency depressurization (ATWS-ED) simulations, NRC staff recommends that the RCIC be modeled with a control system that accounts for the potential loss of net positive suction head (NPSH) when suction is taken from the suppression pool. Figure A.14 shows the temperature and pressure conditions of the suppression pool where NPSH is available. The NRC staff recommendation assumes that the NPSH is not available above 170°F for conservatism [5].

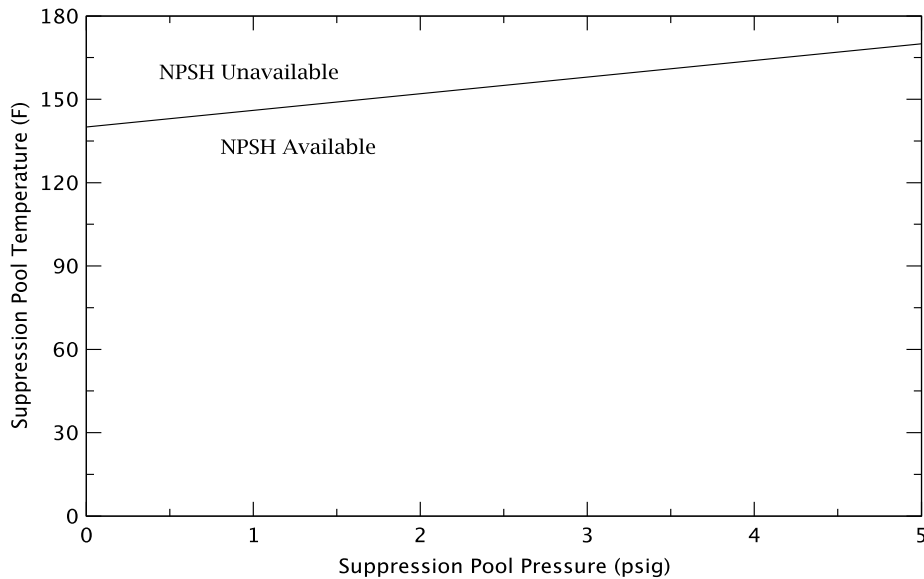


Figure A.14 NPSH Limit [5]

The temperature of the suppression pool below which the NPSH is available can be expressed as,

$$T = \begin{cases} \frac{170-140}{5} P_{SP} + 140^{\circ}\text{F}, & 0 \leq P_{SP} \leq 5 \text{ psig} \\ 170^{\circ}\text{F}, & P_{SP} > 5 \text{ psig} \end{cases}$$

We need to express the above relation in SI units for use by TRACE. Table A.16 shows, in the SI units, the pressure and temperature values shown in Figure A.14.

Table A.16 Pressure and Temperature Values shown in Figure A.14

Variable	British	SI
P_0	0.0 psig	101325 Pa(a)
P_5	5.0 psig	135798.8 Pa(a)
T_{140}	140°F	333.15 K
T_{170}	170°F	349.82 K

The slope and y-intercept of the temperature limit for the availability of the NPSH become,

$$m = \frac{349.82 - 333.15}{135798.8 - 101325} = 4.8346 \times 10^{-4} \frac{\text{K}}{\text{Pa}} \text{ and}$$

$$C = 333.15 - 4.8346 \times 10^{-4} \cdot (101325) = 284.1635 \text{ K}$$

Then the suppression pool temperature limit for NPSH in SI units is given by,

$$T = \begin{cases} 4.8346 \times 10^{-4} P_{SP} + 284.1635 \text{ K}, & 101325 \leq P_{SP} \leq 135798.8 \text{ Pa(a)} \\ 349.82, & P_{SP} > 135798.8 \text{ Pa(a)} \end{cases}$$

Low Pressure Operation

Under ATWS-ED conditions, the reactor may reach very low pressures following the emergency depressurization (as low as 20 psia or 137.9 kPa). Therefore, it is necessary to simulate RCIC behavior under very low pressure conditions. Figure A.15 illustrates the NRC staff's proposed RCIC flow as a function of reactor pressure. RCIC is assumed to operate at a fraction of rated flow between reactor pressures of 40 psia and 165 psia and is inoperable below 40 psia. Table A.17 shows the relationship between the reactor pressure and RCIC flow shown in Figure A.15. The 100% RCIC flow is 39.414 kg/s.

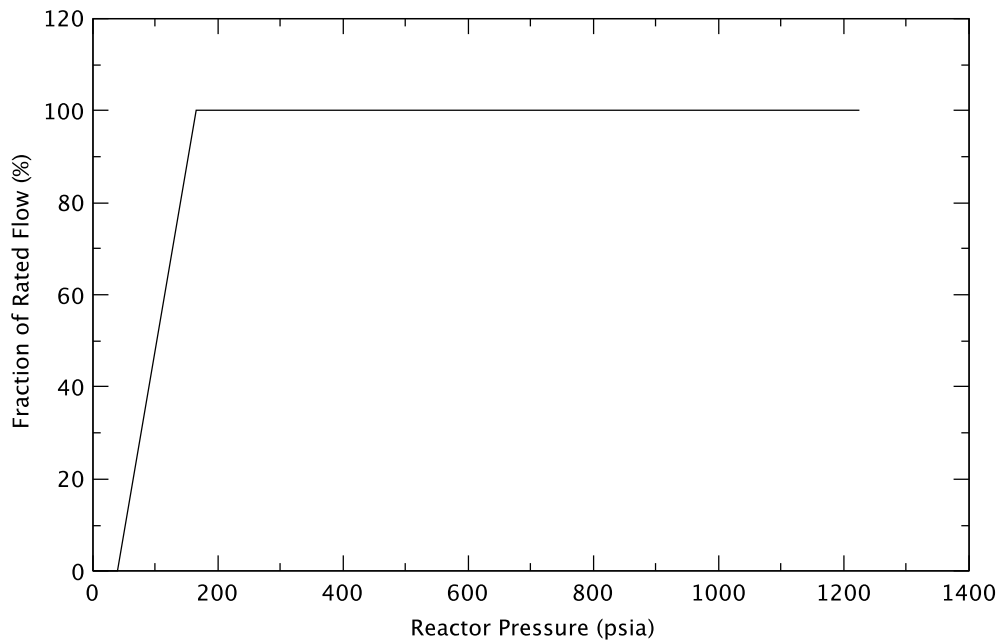


Figure A.15 RCIC Flow vs. Reactor Pressure [5]

Table A.17 RCIC Flow vs. Reactor Pressure Shown in Figure A.15

Reactor Pressure		RCIC Flow	
British (psia)	SI (Pa(a))	Percentage	kg/s
0	101325	0	0
40	275790.3	0	0
165	1137634.9	100	39.414
1225	8446077.3	100	39.414

Condensate Storage Tank Capacity

The NRC staff recommends considering the CST capacity of 630,000 gallons for the feedwater water and the CST capacity of 270,000 gallons for the RCIC flow [5]. The total capacity of the CST is 900,000 gallons. Table A.18 summarizes the CST capacities for the feedwater flow and the RCIC flow. In the conversion of volume to mass, a fluid density of 999.5519 kg/m³ (62.4 lbm/ft³) is used.

Table A.18 CST Capacities

Description	British-Volume (gal)	SI-Volume (m ³)	SI-Mass (kg)
For feedwater flow	630000	2384.81	2383740.6
For RCIC flow	270000	1022.06	1021603.1

RCIC Control Systems

The development of the control system for the RCIC flow from the CST and the suppression pool (SP) is discussed below.

CST Capacity for Feedwater Flow

Figure A.16 shows the control systems to stop the feedwater when its integrated value (i.e., the feedwater mass discharged into the reactor vessel), after MSIV closure, reaches 2,383,740.6 kg (630,000 gallons), the CST capacity reserved for the feedwater. Table A.19 shows the signal variables, control blocks, and trips used in this control logic.

CB-52 is used as “Liquid Flow Controller” of FILL-62 which simulates the feedwater supplier as shown in Figure A.10. CB-76 is the FW demand as determined by the FW control logic (see Section 1.13 and Figure A.11). The FW flow coastdown function represented by CB-49 prescribes the FW flow to decrease linearly to zero in 0.001 s after a trip to stop FW has been initiated.

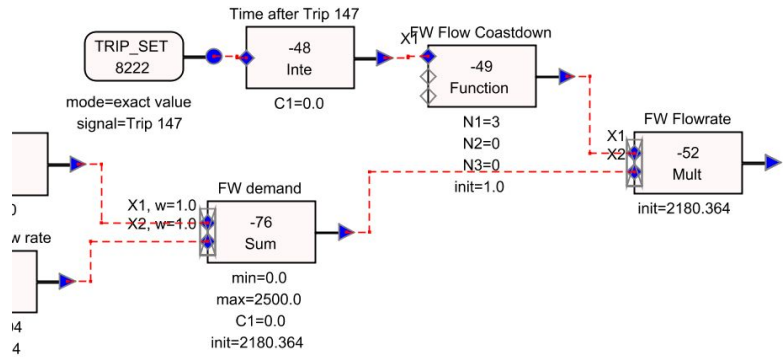
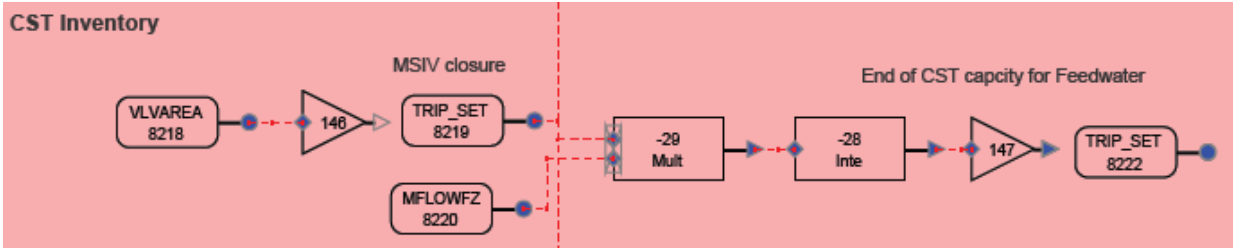


Figure A.16 Control System for Stopping Feedwater

Table A.19 Signal Variables, Control Blocks, and Trips Used in Control Logic for Stopping Feedwater

Trips					
Trip # (IDTD)	Signal range type # (ISRT)	Variable (IDSG)	Setpoint 1 (setp-1)	Setpoint 2 (setp-2)	Remark
146	1	MSIV valve area (SV-8218)	0.0	1.0x10 ⁶	Checking if MSIV is closed
147	2	Integrated feedwater flow after MSIV closing (CB-28)	0.0	2,383,741	To stop feedwater flow
Signal variables					
SV #	Signal	Parameter type			
8218	VALVE-73 (MSIV)	Valve flow area fraction			
8219	TRIP-146	Trip set status value			
8220	VALVE-31 (feedwater)	Liquid mass flow across the Z axis			
8222	TRIP-147	Trip set status value			
Control blocks					
CB #	Type	Gain	Inputs	Remark	
-29	Multiply	1.0	SV-8219 & SV-8220	Feedwater flow after MSIV is closed	
-28	Integrate	1.0	CB-29	Integrating feedwater	
-48	Integrate	1.0	SV-8222	Integrating time after stopping feedwater flow	
-49	Function	1.0	CB-48	Table: Independent variable = CB-48 0.0, 1.0 0.001, 0.0 100000, 0.0	
-52	Mult	1.0	CB-49 & CB-76	Feedwater flowrate becomes zero 0.001 s after trip to stop FW.	

RCIC Flow from CST

Figure A.17 shows the control systems to control the RCIC flow from the condensate storage tank (CST) until it consumes the reserved capacity of 1,021,603.1 kg (270,000 gallons).

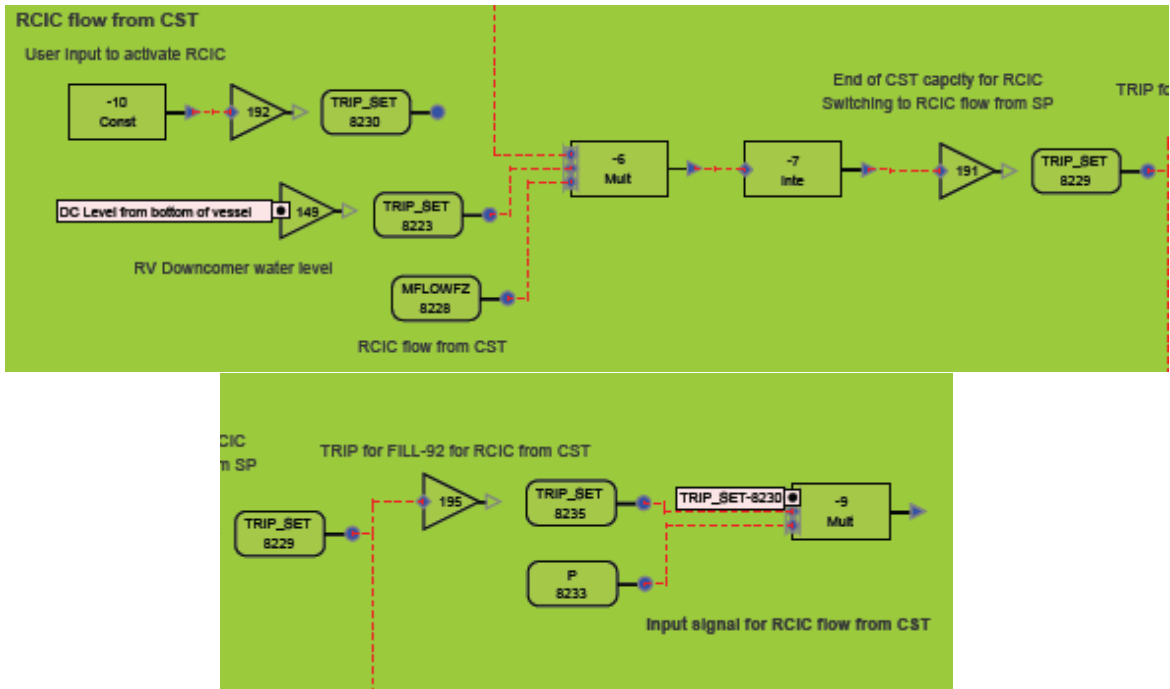


Figure A.17 Control System for RCIC Flow from CST

Table A.20 shows the signal variables, control blocks, and trips used in this control logic. The RCIC flow from the CST is controlled using FILL-92 shown in Figure A.10. Table A.21 shows the input information for FILL-92.

Table A.20 Signal Variables, Control Blocks, and Trips Used in Control Logic for RCIC Flow from CST

Trips					
Trip # (IDTD)	Signal range type # (ISRT)	Variable (IDSG)	Setpoint 1 (setp-1)	Setpoint 2 (setp-2)	Remark
192	2	Constant (CB-10)	0.0	0.9	Checking if RCIC flow is activated
149	1	Downcomer water level (CB-50)	12.9794	14.94536	Checking if downcomer water level is low enough to initiate RCIC
191	2	Integrated RCIC flow from CST after MSIV closing (CB-7)	0.0	1,021,603.1	To stop RCIC flow from CST
195	1	Trip set status value of TRIP-191 (SV-8229)	0.1	0.9	To make RCIC flow from CST until CST becomes empty
Signal variables					
SV #	Signal	Parameter type			
8219	TRIP-146	Trip set status value			
8230	TRIP-192	Trip set status value			
8223	TRIP-149	Trip set status value			
8228	FILL-92 (RCIC from CST)	Liquid mass flow across the Z axis			
8229	TRIP-191	Trip set status value			
8235	TRIP-195	Trip set status value			
8233	Reactor Vessel Dome	Pressure			
Control blocks					
CB #	Type	Gain	Inputs	Remark	
-10	Constant	1.0	User input	C=1.0: To activate RCIC C=0.0: Not to activate RCIC	
-6	Multiply	1.0	SV-8219, SV-8228, & SV-8223	RCIC flow from CST: when MSIV is closed, and DC water level is low enough 0.0: otherwise	
-7	Integrated	1.0	CB-6	Integrated RCIC flow from CST	
-9	Multiply	1.0	SV-8230, SV-8235 & SV-8233	RV dome pressure: when CST for RCIC flow is not empty and RCIC flow is activated 0.0: otherwise	

Table A.21 Input Information for FILL-92

Input variable	Input	Remark
Fill type	Mass flow table: 5	Table: (Input signal vs. Mass flow (kg/s))
		0.0 0.0
		2.757903E5 0.0
		1.137635E6 39.414
1.0E8 39.414		
Valve table signal	CB-9	Reactor vessel dome pressure

RCIC Flow from SP

RCIC switches suction from the CST to the suppression pool when the RCIC flow has depleted the CST reserved capacity of 1,021,603.1 kg (270,000 gallons). Figure A.18 shows the control systems to control the RCIC flow from the suppression pool when the NPSH and the reactor pressure satisfy the performance criteria discussed at the beginning of this section. Table A.22 shows the signal variables, control blocks, and trips used in this control logic.

The RCIC controller incorporates a user-specified time delay between the suppression pool exceeding the NPSH temperature criterion (349.82 K (170°F)) and the loss of RCIC availability. Currently, this delay is set to 20 seconds via input to CB-24.

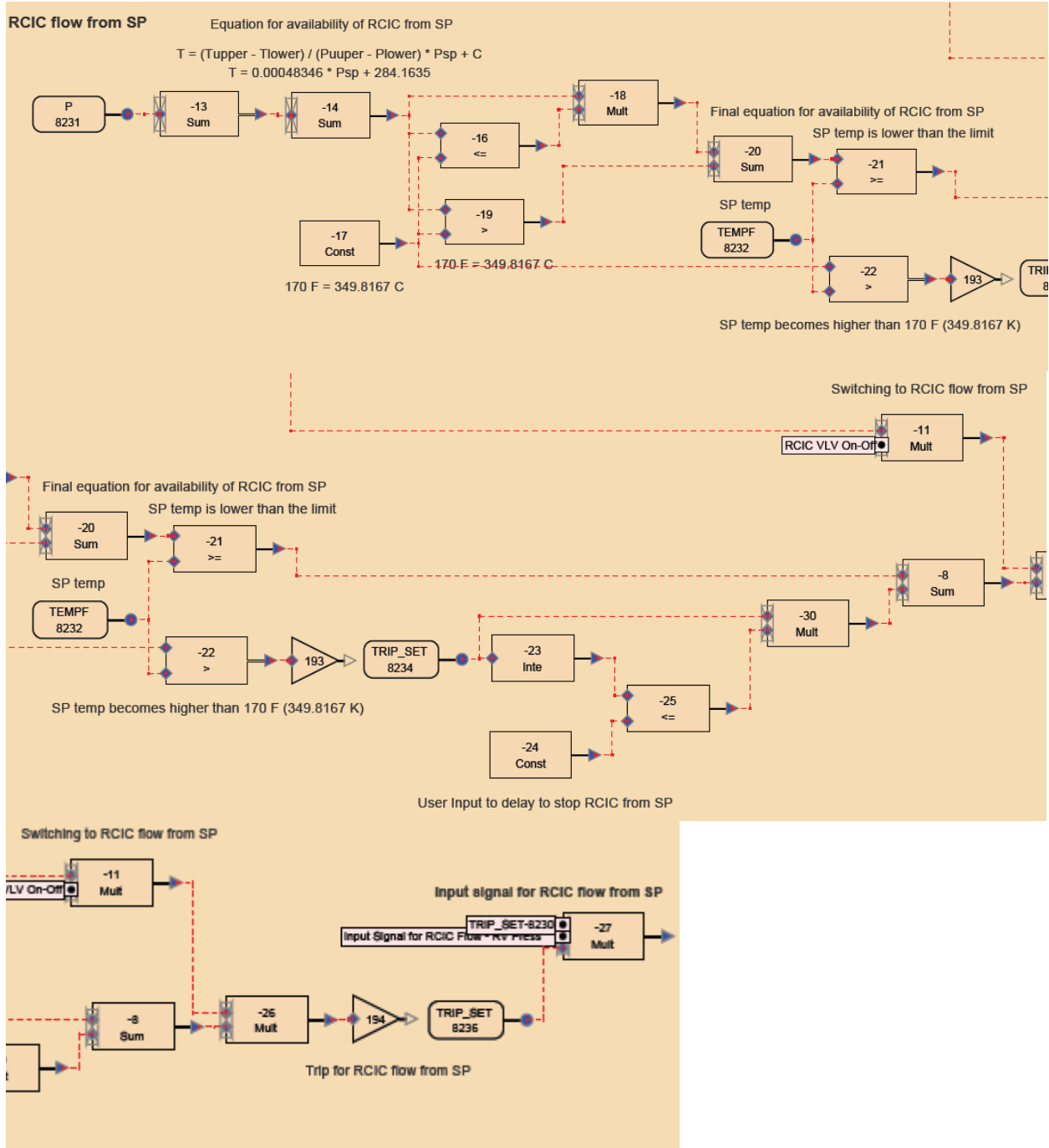


Figure A.18 Control System for RCIC Flow from SP

Table A.22 Signal Variables, Control Blocks, and Trips Used in Control Logic for RCIC Flow from SP

Trips					
Trip # (IDTD)	Signal range type # (ISRT)	Variable (IDSG)	Setpoint 1 (setp-1)	Setpoint 2 (setp-2)	Remark
193	2	Status of SP temp. (CB-22)	-0.1	0.9	Checking if SP temp. is higher than 349.82 K (170°F)
194	2	Multiplying several status values: See below (CB-26)	0.0	0.9	To control RCIC flow from SP
Signal variables					
SV #	Signal	Parameter type			
8230	TRIP-192	Trip set status value			
8231	FILL-91	Pressure: SP pressure			
8232	FILL-91	Temperature: SP temperature			
8234	TRIP-193	Trip set status value			
8236	TRIP-194	Trip set status value			
8223	TRIP-149	Trip set status value (to check if downcomer water level is low enough to initiate RCIC flow)			
8229	TRIP-191	Trip set status value (to stop RCIC flow from CST)			
8233	Reactor Vessel Dome	Pressure			
Control blocks					
CB #	Type	Gain	Inputs	Remark	
-13	Sum	4.8346×10^{-4}	SV-8231: SP pressure	(Slope of SP temp. equation) \times (SP press.)	
-14	Sum	1.0	CB-13+284.16	Adding y-intercept to CB-13: SP temp. equation	
-17	Constant	1.0	349.82 K (170°F)	Upper limit of SP temp. equation	
-16	\leq	1.0	CB-14 \leq CB-17	1.0: when output of SP temp. equation (CB-14) \leq 349.82 K 0.0: Otherwise	
-18	Multiply	1.0	CB-14 and CB-16	CB-14: when output of SP temp. equation (CB-14) \leq 349.82 K 0.0: otherwise	
-19	$>$	349.82	CB-14 $>$ CB-17	349.82 K: when output of SP temp. equation $>$ 349.82 K 0.0: otherwise	
-20	Sum	1.0	CB-18 and CB-19	Final SP temp. equation for availability of RCIC from SP (see Figure A.14)	

-21	\geq	1.0	CB-20 \geq SV-8232 (SP temp.)	1.0: when limit of SP temp (CB-20) is higher than actual SP temp. 0.0: otherwise
-22	$>$	1.0	SV-8232 (SP temp.) $>$ CB-17 (349.82 K)	1.0: when SP temp is higher than 349.82 K (170°F) 0.0: otherwise
-23	Integrate	1.0	SV-8234	Integrated time after SP temp. exceeds 349.82 K (170°F)
-24	Constant	1.0	User input; a 20 s delay is assumed	Time delay to still allow RCIC flow from SP after SP temp. exceeds 349.82 K (170°F)
-25	\leq	1.0	CB-23 \leq CB-24	1.0: when integrated time \leq user input of the delay time 0.0: otherwise
-30	Multiply	1.0	CB-25 and SV-8234	To avoid giving an incorrect signal from CB-25 ¹
-8	Sum		CB-21 and CB-30	1.0: when SP temp. is lower than the limit or integrated time is less than the delay time if SP temp. becomes higher than 349.82 K (170°F) 0.0: otherwise
-11	Multiply	1.0	SV-8229 and SV-8223	1.0: when CST is empty for RCIC flow and the DC water level is low enough 0.0: otherwise
-26	Multiply	1.0	CB-8 and CB-11	1.0: when CB-8=1.0 & CB-11=1.0 0.0: otherwise
-27	Multiply	1.0	SV-8230, SV-8233 and SV-8236	RV dome pressure: when RCIC flow from SP is activated and RCIC flow is activated 0.0: otherwise

¹ CB-25 gives the incorrect output value of 1.0 when the time delay specified in CB-24 is 0.0 s and the SP temperature is below the 349.82 K (170°F) limit. In order to prevent this from happening, the output of CB-25 is multiplied by the output of the trip set status of TRIP-193 that checks if the SP temperature is higher than the upper limit of 349.82 K (170°F) for the RCIC availability.

The RCIC flow from the SP is controlled using FILL-91 shown in Figure A.10. Table A.23 shows the input information for FILL-91.

Table A.23 Input Information for FILL-91

Input variable	Input	Remark
Fill type	Mass flow table: 5	Table: (Input signal vs. Mass flow (kg/s))
		0.0 0.0
		2.757903E5 0.0
		1.137635E6 39.414
1.0E8 39.414		
Valve table signal	CB-27	Reactor vessel dome pressure

Preliminary test calculations indicated unusual behavior of the reactor core isolation cooling system (RCIC) during steady-state calculations. This was due to the calculational procedure in TRACE for steady-state calculations. While the logical control system was properly established to initiate and deactivate RCIC based on RPV reactor water level (RWL) signals, the steady-state flow rate was established based on the input to the FILL component without consideration of the control system (CS). The CS features are generally disabled in steady-state calculations with TRACE to override features such as transient trips. To correct the behavior of the RCIC during steady-state calculations it was necessary to input an initial flow rate of zero into the TRACE FILL component representing the RCIC.

1.15 Standby Liquid Control System

The standby liquid control system (SLCS) is ultimately responsible for terminating the ATWS event and bringing the reactor to a hot shutdown and stable condition. Two alternative SLCS configurations are required for the current analysis of ATWS. In the case of ATWS-I the SLCS injection point is into the upper plenum inside the shroud (typical for BWR/5). For the ATWS-ED scenario the SLCS injection point is into the lower plenum (typical for BWR/4).

The modeling of SLCS is done by use of a FILL component that injects borated solution into the appropriate node within the VESSEL component in TRACE. The important parameters to specify for the SLCS FILL are: (1) flow rate, (2) boron concentration, and (3) initiation time.

The SLCS injection rate and concentration are based on the TRACG analysis [2]. The basis for the TRACG analysis is a 13 weight percent (w/o) solution of sodium pentaborate (SPB) that is injected into a 251 inch vessel at a flow rate of 86 gpm. The SPB solution is presumed to have natural boron, as opposed to enriched boron. The concentration and flow rate are fully consistent with the provisions of the ATWS-rule [21] (10 CFR 50.62).

In the TRACE model, boron solution is delivered from a FILL to the VESSEL injection point via a 2-meter pipe of 0.05067 m² flow area. The full flow velocity of boron solution is calculated as,

$$(86 \text{ gpm}) \times (\text{min}/60 \text{ s}) \times (0.0037854 \text{ m}^3/\text{gal}) / 0.05067 \text{ m}^2 = 0.1071 \text{ m/s.}$$

The initial conditions of the FILL are based on the TRACG inputs [2]:

- Initial liquid temperature = 316.48 K
- Initial pressure = 8.7217 MPa

The TRACG input shows a boron concentration of 23.517 kg/m³ and a water density of 992.7 kg/m³. Thus the initial boron solute ratio (a TRACE input for the FILL) is calculated as,

$$(23.517 \text{ kg/m}^3) / (992.7 \text{ kg/m}^3) = 0.02369.$$

It is noted that the boron concentration, to be consistent with the nuclear cross-section data, is in natural boron equivalent. Based on the molecular weight of sodium pentaborate ($\text{Na}_2\text{O} \cdot 5\text{B}_2\text{O}_3 \cdot 10\text{H}_2\text{O}$) at 13 w/o in solution, the boron in solution is approximately 2.38% and agrees with the derived value from the TRACG deck.

Each boron injection configuration is represented by a combination of FILL and PIPE, FILL 196 and PIPE 195 for the lower plenum injection and FILL 191 and PIPE 190 for the upper plenum injection. The injection location is arbitrated by activating the corresponding trip, TRIP 196 for the lower plenum injection and TRIP 190 for the upper plenum injection. The timing of both trips is based on the TRACG assumptions [17]. For the ATWS-ED cases (lower plenum injection) the SLCS injection is initiated 201 seconds after initiation of MSIV closure. For the ATWS-I cases (upper plenum injection) the SLCS injection is initiated 120 seconds after initiation of turbine trip. A table is used in FILL 196 and 190 to ramp up the flow velocity linearly from zero to full flow in 60 seconds [17].

1.16 Lower Plenum Flow Valve¹¹

NRC staff provided technical direction on the modeling of boron mixing in the reactor vessel when the SLCS injection is to the lower plenum of the vessel [4, 6, 8]. Boron transport for lower plenum injection configurations is modeled using a valve (Valve 34) inside the vessel lower plenum that opens and closes to simulate the effect of boron stratification and remixing. Below the stratification core flow rate setpoint, the lower plenum valve (LPV) closes to isolate the lower regions of the lower plenum and prevent effective entrainment of borated water into the active core region. When the core flow rate increases above the remixing threshold the LPV opens with a flow gradient based area curve to simulate increased remixing effectiveness. It is noted that for the BWR/5 the SLCS injects into the upper plenum and the modeling of the lower plenum valve is less important for the ATWS-I cases than for cases involving lower plenum SLCS injection, i.e. the ATWS-ED cases.

For the ATWS-I cases the flow valve is modeled with two cells and is located in ring 2 between the top of axial level 3 and the top of axial level 2 (see footnote 11).

Geometric data of the 2-cell flow valve:

Cell edge flow area = 5.0524 m²
Cell length = 0.2159 m
Hydraulic diameter = 0.65027 m
Kfac = 0.1 (forward at cell edge 2)
Kfac = 0.1 (reverse at cell edges 1 and 3)

Lower plenum injection can be broken down into two phases: mixing and remixing. Control logic, as shown in Figure A.19 has been implemented to regulate the fractional flow area of the flow control valve. In mixing one considers the operator action to reduce level and the

¹¹ For the modeling of boron mixing in the lower plenum, the lower plenum flow valve will be replaced in the ATWS-ED analysis by a control logic that releases the appropriate amount of boron into the core flow to emulate the effect of boron mixing/remixing.

subsequent decrease in core flow. Eventually the flow rate will drop below the mixing threshold at which point the controller must recognize that the mixing phase has ended. Once the mixing phase has ceased, the boron mixing valve in the lower plenum should fully close and remixing logic should take over. In remixing, the threshold value and a remixing effectiveness curve based on GEH data is used. However, the valve will never fully open in remixing based on the curve. Control logic should be established that recognizes the end of the mixing phase such that the lower plenum valve may be controlled by a separate flow based table. The remixing flow based table should be based on a ramp function that correlates the effectiveness of remixing with flow rate. This ramp function will reduce the amplitude of lower plenum valve cycling during transient oscillations and improve the calculation convergence. The NRC staff provided guidance on the ramp function [8]. The suggested ramp is based on GEH data supplied in MFN 09-681 [2]. While the data provided are for remixing coefficients, the effectiveness of remixing is adjusted using the valve area as a surrogate and is assumed to ramp with the remixing coefficient supplied by GEH.

The functions of the various control components shown in Figure A.19 are summarized in Table A.24.

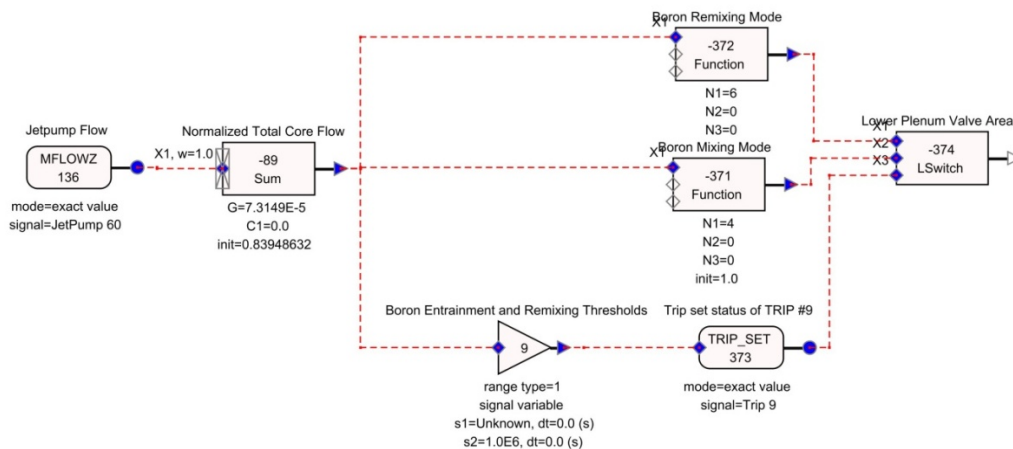


Figure A.19 Lower Plenum Flow Valve Control Logic

Table A.24 Control Components for Valve 34

Control Component	Function
SV 136	Mixed mass flow at the discharge of JetPump 60
CB 89	Core flow normalized to 100% flow of 1.367077×10^4 kg/s
Trip 9	Uses input from (CB 89) and is set to ON when normalized core flow is less than or equal to the threshold value [8]. Once ON the trip signal does not change to OFF (isrt=1 and SETP2=1.0E6).
CB 371	The lookup table gives the valve fractional flow area as a function of normalized core flow (output from CB 89). This applies to the remixing phase. Table entries are based on NRC staff guidance [8].
CB 372	The lookup table gives the valve fractional flow area as a function of normalized core flow (output from CB 89). This applies to the remixing phase. Table entries are based on NRC staff guidance [8].
SV 373	Trip set status of (Trip 9)
CB 374	The logic input switch produces an output according to the logical value of (SV 373): Output = Output of (CB 372) if (SV 373)=1.0 Output = Output of (CB 371) if (SV 373)=0.0

1.17 Containment¹²

Suppression Pool Cooling

The SRVs are connected to the wetwell of the CONTAN component and the discharge of steam will heat up the suppression pool. The built-in cooler of the CONTAN component can only be on or off and it is impossible to activate and deactivate the containment wetwell cooler with a control system. In order to enable the activation of suppression pool cooling by control logic a scheme was developed to remove energy from the suppression pool water by feed and bleed (remove warm pool water and replenish with cold water). The two parts of the scheme, a source to supply the feed and a sink to receive the bleed, are shown in Figure A.20. The connections to the wetwell are by the use of two BREAK components. The required mass flow to remove a certain amount of energy from the suppression pool is calculated by noting the heat removal capacity of the suppression pool cooler, as expressed in the following equation.

$$Q = H(T_{SP} - T_{SW})$$

where, Q is the heat removal rate,
H is the heat transfer coefficient,
 T_{sp} is the suppression pool temperature, and
 T_{sw} is the service water temperature.

If this heat removal were to be approximated by a mass exchange, the mass would be removed from the SP at a temperature of T_{sp} and restored to the SP at a temperature of T_{sw} . The rate of mass exchange would be given by the following equation.

$$Q = H(T_{SP} - T_{SW}) = wC_p T_{SP} - wC_p T_{SW}$$

$$w = \frac{H}{C_p}$$

where, w is the mass flow rate and
Cp is the average heat capacity of water over the temperature range of interest.

In modeling the cooler the mass flow w is provided by a single junction valve and the source and sink are again represented by two BREAK components.

The suppression pool cooler is modeled to emulate the suppression pool cooling mode of the residual heat removal system (RHR)¹³. The RHR heat exchanger K-value (design) for a typical BWR/5 plant is 260 BTU/s-°F or 4.9377×10^5 W/K (Table 2.6-3 of Reference [22]). The specific heat capacity of water at 1 bar and ~70°C is 4185.41 J/kg-K. Thus, the mass flow rate for the cooler is calculated as:

$$w = 4.9377 \times 10^5 / 4185.41 = 118.0 \text{ kg/s.}$$

¹² Heat structures in the wetwell of the containment will be incorporated in the ATWS-ED analysis.

¹³ The ATWS-I analysis assumed one train of the RHR was operational. In the ATWS-ED analysis two trains of RHR will be assumed to be operational and thus two suppression pool coolers will be modeled.

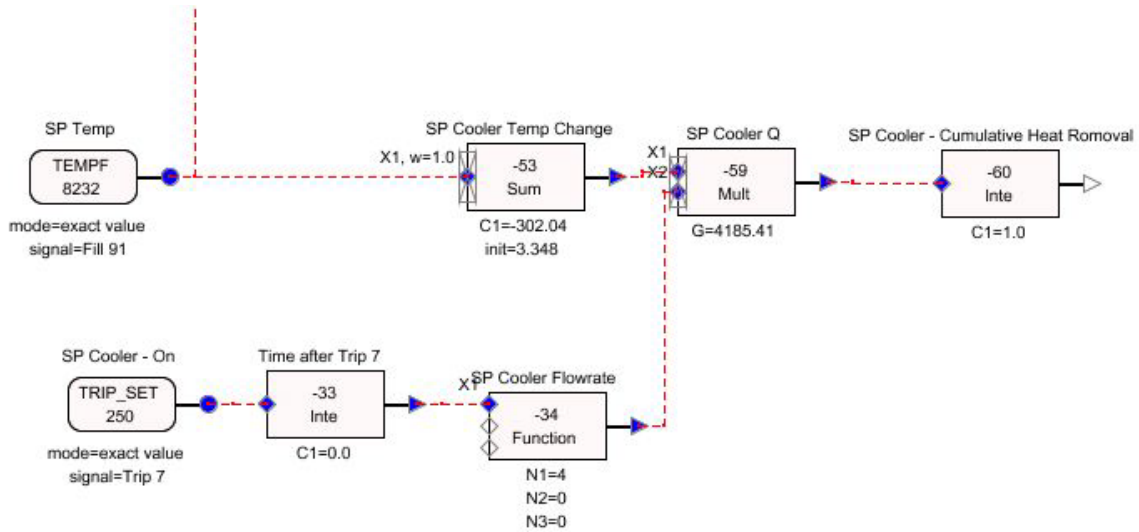


Figure A.21 Control Logic for the Suppression Pool Cooler

Table A.25 Control Components for the Suppression Pool Cooler

Control Component	Function										
SV 8232	Suppression pool temperature (T_{SP}). This variable is inferred from the temperature of FILL 91 that is connected to the wetwell of the CONTAN component.										
Trip 7	A time based trip to turn on the cooler, currently set at $t=600$ sec.										
SV 250	Trip set status of Trip 7.										
CB 33	Integrate (SV 250) to determine the time since (Trip 7) is TRUE.										
CB 34	Table look up to determine the flow rate through the cooler as a function of the output from (CB 33). <table border="1" style="margin-left: auto; margin-right: auto;"> <thead> <tr> <th>Time (s)</th> <th>Mass Flow (kg/s)</th> </tr> </thead> <tbody> <tr> <td>-1.0</td> <td>0.0</td> </tr> <tr> <td>0.0</td> <td>0.0</td> </tr> <tr> <td>60.0</td> <td>118.0</td> </tr> <tr> <td>1.0E4</td> <td>118.0</td> </tr> </tbody> </table> <p>The cooler flow rate is assumed to ramp up linearly from zero to the rated flow in 60 sec [17].</p>	Time (s)	Mass Flow (kg/s)	-1.0	0.0	0.0	0.0	60.0	118.0	1.0E4	118.0
Time (s)	Mass Flow (kg/s)										
-1.0	0.0										
0.0	0.0										
60.0	118.0										
1.0E4	118.0										
CB 53	Calculate ($T_{SP} - T_{SW}$) using input from (SV 8232) and a constant T_{SW} of 302.04 K										
CB 59	Calculate the heat removal rate of the cooler by getting the product of the outputs from (CB 34) and (CB 53) and a constant representing the specific heat capacity of water (4185.41 J/kg-K).										
CB 60	Integrate (CB 59) to calculate the cumulative heat removal from the suppression pool by the cooler.										

1.18 Boron Inventory in the Core

Using TRACE control system components an approach was developed for approximating the boron inventory in the core in order to understand what the model was predicting. Since the core model is comprised of a large number of fuel channels, tracking the boron inventory in each fuel channel is burdensome. The simplified approach tracks the boron inventory in a control volume around the core. This control volume includes one vessel node below the active core and two vessel nodes above the active core. Considering this control volume, there are only eight available flow paths for boron ingress or egress. These flow paths include: (1) the HPCS sparger, (2) the upper plenum SLCS injection line, (3) the ring one (R1) separators, (4) the ring two (R2) separators, (5) the R1 control rod guide tubes (CRGTs), (6) the R2 CRGTs, (7) the R1 lower plenum, and (8) the R2 lower plenum.

A control system was set up to integrate the boron continuity equation for the control volume. This was done by integrating the rate of boron exchanges at the interfaces. Integrating this equation would allow the inventory with a volume slightly larger than the active core to be calculated. To set up the continuity equation, however, it is necessary to implement a logical control system that identifies interface flows as either ingress or egress. Once the donor cells are identified the liquid mass flow rates at the interfaces are multiplied by the corresponding boron concentration in the donor cell. The product gives the rate of boron transport at the interfaces with a positive contribution for ingress and a negative for egress from the control volume.

Based on the extent of the core region defined for the calculation of boron inventory in the core there are a total of eight flow paths interfacing with the control volume. The rate of change of boron inventory in the core is given by the following continuity equation that accounts for the contribution from each flow path,

$$\frac{dB_c}{dt} = \sum_{i=1}^8 W_{l,i} B_i S_i$$

where

B_c is the boron inventory in the core.

$W_{l,i}$ is the water mass flow rate in the i^{th} flow path at the interface with the control volume.

B_i is the boron concentration in the donor cell. The donor cell is identified by noting the flow direction of $W_{l,i}$; it is the upstream volume for the flow associated with the i^{th} flow path.

S_i is a directional index based on the positive flow direction for the hydraulic component associated with the i^{th} flow path. If the positive flow direction is towards the control volume then $S_i = 1$ (ingress), otherwise $S_i = -1$ (egress).

The core boron inventory as a function of time is then evaluated by integrating the continuity equation, assuming $B_c(0)=0$.

$$B_c(t) = \sum_{i=1}^8 S_i \int_0^t W_{l,i} B_i dt$$

The control system diagram is shown in Figure A.22. The boron inventory is calculated in the final SUM block. Each interface includes a logical check to identify flow direction and associated donor cell and the boron concentration in each donor cell. The instantaneous

ingress or egress rate (liquid mass flow rate) is then multiplied by the corresponding boron concentration for the donor cell and the product fed into an individual integrator for each interface. This approach allows for detailed analysis of the boron flow by tracking each interface separately upstream of the SUM block.

Table A.26 summarizes the control components (signal variables and control blocks) that constitute the control system for calculating the boron inventory in the core.

Table A.26 Control Components for Calculating the Boron Inventory in the Core Region

Control Component	Function
SV 319	Constant = 0.0
SV 320	Liquid mass flow rate in PIPE 40 (Guidetube 40) at cell edge 5 (closest to the bottom of VESSEL axial level 6)
SV 321	Liquid mass flow rate in PIPE 41 (Guidetube 41) at cell edge 5.
SV 322	Boron concentration in PIPE 40 cell #4
SV 323	Boron concentration in PIPE 40 cell #5
SV 324	Boron concentration in PIPE 41 cell #4
SV 325	Boron concentration in PIPE 41 cell #5
SV 326	Liquid mass flow in VESSEL ring 1, top of axial level 5
SV 327	Liquid mass flow in VESSEL ring 2, top of axial level 5
SV 328	Boron concentration in VESSEL ring 1, axial level 5
SV 329	Boron concentration in VESSEL ring 1, axial level 6
SV 330	Boron concentration in VESSEL ring 2, axial level 5
SV 331	Boron concentration in VESSEL ring 2, axial level 6
SV 332	Liquid mass flow in SEPD 45 at cell edge 1
SV 333	Liquid mass flow in SEPD 46 at cell edge 1
SV 334	Boron concentration in VESSEL ring 1, axial level 11
SV 335	Boron concentration in SEPD 45 cell #1
SV 336	Boron concentration in VESSEL ring 2, axial level 11
SV 337	Boron concentration in SEPD 46 cell #1
SV 338	Liquid mass flow in SLCS PIPE 190 cell edge 3 (injection point)
SV 339	Liquid mass flow in HPCS TEE 183 cell edge 1 (injection point)
SV 340	Boron concentration in PIPE 190 cell #2
SV 341	Boron concentration in VESSEL ring 2, axial level 10
SV 343	Boron concentration in TEE 183 cell #1
CB 319	Define a constant 0.0
CB 320	Use 'greater than or equal to' logic to determine flow direction of (SV 320); output = 1.0 for ingress (positive flow enters the control volume) output = 0.0 for egress (negative flow leaves the control volume)
CB 321	Use 'greater than or equal to' logic to determine flow direction of (SV 321); output = 1.0 for ingress (positive flow enters the control volume) output = 0.0 for egress (negative flow leaves the control volume)
CB 322	Use 'input switch' logic to select boron concentration carried by (SV 320); (SV 322) if (CB 320) = 1.0 (SV 323) if (CB 320) = 0.0
CB 323	Multiply (SV 320) and (CB 322) Boron flow rate in PIPE 40 across cell edge 5, positive for ingress and negative for egress

Control Component	Function
CB 324	Use 'input switch' logic to select boron concentration carried by (SV 321); (SV 324) if (CB 321) = 1.0 (SV 325) if (CB 321) = 0.0
CB 325	Multiply (SV 321) and (CB 324) Boron flow rate in PIPE 41 across cell edge 5, positive for ingress and negative for egress
CB 326	Use 'greater than or equal to' logic to determine flow direction of (SV 326); output = 1.0 for ingress (positive flow enters the control volume) output = 0.0 for egress (negative flow leaves the control volume)
CB 327	Use 'greater than or equal to' logic to determine flow direction of (SV 327); output = 1.0 for ingress (positive flow enters the control volume) output = 0.0 for egress (negative flow leaves the control volume)
CB 328	Use 'input switch' logic to select boron concentration carried by (SV 326); (SV 328) if (CB 326) = 1.0 (SV 329) if (CB 326) = 0.0
CB 329	Multiply (SV 326) and (CB 328) Boron flow rate at core inlet in ring 1, positive for ingress and negative for egress
CB 330	Use 'input switch' logic to select boron concentration carried by (SV 327); (SV 330) if (CB 327) = 1.0 (SV 331) if (CB 327) = 0.0
CB 331	Multiply (SV 327) and (CB 330) Boron flow rate at core inlet in ring 2, positive for ingress and negative for egress
CB 332	Use 'greater than or equal to' logic to determine flow direction of (SV 332); output = 0.0 for ingress (negative flow enters the control volume) output = 1.0 for egress (positive flow leaves the control volume)
CB 333	Use 'greater than or equal to' logic to determine flow direction of (SV 333); output = 0.0 for ingress (negative flow enters the control volume) output = 1.0 for egress (positive flow leaves the control volume)
CB 334	Use 'input switch' logic to select boron concentration carried by (SV 332); (SV 334) if (CB 332) = 1.0 (SV 335) if (CB 332) = 0.0
CB 335	Multiply (SV 332) and (CB 334) Boron flow rate at core outlet through SEPD 45, positive for egress and negative for ingress
CB 336	Use 'input switch' logic to select boron concentration carried by (SV 333); (SV 336) if (CB 333) = 1.0 (SV 337) if (CB 333) = 0.0
CB 337	Multiply (SV 333) and (CB 336) Boron flow rate at core outlet through SEPD 46, positive for egress and negative for ingress
CB 338	Use 'greater than or equal to' logic to determine flow direction of (SV 338); output = 1.0 for ingress (positive flow enters the control volume) output = 0.0 for egress (negative flow leaves the control volume)
CB 339	Use 'greater than or equal to' logic to determine flow direction of (SV 339); output = 0.0 for ingress (negative flow enters the control volume) output = 1.0 for egress (positive flow leaves the control volume)

Control Component	Function
CB 340	Use 'input switch' logic to select boron concentration carried by (SV 338); (SV 340) if (CB 338) = 1.0 (SV 341) if (CB 338) = 0.0
CB 341	Multiply (SV 338) and (CB 340) Boron flow rate at junction where SLCS PIPE 190 injects into vessel , positive for ingress and negative for egress
CB 342	Use 'input switch' logic to select boron concentration carried by (SV 339); (SV 341) if (CB 339) = 1.0 (SV 343) if (CB 339) = 0.0
CB 343	Multiply (SV 339) and (CB 342) Boron flow rate at junction where HPCS TEE 183 connects to vessel , positive for egress and negative for ingress
CB 351	Integrate (CB 323) to calculate cumulative boron delivery to control volume from PIPE 40
CB 352	Integrate (CB 325) to calculate cumulative boron delivery to control volume from PIPE 41
CB 353	Integrate (CB 329) to calculate cumulative boron delivery to control volume from core inlet in ring 1
CB 354	Integrate (CB 331) to calculate cumulative boron delivery to control volume from core inlet in ring 2
CB 355	Integrate (CB 335) to calculate cumulative boron delivery to control volume through SEPD 45; a gain of -1 is applied to account for positive flow direction being away from the control volume.
CB 356	Integrate (CB 337) to calculate cumulative boron delivery to control volume through SEPD 46; a gain of -1 is applied to account for positive flow direction being away from the control volume.
CB 357	Integrate (CB 341) to calculate cumulative boron delivery to control volume from SLCS PIPE 190
CB 358	Integrate (CB 343) to calculate cumulative boron delivery to control volume through HPCS TEE 183; a gain of -1 is applied to account for positive flow direction being away from the control volume.
CB 359	Sum (CB 351, 352, 353, 354, 355, 356, 357, 358). For CB 351 through 358 a positive value indicates ingress while a negative value denotes egress (the sign takes into account the positive flow direction at the flow junctions) Net boron inventory in the control volume.

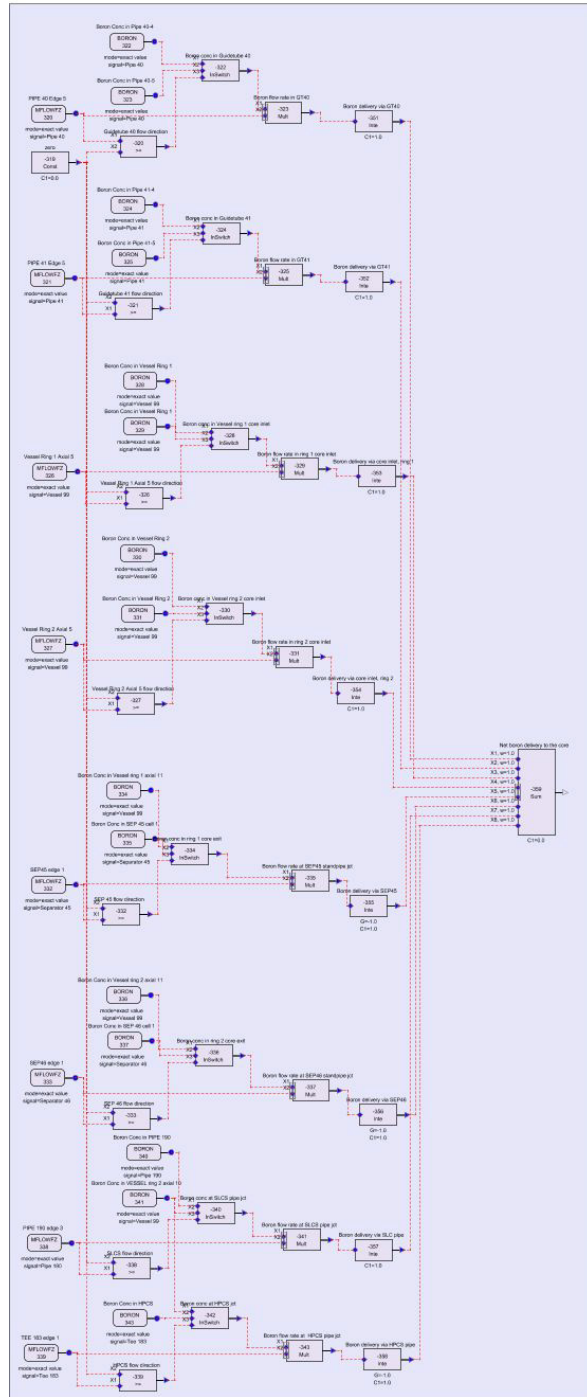


Figure A.22 Control System Diagram for Calculating Boron Inventory

1.19 Signal Variables and Control Blocks for the VESSEL Component

Summarized in Table A.27 are signal variables and control blocks defined for TRACE variables identified with the VESSEL component. The table also includes flow paths (other than CHANs) that interface with the internal nodes of the VESSEL.

Table A.27 Signal Variables and Control Blocks Identified with the VESSEL Component

Control Component	Function
SV 95	Water level in downcomer (isvn=106) relative to IDCL
SV 105	Pressure in ring 1 level 17 (RPV steam dome)
SV 108	Water level in downcomer (isvn=106) relative to IDCL
SV 114	Trip set status of Trip 119 (low-low-low level)
SV 120	Axial flow in ring 1 level 9
SV 121	Axial flow in ring 1 level 10
SV 122	Radial flow in level 10 from ring 1
SV 123	Axial flow in ring 2 level 9
SV 124	Axial flow in ring 2 level 10
SV 127	Axial flow in ring 1 level 5
SV 128	Axial flow in ring 2 level 5
SV 129	Radial flow in level 6 from ring 1
SV 136	Axial flow at jet pump discharge
SV 141	Axial flow in ring 1 level 6 (flow path has zero flow area in current model)
SV 142	Axial flow in ring 2 level 6 (flow path has zero flow area in current model)
SV 146	Axial flow from the outlet of Guidetube 40 (into ring 1 at the top of level 7)
SV 147	Axial flow from the outlet of Guidetube 41 (into ring 2 at the top of level 7)
SV 148	Axial flow in ring 1 level 7
SV 149	Axial flow in ring 2 level 7
SV 150	Radial flow in level 7 from ring 1
SV 201	Liquid saturation temperature in ring 1 level 6 (ring 1 core inlet)
SV 202	Liquid temperature in ring 1 level 6 (ring 1 core inlet)
SV 203	Liquid saturation temperature in ring 2 level 6 (ring 2 core inlet)
SV 204	Liquid temperature in ring 2 level 6 (ring 2 core inlet)
SV 205	Pressure in ring 1 level 6
SV 206	Pressure in ring 1 level 10
SV 207	Pressure in ring 2 level 6
SV 208	Pressure in ring 2 level 10
SV 225	Mixture density in ring 1 level 6
SV 226	Mixture density in ring 2 level 6
SV 227	Mixture density in ring 1 level 10
SV 228	Mixture density in ring 2 level 10
CB 82	Sum of (SV 121) + (SV 122) – (SV 120). This represents the total in-channel flow at the core exit from all CHAN's in ring 1
CB 83	Sum of (SV 124) - (SV 122) – (SV 123). This represents the total in-channel flow at the core exit from all CHAN's in ring 2
CB 84	Sum of (CB 82) + (CB 83). This represents the total in-channel flow at the core exit from all CHAN's in the core
CB 85	Sum of (SV 121) + (SV 124). This represents the total core flow at core exit (in-channel + bypass)

Control Component	Function
CB 86	Sum of (SV 148) + (SV 150) – (SV 141). This represents the total leakage flow from the lower tie plate of CHAN's in ring 1
CB 87	Sum of (SV 149) – (SV 150) – (SV 142). This represents the total leakage flow from the lower tie plate of CHAN's in ring 2
CB 88	Sum of (CB 86) + (CB 87). This represents the total leakage flow from the lower tie plate of all CHAN's in the core
CB 89	Fractional core flow normalized to a 100% core flow of 1.367077×10^4 kg/s
CB 92	Sum of (SV 141) + (SV 142). This represents the total bypass flow across the core support plate but is zero in the current model because of zero flow area for this flow path.
CB 93	Sum of (SV 146) + (SV 147). This represents the total bypass flow from the two Guidetubes
CB 94	Sum of (CB 88) + (CB 92) + (CB 93). This represents the total core bypass flow
CB 95	Sum of (CB 84) + (CB 94). This represents the total core flow at the core exit
CB 96	Sum of (SV 127) - (SV 129) - (SV 141). This represents the total inlet flow to all CHAN's in ring 1
CB 97	Sum of (SV 128) + (SV 129) - (SV 142). This represents the total inlet flow to all CHAN's in ring 2
CB 98	Sum of (CB 96) + (CB 97). This represents the total inlet flow to all CHAN's in the core
CB 201	Sum of (SV 201) – (SV 202). This represents the core inlet subcooling in ring 1
CB 202	Sum of (SV 203) – (SV 204). This represents the core inlet subcooling in ring 2
CB 203	Sum of (CB 225) – (CB 227). This represents the core pressure drop in ring 1
CB 204	Sum of (CB 226) – (CB 228). This represents the core pressure drop in ring 2
CB 225	Sum of (SV 205) – $5.4456 \times (\text{SV } 225)$. This represents the core inlet pressure in ring 1 corrected for the hydrostatic head in level 6 of ring 1. The multiplier to the density is the product of g (9.80665 m/s^2) and the half height of level 6 ($1.1106/2=0.5553 \text{ m}$).
CB 226	Sum of (SV 207) – $5.4456 \times (\text{SV } 226)$. This represents the core inlet pressure in ring 2 corrected for the hydrostatic head in level 6 of ring 2. The multiplier to the density is the product of g (9.80665 m/s^2) and the half height of level 6 ($1.1106/2=0.5553 \text{ m}$).
CB 227	Sum of (SV 206) + $0.91545 \times (\text{SV } 227)$. This represents the core outlet pressure in ring 1 corrected for the hydrostatic head in level 10 of ring 1. The multiplier to the density is the product of g (9.80665 m/s^2) and the half height of level 10 ($0.1867/2=0.09335 \text{ m}$).
CB 228	Sum of (SV 208) + $0.91545 \times (\text{SV } 228)$. This represents the core outlet pressure in ring 2 corrected for the hydrostatic head in level 10 of ring 2. The multiplier to the density is the product of g (9.80665 m/s^2) and the half height of level 10 ($0.1867/2=0.09335 \text{ m}$).

1.20 Signal Variables and Control Blocks for the Representative Channels

Several CHAN components have been selected to provide additional output for figures-of-merit characterizing the different oscillatory modes of the ATWS transient. For the ATWS-I cases four channels have been identified for more detailed output. Based on the PARCS standalone calculation (see Appendix B for more detail) the highest powered fuel assembly is identified with a hydraulic channel in the N-E quadrant of the core (the current TRACE hydraulic model

assumes half-core symmetry with a symmetry line running N to S). Corresponding to this CHAN is its counterpart in the S-E quadrant of the core (this is based on the first harmonic plane, which runs E to W). The PARCS first harmonic calculation produces the location of the fuel assembly with the highest first harmonic power (see Chapter 3 of the main report for more detail). This location is then identified with a CHAN in the N-E quadrant of the core and also its symmetric counterpart in the S-E quadrant of the core.

The location of these four CHANs varies for the different fuel cycle conditions being modeled. Thus the signal variables defined for these CHANs have to be updated in the TRACE transient restart file. A set of surrogate CHANs has been used in building the steady-state input deck and the CHAN identification numbers are from the PARCS standalone calculations for the BOC condition. For the ATWS-ED cases the TRACE hydraulic model lumps fuel assemblies into 27 CHANs and the four CHANs identified for additional output remain the same for all cases. Table A.28 summarizes control components defined for the four representative CHANs.

Table A.28 Control Components for the Representative Channels

Control Component	Function
SV 210	Avg rod surface heat loss from CHAN zzz isvn = 103, ilcn=zzz003 For ATWS-ED cases zzz=251 For ATWS-I cases zzz varies (e.g. for BOC zzz=269)
SV 211	Rod 1 (part length rod) surface heat loss from CHAN zzz isvn = 103, ilcn=zzz004 For ATWS-ED cases zzz=251 For ATWS-I cases zzz varies (e.g. for BOC zzz=269)
SV 212	Rod 2 (gad rod) surface heat loss from CHAN zzz isvn = 103, ilcn=zzz005 For ATWS-ED cases zzz=251 For ATWS-I cases zzz varies (e.g. for BOC zzz=269)
SV 213	Rod 3 (hot rod) surface heat loss from CHAN zzz isvn = 103, ilcn=zzz006 For ATWS-ED cases zzz=251 For ATWS-I cases zzz varies (e.g. for BOC zzz=269)
SV 214	Avg rod surface heat loss from CHAN zzz isvn = 103, ilcn=zzz003 For ATWS-ED cases zzz=451 For ATWS-I cases zzz varies (e.g. for BOC zzz=520)
SV 215	Rod 1 (part length rod) surface heat loss from CHAN zzz isvn = 103, ilcn=zzz004 For ATWS-ED cases zzz=451 For ATWS-I cases zzz varies (e.g. for BOC zzz=520)
SV 216	Rod 2 (gad rod) surface heat loss from CHAN zzz isvn = 103, ilcn=zzz005 For ATWS-ED cases zzz=451 For ATWS-I cases zzz varies (e.g. for BOC zzz=520)
SV 217	Rod 3 (hot rod) surface heat loss from CHAN zzz isvn = 103, ilcn=zzz006 For ATWS-ED cases zzz=451 For ATWS-I cases zzz varies (e.g. for BOC zzz=520)

Control Component	Function
SV 218	Inlet mass flow to CHAN zzz isvn=69, ilcn=zzz For ATWS-ED cases zzz=251 For ATWS-I cases zzz varies (e.g. for BOC zzz=269)
SV 219	Inlet mass flow to CHAN zzz isvn=69, ilcn=zzz For ATWS-ED cases zzz=451 For ATWS-I cases zzz varies (e.g. for BOC zzz=520)
SV 220	Pressure in cell 1 of CHAN zzz isvn=21, ilcn=zzz For ATWS-ED cases zzz=251 For ATWS-I cases zzz varies (e.g. for BOC zzz=269)
SV 221	Pressure in cell 1 of CHAN zzz isvn=21, ilcn=zzz For ATWS-ED cases zzz=451 For ATWS-I cases zzz varies (e.g. for BOC zzz=520)
SV 222	Mass in CHAN zzz isvn=124, ilcn=zzz For ATWS-ED cases zzz=251 For ATWS-I cases zzz varies (e.g. for BOC zzz=269)
SV 223	Mass in CHAN zzz isvn=124, ilcn=zzz For ATWS-ED cases zzz=451 For ATWS-I cases zzz varies (e.g. for BOC zzz=520)
SV 230	Avg rod surface heat loss from CHAN zzz isvn = 103, ilcn=zzz003 For ATWS-ED cases zzz=551 For ATWS-I cases zzz varies (e.g. for BOC zzz=245)
SV 231	Rod 1 (part length rod) surface heat loss from CHAN zzz isvn = 103, ilcn=zzz004 For ATWS-ED cases zzz=551 For ATWS-I cases zzz varies (e.g. for BOC zzz=245)
SV 232	Rod 2 (gad rod) surface heat loss from CHAN zzz isvn = 103, ilcn=zzz005 For ATWS-ED cases zzz=551 For ATWS-I cases zzz varies (e.g. for BOC zzz=245)
SV 233	Rod 3 (hot rod) surface heat loss from CHAN zzz isvn = 103, ilcn=zzz006 For ATWS-ED cases zzz=551 For ATWS-I cases zzz varies (e.g. for BOC zzz=245)
SV 234	Avg rod surface heat loss from CHAN zzz isvn = 103, ilcn=zzz003 For ATWS-ED cases zzz=751 For ATWS-I cases zzz varies (e.g. for BOC zzz=546)
SV 235	Rod 1 (part length rod) surface heat loss from CHAN zzz isvn = 103, ilcn=zzz004 For ATWS-ED cases zzz=751 For ATWS-I cases zzz varies (e.g. for BOC zzz=546)

Control Component	Function
SV 236	Rod 2 (gad rod) surface heat loss from CHAN zzz isvn = 103, ilcn=zzz005 For ATWS-ED cases zzz=751 For ATWS-I cases zzz varies (e.g. for BOC zzz=546)
SV 237	Rod 3 (hot rod) surface heat loss from CHAN zzz isvn = 103, ilcn=zzz006 For ATWS-ED cases zzz=751 For ATWS-I cases zzz varies (e.g. for BOC zzz=546)
SV 238	Inlet mass flow to CHAN zzz isvn=69, ilcn=zzz For ATWS-ED cases zzz=551 For ATWS-I cases zzz varies (e.g. for BOC zzz=245)
SV 239	Inlet mass flow to CHAN zzz isvn=69, ilcn=zzz For ATWS-ED cases zzz=751 For ATWS-I cases zzz varies (e.g. for BOC zzz=546)
SV 240	Pressure in cell 1 of CHAN zzz isvn=21, ilcn=zzz For ATWS-ED cases zzz=551 For ATWS-I cases zzz varies (e.g. for BOC zzz=245)
SV 241	Pressure in cell 1 of CHAN zzz isvn=21, ilcn=zzz For ATWS-ED cases zzz=751 For ATWS-I cases zzz varies (e.g. for BOC zzz=546)
SV 242	Mass in CHAN zzz isvn=124, ilcn=zzz For ATWS-ED cases zzz=551 For ATWS-I cases zzz varies (e.g. for BOC zzz=245)
SV 243	Mass in CHAN zzz isvn=124, ilcn=zzz For ATWS-ED cases zzz=751 For ATWS-I cases zzz varies (e.g. for BOC zzz=546)
SV 251	Coolant density in cell 1 of CHAN zzz isvn=76, ilcn=zzz For ATWS-ED cases zzz=251 For ATWS-I cases zzz varies (e.g. for BOC zzz=269)
SV 252	Coolant density in cell 1 of CHAN zzz isvn=76, ilcn=zzz For ATWS-ED cases zzz=451 For ATWS-I cases zzz varies (e.g. for BOC zzz=520)
SV 253	Coolant density in cell 1 of CHAN zzz isvn=76, ilcn=zzz For ATWS-ED cases zzz=551 For ATWS-I cases zzz varies (e.g. for BOC zzz=245)
SV 254	Coolant density in cell 1 of CHAN zzz isvn=76, ilcn=zzz For ATWS-ED cases zzz=751 For ATWS-I cases zzz varies (e.g. for BOC zzz=546)

Control Component	Function
CB 205	Hydrostatic head ¹ in CHAN zzz For ATWS-ED cases zzz=251 and nchan=44 For ATWS-I cases zzz varies (e.g. for BOC zzz=269) and nchan=2 $\Delta P_{\text{hydro}} = \rho g H = 1053.176 \times (\text{SV } 222) / \text{nchan}$
CB 206	Hydrostatic head ¹ in CHAN zzz For ATWS-ED cases zzz=451 and nchan=52 For ATWS-I cases zzz varies (e.g. for BOC zzz=520) and nchan=2 $\Delta P_{\text{hydro}} = \rho g H = 1053.176 \times (\text{SV } 223) / \text{nchan}$
CB 207	Surface heat loss from all rods in CHAN zzz Sum of (SV 210) + (SV 211) + (SV 212) + (SV 213) For ATWS-ED cases zzz=251 For ATWS-I cases zzz varies (e.g. for BOC zzz=269)
CB 208	Surface heat loss from all rods in CHAN zzz Sum of (SV 214) + (SV 215) + (SV 216) + (SV 217) For ATWS-ED cases zzz=451 For ATWS-I cases zzz varies (e.g. for BOC zzz=520)
CB 209 ³	Inlet pressure loss for CHAN zzz Sum of (CB 225) – (CB 251) For ATWS-ED cases zzz=251 For ATWS-I cases zzz varies (e.g. for BOC zzz=269)
CB 210 ³	Inlet pressure loss for CHAN zzz Sum of (CB 225) – (CB 252) For ATWS-ED cases zzz=451 For ATWS-I cases zzz varies (e.g. for BOC zzz=520)
CB 211 ⁴	Two-phase pressure drop $(\Delta P_{2\phi})^2$ in CHAN zzz Sum of (CB 203) – (CB 209) – (CB 205) For ATWS-ED cases zzz=251 For ATWS-I cases zzz varies (e.g. for BOC zzz=269)
CB 212 ⁴	Two-phase pressure drop $(\Delta P_{2\phi})^2$ in CHAN zzz Sum of (CB 203) – (CB 210) – (CB 206) For ATWS-ED cases zzz=451 For ATWS-I cases zzz varies (e.g. for BOC zzz=520)
CB 213	Ratio of single-phase to two-phase pressure drop for CHAN zzz $(\Delta P_{1\phi} / (\Delta P_{2\phi}))^2 = (\text{CB } 209) / (\text{CB } 211)$ For ATWS-ED cases zzz=251 For ATWS-I cases zzz varies (e.g. for BOC zzz=269)
CB 214	Ratio of single-phase to two-phase pressure drop for CHAN zzz $(\Delta P_{1\phi} / (\Delta P_{2\phi}))^2 = (\text{CB } 210) / (\text{CB } 212)$ For ATWS-ED cases zzz=451 For ATWS-I cases zzz varies (e.g. for BOC zzz=520)
CB 215	Hydrostatic head ¹ in CHAN zzz For ATWS-ED cases zzz=551 and nchan=64 For ATWS-I cases zzz varies (e.g. for BOC zzz=245) and nchan=2 $\Delta P_{\text{hydro}} = \rho g H = 1053.176 \times (\text{SV } 242) / \text{nchan}$
CB 216	Hydrostatic head ¹ in CHAN zzz For ATWS-ED cases zzz=751 and nchan=24 For ATWS-I cases zzz varies (e.g. for BOC zzz=546) and nchan=2 $\Delta P_{\text{hydro}} = \rho g H = 1053.176 \times (\text{SV } 243) / \text{nchan}$

Control Component	Function
CB 217	Surface heat loss from all rods in CHAN zzz Sum of (SV 230) + (SV 231) + (SV 232) + (SV 233) For ATWS-ED cases zzz=551 For ATWS-I cases zzz varies (e.g. for BOC zzz=245)
CB 218	Surface heat loss from all rods in CHAN zzz Sum of (SV 234) + (SV 235) + (SV 236) + (SV 237) For ATWS-ED cases zzz=751 For ATWS-I cases zzz varies (e.g. for BOC zzz=546)
CB 219 ³	Inlet pressure loss for CHAN zzz Sum of (CB 225) – (CB 253) For ATWS-ED cases zzz=551 For ATWS-I cases zzz varies (e.g. for BOC zzz=245)
CB 220 ³	Inlet pressure loss for CHAN zzz For ATWS-ED cases zzz=751 (a CHAN in ring 2) CB = (CB 226) – (CB 254) For ATWS-I cases zzz varies (e.g. for BOC zzz=546) CB = (CB 225) – (CB 254)
CB 221 ⁴	Two-phase pressure drop $(\Delta P_{2\phi})^2$ in CHAN zzz Sum of (CB 203) – (CB 219) – (CB 215) For ATWS-ED cases zzz=551 For ATWS-I cases zzz varies (e.g. for BOC zzz=245)
CB 222 ⁴	Two-phase pressure drop $(\Delta P_{2\phi})^2$ in CHAN zzz For ATWS-ED cases zzz=751 (a CHAN in ring 2) Sum of (CB 204) – (CB 220) – (CB 216) For ATWS-I cases zzz varies (e.g. for BOC zzz=546) Sum of (CB 203) – (CB 220) – (CB 216)
CB 223	Ratio of single-phase to two-phase pressure drop for CHAN zzz $(\Delta P_{1\phi} / (\Delta P_{2\phi}))^2 = (CB 219) / (CB 221)$ For ATWS-ED cases zzz=551 For ATWS-I cases zzz varies (e.g. for BOC zzz=245)
CB 224	Ratio of single-phase to two-phase pressure drop for CHAN zzz $(\Delta P_{1\phi} / (\Delta P_{2\phi}))^2 = (CB 220) / (CB 222)$ For ATWS-ED cases zzz=751 For ATWS-I cases zzz varies (e.g. for BOC zzz=546)
CB 251	Sum of (SV 220) + 1.3612x(SV 251). This represents the pressure at the bottom face of CHAN zzz corrected for the hydrostatic head in cell 1 of the CHAN. The multiplier to the density is the product of g (9.80665 m/s ²) and the half height of cell 1 of the CHAN (0.2776/2=0.1388 m). For ATWS-ED cases zzz=251 For ATWS-I cases zzz varies (e.g. for BOC zzz=269)
CB 252	Sum of (SV 221) + 1.3612x(SV 252). This represents the pressure at the bottom face of CHAN zzz corrected for the hydrostatic head in cell 1 of the CHAN. The multiplier to the density is the product of g (9.80665 m/s ²) and the half height of cell 1 of the CHAN (0.2776/2=0.1388 m). For ATWS-ED cases zzz=451 For ATWS-I cases zzz varies (e.g. for BOC zzz=520)

Control Component	Function
CB 253	Sum of (SV 240) + 1.3612x(SV 253). This represents the pressure at the bottom face of CHAN zzz corrected for the hydrostatic head in cell 1 of the CHAN. The multiplier to the density is the product of g (9.80665 m/s ²) and the half height of cell 1 of the CHAN (0.2776/2=0.1388 m). For ATWS-ED cases zzz=551 For ATWS-I cases zzz varies (e.g. for BOC zzz=245)
CB 254	Sum of (SV 241) + 1.3612x(SV 254). This represents the pressure at the bottom face of CHAN zzz corrected for the hydrostatic head in cell 1 of the CHAN. The multiplier to the density is the product of g (9.80665 m/s ²) and the half height of cell 1 of the CHAN (0.2776/2=0.1388 m). For ATWS-ED cases zzz=751 For ATWS-I cases zzz varies (e.g. for BOC zzz=546)

¹ This is calculated as $\rho g H$

$$g = 9.80665 \text{ m/s}^2$$

$$H = \text{height of CHAN} = 4.5942 \text{ m}$$

$$\rho = (\text{mass of coolant in CHAN}) / (\text{coolant volume in CHAN})$$

$$\text{Coolant volume in CHAN} = \text{free volume inside a single fuel assembly} \times n_{\text{chan}}$$

$$n_{\text{chan}} = \text{number of fuel assemblies represented by the CHAN}$$

$$\text{Free volume inside a single fuel assembly} = 4.27789 \times 10^{-2} \text{ m}^3$$

$$\rho g H = (\text{mass of coolant in CHAN}) \times 9.80665 \times 4.5942 / (4.27789 \times 10^{-2} \times n_{\text{chan}})$$

$$= 1053.176 \times (\text{mass of coolant in CHAN}) / n_{\text{chan}}$$

² As most of the single-phase pressure drop is associated with the inlet loss, the single-phase and two-phase pressure drops can be approximated by

$$\begin{cases} \Delta P_{1\phi} \approx \Delta P_{inlet} \\ \Delta P_{2\phi} \approx \Delta P_{core} - \Delta P_{inlet} - \Delta P_{hydro} \end{cases}$$

where ΔP_{hydro} represents the hydrostatic head in the channel. Thus, the ratio of single- to two-phase pressure drop is given by

$$\frac{\Delta P_{1\phi}}{\Delta P_{2\phi}} = \frac{\Delta P_{inlet}}{\Delta P_{core} - \Delta P_{inlet} - \Delta P_{hydro}}$$

³ For these control blocks the input signal can either be (CB 225) or (CB 226) depending on the location of the CHAN, i.e. in ring 1 or 2 respectively (as indicated by the CHAN input parameter IDROD).

⁴ For these control blocks the input signal can either be (CB 203) or (CB 204) depending on the location of the CHAN, i.e. in ring 1 or 2 respectively (as indicated by the CHAN input parameter IDROD).

The signal variables and control blocks used in the control logic to calculate the ratio of single- to two-phase pressure drop in the representative channels is shown in Figure A.23.

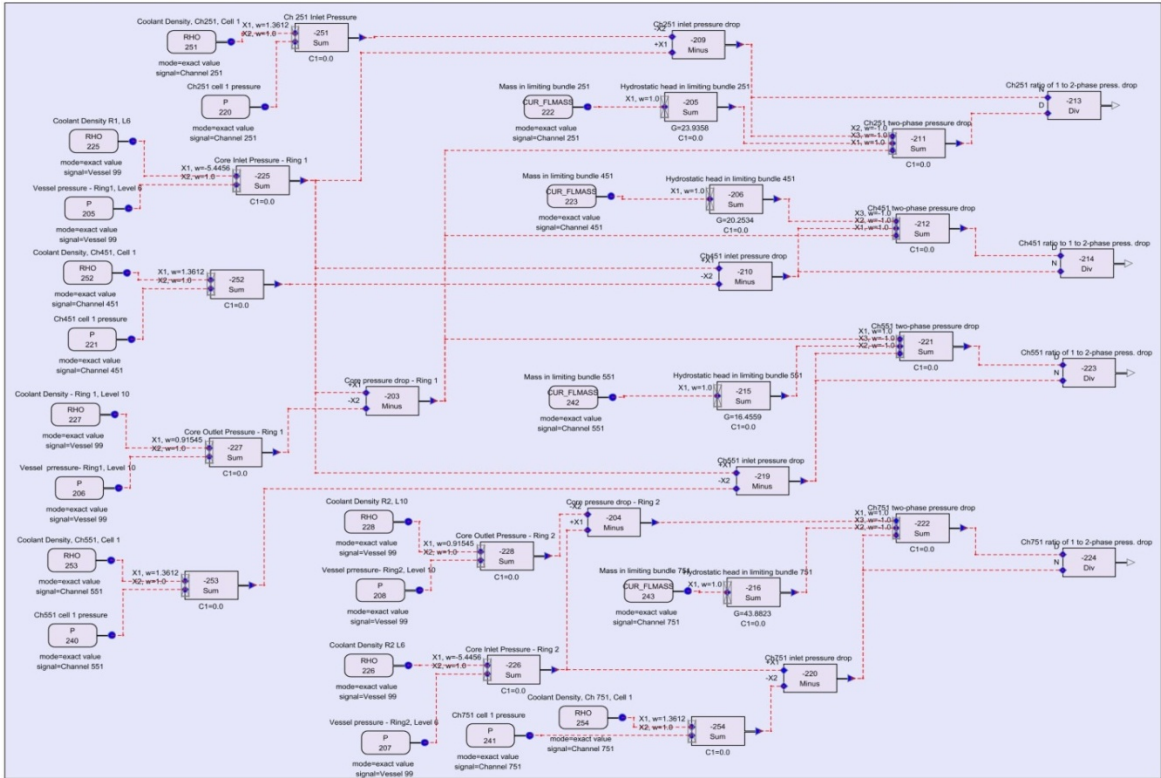


Figure A.23 Control Logic for the Calculation of Pressure Losses in a Channel

2 REFERENCES

1. U.S. Nuclear Regulatory Commission, "Safety Evaluation by the Office of Nuclear Reactor Regulation Related to Amendment No. 140 to Facility Operating License No. NPF-69 Nine Mile Point Nuclear Station, LLC, Nine Mile Point, Unit No. 2, Docket No. 50-410," December 22, 2011, ADAMS Accession No. ML113560333.
2. J. Harrison, GE Hitachi, letter to U.S. Nuclear Regulatory Commission, "Response to NRC's Data Request to Support Confirmatory ATWS Calculations Regarding MELLLA Plus," MFN 09-681, November 4, 2009, ADAMS Accession No. ML093170371.
3. U.S. Nuclear Regulatory Commission, "Summary of Trip Report for Site Visit to Brookhaven National Laboratory August 2010," February 12, 2015, ADAMS Accession No. ML15043A802.
4. U.S. Nuclear Regulatory Commission, "Summary of Trip Report for Site Visit to Brookhaven National Laboratory October 2010," February 12, 2015, ADAMS Accession No. ML15043A803.
5. U.S. Nuclear Regulatory Commission, "Summary of Trip Report for Site Visit to Brookhaven National Laboratory February 2011," February 12, 2015, ADAMS Accession No. ML15043A804.
6. U.S. Nuclear Regulatory Commission, "Summary of Trip Report for Site Visit to Brookhaven National Laboratory April 2011," February 12, 2015, ADAMS Accession No. ML15043A805.
7. U.S. Nuclear Regulatory Commission, "Summary of Trip Report for Site Visit to Brookhaven National Laboratory August 2011," February 12, 2015, ADAMS Accession No. ML15043A806.
8. U.S. Nuclear Regulatory Commission, "Summary of Trip Report for Site Visit to Brookhaven National Laboratory October 2010," February 12, 2015, ADAMS Accession No. ML15043A803.
9. A. Lingenfelter, Global Nuclear Fuels, letter to U.S. Nuclear Regulatory Commission, "NEDE-31152P, Global Nuclear Fuels, Fuel Bundle Designs, Revision 9 and Supplements 5 and 6, May 2007," FLN-2007-019, May 25, 2007, ADAMS Accession No. ML071510285.
10. GE Hitachi Nuclear Energy, "General Electric Systems Technology Manual, Chapter 2.2, Fuel and Control Rods System," U.S. Nuclear Regulatory Commission, September 2011, ADAMS Accession No. 11258A302
11. K.J. Geelhood et al, "FRAPCON-3.4: A Computer Code for the Calculation of Steady-State Thermal-Mechanical Behavior of Oxide Fuel Rods for High Burnup", NUREG/CR-7022, March 2011.
12. L-Y. Cheng et al., "TRACE/PARCS Core Modeling of a BWR/5 for Accident Analysis of ATWS Events," Trans. Am. Nucl. Soc. 109, pp 979-982, November 2013.

13. A. Lingenfelter, Global Nuclear Fuels, letter to U.S. Nuclear Regulatory Commission, "GE14 Compliance with Amendment 22 of NEDE-24011-P-A (GESTAR II), NEDC-32868P, Revision 3, April 2009," MFN 09-235, April 9, 2009, ADAMS Accession No. ML091000638.
14. R. Gamble, GE Nuclear Energy, letter to U.S. Nuclear Regulatory Commission, "Hypothetical ESBWR Core Design for TRACG Comparison," MFN 04-063, June 11, 2004, ADAMS Accession No. ML041740131.
15. A. Lingenfelter, Global Nuclear Fuels, letter to U.S. Nuclear Regulatory Commission, "GE14 Compliance with Amendment 22 of NEDE-24011-P-A (GESTAR II), NEDC-32868P, Revision 3, April 2009," MFN 09-235, April 9, 2009, ADAMS Accession No. ML091000638.
16. C.W. Stewart, et al., "VIPRE-01: A Thermal-Hydraulic Analysis Code for Reactor Cores Volume 1: Mathematical Modeling," NP-2511-CCM, Volume 1, Electric Power Research Institute, April 1983.
17. J. Harrison, GE Hitachi, letter to U.S. Nuclear Regulatory Commission, "Supplemental Response to NRC Information Requests 10, 13, and 14 – Confirmatory ATWS Calculations Regarding MELLLA+," MFN10-213, Supplement 1, October 29, 2010.
18. Nine Mile Point Unit 2 Updated Final Safety Analysis Report Rev 19, October 2010.
19. L-Y. Cheng et al., "TRACE Assessment for BWR ATWS Analysis," BNL-91311-2010-IR, Brookhaven National Laboratory, April 22, 2010.
20. J. Harrison, GE Hitachi, letter to U.S. Nuclear Regulatory Commission, "Accepted Version of GE Licensing Topical Report NEDC-33006P-A, Revision 3 (TAC No. MD0277)," MFN 09-362, June 19, 2009, ADAMS Accession No. ML091800512.
21. *U.S. Code of Federal Regulations*, "Requirements for Reduction of Risk from Anticipated Transients Without Scram (ATWS) Events for Light-Water-Cooled Nuclear Power Plants," Title 10 Section 50.62.
22. GE Hitachi Nuclear Energy, "Safety Analysis Report for Nine Mile Point Nuclear Station Unit 2 Constant Pressure Power Uprate (PUSAR)", NEDO-33351P, Rev. 0, May 31, 2009, ADAMS Accession No. ML091610104

APPENDIX B

PARCS Calculation Notebook

TABLE OF CONTENTS

1	INTRODUCTION	B-3
2	REACTOR AND FUEL BUNDLE PARAMETERS	B-3
3	REACTOR CORE MODEL.....	B-5
3.1	Cross Sections and Other Bundle Parameters.....	B-5
3.1.1	Cross Section Libraries.....	B-5
3.1.2	Xenon and Samarium	B-8
3.1.3	Coolant Density Correction and Direct Moderator Heating.....	B-8
3.1.4	Assembly Discontinuity Factor (ADF) Rotation	B-9
3.2	Core Geometry and Control Rod Banks.....	B-9
3.3	Numerics	B-10
3.4	Miscellaneous Input.....	B-11
3.4.1	Beginning of cycle, Peak Hot Excess and End of full Power Life Models	B-11
3.4.2	Output Options	B-11
3.4.3	Transient Data.....	B-12
3.5	TRACE/PARCS Mapping	B-13
3.6	Exposure and Moderator Density History.....	B-17
4	REFERENCES	B-20

LIST OF FIGURES

Figure B.1	Fuel Rod Isotopic Locations.....	B-4
Figure B.2	Layout of GE14 Fuel Bundle	B-5
Figure B.3	Control Rod Bank Positions in the Core.....	B-10
Figure B.4	Mapping for ATWS-ED - 27 Channels	B-15
Figure B.5	Mapping for ATWS-I - 382 Channels	B-16

LIST OF TABLES

Table B.1	Cross Sections Developed by ORNL	B-6
Table B.2	Final Branch Structure (PMAXS Order).....	B-7
Table B.3	Parameters Specified in the PARAM block	B-11
Table B.4	Output Options.....	B-12
Table B.5	Parameters Specified in the TRAN Block.....	B-13

1 INTRODUCTION

This calculation notebook (non-proprietary information only) documents the development of boiling water reactor (BWR) core models for the neutronics code PARCS [1]. PARCS is a three dimensional reactor core simulator that solves the steady state and time dependent, multi-group neutron diffusion and transport equations in orthogonal and non-orthogonal geometries. The code is coupled directly to the thermal hydraulics system code TRACE [2]. TRACE provides thermal hydraulic conditions to PARCS where the cross sections are a function of exposure, thermal-hydraulic variables, boron concentration, and control rod presence.

The models developed were for a BWR/5 at three different points in the fuel cycle: beginning-of-cycle (BOC), peak-hot-excess-reactivity (PHE), and end-of-full-power-life (EOFPL). They were generated to be used in coupled TRACE/PARCS steady-state calculations, PARCS standalone steady-state calculations, and transient TRACE/PARCS calculations. The PARCS models were developed specifically for the calculation of two types of anticipated transients without scram (ATWS). However, they have broader applicability and can be used for a variety of transients/accidents. The ATWS events of interest are for a plant operating in the MELLLA+ (maximum extended load line limit plus) operating regime on a power-flow operating map. One event is initiated by a turbine trip and goes through a period of instability causing power oscillations. This event is designated ATWS-I. The other event is initiated by the closure of main steam isolation valves and results in an automatic depressurization of the reactor when the heat capacity temperature limit of the suppression pool is reached. This event is designated ATWS-ED.

2 REACTOR AND FUEL BUNDLE PARAMETERS

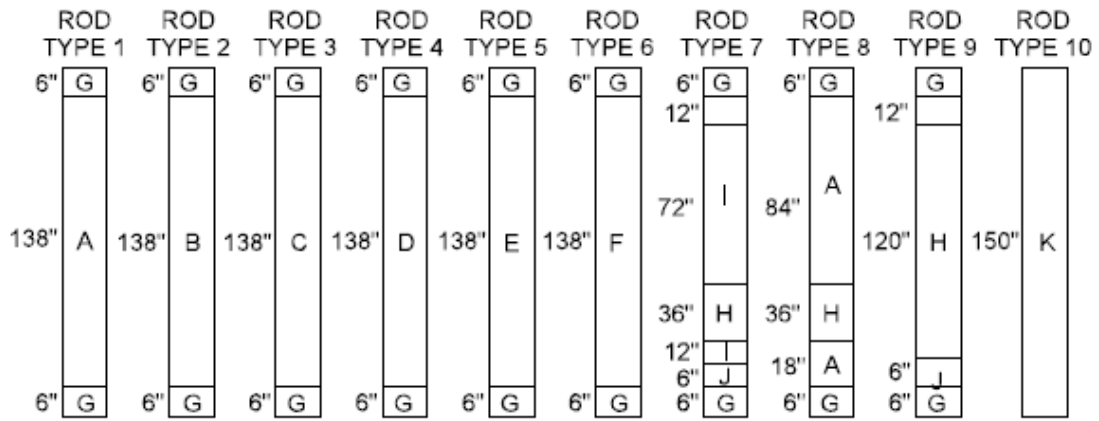
The study considers a hypothetical BWR/5 operating at MELLLA+ conditions. Nine Mile Point Unit 2 (NMP2) is fairly typical of the domestic BWR/5s and was referenced for various plant and core data. It should be noted that NMP2 has not been approved to operate at MELLLA+ conditions, but has been chosen as a reference plant to get certain data to support the model development.

Under MELLLA+ conditions, a BWR/5 can operate at 120% of its original licensed power, at a reduced flow for most of the cycle. At the end of the cycle, the flow is increased to maintain the power level. In the BWR/5 PARCS model, the total thermal power is 3988 MWt, or an average of 5.22 MWt per fuel assembly. The flow is imposed by TRACE, and is not specified in the PARCS model.

The model assumes an equilibrium core of 764 GE14 assemblies. Each assembly is a 10x10 fuel bundle consisting of: [3]

- 78 full length fuel rods (with natural uranium top and bottom blankets)
- 14 partial length fuel rods without gadolinia (with natural uranium bottom blankets only)
- two water rods (2x2 pitch each, hence, eight rod positions)

Some of the full length rods contain gadolinia as a burnable poison. Fuel enrichment varies from rod to rod, and gadolinia concentration changes for different rod types and axial level. Figure B.1 [4] provides an illustration of the rod-by-rod enrichment and gadolinia concentration for distinct axial segments, and Figure B.2 [4] shows the rod layout within the fuel bundle.



- A. 3.00% U²³⁵
- B. 2.60% U²³⁵
- C. 2.20% U²³⁵
- D. 2.00% U²³⁵
- E. 1.70% U²³⁵
- F. 1.30% U²³⁵
- G. 0.711% U²³⁵
- H. 1.70% U²³⁵, 5.0% Gd
- I. 1.70% U²³⁵, 4.0% Gd
- J. 1.70%, 2.0% Gd
- K. Water Rod

Figure B.1 Axial Layout of a Generic GE14 Fuel Bundle

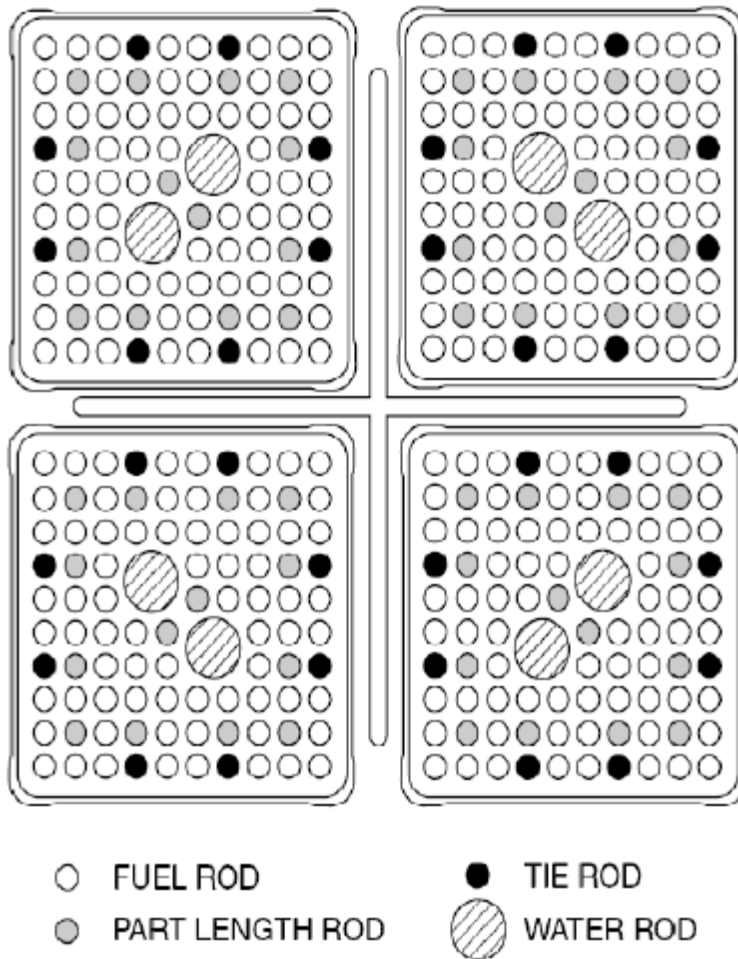


Figure B.2 Layout of GE14 Fuel Bundle

3 REACTOR CORE MODEL

3.1 Cross Sections and Other Bundle Parameters

The base BWR/5 core model described in this calculation notebook is the one used in a coupled TRACE/PARCS steady-state calculation for BOC conditions. The other models are very similar, and the differences are discussed where applicable.

3.1.1 Cross Section Libraries

The cross sections used by PARCS were provided by the U.S. Nuclear Regulatory Commission (NRC) in PMAXS format, which can be directly read by PARCS. They had been generated with SCALE/TRITON and converted to PMAXS format at Oak Ridge National Laboratory [5]. Table B.1 lists the cross section files received¹⁴. The version of the cross section set used in ATWS-I calculations is V3.2. The cross section files for fuel assemblies include four void histories, multiple burnup steps (up to a maximum exposure of 60 GWd/MTU), and 39 branches selected

¹⁴ New cross sections (v4.0) were received in January 2012. The new cross sections will be used for steady-state and transient ATWS-ED calculations.

by combining five moderator densities, three fuel temperatures, four boron concentrations, and two control states (controlled/uncontrolled). Table B.2 shows a sample of the branch structure. The radial reflectors were modeled with constant properties.

Table B.1 Cross Sections Developed by ORNL

File Name	Description
7990.PMAX	Natural uranium bottom blanket
7991.PMAX	Bottom fuel region
7992.PMAX	Lower center fuel region
7993.PMAX	Upper center fuel region
7994.PMAX	Top fuel region
7995.PMAX	Natural uranium top blanket
m+_radref.PMAX	Radial reflector, facing one fuel assembly ¹
m+_cornref.PMAX	Radial reflector (corner), facing two fuel assemblies ¹
m+_botref.PMAX	Bottom reflector
m+_topref.PMAX	Top reflector

¹ The corner reflector cross sections are represented by correcting the scattering cross sections as indicated in Equation 3.29 of [6].

Table B.2 Final Branch Structure (PMAXS Order)

Branch no.	Control rod state (0=out, 1=in)	Moderator Density (g/cm³)	Soluble Boron (ppm)	Fuel Temperature (K)
0	0	0.45843	0	863.15
1	1	0.45843	0	863.15
2	0	0.03653	0	863.15
3	0	0.17716	0	863.15
4	0	0.73970	0	863.15
5	0	1.00000	0	863.15
6	1	0.03653	0	863.15
7	1	0.17716	0	863.15
8	1	0.73970	0	863.15
9	1	1.00000	0	863.15
10	0	0.03653	600	863.15
11	0	0.03653	1400	863.15
12	0	0.03653	2200	863.15
13	0	0.17716	600	863.15
14	0	0.17716	1400	863.15
15	0	0.17716	2200	863.15
16	0	0.45843	600	863.15
17	0	0.45843	1400	863.15
18	0	0.45843	2200	863.15
19	0	0.73970	600	863.15
20	0	0.73970	1400	863.15
21	0	0.73970	2200	863.15
22	0	1.00000	2200	863.15
23	1	0.03653	2200	863.15
24	1	0.17716	2200	863.15
25	1	0.45843	2200	863.15
26	1	0.73970	2200	863.15
27	1	1.00000	2200	863.15
28	0	0.03653	0	293.15
29	0	0.03653	0	2073.15
30	0	0.17716	0	293.15
31	0	0.17716	0	2073.15
32	0	0.45843	0	293.15
33	0	0.45843	0	2073.15
34	0	0.73970	0	293.15
35	0	0.73970	0	2073.15
36	0	1.00000	0	293.15
37	0	1.00000	2200	293.15
38	1	1.00000	0	293.15
39	1	1.00000	2200	293.15

3.1.2 Xenon and Samarium

In the steady-state coupled calculation, the equilibrium number densities of xenon (Xe) and samarium (Sm) are calculated by specifying the following:

```
XE_SM 1 1
```

The resulting equilibrium Xe and Sm number densities are written in the output file with extension “dep.” It was discovered early in the ATWS-I analysis that when the PARCS Xe/Sm transient option was engaged, the code initialized with a large negative reactivity. A work-around was developed and incorporated in a recommended methodology to initialize PARCS [7]. In subsequent calculations (PARCS standalone steady-state or coupled transient), the Xe and Sm number densities are read from the above-mentioned file with extension “dep” by inputting:

```
XE_SM 3 3
```

3.1.3 Coolant Density Correction and Direct Moderator Heating

In PARCS, an effective coolant density model was implemented [8] to account for the impact of multiple fluid region water densities in the new BWR fuel designs. The effective coolant density (ρ_{eff}) is defined as:

$$\rho_{\text{eff}} = \rho_{\text{cool}} + \frac{A_{\text{wr}}}{A_{\text{cool}}} (\rho_{\text{wr}} - \rho_{\text{sat}}) + \frac{A_{\text{byp}}}{A_{\text{cool}}} (\rho_{\text{byp}} - \rho_{\text{sat}})$$

where ρ_{cool} is the density of the coolant in the active heated channel, ρ_{sat} is the saturated moderator liquid density, ρ_{wr} , the moderator density in the water rod, ρ_{byp} , the moderator density in the bypass, and $A_{\text{wr}}/A_{\text{cool}}$ and $A_{\text{byp}}/A_{\text{cool}}$ respectively are the area ratio of water rods to coolant and bypass to coolant. In the BWR/5 model, the effective coolant density model was used, with area fractions calculated from the dimensions given in [9].

The calculation of A_{byp} disregards the curvature of the corners of the channel box and assumes the control blade is present, which is not the case for most channels. The $A_{\text{byp}}/A_{\text{cool}}$ used in the calculations diminishes the importance of the bypass, which a priori is conservative.¹⁵ The calculation also assumed the following as inputs:

$$\begin{aligned} A_{\text{cool}} &= 91.589 \text{ cm}^2 \text{ (obtained from the TRACE model)} \\ \rho_{\text{sat}} &\text{ is found in [10]:} \\ \rho_{\text{sat}} &= 0.7397 \text{ g/cc} \end{aligned}$$

The values above are input in the “CDC_DAT” card of the “TH” block.

The direct energy deposition to the coolant was 1%, to the bypass 0.9%, and to the water rods 0.2% [11].

¹⁵ A test ATWS-I calculation has been performed with a larger and more realistic $A_{\text{byp}}/A_{\text{cool}}$ for PHE, with results virtually identical to the base case.

3.1.4 Assembly Discontinuity Factor (ADF) Rotation

The reference assembly modeled in SCALE/TRITON is the northeast fuel assembly, which means that the control blade is south and west of the fuel. The assemblies have to be rotated according to their position with respect to the control rod. The uncontrolled, peripheral assemblies have been rotated following an alternating pattern. This is specified in the “ADF_ROT” card of block “GEOM”.

3.2 Core Geometry and Control Rod Banks

Unless otherwise noted, the information below is included in the file listed in the main PARCS input deck under the “GEOM” block.

The core model contains 32x32 radial (x-y) meshpoints and 27 axial planes. Radially, a meshpoint represents one of the 764 fuel bundles, or a radial reflector. The meshpoint interval in the radial plane is 15.24 cm (6”), which is the pitch of the fuel bundles in the reactor core. The axial core layout contains 25 layers of fuel, including top and bottom natural uranium blankets. The axial meshpoint interval is 15.24 cm (6”) matching the overall active fuel length of GE14 bundles of 381 cm (150”). Zero flux boundary conditions are used at the outside of the reflectors.

The 27 axial nodes of the model are grouped into planar regions with unique materials, representing two reflectors (top and bottom), and the axial segments of the fuel rods with distinct fuel compositions.

The correspondence between material and actual cross section libraries is defined in the main PARCS input deck in the “DEPL” block. The correspondence is:

- Material 1: m+_botref.PMAX
- Material 2: 7990.PMAX
- Material 3: 7991.PMAX
- Material 4: 7992.PMAX
- Material 5: 7993.PMAX
- Material 6: 7994.PMAX
- Material 7: 7995.PMAX
- Material 8: m+_topref.PMAX
- Material 9: m+_radref.PMAX
- Material 10: m+_cornref.PMAX

The control rods were modeled independently, taking into account the quarter-core symmetry of the core. Figure B.3 shows the location of each of the 54 control rod banks in the core. The control rods can move 48 steps axially, with each step 7.62 cm [12]. In its fully inserted position, the position of the top of a control rod is 52.857 cm below the top of the core (or 15.24 cm below the top of active fuel). The positions of the control rods are defined in the “CNTL” block of the main input deck, and vary throughout the cycle, as follows:

- For BOC: banks 10, 21, 23 – 10 steps inserted; banks 19, 33, 35 – 34 steps inserted; all other banks fully withdrawn
- For PHE: banks 34, 43 – 10 steps inserted; banks 36, 45 – 40 steps inserted; bank 41 – 38 steps inserted; bank 20 – fully inserted; all other banks fully withdrawn.
- For EOFPL: all banks fully withdrawn

Table B.3 Parameters Specified in the PARAM block

Card	Field	Value	Description
N_ITERS	ninmax	10	Maximum number of inner iterations
	noutmax	5000 or 750 ⁽¹⁾	Maximum number of outer iterations for steady-state (5000) or transient (750)
CONV_SS	epseig	10 ⁻⁶⁽¹⁾	Eigenvalue convergence criterion
	epsI2	10 ⁻⁵⁽²⁾	Global fission source convergence criterion
	epsIinf	5x10 ⁻⁴⁽²⁾	Local fission source convergence criterion
	epstf	10 ⁻²⁽¹⁾	Fuel temperature convergence criterion
NODAL_KERN	kernel	HYBRID	ANM/NEM nodal hybrid for steady-state and ATWS-I
DECUSP	idecusp	2	Full control rod decussing
INIT_GUESS	iguess	0	Initial guess for the axial flux shape: cosine

¹As per guidance received from NRC [7].

²Default values

For problems using two-group cross sections, the nodal kernel most commonly used in PARCS is a hybrid between the analytic nodal method (ANM) and the nodal expansion method (NEM). This HYBRID kernel was chosen for the steady-states and the ATWS-I calculations.

3.4 Miscellaneous Input

3.4.1 Beginning-of-Cycle, Peak-Hot-Excess-Reactivity and End-of-Full-Power-Life Models

As it has been noted, this calculation notebook describes in detail the development of a BOC steady-state model. The PHE and EOFPL inputs have different control rod positions (described in Section B.3.2) and burnup and history information. They are generated for each point in the cycle from information received from GEH as described in Section B.3.6.

3.4.2 Output Options

PARCS output can be customized through input. Table B.4 shows the options used in the coupled steady-state input deck.

For the PARCS standalone calculation used for convergence testing and obtaining the first harmonic shape, field "popt(15)" in card "PRINT_OPT" is set to True (T).

Table B.4 Output Options

Block	Card	Field	Value	Description
CNTL	PRINT_OPT	popt(1)	T	Detailed input edit
		popt(2)	F	Iteration history display
		popt(3)	T	Planar power distributions
		popt(4)	F	Detailed pin power distributions
		popt(5)	T	Reactivity edit and adjoint flux
		popt(6)	T	Feedback component reactivity edit
		popt(7)	F	Integrated flux and precursor density edit
		popt(8)	F	Planar flux distributions
		popt(9)	F	Xe/Sm number densities
		popt(10)	T	TH state variables
		popt(11)	T	1D collapsed group constants
		popt(12)	F	Point kinetics data
		popt(13)	T	Radial power shape
		popt(14)	F	Radial flux shape
		popt(15)	F	First harmonic edit
DEPL	OUT_OPT	powp	T ¹	Print power distribution in dep file
		phst	T ¹	Print history distribution in dep file
		pths	T ¹	Print TH state in dep file
		pxesm	T ¹	Print Xe/Sm densities in dep file
		pxss	F ¹	Print cross sections for each region

¹ As per guidance received from the NRC [7]

3.4.3 Transient Data

The TRAN block is required in the transient input deck. The time step and end time are dictated by TRACE, and the corresponding cards in the TRAN block are omitted. The TRAN block also has inputs to activate the white noise model, which has an impact on the timing of the instability onset and initial growth. As per guidance by NRC staff [13], the noise signal in total power is approximately 0.5%. The cards used to specify the characteristics of the noise added to the calculation are EXCI_MOD, WHIT_NOI, DM_AMPLM, TF_AMPLM, and HARMON_F:

EXCI_MOD describes the modes to be excited, 3 entails the following modes will be “noisy”: 1: random, 2: fundamental, 3: harmonic.

WHIT_NOI activates the white noise, the noise will be active from 5.0 s to 400.0 s. The frequency will range between 0.3 and 0.7 Hz with 0.1 Hz increments.

DM_AMPLM specifies the magnitude of the density based noise for each mode, “0.0, 0.0001, 0.0” generates noise in the fundamental mode (which affects total core power) resulting in a noise signal in total power of approximately 0.5%.

TF_AMPLM specifies the magnitude of the temperature noise for each mode, every mode is suppressed.

HARMON_F provides the HAR file from the PARCS standalone calculation, this gives PARCS the shapes necessary for modal noise.

Table B.5 lists the cards used in the TRAN block.

Table B. 5 Parameters Specified in the TRAN Block

Card	Field	Value	Description
CONV_TR	epsr2	10 ⁻⁴	Residual convergence criterion
	epsl2t	10 ⁻⁴	Global fission source convergence criterion
	epslinf	10 ⁻⁴	Local fission source convergence criterion
	epstft	10 ⁻²	Fuel temperature convergence criterion
SUM_EDIT	lsumopt(1)	T	Assembly power density edit
	lsumopt(2)	T	Axial power distribution edit
	lsumopt(3)	F	Assembly flux distribution edit
	lsumopt(4)	F	Axial flux distribution edit
EXCI_MOD	morder	3	Maximum number of spatial modes for noise
	ltimeab	0	Length of time table
WHIT_NOI	exctsta	5.0	White noise starting time
	exctend	400.	White noise ending time
	wnfmin	0.3	Minimal frequency of white noise, in Hz
	wnfmax	0.7	Maximal frequency of white noise, in Hz
	wnfstp	0.1	Frequency step size in white noise, in Hz
DM_AMPLM	dmamplm	0	Amplitudes of noise in coolant density for each spatial mode (random, fundamental and harmonic)
		0.0001	
		0	
TF_AMPLM	tfamplm	0	Amplitudes of noise in fuel temperature for each spatial mode (random, fundamental and harmonic)
		0	
		0	
HARMON_F	fileharm	"xxx.har"	Name of the file containing the harmonic shape necessary for modal noise.

3.5 TRACE/PARCS Mapping

For ATWS-ED the grouping was based on geometrical and fuel cycle considerations. This was possible because in a core with an Extended Power Uprate (EPU), the power shape is flattened and reload fractions are high [14], so position based grouping is similar to power grouping.

Under these circumstances, the fuel assemblies mapped into ring 2 of the vessel component were selected and defined as a peripheral region. The outermost assemblies in the peripheral region (with different effective loss coefficients for the lumped leakage flow path), were lumped together into channel 752, while the remaining assemblies were assigned to channels 751 (fresh assemblies) and 753 (burned assemblies).

The "interior" region of the core, mapped into ring 1 of the VESSEL, was divided in five annular regions with approximately the same number of assemblies. In each annular region, fresh and burned assemblies were separated and assigned to two different channels (251/252 for annular region 1, 351/352 for annular region 2, 451/452 for annular region 3, 551/552 for annular region 4 and 651/652 for annular region 5). Since the bundles that experience significant control would have a different exposure history relative to bundles of similar instantaneous power levels, further detail was introduced around the control rods which are "significantly" inserted (more than 10 steps inserted) either for BOC or PHE; for each of the seven control rods in a quadrant, two new channels were added (for fresh and burned bundles). The result was a

TRACE model with 27 channels, with mapping shown in Figure B.4. The resulting PARCS model is referred to as the 27-channel model.

For ATWS-I, the starting point was a TRACE model with 764 channels and one-to-one correspondence between neutronic and thermal-hydraulic nodes. It was verified that for all cases under consideration (BOC, PHE and EOFPL), the first harmonic plane was along the x-axis implying an axis of geometric symmetry along the y (vertical) axis. Taking this symmetry into account allowed reducing the number of channels from 764 to 382, as indicated in Figure B.5. The PARCS model employing this mapping scheme is identified as the 382-channel model. Section 3 of the main report discusses the comparison of the steady-state power distributions obtained from this model to GEH results, with reasonable agreement.

3.6 Exposure and Moderator Density History

Unless modeling a core with all fresh fuel, PARCS requires node-by-node burnup information. The information is found in the file with extension *.dep listed in the “DEPL” block of the PARCS input, under card “INP_HST.” The file can also contain history information, if available. For the present study, the exposure and moderator density history information was received from GEH [3] for the three points of the cycle under consideration (BOC, PHE, and EOFPL). The information was processed into a format that PARCS can read, by a FORTRAN program. The FORTRAN program performs two minor operations before reformatting the data:

- converts burnup from MWd/ST to MWd/kg
- converts from void history to moderator density history using a reference density of 739.7 kg/m³ [10]

To make use of the history information described above, the following is input in the “DEPL” block:

```
HST_OPT  F T F F F  !HCR HMD HSB HTF HTM
```

The second flag (set to True) indicates that the moderator density history information is to be used. It should be noted that there is no control rod history information available, hence the first flag is set to False. GEH also provided “spectrally corrected” void histories for BOC, PHE, and EOFPL. These files were processed as described above, and used in sensitivity calculations to determine their effect.

4 REFERENCES

1. T. Downar et al, "PARCS v3.0 U.S. NRC Core Neutronics Simulator Users Manual," UM-NERS-09-0001, University of Michigan and U.S. Nuclear Regulatory Commission, October 2010.
2. NRC, "TRACE V5.0 User's Manual," U.S. Nuclear Regulatory Commission, June 4, 2010.
3. J. Harrison, GE Hitachi, letter to U.S. Nuclear Regulatory Commission, "Response to NRC's Data Request to Support Confirmatory ATWS Calculations Regarding MELLLA Plus," MFN 09-681, November 4, 2009, ADAMS Accession No. ML093170371.
4. "General Electric Systems Technology Manual, Chapter 2.2, Fuel and Control Rods System," U.S. Nuclear Regulatory Commission, September 2011, ADAMS Accession No. ML11258A302.
5. L-Y. Cheng et al., "TRACE/PARCS Core Modeling of a BWR/5 for Accident Analysis of ATWS Events," *Trans. Am. Nucl. Soc.* 109, pp 979-982, November 2013.
6. Y. Xu and T. Downar, "GenPMAXS-V5 Code for Generating the PARCS Cross Section Interface File PMAXS," University of Michigan, December 2009.
7. P. Yarsky, "TRACE/PARCS Evaluation of Potentially Limiting ATWS Events with Core Instability for the ABWR," Proceedings of ICAPP 2013, paper F-010, Jeju Island, Korea, April 14-18, 2013.
8. T. Downar and D. Barber, "Final Technical Report," Task 3 of Task Order No. 8, Rev. 1, ESBWR Upgrades to TRAC-M, Under Contract NRC-04-02-054, Subtasks 3.1 and 3.2, Purdue University, February 2003.
9. R. Gamble, GE Nuclear Energy, letter to U.S. Nuclear Regulatory Commission, "Hypothetical ESBWR Core Design for TRACG Comparison," MFN 04-063, June 11, 2004, ADAMS Accession No. ML041740131.
10. D. Wang, B.J. Ade, and A.M. Ward, "Cross Section Generation Guidelines for TRACE/PARCS," NUREG/CR-7164 Oak Ridge National Laboratory, June 2013, ADAMS Accession No. 13204A296.
11. U.S. Nuclear Regulatory Commission, "Summary of Trip Report for Site Visit to Brookhaven National Laboratory October 2010," February 12, 2015, ADAMS Accession No. ML15043A803.
12. J. Harrison, GE Hitachi, letter to U.S. Nuclear Regulatory Commission, "Response to Supplemental NRC Information Requests 8 through 14 – Confirmatory ATWS Calculations Regarding MELLLA+," MFN10-213, July 29, 2010.
13. U.S. Nuclear Regulatory Commission, "Summary of Trip Report for Site Visit to Brookhaven National Laboratory August 2011," February 12, 2015, ADAMS Accession No. ML15043A806.

14. J. Harrison, GE Hitachi, letter to U.S. Nuclear Regulatory Commission, "Accepted Version of GE Licensing Topical Report NEDC-33006P-A, Revision 3 (TAC No. MD0277)," MFN 09-362, June 19, 2009, ADAMS Accession No. ML091800512.

APPENDIX C

MATLAB Script for Generating TRACE CHAN Input

TABLE OF CONTENTS

1	OBJECTIVE.....	C-3
2	INTRODUCTION.....	C-3
3	SPECIFICATIONS.....	C-3
4	INPUT DESCRIPTION.....	C-4
5	PROGRAM STRUCTURE.....	C-6
6	OUTPUT DESCRIPTION.....	C-8
7	LIMITATIONS TO EXPANDED / ALTERNATIVE USES.....	C-10
8	TEST PLAN.....	C-11
9	REFERENCES.....	C-11
	Attachment C1: Calculation of Rod Group-Specific Burnup Factors.....	C-12
	Attachment C2: Pre-Processing of FRAPCON Output.....	C-14

LIST OF TABLES

Table C.1	Inputs Embedded in the MATLAB Script (*.m file).....	C-5
Table C.2	TRACE Inputs Generated by the Channel-Generating Tool - CHAN Components.....	C-9
Table C.3	TRACE Inputs Generated by the Channel-Generating Tool - PIPE Components.....	C-10

1 OBJECTIVE

The objective of the channel-generating tool is to generate the required inputs for modifying an existing TRACE BWR plant model to a multi-CHAN core configuration. The output from the tool is to be inserted directly into the existing TRACE [1,2] plant model (ASCII file) to create a full multi-channel model. This channel-generating tool was implemented in MATLAB for its ease of use and flexibility [3].

2 INTRODUCTION

This channel generating tool is created to simplify the process of generating a multi-channel BWR model. In particular the tool was used to model a BWR/5 in TRACE for ATWS (anticipated transient without scram) analysis. The tool uses the CHAN component from an existing BWR plant model as a template and replicates it to create a multi-channel core. The tool utilizes the requisite PARCS mapping file and dep file to obtain the exposure for each fuel assembly and the grouping of fuel assemblies into different TRACE CHANs. Currently the tool is set up for a BWR core with 764 fuel assemblies; the generalization of the tool for other core sizes is discussed in a later section. Based on the PARCS channel map (supplied as input by the user) the tool determines the number of fuel assemblies represented by each CHAN. The user also specifies the core-averaged radial power factor for a quarter-core and the tool in turn assigns for each CHAN the appropriate radial power factor. The tool is set up to model four rod groups in each CHAN. For each rod group it processes the exposure data and the FRAPCON output (provided by the user as input) to provide the required inputs for the TRACE models for dynamic gap and the Modified Nuclear Fuels Industries (NFI) fuel thermal conductivity [4].

The following sections provide a discussion of features of the tool (Specifications), required inputs internal and external to the MATLAB script (Input Description), description of the structure of the program (Program Structure), integration of tool outputs to the TRACE model (Output Description), limitation and generalization of the tool (Limitations to Expanded/Alternative Uses) and testing of the script (Test Plan). Attachment C1 and C2 provide additional information on the processing of exposure data to provide the burnup for each rod group and the processing of the FRAPCON output, respectively.

3 SPECIFICATIONS

The channel-generating tool will create the required inputs by:

- spawning the multiple CHAN components using a single CHAN template
- using the PARCS channel mapping information to determine the number of fuel assemblies represented by each CHAN
- associating the CHAN components with the appropriate radial ring of the VESSEL component
- spawning a single junction PIPE to represent an effective side leakage path for each CHAN
- defining junction connections from each CHAN (inlet, outlet and side junction) to the VESSEL component
- associating the CHAN components with the POWER component. This is required in a standalone calculation with point kinetics (or a power table), and also in a coupled calculation to allow PARCS to deposit power in the CHAN components

The TRACE model of the BWR/5 used for the ATWS analysis uses advanced features of TRACE which require additional inputs, as described below:

- For each rod group, the input includes fuel rod gap gas properties (composition and pressure). This information is processed from FRAPCON output [5], and is used to provide input to the dynamic gap model of TRACE. The FRAPCON data is used to model the thermal conductivity of the individual gases, their mixtures, and ultimately the thermal conductivity of the gap needed to calculate the heat transfer between the pellet and the cladding.
- For each rod group and each axial location, the input includes burnup and gadolinia (Gd_2O_3) content information, and is used to calculate the fuel thermal conductivity with the Modified Nuclear Fuels Industries (NFI) Model. The assembly-dependent information was obtained from GEH, and individualized for each rod group as described in Attachment C1.
- The radial power profile (1/4 core) obtained from GEH is used to initialize the different channels. The core averaged axial power profile calculated from the GEH assembly-wise axial power profile is implemented in the POWER component to speed up the convergence of a coupled (TRACE/PARCS) steady-state calculation.

Ultimately, a series of text files are created that need to be inserted into the existing TRACE plant model to create a full multi-channel model.

4 INPUT DESCRIPTION

The channel-generating tool has internal and external inputs. The internal inputs are embedded in the MATLAB script (*.m file), and the external inputs are data files read in by the script. The internal inputs for a 764-assembly core are described in Table C.1.

Table C.1 Inputs Embedded in the MATLAB Script (*.m file)

Input Data Number	Input	Description
1	axial_parcs ²	Number of axial nodes in the PARCS model (core region, excludes reflectors) [1] ¹
2	parcs_length ²	Size in cm of the axial nodes in the PARCS model (core region, excludes reflector). [axial_parcs]
3	axial_trace ³	Total number of axial nodes in the TRACE CHAN component. [1]
4	trace_length ³	Size in cm of the axial nodes in the TRACE CHAN component. [axial_trace]
5	Map ²	Mapping between PARCS and TRACE. Same input found in the mapping file, replacing * with 0 [32x32]
6	ring	TRACE ring assignment. All assemblies within a particular channel have to be in the same ring or an error message will be generated. [32x32]
7	periph	Defines the peripheral assemblies with different leak flow path loss coefficients (1 – internal assembly; 2 – peripheral assembly). All assemblies within a particular channel have to be either internal or peripheral or an error message will be generated. This input should remain unchanged regardless of the number of distinct CHAN's to be generated. [32x32]
8	assemblies	Defines location of burnup data in .dep file. This input should remain unchanged regardless of the number of distinct CHAN's to be generated. [32x32]
9	radpowr	Assembly radial power distribution for ¼ core - core-averaged. This input will be different for BOC, PHE and EOFPL. [16x16]
10	axpowr	Radially-averaged axial power distribution This input will be different for BOC, PHE and EOFPL. [27]
11	F_FL	Burnup factors for Full Length (FL) rod group, as described in Attachment C1. [4]
12	F_PL	Burnup factors for Part Length (PL) rod group, as described in Attachment C1. [4]
13	F_GD	Burnup factors for Gadolinia (GD) rod group, as described in Attachment C1. [4]
14	F_HOT	Burnup factors for hot rod (HOT), as described in Attachment C1. [4]
15	filedep	Name (and path) of the dep file. This input is actually not “hardcoded”. During execution, user is prompted to select the dep file from a Windows dialog box. [1]
16	frapcon_FL	Name (and path where appropriate) of the processed FRAPCON output for a full length rod [1]
17	frapcon_PL	Name (and path where appropriate) of the processed FRAPCON output for a part length rod [1]
18	frapcon_GD	Name (and path where appropriate) of the processed FRAPCON output for a rod containing gadolinia [1]

¹ The bracketed numerical value represents the number of inputs required.

² These inputs should be consistent with the PARCS geom file and the mapping file.

³ These inputs should be consistent with the values in the single CHAN template.

The external inputs are the files with names defined in the *.m file, namely:

- Filedep; *.dep file processed from information received from GEH and is to be used as input to a PARCS steady-state calculation. A single use FORTRAN program was used to process the information received from GEH. The script can also read the exposure data in *.dep files as written by PARCS.
- frapcon_FL , frapcon_PL , frapcon_GD; processed FRAPCON output for a full length rod, a part length rod, and a rod containing gadolinia, respectively.

5 PROGRAM STRUCTURE

This section describes the structure of the channel-generating tool. The MATLAB script consists of three basic blocks, namely:

- input section, described above
- data manipulation section, described below
- output section, described in the next section.

In the data manipulation section, the operations are arranged in 22 blocks, as follows:

- Data manipulation block 1: check that the PARCS and TRACE axial dimensions are compatible.
- Data manipulation block 2: check that the dimensions of input arrays “map”, “ring”, “periph” and “assemblies” are compatible.
- Data manipulation block 3: read file with extension .dep into array **data(assembly number,PARCS axial level)**. [Assembly number varies from 1 to 764, and PARCS axial level from 1 to “axial_parcs”].
- Data manipulation block 4: define array **chan** listing the channel numbers (and the dummy value 0). They are obtained from array “map”. [For the 382 channel model, **chan** has 383 elements: 0 and channels number 201 to 582.]
- Data manipulation block 5: define variable **nchan**, number of channels in the model:
 - $nchan = \text{number of elements in “chan”} - 1$ (subtract for dummy value 0)
- Data manipulation block 6: define **n(i)**, the number of fuel assemblies in channel i. It is obtained from “map”. [Index ‘i’ corresponds to the channel, and varies from 2 to nchan+1]
- Data manipulation block 7: calculate **radcore(row, column)**, assembly radial power distribution for the whole core, defined by symmetry from input array “radpower”. [Indices ‘row’ and ‘column’ vary from 1 to 32.]
- Data manipulation block 8: calculate **pwrfra(i)**, channel power for **chan(i)**, by averaging “radcore(j,k)” for the fuel assemblies in **chan(i)**:

$$\text{○ } pwrfra(i) = \frac{\sum_{j,k} radcore(j,k)}{n(i)} \quad \forall (j,k) | \text{map}(j,k) = \text{chan}(i)$$

- Data manipulation block 9: define **ass_index(i,j)**, containing the MATLAB indices (identifiers equivalent to row and column) of the PARCS fuel assemblies in **chan(i)**. [Index ‘i’ varies from 2 to nchan+1, and index ‘j’ varies from 1 to n(i).]
- Data manipulation block 10: define **assid(i,j)**, containing the PARCS fuel assembly numbers in chan(i) corresponding to the MATLAB identifiers **ass_index(i,j)**. The PARCS

fuel assembly numbers are read from input array “assemblies”, for the positions identified by the MATLAB indices **ass_index(i,j)**. [Index ‘i’ varies from 2 to nchan+1, and ‘j’ varies from 1 to n(i).]

- Data manipulation block 11: determine whether **chan(i)** is interior (**int=1**) or peripheral (**int=2**). This information is read from input array “periph”, for the positions identified by the MATLAB indices **ass_index(i,1)**
- $int(i) = periph(ass_index(i,1))$ for $i = 2$ to $nchan+1$
- Data manipulation block 12: check that all fuel bundles in the channel are interior / peripheral:
- $periph(ass_index(i,j)) = periph(ass_index(i,1))$ for $i = 2$ to $nchan+1$ and $j = 2$ to $n(i)$
- Data manipulation block 13: determine in which ring (**trace_ring(i)**) each channel is located. This information is read from input array “ring”, for the positions identified by the MATLAB indices **ass_index(i,1)**
- $trace_ring(i) = ring(ass_index(i,1))$ for $i = 2$ to $nchan+1$
- Data manipulation block 14: check that all fuel bundles in the channel are in the same ring:
- $ring(ass_index(i,j)) = ring(ass_index(i,1))$ for $i = 2$ to $nchan+1$ and $j = 2$ to $n(i)$
- Data manipulation block 15: determine **nring**, number of rings in the model:
- $nring = \text{number of unique elements in “ring”} - 1$ (subtract for dummy value 0)
- Data manipulation block 16: calculate average **burnup(channel, PARCS axial level)**:

$$\circ \text{ burnup}(i, j) = \frac{\sum_{k=1}^{n(i)} \text{data}(assid(i, k), j)}{n(i)} \text{ for } i = 2 \text{ to } nchan + 1 \text{ and } j = 1 \text{ to } axial_parcs$$

- Data manipulation block 17: calculate channel average burnup **BU(channel, TRACE axial level)**, interpolating when needed. [Channel varies from 2 to nchan+1, and TRACE axial level from 1 to “axial_trace”.]
- Data manipulation block 18: calculate rod group specific burnup **BU_FL(channel, TRACE axial level), BU_PL(channel, TRACE axial level), BU_GD(channel, TRACE axial level), BU_HOT(channel, TRACE axial level)** using burnup factors “F_FL”, “F_PL”, “F_GD”, and “F_HOT” respectively.
- Data manipulation block 19: calculate **avg_bu(channel, rod group)**, axially averaged burnup for each rod group. It is needed to interpolate in the FRAPCON results. Axially-dependent rod group-specific burnup factors are used ($F_j(k)$, see Attachment C1):

$$avg_bu(i, n) = \frac{\sum_{k=1}^{axial_parcs} F_n(k) \text{ burnup}(i, k)}{\text{length of fuel rod } n} \text{ for } i = 2 \text{ to } nchan + 1 \text{ and } n = FL, PL, GD \text{ or } HOT$$

- Data manipulation block 20: read in FRAPCON results (files `frapcon_FL`, `frapcon_PL` and `frapcon_GD`).

- Data manipulation block 21: use axially averaged burnup (**avg_bu(channel, rod group)**) to interpolate in FRAPCON output to determine gap gas composition for each rod group in a channel (**he(i,n),h(i,n),ni(i,n),ar(i,n),kr(i,n),xe(i,n),h2o(i,n)**). Also calculate initial gap gas pressure **pres(i,n)**, interpolating P_g from FRAPCON output and based on Eq. 8-58 in [2]:

$$P_{g_i} = P_g \frac{T_{g_i}}{T_f}, \text{ where } T_{g_i} \text{ is the plenum gas temperature (assumed to be 298 K), and } T_f$$

is the fluid temperature at the top of the core (286°C). [Index 'i' varies from 2 to nchan+1, and index 'n' is FL, PL, GD or HOT.]

- Data manipulation block 22: renormalize so that:
- $he(i,n)+h(i,n)+ni(i,n)+ar(i,n)+kr(i,n)+xe(i,n)+h2o(i,n)=1$.

6 OUTPUT DESCRIPTION

The outputs of the channel-generating tool are six text files that are to be used to replace the corresponding components in the TRACE plant model. The files to be inserted into the existing TRACE model are (XXX is the number of channels in the model, and YYY is the point in the cycle, i.e., beginning-of-cycle, BOC, peak hot excess [reactivity], PHE, or end-of-full-power-life, EOFPL):

- headXXX_YYY.inp: contains the list of components (CHAN and PIPE components), to be pasted at the end of the "main data" section of the input deck.
- chanXXX_YYY.inp: full input for a custom number of channels (CHAN components), to be pasted in the "component data" section of the input deck. Table C.2 shows the TRACE inputs that require specialization from the MATLAB script. The rest of the inputs are merely echoed from the template.
- vesselXXX_YYY.inp: vessel source-connection cards, to be pasted in the appropriate place within the VESSEL component input. These inputs define the junctions from CHAN and PIPE components to the VESSEL. Each CHAN or PIPE is connected to the appropriate axial level and ring (trace_ring(i)) in the VESSEL component.
- sjcXXX_YYY.inp: custom number of single junctions, to be pasted in the "component data" section of the input deck. Each CHAN component is associated with a PIPE, defining the junction for the effective leak path for that CHAN. Table C.3 shows the TRACE inputs set by the MATLAB script.
- powerXXX_YYY.inp: POWER component, to be pasted in the "component data" section of the input deck. The POWER component lists all CHAN components, and specifies a radially-averaged axial power profile generated from data received from GEH (axpwr(z)).

Table C.2 TRACE Inputs Generated by the Channel-Generating Tool - CHAN Components

TRACE input (Card number)	Value	Defined in Manipulation Block #	Description
NUM (Card # 1)	chan(i)	4	CHAN component number
ID (Card # 1)	chan(i)	4	CHAN component user ID number
CTITLE (Card # 1)	\$chan(i)\$	4	CHAN component description
JUN1 (Card # 2)	1chan(i) ¹	4	Inlet junction
JUN2 (Card # 2)	2chan(i)	4	Outlet junction
JUNLK (Card # 4)	3chan(i) 4chan(i) 5chan(i)	4	Water rod inlet junction Water rod outlet junction Leak path junction
NCHANS (Card # 10)	n(i)	6	Number of bundles represented by CHAN chan(i)
FRIC (Card # 21)	depends on value of int(i)	11 (defines int(i))	Forward loss coefficients (value dependent on whether CHAN is interior or peripheral)
FRICR (Card # 22)	depends on value of int(i)	11 (defines int(i))	Reverse loss coefficients (value dependent on whether CHAN is interior or peripheral)
IDROD (Card Set # 42)	trace_ring(i)	13	Vessel ring number that the outer surface of the canister is connected to.
RADPW (Card Set # 55)	pwrfra(i)	8	Core wide radial CHAN-to-CHAN power peaking factor (axial dependence is taken into account in the POWER component).
GMIX (Card Set # 58)	he(i,n),ar(i,n),xe(i,n),kr(i,n),h(i,n),ni(i,n),h2o(i,n)	22	Mole fraction (–) of gap-gas constituents for rod group n (helium; argon; xenon; krypton; hydrogen; air/nitrogen; water vapor). Given for all rod groups.
PGAPT (Card Set # 59)	pres(i,n)	21	Average initial gap-gas pressure (Pa) for rod group n. Given for all rod groups
BURN (Card Set # 60)	BU(i,j)	18	Fuel burnup at each axial location j (MWD/MTU). Given for all rod groups (rod group factors described in Attachment C1 apply).

¹ Strings are concatenated to obtain unique junction numbers for each CHAN.

Table C.3 TRACE Inputs Generated by the Channel-Generating Tool - PIPE Components

TRACE input (Card number)	Value	Defined in Manipulation Block #	Description
NUM (Card # 1)	6chan(i)	4	PIPE component number
ID (Card # 1)	6chan(i)	4	PIPE component user ID number
CTITLE (Card # 1)	\$6chan(i)\$	4	PIPE component description
JUN1 (Card # 3)	5chan(i)	4	Leak path junction to CHAN component
JUN2 (Card # 3)	7chan(i)	4	Leak path junction to VESSEL component
NPIPES (Card # 10)	n(i)	6	Number of parallel pipes represented by PIPE 6chan(i)
FRIC (Card # 19)	depends on value of int(i)	11 (defines int(i))	Forward loss coefficients (value dependent on whether CHAN is interior or peripheral)
FRICR (Card # 20)	depends on value of int(i)	11 (defines int(i))	Reverse loss coefficients (value dependent on whether CHAN is interior or peripheral)

The following TRACE input parameters need to be manually updated:

- ncomp (number of components) – each new CHAN results in the addition of two new components
- njun (number of junctions) – each new CHAN results in the addition of four new junctions
- ncsr (number of junction connections to VESSEL) – each new CHAN results in the addition of three new junction connections

7 LIMITATIONS TO EXPANDED / ALTERNATIVE USES

The channel-generating tool was developed to generate inputs for a BWR/5 for ATWS analysis. While some flexibility has been implemented to accomplish the objectives set for this application, there are some limitations to a potential use in different applications:

- BWR/5- and ATWS- specific information was used to generate the templates used by the channel-generating tools. This information includes:
 - the number of fuel assemblies in the core – 764
 - the number of rod groups in each CHAN – 4
 - the number of rod types - 3
 - core symmetry – 1/4
 - gadolinia concentration for each rod group (assumed to be the same for all fuel assemblies)
 - inlet loss coefficients for interior and peripheral assemblies
 - loss coefficients for leak path junctions (different for interior/peripheral fuel assemblies)
- Other information that has been hard-coded includes:
 - the multiplicative factors to assign burnup to rod groups, as explained in Attachment C1.
 - the reference temperature to calculate the initial gap pressure

It should be noted that all these parameters can be easily changed in the script, but they have not been assigned to a variable or considered an input.

The script has been set up to potentially allow a user-specified number of axial nodes in the TRACE model. However, the initial conditions for the CHAN inputs (such as temperature, pressure, and flow velocity) included in the template assume a specified number of axial nodes (37). The generalization is straightforward by specifying reasonable initial values for the axial_trace nodes. In the current script all CHANs inherit the same initial conditions from the single CHAN template and there is no provision to allow specifying realistic profiles for each CHAN separately that might speed up convergence.

8 TEST PLAN

The data manipulations performed during execution are very basic, and take advantage of built-in MATLAB functions. However, the amount of information processed through the script is very large, and it is important to guarantee the accuracy of the flow of data. To verify it, the script was modified in the following manner:

- The array “map” was modified to include a new channel with two fuel assemblies (# 19 and # 20).
- The vector “parcs_length” was modified so that some TRACE nodes spread over two PARCS nodes, requiring interpolation.

The burnups calculated and output by the script were compared against manually calculated results, and found to be in agreement. The gas composition data were also spot-checked against manually calculated results and found in agreement.

9 REFERENCES

1. NRC, “TRACE V5.0 User’s Manual,” U.S. Nuclear Regulatory Commission, June 2010.
2. NRC, “TRACE V5.0 Theory Manual,” U.S. Nuclear Regulatory Commission, June 2010.
3. The Mathworks, Inc., “R2011a Documentation – MATLAB”, Retrieved June 30, 2011, from <http://www.mathworks.com/help/techdoc/>
4. K. Ohira and N. Itagaki, "Thermal Conductivity Measurements of High Burnup UO₂ Pellet and a Benchmark Calculation of Fuel Center Temperature," Proceedings of the ANS International Topical Meeting on LWR Fuel Performance, pp. 541-549, Portland, Oregon, March 2-6 1997.
5. K.J. Geelhood and W.G. Luscher, “FRAPCON-3.4: A Computer Code for the Calculation of Steady-State Thermal-Mechanical Behavior of Oxide Fuel Rods for High Burnup”, NUREG/CR-7022, Pacific Northwest National Laboratory, March 2011.
6. J. Harrison, GE Hitachi, letter to U.S. Nuclear Regulatory Commission, “Response to NRC’s Data Request to Support Confirmatory ATWS Calculations Regarding MELLLA+,” MFN 09-681, November 4, 2009, ADAMS Accession No. ML093170371.
7. R. Kingston, GE Hitachi, letter to U.S. Nuclear Regulatory Commission, “Response to Portion of NRC Request for Additional Information Letter No. 350, ESBWR Design

Attachment C1:

Calculation of Rod Group-Specific Burnup Factors

The correlation chosen to calculate the fuel thermal conductivity for UO₂ fuel includes the effects of burnup and gadolinia (Gd₂O₃) content. Those parameters are input specified, and vary according to axial height and rod group.

The information received from GEH [6] provides the average assembly burnup for each axial level. This information needs to be converted into the rod group specific burnup used by TRACE. The burnup for rod group i (BU_i) is defined as:

$$BU_i(z) = \frac{\frac{n_i(z) E_i(z)}{n_i(z) m_i(z)}}{\frac{\sum_j n_j(z) E_j(z)}{\sum_j n_j(z) m_j(z)}} \times BU(z) = F_i(z) \times BU(z) \quad \text{Eq. 1}$$

Where BU(z) is the average assembly burnup provided by GEH, n_j the number of rods in group j, and E_j and m_j the energy generated and mass of uranium respectively for rods in rod group j. The relative burnup factors F_i then are:

$$F_i(z) = \frac{\frac{n_i(z) E_i(z)}{\sum_j n_j(z) E_j(z)}}{\frac{n_i(z) m_i(z)}{\sum_j n_j(z) m_j(z)}} \quad \text{Eq. 2}$$

Four different rod groups are represented in the BWR/5 ATWS TRACE model [6]:

- full length rod group with 62 rods (FL)
- part length rod group with 14 rods (PL)
- gadolinia rod group with 15 rods with 7 wt% Gd₂O₃ (8% gadolinia rods and partial length gadolinia rods are included here) (GD)
- hot rod – assumed to be a full length rod (HOT)

Each rod group is tied to a different type of fuel rod. The mass of uranium varies in different fuel rods and it is denoted by a rod-specific variable:

m_{FL} = m_{HOT} = mass of uranium in a full length fuel rod
 m_{GD} = mass of uranium in a fuel rod with gadolinia
 m_{PL} = mass of uranium in a partial length fuel rod

The hot rod is assumed to become hot instantaneously, i.e. it is burned like a regular full length rod. The part length and full length rods are assumed to have the same power density. Thus

$E_{PL}(z) = E_{FL}(z)$ for the length of the partial length rod. For the rods with gadolinia a power suppression factor, P_{sf} [7], is applied and,

$$E_{GD} = (1 - P_{sf}) E_{FL} \quad \text{Eq. 3}$$

The E_j and m_j that are required to calculate the F_i in Eq. 1 are summarized below for each axial segment of the fuel rods.

- Bottom natural uranium blanket:
 - $m_{FL}(z) = m_{PL}(z) = m_{GD}(z) = m_{HOT}(z)$
 - $E_{FL}(z) = E_{PL}(z) = E_{GD}(z) = E_{HOT}(z)$
 - $F_{FL}(z) = F_{PL}(z) = F_{GD}(z) = F_{HOT}(z) = 1$

- Within the Enriched uranium segment of the partial length fuel rod:
 - $m_{FL}(z) = m_{PL}(z) = m_{HOT}(z)$
 - $m_{GD}(z) = m_{FL}(z) * m_{GD} / m_{FL}$
 - $E_{FL}(z) = E_{PL}(z) = E_{HOT}(z)$
 - $E_{GD}(z) = (1-P_{sf}) E_{FL}(z)$

- Segment above the partial length rods:
 - $m_{FL}(z) = m_{HOT}(z)$
 - $m_{GD}(z) = m_{FL}(z) * m_{GD} / m_{FL}$
 - $m_{PL}(z) = 0$
 - $E_{FL}(z) = E_{HOT}(z)$
 - $E_{PL}(z) = 0$
 - $E_{GD}(z) = (1-P_{sf}) E_{FL}(z)$
 - $F_{FL}(z) = F_{HOT}(z)$
 - $F_{PL}(z) = 0$ (part length rod not present)
 - $BU_{PL} = 0$

- Top natural uranium blanket :
 - $m_{FL}(z) = m_{HOT}(z)$
 - $m_{GD}(z) = m_{PL}(z) = 0$
 - $E_{FL}(z) = E_{HOT}(z)$
 - $E_{PL}(z) = E_{GD}(z) = 0$
 - $F_{FL}(z) = F_{HOT}(z) = 1$
 - $F_{PL}(z) = F_{GD}(z) = 0$ (part length and gadolinia rods not present)

Attachment C2:

Pre-Processing of FRAPCON Output

Table C2.1 FRAPCON Output Filenames

Filename	Description
GE14FLRc1	FRAPCON output for a full length rod
GE14plra1	FRAPCON output for a partial length rod
GE14gad07	FRAPCON output for a rod with gadolinia

The following FORTRAN program pre-processes output from FRAPCON -3.4a (filenames above) into a format read by the MATLAB script.

```
c  program to extract information from FRAPCON-3.4a
c  and re-format it to be read by a matlab script.
  character*15 line
  character*120 space
  bu_last=-1.
10 continue
  read(5,20,end=999) line
  if(line.ne.'power-time step') go to 10
20 format(57x,a15,i4)
  backspace 5
c  time step number
  read(5,20) line,no
  read(5,*)
c  burnup (MWd/mtU)
  read(5,30) bu
30 format(65x,f6.0)
  if (bu==bu_last) then
    bu=bu+0.1
  endif
  do i=1,4
    read(5,40) space
  enddo
40 format(a120)
c  he gas composition cumulative fraction
  read(5,50) frhe
50 format(120x,f5.3)
60 format(f5.3)
c  h gas composition cumulative fraction
  read(5,50) frh
c  plenum temperature (K) and n gas composition cumulative fraction
  read(5,55) plenum,frn
55 format(36x,f4.0,80x,f5.3)
c  gap temperature (K) and ar gas composition cumulative fraction
  read(5,55) gap,frar
c  kr gas composition cumulative fraction
  read(5,50) frkr
c  xe gas composition cumulative fraction
```

```

    read(5,50) frxe
c   h2o gas composition cumulative fraction
    read(5,50) frh2o
    do i=1,3
    read(5,40) space
    enddo
c   rod internal gas pressure (mpa)
    read(5,70) rigp
    70 format(54x,f5.3)
    write(6,90) no,bu,plenum,gap,frhe,frh,frn,frar,frkr,frxe,frh2o,
    & rigp
    90 format(i4,2x,f7.1,2f6.0,8f8.3)
c   go to next time step
    bu_last=bu
    go to 10
999 continue
    End

```


BIBLIOGRAPHIC DATA SHEET

(See instructions on the reverse)

1. REPORT NUMBER
(Assigned by NRC, Add Vol., Supp., Rev., and Addendum Numbers, if any.)

NUREG/CR-7179
BNL-NUREG-105325-2014

2. TITLE AND SUBTITLE

BWR Anticipated Transients Without Scram in the MELLLA+ Expanded Operating Domain Part 1: Model Developments and Events Leading to Instability

3. DATE REPORT PUBLISHED

MONTH	YEAR
June	2015

4. FIN OR GRANT NUMBER

V6150 / F6018

5. AUTHOR(S)

Lap-Yan Cheng, Joo-Seok Baek, Arantxa Cuadra, Arnold Aronson, David Diamond, Peter Yarsky

6. TYPE OF REPORT

Technical

7. PERIOD COVERED (Inclusive Dates)

6/1/10 - 6/30/15

8. PERFORMING ORGANIZATION - NAME AND ADDRESS (If NRC, provide Division, Office or Region, U. S. Nuclear Regulatory Commission, and mailing address; if contractor, provide name and mailing address.)

Nuclear Science & Technology Department
Brookhaven National Laboratory
Upton, NY 11973-5000

9. SPONSORING ORGANIZATION - NAME AND ADDRESS (If NRC, type "Same as above", if contractor, provide NRC Division, Office or Region, U. S. Nuclear Regulatory Commission, and mailing address.)

Division of Systems Analysis
Office of Nuclear Regulatory Research
U.S. Nuclear Regulatory Commission
Washington, DC 20555-0001

10. SUPPLEMENTARY NOTES

Tarek Zaki, NRC Project Manager

11. ABSTRACT (200 words or less)

We developed models of a BWR/5 boiling water reactor for use with TRACE/PARCS and thereafter to analyze anticipated transients without scram (ATWS). We established the models for three different times during a fuel cycle, and included therein all systems needed for events initiated by turbine trip or the closure of a main steamline isolation valve. They include the standby liquid-control system, recirculation pumps, feedwater and water level control, reactor core isolation cooling system, safety and relief valves, suppression-pool cooling, and other systems. The modeling in the core that we undertook is detailed relative to state-of-the-art models, with four different fuel-rod types included in each fuel assembly, and 382 channels to represent all assemblies, taking into account half-core symmetry.

The models we developed can be used for multiple ATWS applications, and for many transients with the reactor trip operational. The regulatory purpose of the current work is to demonstrate the use of TRACE/PARCS in evaluating the potential consequences of ATWS events in BWRs operating under MELLLA+ conditions. Our study offers insights into the reactor's behavior during these events, and in particular the impact of assumed operator actions on the observed oscillatory behavior caused by the reactor's instability and on the eventual shutdown of the reactor. In addition, our study examined the ability of the TRACE/PARCS code system to calculate the complex phenomena during these events. We also gained insights into effective modeling of those phenomena. Hence, this study may be used as a basis for developing rigorous modeling guidance for similar application.

12. KEY WORDS/DESCRIPTORS (List words or phrases that will assist researchers in locating the report.)

TRACE/PARCS; Anticipated Transients Without Scram (ATWS); Boiling Water Reactor (BWR); operator action; safety analysis; stability analysis; Maximum Extended Load Line Limit Analysis Plus (MELLLA+)

13. AVAILABILITY STATEMENT

unlimited

14. SECURITY CLASSIFICATION

(This Page)

unclassified

(This Report)

unclassified

15. NUMBER OF PAGES

16. PRICE



Federal Recycling Program



**UNITED STATES
NUCLEAR REGULATORY COMMISSION**
WASHINGTON, DC 20555-0001

OFFICIAL BUSINESS



NUREG/CR-7179

**BWR Anticipated Transients Without Scram in the MELLLLA+ Expanded
Operating Domain, Part 1**

June 2015